



**University of Sheffield
Department of Mechanical Engineering**

Hybrid RANS-LES Simulations for Separated Flows Using Dynamic Grids

N. I. Durrani

Supervised by Prof. Ning Qin

March 2009

This thesis is submitted to University of Sheffield in partial fulfilment of the requirement for the degree of Doctor of Philosophy.

Abstract

A hybrid RANS-LES approach is used in this thesis to simulate the unsteady aerodynamic flows. Different cases are investigated such as high Reynolds number flows around a circular cylinder, flows over an Aerospatiale A-aerofoil at stall conditions and flows around a flapping wing with mesh deformation. The Dynamic Grid Detached Eddy Simulation (DG-DES) is an in-house solver developed at the University of Sheffield. It is a message passing interface (MPI) code which uses the URANS, DES and DDES techniques with dynamic grid capability. The RANS formulation is used in the code with one equation Spalart-Allmaras (S-A) turbulence model. The S-A turbulence model is used in the frame work of a common hybrid RANS-LES formulation termed as the Detached-Eddy Simulation (DES) and Delayed Detached-Eddy Simulation (DDES).

The results presented in this research contain the simulations of the transonic speed steady state flows over the RAE2822 and the ONERA M6 wing. These simulations are carried out using single and double precision versions of the solver with different simulation techniques. A good comparison of results with the experimental data is achieved. It has also served as a validation of new additions in the code made by the author. These include addition of the inviscid flux calculation schemes (AUSM and HLLC schemes), the turbulence scheme (DDES) and double precision implementation in the solver.

A detailed analysis of the A-airfoil at the Reynolds number of 2×10^6 and angle of attack $\alpha = 13.3^\circ$ has been carried out using the URANS, DES and DDES schemes. Encouraging results were obtained for different flow parameters including lift coefficient, drag coefficient and modelled stresses in comparison with the experimental data. It was observed that for this particular case, the DES scheme does not function in accordance with its original concept. Due to the thick trailing edge boundary layer, the switching to LES mode is done by the DES within the boundary layer. As per the basic principle of the DES scheme, the whole of the boundary layer is to be treated in RANS mode. This premature switching is known to cause the modelled stress depletion (MSD) in the flow domain. The implementation of DDES solves this irregularity and the LES to RANS switching is delayed to work in accordance with the basic DES principle by

treating the whole of the attached boundary layer in the RANS mode. A detailed comparison of the Reynolds stresses is also carried out on the suction side with the experimental data. It is concluded that due to the premature switching from RANS to LES mode, the Reynolds stresses computed by the DES scheme are reduced at the trailing edge of the suction side. However, the DES simulation also predicts the flow separation at the suction side of the trailing edge in accordance with the experimental observations. The Reynolds stresses computed by the DDES scheme are similar to the URANS results. Both the URANS and DDES simulations fail to predict the trailing edge separation. It is argued that despite the premature switching, the DES scheme presents a better flowfield picture as compared with the DDES which is found to be overly dissipated for this particular case. It can be observed that this case may not be a well posed 'natural DES problem' because the flow separation is not very rapid as required by natural DES flows. The results from the DES solution clearly show that a reduced dissipative level for the thick boundary layers near trailing edge presents better quality of the solution, in contrast with RANS and DDES. Modelled and resolved turbulent stresses were calculated using DES and DDES schemes. It is observed that for this particular case the major contribution is from modelled stresses and the resolved stresses are negligible.

The circular cylinder flow with aspect ratio of 2 is simulated at different Reynolds numbers of 1.4×10^5 , 3.6×10^6 and 8×10^6 . The comparison of the resolved stresses is carried out with the experimental data and satisfactory results are obtained. The comparison of the modelled and resolved stresses is also carried out to highlight the impact of the resolved and modelled stresses for highly separated flows. A probe point is located two diameters downstream of the circular cylinder at the symmetry plane and instantaneous data for primitive variables is stored to compare the instantaneous results of primitive variables from the DES and DDES schemes. The power spectral density plot at the same point for both the DES and DDES schemes is compared to show the energy content with the size of the eddies (high frequency corresponds to smaller eddies). This shows the energy decay as represented by the Kolmogorov's energy spectrum.

Two and three dimensional Delaunay Graph based mesh deformation was incorporated in the respective two and three dimensional versions of the solver DG-

DES. Initial results from both 2D and 3D solvers are presented. NACA0033 with a flexible tail is simulated using the 2D Delaunay Graph based mesh deformation. The results capture the flow physics well including the vorticity contours during the flapping motion. The computed coefficient of thrust (C_T) for the case with the tail thickness $b/c=0.56 \times 10^{-3}$ at Strouhal number of 0.34 is compared with the experimental data and produces 30% lower values. The MPI version of the DGDES solver is used to simulate the numerical simulation of flow over a NACA0012 wing with the mesh deformation capability. The NACA0012 wing (with a span of 4 times chord length) is simulated for oscillating motion. The wing is fully rigid and this case is essentially 2D oscillating wing. The resultant instantaneous coefficient of thrust is in good agreement with the experimental data.

Road map of thesis

Chapter 1: An introduction of the computational aerodynamics, insight of the turbulence and energy cascade mechanism as envisaged by Kolmogorov is presented. It covers a brief introduction of the numerical techniques used in the CFD. It covers the RANS, LES, DNS and DES schemes.

Chapter 2: The basic formulation and discretization techniques used in the solver DG-DES, are covered in this chapter. It also covers the dual-time stepping with the arbitrary Lagrangian-Eulerian formulation (ALE), one equation Spalart-Allmaras (S-A) turbulence model with the details of switching to the detached-Eddy simulation (DES). The discretization methodology and boundary conditions are also discussed.

Chapter 3: The simulation results from two steady state validation cases; the RAE2822 airfoil and Onera M6 wing are presented with all the different available options in the DG-DES solver.

Chapter 4: A detailed analysis of the Aerospatiale A-airfoil is presented in this chapter. The importance of a basic requirement of the DES that the whole of boundary layer is to be treated in the RANS mode is highlighted. The modelled stress depletion (MSD), due to the premature switching of this original DES is discussed. The DDES simulations are carried out in order to avoid this premature switching problem. The turbulence parameters from the URANS, DES and DDES are compared with the experimental data. It also includes the comparison of the modelled stresses computed using the DES and DDES with the experimental data.

Chapter 5: A circular cylinder with massive flow separation is simulated at high Reynolds numbers. Three different Reynolds numbers of 1.4×10^5 , 3.6×10^6 and 8×10^6 are simulated. The comparison of the simulated results with the experimental data is presented as well.

Chapter 6: The moving mesh cases of in the two and three dimensions are presented in this chapter. The deformation of the grid is based on using the Delaunay triangulation based methodology.

Chapter 7: It contains the conclusions from present research and future work recommendations.

*To my parents and whole of my
family....*

Acknowledgements

I would like to thank the almighty Allah for enabling and empowering me for whatever I have been able to do.

My foremost gratitude and thanks are for my supervisor, Professor Ning Qin; who has transformed me to a very different person as compared with what I was at the start of my PhD, in terms of the knowledge, rational approach and personality. I am highly indebted to his guidance, advice and encouragement that he has given to me over the years. I am certain that I could not have made it this far without his help and support; both administratively and academically. His kindness and patience throughout my studies is gratefully acknowledged. I am very happy and satisfied with whatever I have been able to achieve during my studies under his supervision.

I want to acknowledge the dedication, love and diligence of whole of my family during my studies. My parents were hospitalized in my absence but they asked me to carry on with my studies despite my strong desire to stay back with them. Unfortunately, my father passed away without seeing his dreams come true. Nevertheless, he remains the biggest source of motivation for all my endeavours. A big credit goes to my wife Mubashra and my kids Alishba, Huzaifah and Aleeza for their love and support through all these extremely depressing and grief-stricken times. Aleeza was born 3 months before the submission of this thesis and I have all my praises for courage and support of Mubashra during this time. I also deeply appreciate the support and help from my loving brother Shahzad and sisters Iram and Arjumand.

I would like to thank my senior colleague Dr. Sajid Raza Ch. for his selfless and sincere efforts for me. It would have been extremely difficult for me to reach to this stage without his support. I would also like to thank Dr. Frank Nicolleau for his very kind guidance and encouragement to me, especially during the last part of my MSc. I would also like to thank Prof. Rob-Dwyer Joyce, Hassan Masood and Mrs. Jean Hoskins for their help.

I would like to thank all my group mates; Sam Wong, Demian Defeo, Hongwei Zheng, Mahmoud Ahmed, Mohamed Mohamed, Ezzidine Elarabi, Elhadi Elhadi, Gamal Abo Elyamin, Wil Dube, Yibin Wang and all others for supporting and helping me throughout my study here. I am thankful to Mohamed for teaching me the Arabic

language. Mahmoud Ahmed and Gamal Abo Elyamin have also helped me with Arabic. I would like to appreciate the special help and support from Alan Le Moigne, Hao Xia and Greg Carnie. I have learned a lot from Hao Xia and I am grateful for his untiring support and guidance to me. Without his help I would have struggled a lot.

I would like to thank Chris Armstrong from NAG, Oxford for being very helpful in porting our code to HECToR cluster and helping in sorting some coding bugs with different compilers. I would like to thank Charles Mockett for some enlightening discussions on turbulence. I would also like to thank Dr. Phillipe Spalart and Dr. Florian Menter for their guidance and discussions over DES, DDES and SAS.

It is gratefully acknowledged that this research was funded by an Overseas Research Scholarship (ORS) and the departmental fee waiver from the Department of Mechanical Engineering, University of Sheffield. I also want to acknowledge the use of different computational facilities I have been able to use namely; Hector, Bluegrid, Greengrid and Snowdon.

Table of Contents

Abstract.....	i
Road map to thesis.....	iv
Dedication.....	vi
Acknowledgment.....	vii
Table of Contents.....	ix
List of Figures.....	xiv
List of Tables.....	xxiv
Nomenclature.....	xxvi

1 Introduction

1.1 Computational Aerodynamics.....	1
1.2 Turbulence.....	3
1.2.1 Physical description of the turbulence.....	4
1.2.2 Kolmogorov's energy spectrum.....	5
1.3 Turbulence modelling.....	6
1.3.1 Averaging/ filtering.....	7
1.3.1.1 Conventional Reynolds averaging.....	7
1.3.1.2 Favre (density) averaging – RANS formulation.....	8
1.3.1.3 Spalart-Allmaras (S-A) turbulence model.....	10
1.3.1.4 Spatial averaging/ filtering – LES formulation.....	13
1.3.1.5 Comparison of resulting equations of RANS and LES.....	14
1.4 CFD approaches to the turbulence simulation.....	15
1.4.1 Direct numerical simulation (DNS).....	16
1.4.2 Large eddy simulation (LES)	19
1.4.3 Reynolds's averaged Navier-Stokes equations (RANS).....	21
1.4.4 Hybrid schemes.....	24
1.4.4.1 Detached eddy simulation (DES).....	25

1.4.4.2	Delayed Detached Eddy Simulation (DDES).....	28
1.5	Turbulent Reynolds Stresses.....	29
1.5.1	Derivation of the Modelled Reynolds Stress formula [based on Bradshaw’s Formulation].....	29
1.5.2	Resolved Turbulent Reynolds Stresses.....	32
1.6	A brief description of the present research work.....	32
1.6.1	Work related to programming-Contributions to the in-house solver development.....	32
1.6.2	Scientific research contributions.....	33

2 Mathematical Formulations of Governing Equations

2.1	Introduction.....	34
2.2	Discretization of the governing equations.....	37
2.3	Pre-conditioning.....	42
2.4	Dual time stepping procedure.....	46
2.5	Runge-Kutta time stepping scheme.....	51
2.6	Reconstruction of the solution variables.....	52
2.6.1	Evaluation of the gradient at the face centre	53
2.7	Calculations of the Inviscid Fluxes.....	54
2.7.1	Roe’s flux difference splitting scheme.....	54
2.7.1.1	Dissipation control through the Upwinding parameter.....	57
2.7.2	AUSM flux splitting scheme.....	58
2.7.2.1	Mass flux.....	59
2.7.2.2	Pressure flux.....	59
2.7.3	HLLC flux splitting scheme.....	60
2.8	Moving mesh with the arbitrary Lagrangian-Eulerian formulation.....	62
2.9	Spring tension analogy.....	64
2.10	Delaunay graph mapping.....	65
2.11	Geometric conservation law (GCL).....	65

3 Preliminary Validation for Steady-state Cases

3.1	RAE2822 aerofoil.....	66
3.2	Onera M6 Wing at Transonic Mach Number.....	69
3.2.1	Case setup.....	69
3.2.2	Mesh details.....	69
3.2.3	Results and discussion.....	69
3.3	Conclusions.....	76

4 A-Airfoil at Maximum Lift Configuration

4.1	Introduction.....	77
4.2	CFD simulation.....	81
4.2.1	Geometry.....	81
4.2.2	Computational Mesh.....	81
4.2.3	Boundary conditions.....	83
4.2.4	Computational time statistics	83
4.2.5	URANS and the DES simulation results.....	86
4.2.6	DDES simulation results.....	96
4.2.7	Time statistics of all the schemes used.....	102
4.2.8	Convergence of the simulations.....	104
4.2.9	Comparison of the lift and drag coefficients.....	104
4.2.10	Observation regarding the RANS-LES region in the DDES.....	104
4.3	Comparison of the Turbulent Reynolds Stresses using the RANS, DES and DDES with the experimental data.....	105
4.3.1.1	Suction side of the A-airfoil.....	105
4.3.1.2	Wake region analysis.....	114
4.4	Conclusions.....	117

5 High Reynolds number flows over a Circular Cylinder

5.1	Introduction.....	119
-----	-------------------	-----

5.2	Reynolds Number 1.4×10^5	120
5.2.1	Mesh Statistics.....	120
5.2.2	Numerical simulation details.....	120
5.2.3	Results with 1 st order spatial accuracy.....	122
5.2.4	Results with 2 nd order spatial accuracy.....	124
5.2.5	Probe data extraction for DES and DDES flowfield analysis.....	129
5.2.6	Summary of the results $Re=1.4 \times 10^5$	131
5.2.7	Comparison of the velocity flowfield in the domain.....	131
5.2.8	Comparison of the Reynolds stresses from the DES simulation with the experimental data.....	133
5.3	Reynolds Number 3.6×10^6	134
5.3.1	Yplus.....	134
5.4	Circular cylinder at the Reynolds number 8×10^6	138
5.4.1	Yplus.....	138
5.4.2	C_l C_d plot circular cylinder at Reynolds number 8×10^6	139
5.4.3	Vorticity Magnitude contours.....	139
5.4.4	URANS.....	141
5.4.5	Laminar Flow.....	141
5.4.6	Comparison of the modelled and resolved stresses using the DES scheme.....	143
5.5	Conclusions.....	145

6 Flapping Wing with Delaunay based moving mesh

6.1	Introduction.....	146
6.2	Case setup and Mesh Deformation.....	148
6.2.1	Mesh Details.....	149
6.2.2	Tail motion specification.....	151
6.2.3	Fast Grid Deformation using Delaunay Graph Mapping.....	152
6.2.4	Numerical Simulation of Flapping aerofoil.....	157
6.2.5	Comparison of fluid properties for numerical simulation	

	and the experimental data	158
6.2.6	Defining Stiffness of different thickness flat plates.....	159
6.2.7	Results.....	160
6.2.8	Conclusions.....	163
6.3	3D implementation of Delaunay Graph Mapping based mesh deformation in the DGDES solver.....	164
6.3.1	Oscillating NACA0012 Wing.....	164
6.3.2	Case details.....	166
6.3.3	Boundary Conditions.....	167
6.3.4	Results.....	167
6.3.5	Conclusions.....	172
7	Concluding Remarks, Recommendations and Future Work Perspectives	
7.1	Conclusions.....	173
7.2	Future Work Perspectives-Short recap and new trends	175
7.2.1	Generation of LES content.....	176
7.2.2	NASA Common Research Model (CRM).....	177
7.2.3	Pre-processing tool (Gambit or Gridgen).....	178
7.3	Hybrid RANS-LES methodology for wall layer models for LES.....	178
7.4	Hybrid RANS-LES methods with moving grids.....	179
	References.....	180
	List of publications.....	189
Appendix A	3D preconditioning matrix	190
Appendix B	Implementation of reading the Gridgen FVUNS format input in DGDES – A test case of DLR-F6 Aircraft (wing-body-nacelle).....	195

List of Figures

Figure 1.1	<i>First documented sketch of turbulence.....</i>	<i>3</i>
Figure 1.2	<i>Turbulent flow over circular cylinder at Reynolds number 3.6×10^6.....</i>	<i>3</i>
Figure 1.3	<i>Sketch of Kolmogorov's Energy spectrum with energy distribution.....</i>	<i>6</i>
Figure 1.4	<i>Spatial filtering in 1-D with $\Delta x = 0.02$.....</i>	<i>13</i>
Figure 1.5	<i>Concept of the different approaches for turbulence Simulation.....</i>	<i>16</i>
Figure 1.6	<i>General range of RANS, LES and DNS based on Reynolds number for real life industrial applications.....</i>	<i>18</i>
Figure 1.7	<i>Gaussian Cutoff Filtering.....</i>	<i>20</i>
Figure 1.8	<i>Sketch showing LES with the perspective of Kolmogorov Energy spectrum.....</i>	<i>20</i>
Figure 1.9	<i>Ensemble averaging in stationary and non-stationary flows.....</i>	<i>22</i>
Figure 2.1	<i>Knudsen number regimes.....</i>	<i>36</i>
Figure 2.2	<i>Size in meters of different objects and flow domains under CFD simulation.....</i>	<i>37</i>
Figure 2.3	<i>Flow chart of dual time stepping.....</i>	<i>47</i>
Figure 2.4	<i>Representation of effect of lower and higher order reconstruction.....</i>	<i>52</i>
Figure 2.5	<i>A simple 2d domain with 2 cells and 6 faces for evaluation of gradient.....</i>	<i>53</i>
Figure 3.1	<i>Top(Left): Domain with mesh Top(right) Zoom view of RAE2822 aerofoil mesh Bottom: RANS-LES switching</i>	<i>67</i>
Figure 3.2	<i>Contour plots of Mach number and Pressure over RAE2822 aerofoil.....</i>	<i>68</i>
Figure 3.3	<i>Comparison of pressure coefficient using RANS (1st order, AUSM, HLLC), DES and DDES with experimental data.....</i>	<i>68</i>
Figure 3.4	<i>Left: Mesh along the symmetry plane with M6 Wing surface colour with pressure contour Right: M6 Wing surface colour with Y^+</i>	<i>70</i>
Figure 3.5	<i>Onera M6 wing surface pressure plot (flood mode) and symmetry plane Mach number plot (line mode).....</i>	<i>70</i>
Figure 3.6	<i>Onera M6 wing comparisons of pressure coefficient results from single and double precision solver using DES (ROE scheme based) at different spanwise locations. Single precision results are represented with "+" sign and double precision with a green colour circle.....</i>	<i>71</i>

Figure 3.7[a-f]	<i>Surface C_p comparison of different turbulent flow simulation schemes at different spanwise locations (η with experimental data</i>	<i>74</i>
Figure 4.1	<i>Schematics of different flow regimes on Aerospatiale A-airfoil.....</i>	<i>79</i>
Figure 4.2	<i>C_p plot experimental data F2.....</i>	<i>79</i>
Figure 4.3	<i>Skin friction coefficient plot for experimental data F1 and F2. Top: Zoom view showing turbulent separation around 83% chord on suction side near trailing edge F2 (solid blue line is at $y=0$).....</i>	<i>80</i>
Figure 4.4	<i>Bottom: Domain mesh with 120 partitions with different colours Middle: 3D breakdown of the mesh Top: Zoomed view of leading and trailing edge in black colour.....</i>	<i>82</i>
Figure 4.5	<i>Y^+ values on Aerospatiale A-airfoil.....</i>	<i>83</i>
Figure 4.6	<i>a) Parallel performance of the solver part of code with different number of processors. Inset is the time breakdown of main parts of code b) Parallel efficiency of the parallelizable part of code with different number of processors.....</i>	<i>84</i>
Figure 4.7	<i>Comparison of computed time averaged (T_{av}) coefficient of lift (C_l) from URANS and DES on Aerospatiale A-airfoil with experimental data F2.....</i>	<i>86</i>
Figure 4.8	<i>Comparison of time averaged skin friction coefficient C_f from URANS and DES on suction side of Aerospatiale A-airfoil with suction side profile. Zoomed leading and trailing edge on top.....</i>	<i>87</i>
Figure 4.9	<i>DES computation of leading edge Line contours of pressure on leading and trailing edge a) Line contours of press at leading edge b) Vector plot colour by x-direction velocity at the suction side of leading edge c) Line contours of pressure at trailing edge d) Zoom view of c) with streamlines.....</i>	<i>88</i>
Figure 4.10	<i>URANS computation of leading edge Line contours of pressure on leading and trailing edge a) Line contours of press at leading edge b) Vector plot colour by x-direction velocity at the suction side of leading edge c) Lind contours of pressure at trailing edge d) Zoom view of c) with streamlines.....</i>	<i>89</i>
Figure 4.11	<i>Comparison of computed time averaged (T_{av}) coefficient of lift (C_l) from the DES simulation using ROE, AUSM and HLLC inviscid flux</i>	

	<i>computing schemes on Aerospatiale A-airfoil with experimental data F2.....</i>	<i>90</i>
Figure 4.12	<i>Comparison of skin friction coefficient C_f on suction side of Aerospatiale A-airfoil with suction side profile. Zoomed leading and trailing edge on top.....</i>	<i>91</i>
Figure 4.13	<i>Time averaged Flowfield details from the DES simulation a) Velocity magnitude contours b) Velocity magnitude contours with streamlines at trailing edge c) Velocity vectors around trailing edge from mid-plane of 3D aerofoil d) x-vorticity e) y-vorticity f) z-vorticity plots.....</i>	<i>92</i>
Figure 4.14	<i>Time averaged Flowfield details from the RANS solution a) Velocity magnitude contours b) Velocity magnitude contours with the streamlines at trailing edge c) Velocity vectors around trailing edge from mid-plane of 3D aerofoil.....</i>	<i>93</i>
Figure 4.15	<i>Comparison of the computed parameters from the RANS and the DES on leading edge suction side at $x=0.01$ (first column), $x=0.02$ (middle column) and $x=0.03$ (third column). Leading edge is $x=0$ and trailing edge $x=0.6$. Top row: P/P_{inf}, Middle row: T/T_{inf}, bottom row: Nu^* (working parameter of S-A model)</i>	<i>94</i>
Figure 4.16	<i>Contours of the time averaged velocity magnitude- flowfield computed with DES plotted with experimental displacement thickness (square box) and momentum thickness (circles).....</i>	<i>95</i>
Figure 4.17	<i>LES-RANS switching region computed with the DES plotted with the experimental displacement thickness (square box) and momentum thickness (circles).....</i>	<i>95</i>
Figure 4.18	<i>Time averaged DDES solution a) Velocity magnitude contours with plotted with experimental displacement thickness (square box) and momentum thickness (circles) b) RANS-LES region boundary around the aerofoil at the trailing edge side.....</i>	<i>97</i>

Figure 4.19	<i>Flowfield details from the time averaged DDES solution a) Velocity magnitude contours b) Velocity magnitude contours with streamlines at trailing edge c) Velocity vectors around trailing edge from mid-plane of 3D aerofoil.....</i>	<i>98</i>
Figure 4.20	<i>Comparison of the computed time averaged (T_{av}) coefficient of lift (C_l) from the RANS, DES and DDES on Aerospatiale A-airfoil with experimental data F2.....</i>	<i>99</i>
Figure 4.21	<i>Comparison of the time averaged skin friction coefficient (C_f) from the RANS, DES and DDES simulations on suction side of Aerospatiale A-aerofoil with suction side profile. Zoomed leading and trailing edge on top.....</i>	<i>100</i>
Figure 4.22	<i>Bottom: Comparison of the RANS to LES switching zones for the DES (inner side shown in green colour) and the DDES (outer side red colour), plotted with experimental displacement thickness (square box) and momentum thickness (circles) Top: Zoomed view at leading and trailing edge.....</i>	<i>101</i>
Figure 4.23	<i>Comparison of time averaged computed parameters from the RANS, DES and DDES on leading edge suction side at $x=0.01$ (first column), $x=0.02$ (middle column) and $x=0.03$ (third column). Leading edge is $x=0$ and trailing edge $x=0.6$. Top row: P/P_{inf}, Middle row: T/T_{inf}, bottom row: Nu^* (working parameter of S-A model).....</i>	<i>102</i>
Figure 4.24	<i>a) DDES flow field – contours of turbulent viscosity parameter Nu^* (working parameter of S-A equation) b) RANS to LES switching zone of DES c) RANS to LES switching zone of DDES</i>	<i>105</i>
Figure 4.25	<i>A-airfoil with probes location for data extraction. Surface coloured by static pressure. Flow direction is in +x-axis direction.....</i>	<i>106</i>
Figure 4.26[a-k]	<i>Comparison of the turbulence parameters from the RANS, DES and DDES with experimental data F2. Figure (a-f) are computed normal to aerofoil surface, g) is computed normal to freestream flow direction at specified location.</i>	

	<i>Top (left): normalized time averaged x-direction velocity (right): Pressure coefficient</i>	
	<i>Bottom: Normalized modelled Reynolds stresses.....</i>	<i>112</i>
Figure 4.27	<i>Trailing edge of A-airfoil with time averaged velocity vectors (colour with velocity magnitude).....</i>	<i>113</i>
Figure 4.28 [a-e]	<i>Comparison of the flowfield parameters in the wake region from the RANS, DES and DDES with the experimental data F2. Figure 4.28(a-c) are computed normal to freestream flow direction at specified locations.</i>	
	<i>Top (left): time averaged x-direction velocity (middle): time averaged y-direction velocity</i>	
	<i>(right): time averaged pressure coefficient.....</i>	<i>116</i>
Figure 5.1	<i>Different views of Mesh over circular cylinder with L/D=2 for $Re=1.4 \times 10^5$</i>	<i>122</i>
Figure 5.2	<i>Y+ values over the surface of circular cylinder at $Re=1.4 \times 10^5$</i>	<i>122</i>
Figure 5.3	<i>Instantaneous Isosurface of vorticity magnitude colour by Pressure of circular cylinder at $Re=1.4 \times 10^5$ using DDES scheme with 1st order spatial accuracy. Vorticity magnitude level is 8000 and pressure range is 65000 to 102500. Physical time ≈ 2.1 sec</i>	
	<i>Top (left) : View from bottom side Top(right) View from side Bottom: Isometric View.....</i>	<i>123</i>
Figure 5.4	<i>Comparison of time averaged C_l and C_d values computed by DGDES using DES with 1st order spatial accuracy.....</i>	<i>123</i>
Figure 5.5	<i>Comparison of time averaged C_l and C_d values computed by DGDES using DES and DDES. Time step is very small, 5×10^{-7} seconds with data showing around 12000 iterations data. x-axis represents physical time in seconds.</i>	<i>124</i>
Figure 5.6	<i>Comparison of time averaged C_l and C_d values computed by DGDES using DES and DDES. Time step is 5×10^{-5}</i>	<i>125</i>
Figure 5.7	<i>Comparison of C_f values computed by DGDES using DES and DDES with experimental and other studies at $Re=1.4 \times 10^5$</i>	<i>126</i>

Figure 5.8	<i>Comparison of C_p values computed by DGDES using DES and DDES with experimental data at $Re=1.4 \times 10^5$</i>	<i>127</i>
Figure 5.9	<i>Instantaneous Isosurface of vorticity magnitude colour by Pressure of circular cylinder at $Re=1.4 \times 10^5$ using DES scheme. Vorticity magnitude level is 8000 and pressure range is 65000 to 102500. Physical time ≈ 2.1 sec Top (left) : View from bottom side Top(right) View from side Bottom: Isometric View.....</i>	<i>128</i>
Figure 5.10	<i>Instantaneous Isosurface of vorticity magnitude colour by Pressure of circular cylinder at $Re=1.4 \times 10^5$ using DDES scheme. Vorticity magnitude level is 8000 and pressure range is 65000 to 102500. Physical time ≈ 2.1 sec Top (left) : View from bottom side Top(right) View from side Bottom: Isometric View.....</i>	<i>128</i>
Figure 5.11	<i>Power spectral density (PSD) estimate of pressure data stored at a probe in wake region, using the DES and DDES schemes.....</i>	<i>129</i>
Figure 5.12(a-c)	<i>Recorded data at probe using the DES and DDES schemes a) Turbulent viscosity b) static pressure c) x-direction velocity.....</i>	<i>130</i>
Figure 5.13	<i>a) Comparison of time averaged normalized velocity field by Travin et. al.^[18] with experimental data. Travin et. al. results (upper side) with experiment data on lower side (picture from Ref [18]). b) Centre line velocity comparison downstream cylinder surface. Black solid and dashed lines are results from Travin et al.^[18] with experimental data plotted as circles c) Upper side Travin et. al.^[18] and lower side present computation using DG-DES d) Upper side DG-DES simulation lower side Travin et. al.....</i>	<i>132</i>
Figure 5.14	<i>Comparison of the experimental Reynolds stresses^[127] at $Re=1.4 \times 10^5$ with the DES simulation at $Re=1.4 \times 10^5$</i>	<i>134</i>
Figure 5.15	<i>Y^+ values over the surface of circular cylinder at $Re=3.6 \times 10^6$</i>	<i>134</i>
Figure 5.16	<i>DES simulation at $Re=3.6 \times 10^6$</i>	

	<i>Left: C_p comparison circular Right: C_f comparison</i>	135
Figure 5.17	<i>C_l and C_d of DES simulation at $Re=3.6 \times 10^6$ with freestream velocity 100 m/sec</i>	136
Figure 5.18	<i>C_l and C_d of the DES simulation at $Re=3.6 \times 10^6$ with freestream velocity 150 m/sec</i>	137
Figure 5.19	<i>DES flow simulation of circular cylinder at Reynolds number = $8e6$ at $t=0.4575$sec with freestream velocity of 150 m/sec. Instantaneous iso-surface plot of vorticity magnitude 1000 coloured by static pressure at physical time ≈ 1.2sec Top (left) : View from bottom side Top(right) View from side Bottom: Isometric View</i>	137
Figure 5.20	<i>DES flow simulation of circular cylinder at Reynolds number = $8e6$ at $t=0.4575$sec with freestream velocity of 100 m/sec. Instantaneous iso-surface plot of vorticity magnitude 1000 coloured by static pressure at physical time ≈ 1.2sec Top (left) : View from bottom side Top(right) View from side Bottom: Isometric View</i>	138
Figure 5.21	<i>Y^+ values over the surface of circular cylinder at $Re=8 \times 10^6$</i>	138
Figure 5.22	<i>C_l and C_d of circular cylinder at $Re=8 \times 10^6$ using the DES scheme</i>	139
Figure 5.23	<i>DES flow simulation of circular cylinder at Reynolds number = $8e6$ at $t=0.4575$sec. Instantaneous iso-surface plot of vorticity magnitude 1000 coloured by static Pressure Top (left) : View from bottom side Top(right) View from side Bottom: Isometric View</i>	140
Figure 5.24	<i>DES flow simulation of circular cylinder at Reynolds number $8e6$. Instantaneous iso-surface plot of vorticity magnitude 1000 at $t=0.4575$sec., coloured by static Pressure Top (left) : View from bottom side Top(right) View from side Bottom: Isometric View</i>	140
Figure 5.25	<i>URANS flow simulation of circular cylinder at Reynolds number $8e6$. Instantaneous iso-surface plot of vorticity magnitude 1000 at $t=0.4575$sec., coloured by static Pressure Top (left) : View from bottom side Top(right) View from side Bottom: Isometric View</i>	141

Figure 5.26 *Laminar flow simulation of circular cylinder at Reynolds number $8e6$. Instantaneous iso-surface plot of vorticity magnitude 1000 at $t=0.4575\text{sec.}$, coloured by static Pressure*
Top (left) : View from bottom side Top(right) View from side Bottom: Isometric View.....142

Figure 5.27 *C_l and C_d plots at $Re=8 \times 10^6$ using DES, URANS and Laminar flow..142*

Figure 5.28 *C_p and C_f plot using DES simulation at $Re=8 \times 10^6$*
Left: C_p comparison circular Right: C_f comparison143

Figure 5.29 *Comparison of modelled and resolved stresses using DES simulation at $Re=8 \times 10^6$*
Upper half is modelled stresses and lower half is resolved stresses.
*a) $\langle u^*u^* \rangle / U_{inf}^2$ b) $\langle u^*v^* \rangle / U_{inf}^2$ c) $\langle v^*v^* \rangle / U_{inf}^2$ 144*

Figure 6.1 *Schematic diagram of flapping aerofoil with flexible tail heaving sinusoidally in vertical (cross-flow) direction.....148*

Figure 6.2 *Flapping aerofoil snapshots at different interval of time during pitching motion showing relative tail motion.....149*

Figure 6.3 *Mesh details of the flapping aerofoil comprising of aerofoil section NACA0033 and flexible tail section of attached flat plate: a) complete domain mesh; b) outline of the flapping aerofoil element; c) mesh around flapping aerofoil element; d) close-up view of aerofoil section; e) close-up view of tail section.....150*

Figure 6.4 *Due to finite thickness of the flapping tail, the curvature effects will cause the trailing edge to have different x-axis location for upper and lower surface with fixed length.....151*

Figure 6.5 *A Graph element ΔABC with a mesh node P.....152*

Figure 6.6 *A deformed Graph element ΔABC^* with a relocated mesh node P^* ...154*

Figure 6.7 *Delaunay Graph generation over the flapping aerofoil: a) complete domain showing only Delaunay triangles; b) close up view of Delaunay triangles around flapping aerofoil element; c) close-up view of aerofoil section; d) close-up view of tail section.....155*

Figure 6.8 *Location of all interior mesh nodes (represented by '+' symbol) through Delaunay graph.....156*

Figure 6.9	<i>Deformed mesh over the flapping aerofoil element during maximum downward tail deflection: a) complete domain mesh; b) close up view of flapping aerofoil element; c) close up view of aerofoil section; d) close up view of tail section.....</i>	<i>156</i>
Figure 6.10	<i>Deformed mesh over the flapping aerofoil element during maximum upward tail deflection: a) complete domain mesh; b) close up view of flapping aerofoil element; c) close up view of aerofoil section; d) close up view of tail section.....</i>	<i>157</i>
Figure 6.11-a	<i>Leading-edge and trailing-edge displacement as a function of time; $Re=9,000$, $b/c = 0.56 \times 10^{-3}$, $Sr = 0.34$.....</i>	<i>157</i>
Figure 6.11-b	<i>Leading-edge displacement, trailing-edge displacement and their difference as a function of time; $Re=9,000$, $b/c = 0.56 \times 10^{-3}$, $Sr = 0.34$.....</i>	<i>157</i>
Figure 6.12	<i>Comparison of experimental and numerical instantaneous vorticity a) $Re= 9000$, $Sr=0.27$, $b/c= 0.85 \times 10^{-3}$ b) Numerical simulation $Re=9000$, $Sr=0.34$, $b/c=0.56 \times 10^{-3}$.....</i>	<i>160</i>
Figure 6.13	<i>Z-vorticity of flapping aerofoil during one cycle; $Re=9,000$, $b/c = 0.56 \times 10^{-3}$, $Sr = 0.34$ a-b Mean position while going up and coming down c-d Top and bottom peak cycle with tail in horizontal position during flapping e-f bottom position while flapping up and down.....</i>	<i>162</i>
Figure 6.14	<i>Variation of F_x with time.....</i>	<i>162</i>
Figure 6.15	<i>Domain and Delaunay Graph meshes a) Mesh of the domain b) Delaunay Graph with the 3D mesh c) Delaunay Graph only d) Zoom view of the wing.....</i>	<i>165</i>
Figure 6.16	<i>Mesh deformations during the wing oscillation with 17.5% c amplitude a) Top peak location b) 3D wing mesh c) Bottom peak location.....</i>	<i>166</i>
Figure 6.17	<i>Tip displacements as a function of time, $Re=30,000$, $k_G=1.82$.....</i>	<i>167</i>
Figure 6.18	<i>Instantaneous thrust coefficient as a function of time at $Re=30,000$, $k_G=1.82$.....</i>	<i>168</i>

Figure 6.19 *Coefficient of thrust plotted against non dimensional t/T ; Trajectory during flapping motion: Amplitude of motion (m) plotted against time (sec). Flowfield data at Pt1, Pt2, Pt3 and Pt4, represented by blue rectangles.....169*

Figure 6.20 *Vector plots of velocity colored with velocity magnitude (every 10^h vector is plotted for clarity). Flowfield description at Pt1, Pt2, Pt3 and Pt4 (from top to bottom).....170*

Figure 6.21 *Line contour plots of vorticity magnitude. Flowfield description at Pt1, Pt2, Pt3 and Pt4 (from top to bottom).....171*

List of Tables

Table 1.1	Table 1.1 2D and 3D Reynolds numbers limit for DNS, corresponding to number of nodes $N=10^7$18
Table 1.2	General Range of the Reynolds Number for different flows.....18
Table 2.1	Different numerical approaches for Knudsen number regimes.....37
Table 2.2	Selection of parameters for 1 st and 2 nd order temporal accuracy.....51
Table 3.1	Operating conditions for simulation of RAE2822.....66
Table 3.2	Mesh statistics for simulation of RAE2822.....66
Table 3.3	Case setup of Onera M6 wing at transonic speeds.....69
Table 3.4	Mesh size details.....69
Table 3.5	Span wise location for surface C_p comparison.....71
Table 3.6	Comparison of different mesh parameters using the DG-DES solver with different options with other studies.....76
Table 4.1	Mesh details of the mesh used in present study.....81
Table 4.2	Time efficiency of different simulations with 120 processors.....103
Table 4.3	Comparison of Lift and Drag coefficients on the Aerospatiale A-airfoil.....104
Table 5.1	Details of different available experimental data.....120
Table 5.2	Mesh statistics of circular cylinder with $L/D=2$ for $Re=1.4 \times 10^5$120
Table 5.3	Case details of simulation.....120
Table 5.4	Summary of results $Re=1.4 \times 10^5$131
Table 5.5	Numerical scheme details.....135
Table 5.6	Mesh details for $Re=3.6 \times 10^6$ simulation.....135
Table 6.1	Various possible situations during Graph element location of all the mesh points in the moving mesh domain.....153
Table 6.2	Area ratio of the different elements153
Table 6.3	Comparsion of CFD and Exeperimental variables.....158
Table 6.4	Reynolds Number of CFD and Experiment.....158
Table 6.5	Calculation of frequency from Strouhal Number.....159
Table 6.6	Effect of bending stiffness on shape.....160

Table 6.7 *Mesh statistics of NACA0012 wing at Reynolds number 30,000.....166*

Table 6.8 *CFD simulation setup of NACA0012 wing at Reynolds number 30,000.....167*

Nomenclature

English symbols:

A	surface area
C_d	Drag coefficient
c	Speed of sound, chord length
C_{DES}	model constant taken as 0.65
C_l	Lift Coefficient
C_p	specific heat at constant pressure
C_{pb}	base pressure
C_v	specific heat at constant volume
d	wall distance, length scale for turbulence model
dA	differential surface area
$E(k)$	Energy contained by length scales
F	Inviscid flux vector
f	shedding frequency
G	Viscous flux vector
h	mesh size
H	Enthalpy
k	wave number
Kn	Knudsen number
M	Modal matrix, Mach number
n	normal area vector
N	number of vertices
P, p	Pressure
Pr	Prandtl number
q	Heat flux
Q	Primitive variables vector
R	Gas constant
Re	Reynolds number
S	Strain rate tensor

Sr	Strouhal number ($\frac{\text{shedding frequency (f)} * \text{characteristic length (c)}}{\text{freestream velocity (Uinf)}}$)
t	temporal symbol representing time
T	Temperature
$u, v, \text{ and } w$	Cartesian velocity components
u	Instantaneous velocity
\bar{u}	Averaged velocity
U_r	Reference velocity
U_{inf}	free stream velocity
V	Volume
W	Conserved variables vector
X	Position vector in x, y and z direction

Geometric symbols:

$\bar{\quad}$ (over bar)	Time averaged quantity
$\langle \quad \rangle$	Time averaged quantity
'	fluctuating quantity

Greek symbols:

α	Incidence angle
α_i	Stability criteria
γ	ratio of specific heats
Δ	Gradient, increment
ε	Accuracy
Γ	preconditioning matrix
∇	local grid spacing
λ	Mean free path, eigen value
μ	molecular viscosity
μ_0	μ at reference state
μ_T	turbulent or eddy viscosity
ν_T	kinematic eddy viscosity

$\tilde{\nu}$	modified kinematic eddy viscosity
Ω	Rotation rate tensor
ρ	density
ρ'	instantaneous fluctuation term in Reynolds-averaging
ρ_p	$\frac{\partial \rho}{\partial p}$ at constant temperature
ρ_T	$\frac{\partial \rho}{\partial T}$ at constant pressure
$\tau = [\tau_{ij}]$	stress tensor
τ	pseudo time
τ_w	wall shear stress
θ	preconditioning variable, replacing ρ_p
η	span wise location
ψ	variable defined in HLLC scheme $[1 \ u \ v \ w \ H]^T$
ϕ	variable defined in HLLC scheme $[0 \ n \ 0]^T$

Acronyms:

ALE	Arbitrary Lagrangian Eulerian
AUSM	Advective Upstream Splitting Method
CFD	Computational Fluid Dynamics
CFL	Courant–Friedrichs–Lewy condition
DDES	Delayed Detached Eddy Simulation
DES	Detached Eddy Simulation
DG-DES	Dynamic Grid-Detached Eddy Simulation (Sheffield University Code)
DNS	Direct Numerical Simulation
FDS	Flux Difference Splitting
GCL	Geometric Conservation Law
GIS	Grid Induced Separation
HLLC	Hartan-Lax-van Leer with Contact restoration scheme
IDDES	Improved Delayed-Detached-Eddy Simulation

LES	Large Eddy Simulation
MAV	Micro Aerial Vehicle
MPI	Message Passing Interface
MSD	Modified Stress Depletion
NS	Navier-Stokes
RANS	Reynolds Averaged Navier Stokes Equations
S-A	Spalart-Allmaras turbulence model
SAS	Scale Adoption Simulations
SGS	Sub-grid-scale
URANS	Unsteady RANS
WMLES	Wall Modelled Large Eddy simulation

1 INTRODUCTION

A basic view of the computational aerodynamics and its most challenging feature “turbulence” is covered in this chapter. Furthermore, the physical description of the “turbulence” and its energy cascade mechanism is presented as envisaged by Kolmogorov. A brief description is presented regarding different numerical approaches for turbulent flow simulation. All the topics discussed in this chapter lay the foundation of subsequent work and are directly relevant to the present research work.

1.1 Computational Aerodynamics

Fluid mechanics has fascinated humankind ever since the dawn of civilization. Its application spectrum ranges from the breathing to the physiological flows in the body, from walking to numerous travelling modes, from body temperature to the global meteorology, from gust of wind to the hurricanes, from falling apple to a rising space shuttle, from flow of water in a stream to oceans and almost every sphere of life. Its application areas in science include aeronautics, acoustics, biomechanics, oceanography, meteorology, hydraulics, gas and petroleum, nuclear engineering, chemical engineering and environmental sciences etc.

Fluid dynamics involves various physical properties of fluids such as pressure, temperature, velocity, density and viscosity etc. as a function of space and time. Although the fluid involves both liquid and gasses in broader sense, this study will be specific to the fluid media as gaseous with “air” as the working fluid termed as “aerodynamics”.

There are three fundamental approaches in Aerodynamics described as follows:

1. Experimental Aerodynamics
2. Analytical Aerodynamics
3. Numerical or Computational Aerodynamics

The experimental aerodynamics approach is commonly viewed as the most trusted one. It has played an important role in validating and delineating various approximations to the governing equations to judge their extent of accuracy. The wind tunnel, as a piece of experimental equipment, provides an effective means of simulating real life flows. A scale down model is mounted in the wind tunnel test section with recording mechanism to present different flow variables at different flow conditions. Traditionally, this has provided a relatively cost-effective alternative to the full-scale

prototype measurements. However, there are limitations to this approach in terms of different flow variables such as the Reynolds number (ratio of the inertial and viscous forces), size of the object and the test section and different flow conditions and configurations. Errors are incorporated due to the limitation of the test section size, turbulence in the flow, drag by the holding device (referred as tare drag) and correlation of the experimental data with the real life problems etc. Whereas, the body forces are generally measured using the strain gauges, the flow field visualization is traditionally done using hot wire anemometers. In order to achieve better accuracy for the visualization and estimation of turbulence parameters, the focus has shifted now to more accurate approaches such as the Laser Doppler Velocimetry (LDV) and Particle Image Velocimetry (PIV) etc.

The analytical aerodynamics is focused on the construction of an analytical solution of the governing equations for the different categories of aerodynamics and the study of the effect of various approximations to these equations. With the exception of very simple cases in which the theoretical or analytical solutions can be obtained, most of these processes have a complex domain subjected to a set of initial and boundary conditions. Therefore, the analytical methods cannot be applied for majority of real life problems.

The computational aerodynamics is described in context of its general application to fluids as the computational fluid dynamics (CFD). CFD is a numerical procedure to simulate various bounded physical systems which involve fluid flows, heat and mass transfer etc. under particular operating conditions, through a computer based numerical simulation. This simulation is based on a numerical program solving the fundamental governing equations of the fluid to represent flow physics. These fundamental governing equations are the continuity (conservation of mass), the momentum (Newton's second law dealing with the conservation of momentum) and the energy equations (conservation of energy). These fundamental principles are then imposed on a model of fluid flow and governing mathematical equations are obtained, generally termed as Navier Stokes equations. These equations are complex and highly non-linear in nature. Hence, the efficient numerical methods are used to iteratively solve these equations to obtain an approximate solution. CFD is a very flexible and useful approach capable to study systems under the conditions where the experiments are difficult or very expensive to be carried out. For instance, stall conditions of an aircraft, blast propagation and nuclear contamination propagation etc.

Almost all practical flows are turbulent in nature. It is the effective level of this turbulence which provides a basis to bifurcate them into laminar and turbulent types of flows. Arguably, the accurate modelling of turbulent flows or “turbulence simulation” is one of the toughest fronts faced by scientific community that still stays far from solution.

1.2 Turbulence

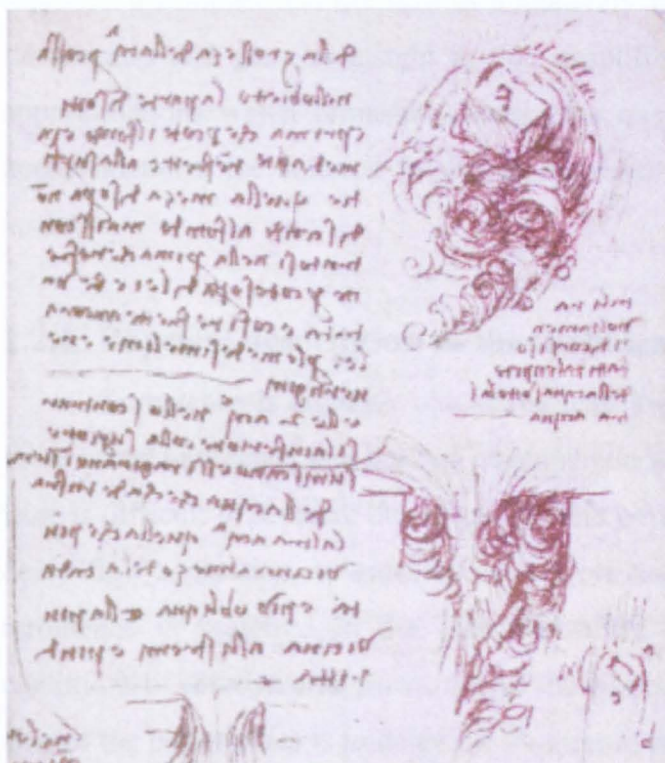


Figure 1.1^[3] First documented sketch of turbulence

“Turbulence” has posed an uphill challenge ever since its first observation as a physical phenomenon. In 1510, Leonardo da Vinci accompanied a drawing (figure 1.1) of the vortices shed behind a blunt obstacle. He made the following observation about turbulence; which he called as “Turbolenza”:

“Observe the motion of the water surface, which resembles that of hair that has two motions: one due to the weight of the shaft, the other

to the shape of the curls; thus, water has eddying motions, one part of which is

due to the principal current, the other to the random and reverse motion.”

In spite of the fact that it was just an observation without any scientific explanation or reasoning, it may be taken as similar to what is termed now as the Reynolds

decomposition of the flow into mean and fluctuating parts as discussed in Chapter 2.

Turbulence is a phenomenon that occurs frequently in various spheres of nature. Figure 1.2 indicates iso-surfaces of vorticity magnitude coloured by pressure from a turbulent flow simulation.

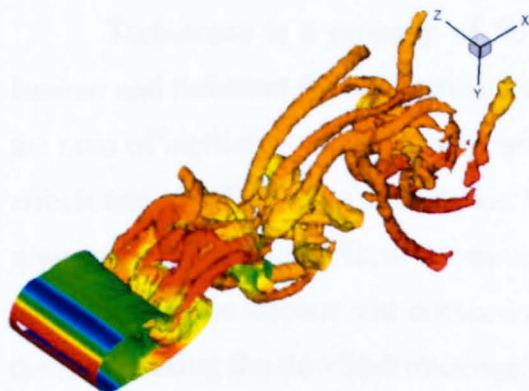


Figure 1.2 Turbulent flow over circular cylinder at Reynolds number 3.6×10^6 .

The air flow around the cars, buses, buildings and airplanes etc. is mainly turbulent. It dominates internal as well as external flows and

hence is of great importance in performance evaluation of any aerodynamic system. The approach to tackle turbulence, until now, has been to circumvent the ‘turbulence impasse’ through certain assumptions by accepting some error range and to be optimistic for this error range to reduce with the advent of new high tech machines and better numerical methodologies. There is although a widespread pessimism about being able to solve this problem completely in the near future. In practice, certain assumptions are done to represent a complex real life flow as a relatively simplified flow to be able to simulate it numerically and gain an insight to this simplified flow. It is further the level of the approximations which primarily dictates the quality of the solution. With the higher approximations, the solution feasibility increases but the accuracy decreases and vice versa.

1.2.1 Physical description of the turbulence

Turbulence is arguably one of the least known subjects, even today. In practice, some times turbulence is a desired phenomenon and some time it is avoided. Turbulent flow is difficult to separate due to its inherent nature. In some practical cases such as to delay flow separation, to enhance mixing, or to achieve more effective heat transfer, turbulence is preferred in the flow. However, in normal straight and level cruise conditions of aerodynamic flows, one of the aim is to optimize lift to drag ratio $(L/D)_{max}$. One of the possibilities is to delay the laminar-to-turbulent transition reducing the profile drag.

Although there is no universally accepted definition of turbulence, it can be categorized as a turbulent flow on the basis of certain characteristic observations. All these observations may be linked to figure 1.2 for better understanding of a turbulent flow. “Album of Fluid Motion” by Van Dyke ^[5] is a good reference to familiarize with the concept of turbulence in different types of flows.

Turbulence is a property of flow, not of fluid. A same fluid can produce both laminar and turbulent flows depending upon the flow characteristics. Reynolds number is the ratio of inertial to viscous forces without considering effects such as electromagnetic effects and Van Der Waal’s forces etc. For low Reynolds Number flows, instabilities are suppressed by viscous effects. However, at high Reynolds number flows, the complex interaction of the viscous and convective (inertial) influences increase the instabilities in the flow making the flowfiled rotational and highly irregular. Irregularity voids the use of any deterministic approach to the solution of turbulence. Therefore, turbulent motion cannot be described in all details as a function of space and time. However, the

probabilistic approach can be used by taking the lower order statistics (average, mean etc) to describe turbulence. Turbulent flows are diffusive, causing rapid mixing and high momentum linked with heat and mass transfer. Turbulent flows are dissipative in nature. Viscosity effects at smallest scales result in the conversion of kinetic energy of the flow into heat. If there is no external source of energy to make up for this kinetic energy loss, the turbulent motion will decay. Turbulent flows are a continuum phenomenon. Even the smallest scales in a turbulent flow are much larger than the molecular length scale. Turbulence dominates the state of the continuum in the fluid dynamics at higher Reynolds numbers. The mechanism of turbulent flows can be linked to their interaction of the viscous terms and the non-linear inertia terms in the Navier-Stokes equation, producing a complicated unsteady flow field. This flow field contains a large number of length scales of motions, in contrast with the laminar flow. Therefore, energy cascade occurs through these large scales by transfer of energy from largest coherent to the smallest incoherent (Kolmogorov's) scale (discussed in the section 1.3). At this point viscosity acts as a converter of energy into heat. The largest length scales are mainly responsible for the transport and generation of turbulence energy while the smallest scales (also called as Kolmogorov's scale) are to dissipate energy cascaded from the larger length scales. The Kolmogorov's energy spectrum provides an insight to the energy distribution with length scales and structure of the turbulent energy in the turbulent flows. It is worth to describe it at this stage for coherence.

1.2.2 Kolmogorov's energy spectrum

Kolmogorov's universal equilibrium is undoubtedly one of the most significant achievements in the history of turbulence research. It is related with the cascade of energy and an inertial subrange in the frequency domain. Kolmogorov's this influential theory of homogeneous (or statistically invariant under translation), isotropic (or statistically invariant under rotation or reflection) ^[2], incompressible turbulence provides an insight to energy spectrum of fluid flows. It is discussed in various introductory fluid dynamics books such as Reference [2]. Energy is injected at largest or integral scales. Due to the shear instabilities the smaller scales are shed drawing energy from these large scales. This transfer continues to smaller and smaller inertial scales. The energy transfer occurs till Kolmogorov or dissipation scales where energy is dissipated as heat. It is assumed that energy transfer between eddies on intermediate scales does not have any losses. Kolmogorov's idea was that the velocity fluctuations in the internal sub-range are independent of initial and boundary conditions (i.e., they have no memory of the effect of

anisotropic excitation at smaller wave numbers). The turbulent motions in this sub-range therefore show universal statistics and the flow is self-similar.

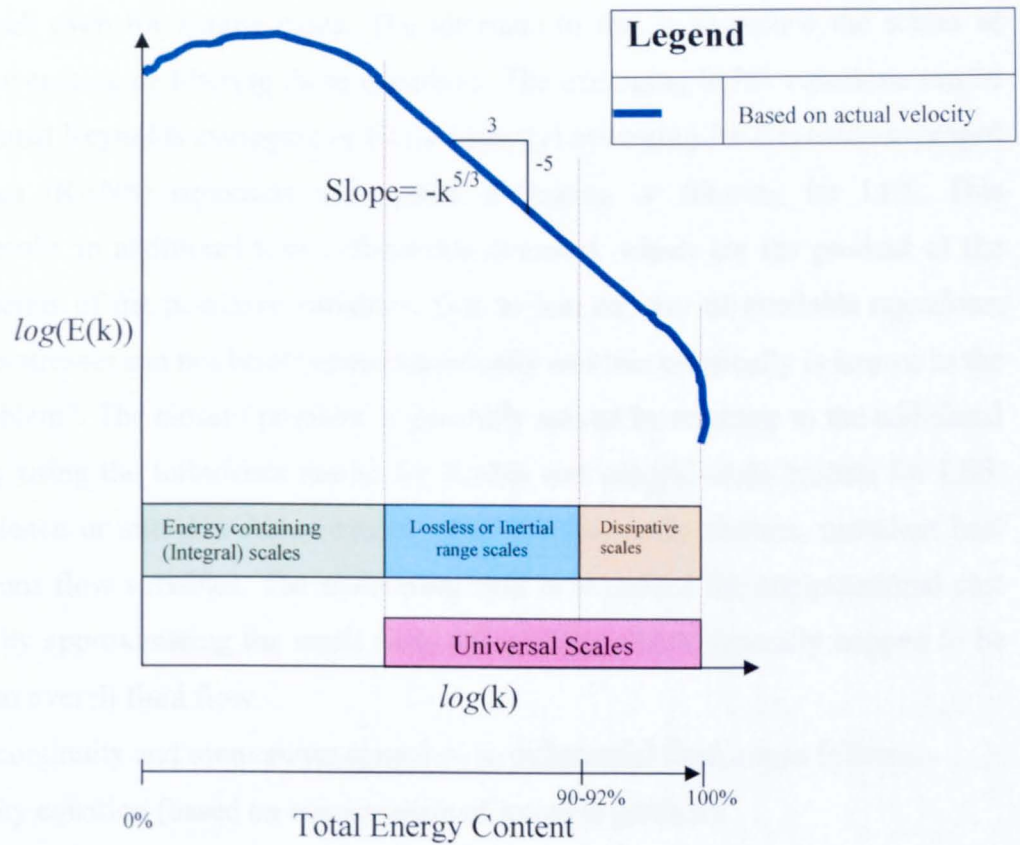


Figure 1.3 Sketch of Kolmogorov's Energy spectrum with energy distribution

Figure 1.3 (based on Ref [6], [7]) presents the Kolmogorov energy spectrum. 'k' is called wave number, which is proportional to inverse of length scales and 'E' describes the energy contained by length scales. Despite some flaws in arguments supporting it, this theory is widely regarded as correct. This theory has been proven number of times experimentally^[6]. Therefore, for any effective simulation of turbulence, the phenomenon delineated by Kolmogorov energy spectrum regarding energy scales and its dissipation have to be observed.

1.3 Turbulence modelling

The detailed formulations of the governing equations used in the DG-DES are covered in the chapter 2. However, apropos to the present topic of turbulence modelling, the important concept of averaging is covered in this section. CFD simulations are carried out by solving the flow governing equations based on fundamental laws of conservation of mass, momentum and energy, applied on a continuum domain with the appropriate boundary conditions using numerical methods. If these equations, generally termed

collectively as Navier-Stokes equations, are solved in their full details in time and space domains, the simulation technique is termed as the direct numerical simulation (DNS). However, generally, it becomes computationally infeasible to solve these equations using DNS approach even for simple cases. The alternate to this is to reduce the scales of motions by averaging or filtering these equations. The averaging in NS equations can be the conventional Reynolds averaging or Favre (density) averaging for Reynolds-averaged Navier-Stokes (RANS) equations and spatial averaging or filtering for LES. This averaging results in additional terms (Reynolds stresses), which are the product of the fluctuating terms of the primitive variables. Due to less number of available equations, the Reynolds stresses can not be obtained numerically and this classically is known as the “closure problem”. The closure problem is generally solved by recourse to the additional equations by using the turbulence model for RANS and subgrid-scale models for LES. These turbulence or sub-grid-scale models relate the Reynolds stresses, turbulent heat flux and means flow variables. The underlying idea is to reduce the computational cost appreciably by approximating the small scale fluctuations which generally happen to be less critical to overall fluid flow.

The continuity and momentum equations in differential form are as follows:

The continuity equation (based on conservation of mass) is given as:

$$\frac{\partial \rho}{\partial t} + \frac{\partial}{\partial x_j}(\rho u_j) = 0 \quad (1.1)$$

The momentum equation (based on Newton’s second law or conservation of momentum) is described as:

$$\frac{\partial}{\partial t}(\rho u_i) + \frac{\partial}{\partial x_j}(\rho u_i u_j) = -\frac{\partial p}{\partial x_i} + \mu \nabla^2 u_i \quad (1.2)$$

It is to be noticed that the Reynolds stresses are generated due to the averaging/ filtering of momentum equation only.

1.3.1 Averaging/ filtering

1.3.1.1 Conventional Reynolds averaging

In conventional Reynolds decomposition, the randomly changing flow variables are replaced with the time average plus instantaneous fluctuations at a particular instant of time. Let f be any primitive variable of the flow that is decomposed into its mean and instantaneous fluctuating values.

$$f(x, t) = \bar{f}(x, t) + f'(x, t) \quad (1.3)$$

where, the time average of fluctuating part is always assumed to be zero.

$$\overline{f'}(x,t) \equiv \frac{1}{T} \int_{t_0}^{t_0+T} f'(x,t) dt \equiv 0, \quad T1 \ll T \ll T2 \quad (1.4)$$

$T1$ is the period of random fluctuations due to turbulence in the fluid (also called fluctuation time scale) and $T2$ is the time constant for slow variations (also called mean flow time scale). However, if the mean flow characteristics $T2$ are of the order of fluctuation time scale $T1$, ensemble averaging is done as shown in figure 1.9. It means that the experiment is repeated a number of times and its average is taken over same time period to have its ensemble average.

For two symbolic flow variables f and g , the following relations hold:

$$\overline{f'g'} = 0 \quad \overline{fg} = \overline{f} \overline{g} \quad \overline{f+g} = \overline{f} + \overline{g}$$

It is important to note that although $\overline{f'} \equiv 0$, $\overline{f'f'} \neq 0$. It is known as turbulence intensity and is an important turbulence parameter. Further details can be found in reference [9].

1.3.1.2 Favre (density) averaging – RANS formulation

For compressible flow and mixture of gases in particular, mass-weighted averaging of Navier-Stokes (NS) Equations, also called as Favre averaging is preferred as it makes the governing equations much simpler^[9].

Thus, the mass-weighted flow variables become:

$$\tilde{f}(x,t) = \frac{1}{\bar{\rho}T} \int_{t_0}^{t_0+T} \rho(x,t) f(x,t) dt, \quad T1 \ll T \gg T2 \quad (1.5)$$

where, $\bar{\rho}$ is the Reynolds averaged density and a tilde symbol, " \sim ", represents the Favre or density averaging.

$$\tilde{u} = \frac{\overline{\rho u}}{\bar{\rho}} \quad \tilde{v} = \frac{\overline{\rho v}}{\bar{\rho}} \quad \tilde{w} = \frac{\overline{\rho w}}{\bar{\rho}} \quad \tilde{h} = \frac{\overline{\rho h}}{\bar{\rho}} \quad \tilde{H} = \frac{\overline{\rho H}}{\bar{\rho}}$$

It is noted that only the velocity components and thermal variables are mass-averaged. In order to differentiate the Favre averaging from time averaging, the mean and Instantaneous functions are represented by:

$$f(x,t) = \tilde{f}(x,t) + f''(x,t) \quad (1.6)$$

Fluid properties such as density and pressure are treated as before. To substitute into the conservation equations, now the mass-averaged and instantaneous components are defined as:

$$u = \tilde{u} + u'' \quad v = \tilde{v} + v'' \quad w = \tilde{w} + w'' \quad h = \tilde{h} + h'' \quad T = \tilde{T} + T'' \quad H = \tilde{H} + H''$$

Unlike the conventional averaging, the time average of the fluctuating part is not zero unless $\rho' = 0$ and $\overline{\rho f''} = 0$.

Following relations hold true $\bar{u}'' = -\frac{\overline{\rho' u'}}{\bar{\rho}}$ $\bar{v}'' = -\frac{\overline{\rho' v'}}{\bar{\rho}}$

After replacing these mass-averaged variables in the continuity equation in differential form,

$$\frac{\partial \bar{\rho}}{\partial t} + \frac{\partial}{\partial x_j} (\bar{\rho} \bar{u}) = 0 \quad (1.7)$$

The momentum equation with mass-averaged variables substituted results:

$$\frac{\partial}{\partial t} (\bar{\rho} \bar{u}_i) + \frac{\partial}{\partial x_j} (\bar{\rho} \bar{u}_i \bar{u}_j) = -\frac{\partial \bar{p}}{\partial x_i} + \frac{\partial}{\partial x_j} (\bar{\tau}_{ij} - \overline{\rho u_i'' u_j''}) \quad (1.8)$$

$$\frac{\partial}{\partial t} (\bar{\rho} \bar{u}_i) + \frac{\partial}{\partial x_j} (\bar{\rho} \bar{u}_i \bar{u}_j) = -\frac{\partial \bar{p}}{\partial x_i} + \frac{\partial}{\partial x_j} (\bar{\tau}_{ij} + \tau_{ij}^R) \quad (1.9)$$

where, τ_{ij}^R represents the Reynolds stresses. Neglecting the viscosity fluctuations, $\bar{\tau}_{ij}$ becomes:

$$\bar{\tau}_{ij} = \mu \left[\left(\frac{\partial \bar{u}_i}{\partial x_j} + \frac{\partial \bar{u}_j}{\partial x_i} \right) - \frac{2}{3} \delta_{ij} \frac{\partial \bar{u}_k}{\partial x_k} \right] + \mu \left[\left(\frac{\partial \bar{u}_i''}{\partial x_j} + \frac{\partial \bar{u}_j''}{\partial x_i} \right) - \frac{2}{3} \delta_{ij} \frac{\partial \bar{u}_k''}{\partial x_k} \right] \quad (1.10-a)$$

Although, the above term seems complicated, in practice, the terms involving the doubly primed fluctuations can be neglected as they are expected to be small and likely candidate for being neglected on the basis of order of magnitude arguments.

$$\bar{\tau}_{ij} = \mu \left[\left(\frac{\partial \bar{u}_i}{\partial x_j} + \frac{\partial \bar{u}_j}{\partial x_i} \right) - \frac{2}{3} \delta_{ij} \frac{\partial \bar{u}_k}{\partial x_k} \right] \quad (1.10-b)$$

Therefore, the only unknown terms are $\overline{\rho u_i'' u_j''}$, where, $i, j = 1, 2, 3$ represent x, y and z directions.

Similarly the resultant energy equations in terms of mass-averaged variables is

$$\frac{\partial}{\partial t} (\bar{\rho} \bar{H}) + \frac{\partial}{\partial x_j} (\bar{\rho} \bar{u}_j \bar{H} + \overline{\rho u_j'' H''} - k \frac{\partial \bar{T}}{\partial x_j}) = -\frac{\partial \bar{p}}{\partial x_i} + \frac{\partial}{\partial x_j} (\bar{u}_i \bar{\tau}_{ij} + \overline{u_i'' \tau_{ij}''}) \quad (1.11)$$

$\bar{\tau}_{ij}$ can be evaluated as before in equation (1.10).

The resultant equations of state is described as:

$$\overline{\bar{p} + p'} = \overline{(\bar{\rho} + \rho') R (\bar{T} + T'')} \Rightarrow \bar{p} = \bar{\rho} R \bar{T} \quad (1.12)$$

How to obtain additional equations for the evaluation of Reynolds stress terms τ_{ij}^R remained an impasse for many decades. Boussinesq eddy-viscosity assumption

provided a mean to solve the closure problem by relating the Reynolds stress with the eddy viscosity.

$$\tau_{ij}^R = -\overline{\rho u_i' u_j'} = 2\mu_T S_{ij} + \lambda_T \frac{\partial \tilde{u}_k}{\partial x_k} \delta_{ij} - \frac{2}{3} \overline{\rho} k \delta_{ij} \quad (1.13)$$

μ_T is the eddy viscosity, λ_T is the “second eddy viscosity”, k is the turbulent kinetic energy and S_{ij} is the mean strain-rate tensor, defined by

$$S_{ij} = \frac{1}{2} \left(\frac{\partial \tilde{u}_i}{\partial x_j} + \frac{\partial \tilde{u}_j}{\partial x_i} \right).$$

Neglecting the contribution from the turbulent kinetic energy, we can re-write the momentum equation as follows:

$$\boxed{\begin{aligned} \frac{\partial}{\partial t} (\overline{\rho \tilde{u}_i}) + \frac{\partial}{\partial x_j} (\overline{\rho \tilde{u}_i \tilde{u}_j}) &= -\frac{\partial \overline{p}}{\partial x_i} + \frac{\partial}{\partial x_j} (\overline{\tau}_{ij} + \tau_{ij}^R) \\ \frac{\partial}{\partial t} (\overline{\rho \tilde{u}_i}) + \frac{\partial}{\partial x_j} (\overline{\rho \tilde{u}_i \tilde{u}_j}) &= -\frac{\partial \overline{p}}{\partial x_i} + \frac{\partial}{\partial x_j} \left[\underbrace{\left[2\mu S_{ij} - \frac{2}{3} \mu \frac{\partial \tilde{u}_k}{\partial x_k} \delta_{ij} \right]}_{\overline{\tau}_{ij}} - \underbrace{\left[2\mu_T S_{ij} - \frac{2}{3} \mu_T \frac{\partial \tilde{u}_k}{\partial x_k} \delta_{ij} \right]}_{\tau_{ij}^R} \right] \end{aligned}} \quad (1.14)$$

The closure approximation for the turbulent heat flux vector, q_T , is achieved by applying Reynolds momentum-heat transfer analogy^[40].

$$q_{Tj} = -\frac{\mu_T c_p}{Pr_T} \frac{\partial \tilde{T}}{\partial x_j}$$

Pr_T is called as turbulent Prandtl number and its values ranges from 0.89-0.90^[41]. The only unknown is μ_T and it is computed using some turbulence model. One equation Spalart-Allmaras (S-A) turbulence model is one of the most widely used turbulence model.

2.8.2 Spalart-Allmaras (S-A) turbulence model^[39]

The S-A model is one of the most popular approaches in aerodynamic flow simulations. It solves a single partial differential transport equation for the eddy viscosity. The governing differential equation was derived by using empiricism and arguments of dimensional analysis, Galilean invariance and the selected dependence on the molecular viscosity^[39]. The main objective is to solve closure by computing turbulent eddy viscosity μ_T .

A working variable $\tilde{\nu}$, called as the modified kinematic eddy viscosity is defined as

$$\tilde{\nu} = \frac{\nu_T}{f_{v1}} \quad (1.15)$$

ν_T is the kinematic eddy viscosity related to the turbulent eddy viscosity,

$$\mu_T = \bar{\rho} \nu_T \quad (1.16)$$

The most popular form of the model, including a wall destruction term that reduces the eddy viscosity in the log layer and the laminar sub-layer, is described as:

$$\begin{aligned} \frac{D\tilde{\nu}}{Dt} &= \Pi_{production f(S, \tilde{\nu}, d)} - \Pi_{destruction f(\tilde{\nu}, d)} + \Pi_{diffusion f(\tilde{\nu})} \\ \frac{D\tilde{\nu}}{Dt} &= c_{b1} \tilde{S} \tilde{\nu} - c_{w1} f_w \left(\frac{\tilde{\nu}}{d} \right)^2 + \frac{1}{\sigma} \left[\nabla \cdot ((\nu + \tilde{\nu}) \nabla \tilde{\nu} + c_{b2} (\nabla \tilde{\nu})^2) \right] \end{aligned} \quad (1.17)$$

where $\frac{D\tilde{\nu}}{Dt} = \frac{\partial}{\partial t} + \tilde{u}_i \frac{\partial}{\partial x_i}$ is the material derivative.

The other symbols in the model are either closure functions or the closure coefficients. These closure coefficients are described in the following list,

$$c_{b1} = 0.1355, c_{b2} = 0.622, c_{v1} = 7.1, \sigma = \frac{2}{3}$$

$$\kappa = 0.41, c_{w1} = \frac{c_{b2}}{\kappa^2} + \frac{1 + c_{b2}}{\sigma}, c_{w2} = 0.3, c_{w3} = 2$$

And the closure functions are defined as :

$$\begin{aligned} \chi &= \frac{\tilde{\nu}}{\nu}, f_{v1} = \frac{\chi^3}{\chi^3 + c_{v1}^3} \\ f_{v2} &= 1 - \frac{\chi}{1 + \chi f_{v1}}, \tilde{S} = S + \frac{\tilde{\nu}}{\kappa^2 d^2} f_{v2} \end{aligned} \quad (1.18)$$

$$r \equiv \frac{\tilde{\nu}}{\tilde{S} \kappa^2 d^2}, g = r + c_{w2}(r^6 - r), f_w = g \left[\frac{1 + c_{w3}^6}{g^6 + c_{w3}^6} \right]^{\frac{1}{6}}$$

where the d is the distance to the closest wall and S denotes the vorticity. The vorticity is usually represented in terms of mean rotation-rate tensor Ω_{ij} ,

$$S = |\Omega| = \sqrt{2\Omega_{ij}\Omega_{ij}}, \text{ where } \Omega_{ij} = \frac{1}{2} \left(\frac{\partial \tilde{u}_i}{\partial x_j} - \frac{\partial \tilde{u}_j}{\partial x_i} \right)$$

The S-A model makes another approximation, explained in Reference [39], that the turbulent kinetic energy $-\frac{2}{3} \bar{\rho} k \delta_y$ in the equation (1.13) is ignored in the model, which has no significant effects in thin shear flows and can be modelled through other ways.

Thus the closure of Reynolds stress, τ_{ij} , and the turbulent heat-flux vector, q_T , is complete. It can be put together with the mean stress and mean heat-flux, i.e.,

$$\tau_{ij} + t_{ij} = 2(\mu + \mu_T) S_{ij} + (\lambda + \lambda_T) \frac{\partial u_m}{\partial x_m} \quad (1.19)$$

$$q_j + q_{Tj} = c_p \left(\frac{\mu}{Pr} + \frac{\mu_T}{Pr_T} \right) \frac{\partial T}{\partial x_j} \quad (1.20)$$

where, for convenience, “-” and “~” above the averaged variables are removed without any confusion. Furthermore, in future conversation, a single μ will represent $(\mu + \mu_T)$

$$\frac{\partial \tilde{v}}{\partial t} + \tilde{u}_i \frac{\partial \tilde{v}}{\partial x_i} = c_{b1} \tilde{S} \tilde{v} - c_{w1} f_w \left(\frac{\tilde{v}}{d} \right)^2 + \frac{1}{\sigma} \left[\nabla \cdot ((v + \tilde{v}) \nabla \tilde{v} + c_{b2} (\nabla \tilde{v})^2) \right] \quad (1.21)$$

Adding $\tilde{v} \nabla \cdot v$ on both sides of equality

$$\frac{\partial \tilde{v}}{\partial t} + \tilde{u}_i \frac{\partial \tilde{v}}{\partial x_i} + \tilde{v} \nabla \cdot v = c_{b1} \tilde{S} \tilde{v} - c_{w1} f_w \left(\frac{\tilde{v}}{d} \right)^2 + \frac{1}{\sigma} \left[\nabla \cdot ((v + \tilde{v}) \nabla \tilde{v} + c_{b2} (\nabla \tilde{v})^2) \right] + \tilde{v} \nabla \cdot v$$

$$\frac{\partial \tilde{v}}{\partial t} + v \cdot \nabla \tilde{v} + \tilde{v} \nabla \cdot v = c_{b1} \tilde{S} \tilde{v} - c_{w1} f_w \left(\frac{\tilde{v}}{d} \right)^2 + \frac{1}{\sigma} \left[\nabla \cdot ((v + \tilde{v}) \nabla \tilde{v} + c_{b2} (\nabla \tilde{v})^2) \right] + \tilde{v} \nabla \cdot v$$

After rearranging the terms, by putting time-derivative and divergence terms on the left and all the rest terms on the right, the conservative form is obtained.

$$\frac{\partial \tilde{v}}{\partial t} + \nabla \cdot \left[\tilde{v} v - \frac{1}{\sigma} (v + \tilde{v}) \nabla \tilde{v} \right] = (c_{b1} \tilde{S} + \nabla \cdot v) \tilde{v} - c_{w1} f_w \left(\frac{\tilde{v}}{d} \right)^2 + \frac{c_{b2}}{\sigma} (\nabla \tilde{v})^2 \quad (1.22)$$

where all the terms on right hand side are called as ‘source terms’ denoted by ‘src’

$$\frac{\partial \tilde{v}}{\partial t} + \nabla \cdot \left[\tilde{v} v - \frac{1}{\sigma} (v + \tilde{v}) \nabla \tilde{v} \right] = src$$

The above equation can be re-organized to display the various terms in more physically descriptive fashion with various contributing terms as follows:

$$\underbrace{\frac{1}{\sigma} \left[\nabla \cdot ((v + \tilde{v}) \nabla \tilde{v}) + c_{b2} (\nabla \tilde{v})^2 \right]}_{\text{Diffusion Term}} ; \underbrace{c_{b1} \tilde{S} \tilde{v} - c_{b1} f_{v2} \tilde{S} \tilde{v}}_{\text{Production Term}} ; f_{v2} = 1 - \frac{\chi}{1 + \chi f_{v1}}$$

$$\underbrace{c_{w1} f_w \left(\frac{\tilde{v}}{d} \right)^2 - \frac{c_{b1}}{\kappa^2} \left(\frac{\tilde{v}}{d} \right)^2}_{\text{Destruction Term}}$$

Furthermore, the above equation is integrated over an arbitrary control volume V with boundary ∂V , and the pseudo time term is included for dual time stepping. Following turbulent equation in integral form for dual time stepping is achieved:

$$\frac{\partial}{\partial t} \iiint_V \tilde{v} dV + \frac{\partial}{\partial \tau} \iiint_V \tilde{v} dV + \iint_{\partial V} \left[\tilde{v} \mathbf{v} - \frac{1}{\sigma} (\mathbf{v} + \tilde{v}) \nabla \tilde{v} \right] \cdot \mathbf{n} dA = \iiint_V src dV \quad (1.23)$$

1.3.1.4 Spatial averaging – LES formulation

Figure 1.4 describes the effect of a spatial filter based on the grid size applied to the instantaneous velocity signal. It is assumed that the velocity signal is along a line $y=0$ and $z=0$ planes. It is evident that with the decrease in filter width (Δx), the quality of the filtered signal improves and vice versa.

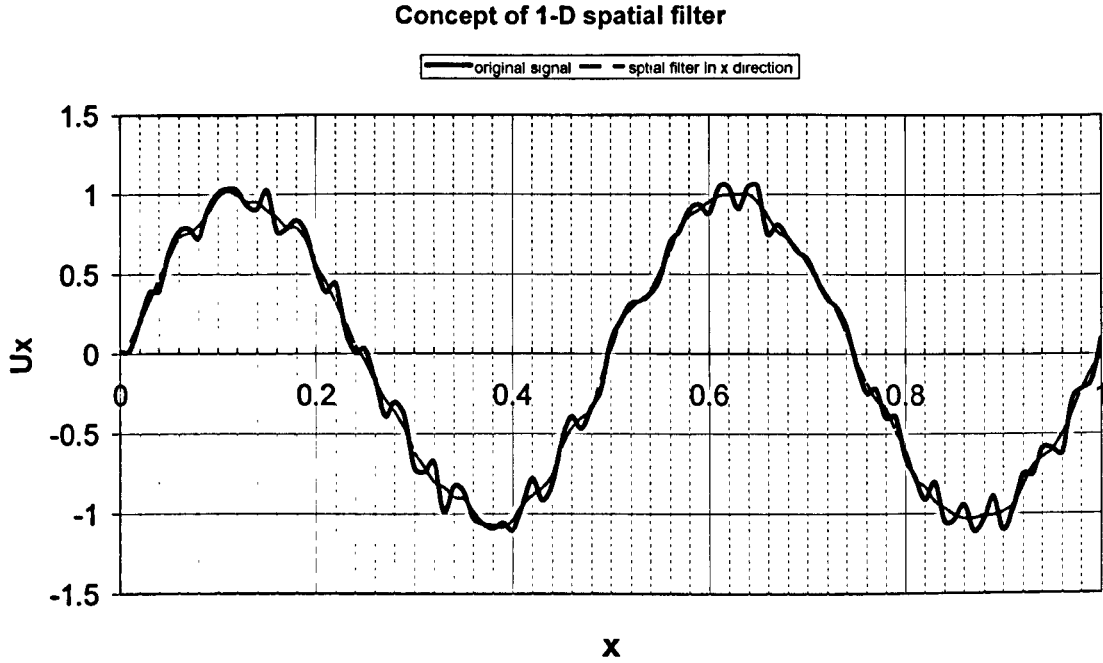


Figure 1.4 Spatial filtering in 1-D with $\Delta x = 0.02$

The main idea of the LES is to compute both the mean flow and the large, energy-containing eddies exactly^[142]. The small-scale structures are not simulated, but their influence on the rest of the flow is modelled generally using sub-grid-scale (SGS) model. It is assumed that the operations of filtering and differentiation commute. It means that

$$\frac{\partial \bar{u}_x}{\partial t} = \overline{\left(\frac{\partial u_x}{\partial t} \right)}, \quad \frac{\partial \bar{u}_x}{\partial x} = \overline{\left(\frac{\partial u_x}{\partial x} \right)}$$

The instantaneous velocity ‘ u ’ is defined in terms of filtered and residual components.

$$u = \bar{u} + u'$$

where \bar{u} is referred to as the filtered velocity and u' as the residual velocity. It is similar to the conventional Reynolds averaging as described in section 2.8.1.1. However, there are some differences in temporal and spatial averaging. Unlike the temporal averaging, the following rules hold for the spatial averaging:

$\overline{\overline{u}} \neq \overline{u}$ and $\overline{u'} \neq 0$. It implies that the spatial filtering of a filtered signal in space is different from that filtered signal and the filtered residual velocity is non-zero.

Applying the spatial filtering to the momentum equation (eq. 1.2) and remembering that the operations of filtering and differentiation commute, the resultant equation as given in Ref. 142 is:

$$\frac{\partial}{\partial t}(\rho \overline{u}_i) + \frac{\partial}{\partial x_j}(\rho \overline{u}_i \overline{u}_j) = -\frac{\partial \overline{p}}{\partial x_i} + \frac{\partial}{\partial x_j}(\tau_{ij}^R) + \nu \nabla^2 \overline{u}_i \quad (1.24)$$

where τ_{ij}^R is the residual stress tensor and is described as:

$$\tau_{ij}^R = \rho [\overline{u_i u_j} - \overline{u}_i \overline{u}_j]$$

In order to account for the un-resolved scales which arise from filtering, an eddy-viscosity model is used commonly. It represents the residual stress tensor τ_{ij}^R as

$$\tau_{ij}^R = 2\mu_R \overline{S}_{ij} + \frac{1}{3} \delta_{ij} \tau_{kk}^R$$

It results in the filtered momentum equations as:

$$\frac{\partial}{\partial t}(\rho \overline{u}_i) + \frac{\partial}{\partial x_j}(\rho \overline{u}_i \overline{u}_j) = -\frac{\partial \overline{p}^*}{\partial x_i} + \frac{\partial}{\partial x_j} [2(\mu + \mu_R) \overline{S}_{ij}] \quad (1.25)$$

where \overline{p}^* represents the modified pressure term.

In LES, there are different methodologies to find out μ_R . From the Smagorinsky model, μ_R is given as:

$$\mu_R = \rho C_S^2 L^2 (2\overline{S}_{ij} \overline{S}_{ij})^{1/2} \quad (1.26)$$

C_S is a dimensionless constant called as Smagorinsky constant and its value is usually ~ 0.1 . It can be observed that the unknown term $\mu_R \alpha (\rho^* L^2 * \overline{S}_{ij})$

1.3.1.5 Comparison of resulting equations of RANS and LES

RANS formulation:

The favre-averaged RANS equation is given as:

$$\frac{\partial}{\partial t}(\overline{\rho \tilde{u}}_i) + \frac{\partial}{\partial x_j}(\overline{\rho \tilde{u}}_i \tilde{u}_j) = -\frac{\partial \overline{p}}{\partial x_i} + \frac{\partial}{\partial x_j}(\overline{\tau}_{ij} + \tau_{ij}^R) \quad (1.27)$$

where, $\tau_{ij}^R = -\overline{\rho u_i'' u_j''} = 2\mu_T S_{ij} + \lambda_T \frac{\partial \tilde{u}_k}{\partial x_k} \delta_{ij}$

The only unknown variable μ_T is calculated using the S-A turbulence model. In the regions, away from the wall, the production of the turbulent viscosity is equal to the destruction term.

$$\underbrace{c_{b1}\tilde{S}\tilde{v} - c_{b1}f_{v2}\tilde{S}\tilde{v}}_{\text{Production Term}} \approx \underbrace{c_{w1}f_w\left(\frac{\tilde{v}}{d}\right)^2 - \frac{c_{b1}}{\kappa^2}\left(\frac{\tilde{v}}{d}\right)^2}_{\text{Destruction Term}} \quad (1.28)$$

This gives the relationship

$$c_{b1}\tilde{S}\tilde{v} \sim c_{w1}f_w\left(\frac{\tilde{v}}{d}\right)^2 \text{ i.e., } \tilde{v} \propto \tilde{S}d^2$$

$$\text{Or } \boxed{\mu_T \propto \tilde{S}d^2} \quad \because \tilde{v} = \frac{\mu_T}{\rho f_{v1}}$$

where d is the distance to the closest wall

LES formulation:

The filtered momentum equation for LES is given as

$$\frac{\partial}{\partial t}(\rho\bar{u}_i) + \frac{\partial}{\partial x_j}(\rho\bar{u}_i\bar{u}_j) = -\frac{\partial \bar{p}}{\partial x_i} + \frac{\partial}{\partial x_j} \left[2(\mu + \mu_R)\bar{S}_{ij} \right] \quad (1.29)$$

where, for the Smagorinsky model $\mu_R = \rho C_s^2 L^2 (2\bar{S}_{ij}\bar{S}_{ij})^{1/2}$

$$\text{Or } \boxed{\mu_R \propto \bar{S}_{ij} L^2}$$

where L is the width of the filter.

The space filtered momentum equation for LES (eq. 1.29) looks remarkably similar to the momentum equation of the RANS formulation described by equation 1.14. By observing the spatial filtering for LES, it is evident that the effect of the filtering is to introduce fictitious stresses termed as “residual stresses”. These residual stresses are similar to the Reynolds stresses introduced by the time-averaging. In short, the structure of the RANS and LES equations in the region away from wall is quite similar. This similarity holds away from the wall because in the region away from the wall, the production and destruction terms of the S-A turbulence model for RANS balance each other and the resultant set of equations is similar to space filtered LES equations using Smagorinsky model.

1.4 CFD approaches to the turbulence simulation

With the detailed discussion of averaging and filtering of Navier-Stokes equations for RANS and LES formulations, it is convenient to discuss their usage in the framework of CFD approaches. Traditionally, the main approaches to the turbulence simulation include the Reynolds-averaged Navier-Stokes simulation (RANS), large-eddy simulation (LES) and direct numerical simulation (DNS). More recently hybrid RANS-LES schemes, in particular Detached Eddy Simulation (termed as DES97 now) have surfaced. The choice of any of these schemes is based on the accuracy of solution

required and the available resources in terms of the computational time and cost. The output from these schemes can be described by considering the sketch of unsteady flow over a circular cylinder at high Reynolds number as shown in the Figure 1.5. On the left hand side of this figure, the domain is sketched with a probe point P in the region of vortex shedding.

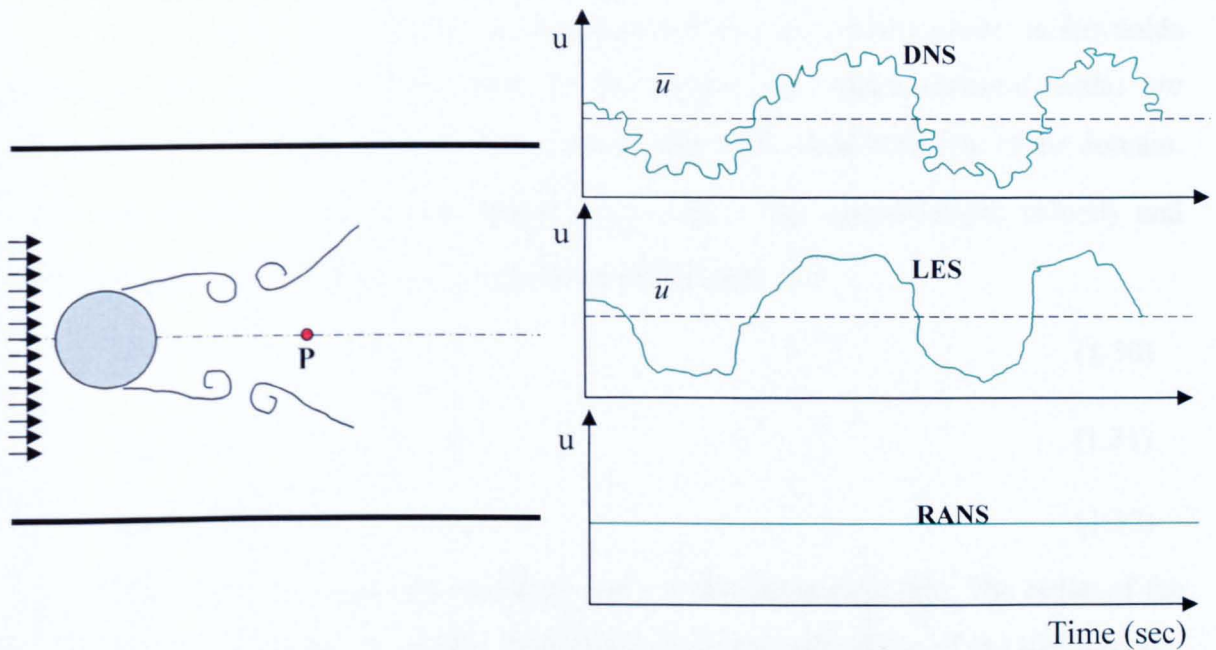


Figure 1.5 *Concept of the different approaches for turbulence simulation for high Reynolds number flow over a circular cylinder*

The sketch of velocity output versus time recorded at point P by DNS, LES and RANS is presented in figure 1.5. It is aimed to present the different scales of motion or flow details predicted by different CFD schemes. It is evident that the direct numerical simulation is at one extreme of the spectrum of turbulence simulation methods where the unsteady three dimensional Navier-Stokes equations are solved directly with no turbulence modelling approximations. All of the essential turbulence scales in space and time are computationally resolved in a DNS solution. In order to achieve this level of DNS resolution, an extremely large number of grid points are required. As a result, DNS has been restricted to flows with low Reynolds number and very simple geometries. In order to reduce the amount of scales, an ensemble averaging operator can be applied to the Navier-Stokes equations, leading to the Reynolds-averaged Navier-Stokes equations (RANS).

1.4.1 Direct numerical simulation (DNS)

In this approach, NS equations are directly discretized and solved without any approximation. Due to this, all the flow structures are solved directly by taking into

consideration the persisting eddies described by the Kolmogorov's law (section 1.3). DNS simulation attempts to solve NS equations for all spatial and temporal scales of motion present in the flow. When it can be applied, it is unrivalled in accuracy and in the level of description provided. But the presence of huge scale differences makes its application impossible to more realistic flows.

The range of scales of motions in turbulent flow grows with increase in Reynolds number. From figure 1.3, the eddies in the largest size range (integral scale) are characterise by the length scale l_0 that is comparable to the geometric size of the domain. The characteristic velocity is represented as $u_0 = u(l_0)$. The unique length, velocity and time scale based on Kolmogorov's hypothesis are defined as^[2]:

$$\eta \equiv (\nu^3/\varepsilon)^{1/4} \quad (1.30)$$

$$u_\eta \equiv (\varepsilon\nu)^{1/4} \quad (1.31)$$

$$\tau_\eta \equiv (\nu/\varepsilon)^{1/2} \quad (1.32)$$

where, ν is the kinematic viscosity and ε is the dissipation rate. The ratios of the smallest to largest scales are readily determined from the definitions of the Kolmogorov scales and from the scaling $\varepsilon \sim u_0^3/l_0$. The results of length, velocity and time scale in three dimensional space are^[2]:

$$\eta/l_0 \sim \text{Re}^{-3/4} \quad (1.33)$$

$$u_\eta/u_0 \sim \text{Re}^{-1/4} \quad (1.34)$$

$$\tau_\eta/\tau_0 \sim \text{Re}^{-1/2} \quad (1.35)$$

where, l_0 , u_0 and τ_0 are length, velocity and time scale for largest eddy.

To capture all the scales on a grid, a grid size of $h \approx \text{Re}^{-3/4}$ is required to be able to capture smallest scales. If this smallest scale is to be approximated with number of nodes, it can be represented in 1D as:

$$N \approx l_0/\eta \quad (1.36)$$

Thus, as shown in the table 1.1, the number of grid points needed to perform a two and three-dimensional DNS are computed from equation 1.33-1.37. The non-dimensional length scale η/l_0 is replaced by grid parameter h . This implies that:

$$N \approx l_0/\eta \approx h^{-1} \text{ for 1D}$$

$$N \approx (l_0/\eta)^3 \approx h^{-3} \text{ for 3D space}$$

<i>Dimension</i>	<i>Size Order of Kolmogorov Scale</i>	<i>Required Mesh Size (h)</i>	<i>Total no of mesh vertices N</i>	<i>Modern Computer Limit</i>
3D	$Re^{-3/4}$	$Re^{-3/4}$	uniform Hexahedron ($h \approx Re^{-3/4}$) $N=h^{-3} \Rightarrow Re^{9/4}$ or $Re \approx N^{4/9}$	$N=10^7$ provides $Re \sim 10^{28/9} = 1292$
2D	$Re^{-1/2}$	$Re^{-1/2}$	Square ($h \approx Re^{-1/2}$) $N=h^{-2} \Rightarrow Re$	$N=10^7$ provides $Re \sim 10^7$

Table 1.1 2D and 3D Reynolds numbers limit for DNS, corresponding to number of nodes $N=10^7$ [based on ref. 140 and ref. 2]

To understand the limitations of DNS, following table presents the Reynolds number range of general flows at standard sea level conditions.

Application	Characteristics	Reynold's Number
Model Airplane	Length = 1m, Velocity = 20 m/s	$\approx 1.3 \times 10^6$
Fighter Airplane (JSF-X35)	Length \approx 14m, Velocity \approx 417 m/s (Mach 1.2)	$\approx 3.6 \times 10^8$
Airbus A380	Length \approx 73m, Velocity \approx 310 m/s (Mach 0.89)	$\approx 1.4 \times 10^9$
Passenger Car	Length = 4 m, Velocity = 16 m/s (\approx 60 Km/hr)	$\approx 4 \times 10^6$
Arts Tower building (Sheffield, UK)	Height = 78 m, Wind Velocity = 5 m/s	$\approx 2.5 \times 10^7$
Atmospheric Flows		$\approx 2 \times 10^7$

Table 1.2 General Range of the Reynolds Number for different flows

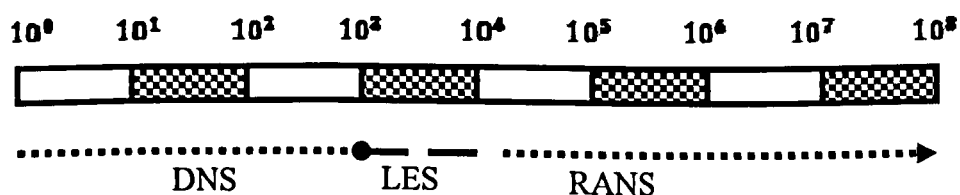


Figure 1.6 General ranges of RANS, LES and DNS based on Reynolds number for real life industrial applications- based on Reference [66]

Figure 1.6 provides the general choice of schemes based on operating Reynolds numbers in the fluid. Another difficulty for a DNS simulation is that the boundary and initial conditions must have the precision, which is required by the smallest scales of flow. Besides the lack of data on every point at the boundary, geometrical aspects such as wall roughness etc. have to be considered. A large Reynolds number flow is inherently unstable and the uniqueness of a (weak) solution is not yet proved in three dimensions for a known initial and boundary conditions. Even small perturbations in these conditions may excite small scales. Thus, the impossibility of prescribing precise initial and boundary conditions causes the resulting flow to have random character.

Flow instabilities lead the transition from laminar to turbulent. For wall bounded flows, it is normally at high Reynolds numbers. However, it can be at extreme low Reynolds numbers e.g., for free shear layer flows (jet flame, wakes, mixing fluids with different densities etc)^[66].

The length and time scales of molecular motion are extremely small compared with human scales. Taking air under atmospheric conditions as an example, the average spacing between molecules is 3×10^{-9} m, the mean free path, λ , is 6×10^{-8} m, and the mean time between successive collision of molecule is 10^{-10} seconds. In comparison, the smallest geometric length scale in a flow, l , is seldom less than $0.1 \text{ mm} = 10^{-4} \text{ m}$, which for flow velocities up to 100 m/sec , yields a flow timescale larger than 10^{-6} s. Thus, even for this example of a flow with small length and time scales, these flow scales exceed the molecular scales by three or more orders of magnitude.

The landmark DNS of plane channel flow at $Re=3300$ by Kim et al^[8], used 2×10^6 grid points, and required approximately 200 hours of CPU time on a Cray YMP. To increase the Reynolds number by a factor of 10 to 33000, 8×10^8 points would be necessary to resolve the flow, and approximately 600000 CPU hours (almost seven year) would have been required on the Cray YMP as described in reference [9]. It provides an idea of the limitation of the available resources for the DNS of the real life flows.

1.4.2 Large eddy simulation (LES)

In LES, only the larger scales of the turbulent motions are explicitly computed, and the effects of the smallest scales on the resolved flows are modelled using subgrid scale (SGS) models with filters, resulting in the approximation at the small scales.

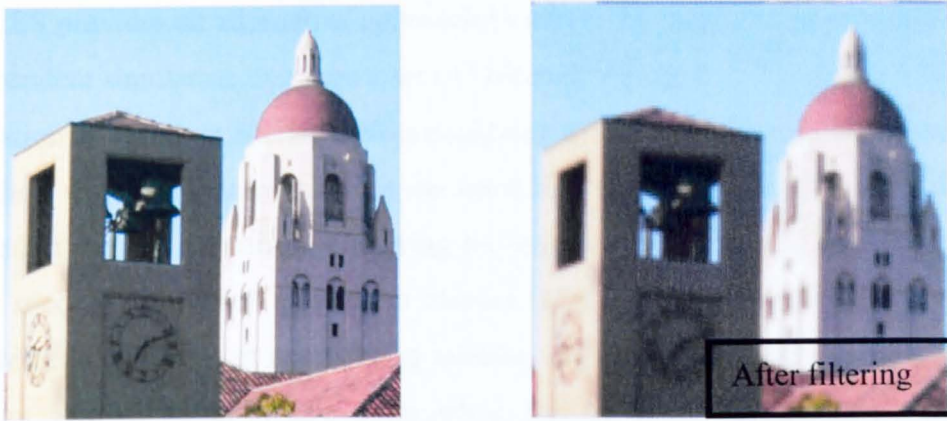


Figure 1.7 *Gaussian Cutoff Filtering*^[10]

The effect of these filters for modelling small fluctuations is better understood by analogy of applying a filter to a real life picture as shown in figure 1.7. It presents the effect of neglecting scales smaller than the applied Gaussian filter. It can be appreciated that although the sharpness of the domain has reduced after applying filter but overall domain is still represented with good approximation. With the increase in filter size, the picture will become more blurred departing further from the actual scene.

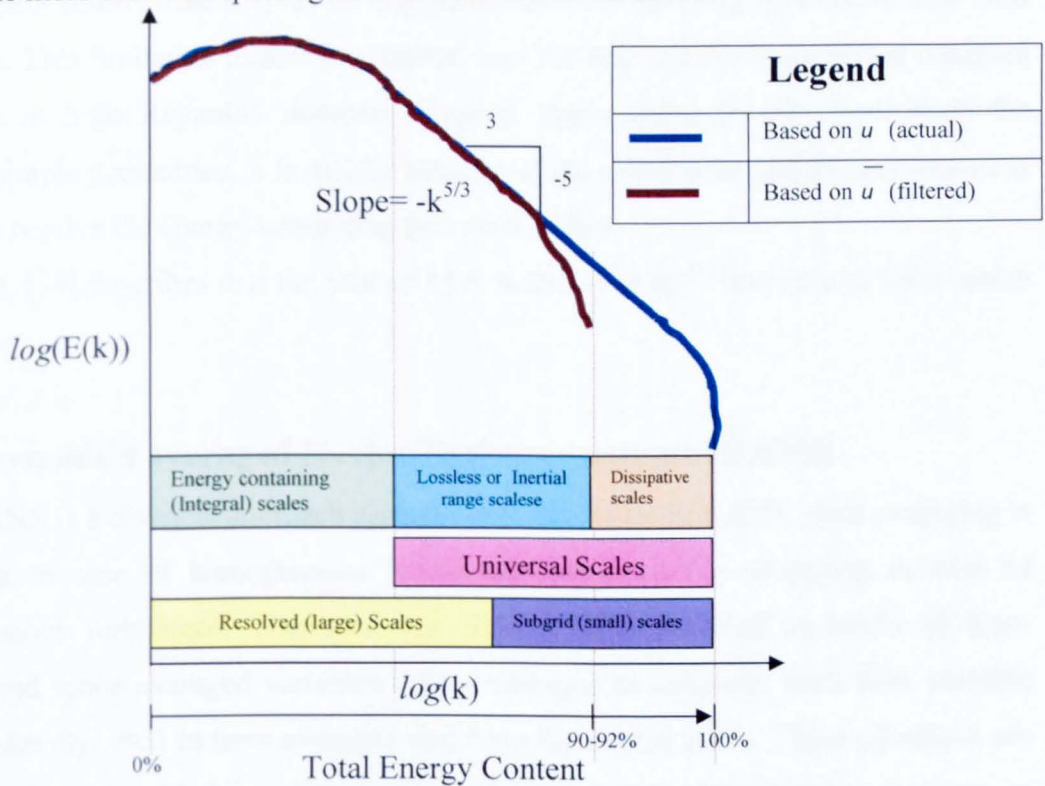


Figure 1.8 *Sketch showing LES with the perspective of Kolmogorov Energy spectrum*

In LES, the filtered scales are approximated through a modelled subgrid scale to improve the performance. Redrawing figure 1.3 and relating it to LES as shown in figure 1.8, presents the underlying theory of LES.

LES provides an alternative approach in which the large eddies are computed in a time-dependent simulation that uses a set of “filtered” equations. Filtering is essentially a manipulation of the exact Navier-Stokes equations to remove eddies smaller than the size of the filter, which is usually taken as the mesh size. Similar to the Reynolds averaging (discussed in the next section), the filtering process creates additional unknown terms that must be modelled in order to achieve closure. Statistics of the mean flow quantities, which are generally of most engineering interest, are gathered during the time-dependent simulation. The attraction of LES approach is that by modelling less of the turbulence (and solving more), the error induced by the turbulence model will be reduced. One might also argue that it ought to be easier to find a “universal” model for the smaller scales, which tend to be more isotropic and less affected by the macroscopic flow features than the large eddies as described in Section 1.2.

It should, however, be stressed that the application of LES to industrial fluid simulations is still not mature. Although LES is less approximate and is supposed to produce better results than RANS, its computational cost becomes formidable near wall boundaries. This limitation makes it a limited tool for real life flows involving complex geometries at high Reynolds numbers. Typical applications to date have been for relatively simple geometries. It is mainly because of the extreme computational resources required to resolve the energy-containing turbulent eddies.

Ref. [74] describes that the cost of LES scales with $Re^{2.4}$ and cost of DES scales with $Re^{3.0}$.

1.4.3 Reynolds’s averaged Navier-Stokes equations (RANS)

RANS is a classical approach used for real life flows. In RANS, time averaging is carried out in case of homogeneous turbulence and ensemble averaging in case of inhomogeneous turbulence. Therefore, the flow is only resolved in terms of time-averaged and space-averaged variables. This technique decomposes each flow variable (velocity, density, etc.) in time averaged and time fluctuating parts. These equations are then manipulated resulting in a number of unknown terms which involve averages of products of fluctuating quantities also called as Reynolds stresses. These equations are then closed by using turbulence models which have coefficients based on the experimentation. No particular turbulence scale is resolved here and all of the effects of the turbulence on the mean flow are modelled. For ergodic or statistically stationary turbulence, RANS nevertheless provides an unbeatable ratio between flow prediction quality and computational cost. However, for unsteady flows, the RANS provides

inaccurate solution as it will function by assuming the flow as a steady case. Unsteady RANS or URANS is proposed to simulate unsteady flows and is discussed in the last part of this section. No universal turbulence model exists for the RANS; therefore, it is highly dependant on the flow nature and the appropriateness of the respective turbulence model. By analysing the results from a wide range of flows simulated using various turbulence models, it is evident that no single turbulence model provides results of good engineering accuracy for all different types of flows.

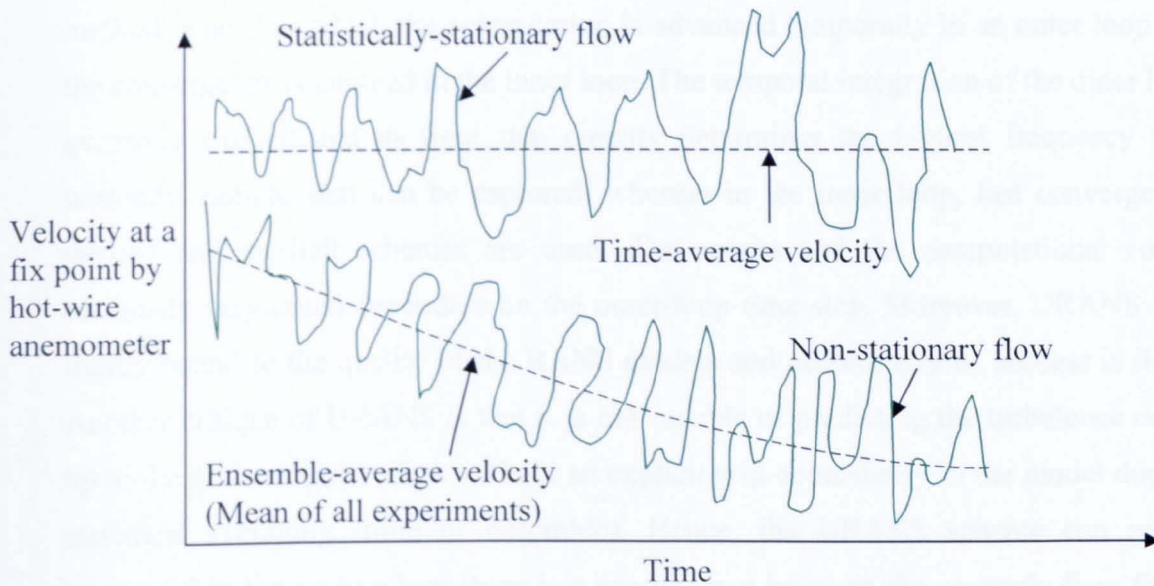


Figure 1.9 *Ensemble averaging in stationary and non-stationary flows*

The principal shortcoming is the fact that the single model must represent a very wide range of scales in light of the energy cascade theory discussed in section 1.3. While the small scales tend to depend only on viscosity and may be somewhat universal, the large ones are affected very strongly by the boundary conditions. Major deficiencies of the latest RANS turbulence models are in turbulent mixing in jet flows, temperature effects, three dimensionality and compressibility effects^[13]. RANS formulation destroys the temporal history of the turbulent eddies. Reynolds-averaging presupposes that the flow is statistically stationary. At the very least, the time-scale associated with the organized unsteady structures must be substantially larger than the turbulent fluctuations. This condition may be satisfied for the low frequency motion such as a very slow pitch before stall, but not necessarily in flutter, buffet, unsteady separation and reattachment, transition or vortex interaction, where the RANS methods reach their limit^[15]. Main disadvantage of Reynolds time averaging is the production of excessive eddy viscosity, which excessively dissipates the unsteady motion of the fluid. Although, modeling the entire spectrum with RANS for the steady flow with no or small separation has met with

some success, the massively separation cases have not been properly resolved by RANS^[12]. For massively detached flows, the detached eddies are essentially geometry dependant and have a typical temporal history. Therefore, modeling them with the RANS is destroying that history and representing them with fairly universal eddies typical of the thin shear layer used for the RANS turbulence model calibration^[14].

The solution proposed by RANS community is unsteady RANS (URANS) technique. In this case the high-frequency turbulent fluctuations are modelled whereas the large-scale motions are resolved as unsteady phenomena. In practice a dual time-stepping method is used in which the computation is advanced temporally in an outer loop while the convergence is pursued in the inner loop. The temporal integration of the outer loop is generally explicit and its time step directly determines the highest frequency of the unsteady motions that can be captured, whereas in the inner loop, fast convergence is desired and implicit schemes are used. The results and the computational cost are obviously very much dependant on the outer-loop time step. Moreover, URANS is still tightly bound to the quality of the RANS models and accordingly its success is limited. Another critique of URANS is that it is not capable of predicting the turbulence cascade up to the grid resolution limit without an explicit grid dependency in the model due to its statistical averaging (time or ensemble). Hence, the URANS scheme can only be successful in the cases where there is a spectral gap between the unsteady flow features and the large turbulent scales.

However, Menter et al. [72] argue that there is no fundamental difference between the momentum equations resulting from the RANS or from the LES approach. In both cases, the flow field is described by the standard momentum equations, augmented by an eddy-viscosity (assuming an eddy-viscosity model). It means that the equations have no memory of their derivation. Therefore, the extent of the prediction of the turbulent structures is dependant on the levels of the eddy viscosity produced by the turbulence model. From this point of view, if the eddy-viscosity produced by URANS model is such that the Reynolds stresses inside a primary vortex (in case of vortex shedding) are produced correctly, then the model, by definition, allows the break up of these eddies and formation of smaller eddies. It is interesting to note that on the basis of the same observation, a variant of LES called MILES (Monotonically Integrated Large Eddy Simulation) exists, which overrules the explicit use of subgrid terms by a filter and relies on the inherent numerical dissipation to represent them. Menter et al. have presented various unsteady cases with their scale-adaptive-simulations (SAS). A further detail can be found in Ref [72]. However, Spalart; a critic to this approach, describes in Ref [69]

that “..The essential feature of SAS, relative to DES, has been not to involve the grid spacing...The new version of SAS now involves the grid size, creating the appearance of an evolutionary convergence with DES” and “..This author has speculated that the original SAS effectively introduces the grid spacing by low-pass filtering the higher derivatives”.

1.4.4 Hybrid schemes

A brief overview of numerical approaches in the CFD was presented in sections 1.4.1-1.4.3. It is also noticed that the LES provides good results for the unsteady flows with largely varying structures but has a very high computational cost in the near wall region. The URANS fails to simulate the unsteady flows with largely varying structures but provides good performance with low cost in the near wall region. The turbulent scales in the near wall region can be well modelled, using a turbulence model. Comparison of the LES and URANS formulations show that the structure of the both is quite similar. Therefore, the URANS (in principle) can be readily extended to work as LES solvers. It has led to the idea to obtain a blended model of LES and URANS to work for complex flows with optimum performance of both. RANS will be used from this point onwards in the context of URANS, on the basis of simplification of Navier-Stokes equations, in line with the general literature. Over the past decade, hybrid RANS-LES methods have received an increasing attention from industry and academia. The idea of being more computationally efficient and viable than LES with better accuracy than the URANS, has proved very tempting to a sizeable community in turbulence research. DESider^[68] (Detached Eddy Simulation for Industrial Aerodynamics) is a European project with a particular focus on the hybrid RANS-LES modelling approaches. Some recent international symposia on the hybrid RANS-LES^[69,70] also highlight the increasing interest in this field of the turbulence-research community.

Limited Numerical Scales (LNS)^[136] is a hybrid RANS-LES methodology that aims to distribute the domain into RANS and LES patches and the LES content is generated by introducing the grid spacing as a function in the turbulence model. Detached Eddy Simulation (DES)^[16] is arguably the most widely used hybrid RANS-LES methodology. Its simplicity, ease of switching from RANS and promising unsteady results has gained attention from the turbulence-research community. It has a continuously expanding spectrum of users from various application perspectives. The original DES is non-zonal in implementation. However, there is a zonal DES method by Deck^[73] as well with very promising results. In the zonal method, the domain is divided

into zones with pre-specified LES and RANS regions. This method avoids the possible switching problem of DES. However, it may be difficult to implement for complex geometries such as an aircraft or automobile engine etc. The DES scheme has also been used as a Wall Modelled LES (WMLES)^[71], an application not intended with the original DES concept. This approach, however, suffered with log-layer mismatch. As commented in Ref [69], “..If it is RANS it should show conclusive steadiness and if it is URANS, it should show conclusive unsteadiness. If it is LES, it has to have some LES content from somewhere.” An inherent problem of getting an input from URANS for LES is the absence of LES content (small unsteady isotropic turbulent structures). Introduction of synthetic turbulence has proved a good solution to this with an objective of generating LES content within boundary layers. Ref. [74] and further references within it, present a good detailed account of this approach. In this study, the main focus of the research is on the original DES (DES97) and DDES; being the most widely used hybrid RANS-LES schemes with an impressive range of results. A recent review by Spalart^[141] presents a detailed overview of DES and its variants. Noticeably it presents DDES and Improved Delayed-Detached Eddy Simulation (IDDES). The main difference between the DDES and IDDES is the definition of the length scale parameter ‘ Δ ’. However, this study is mainly focused on DES and DDES.

1.4.4.1 Detached eddy simulation (DES)

The Detached Eddy Simulation approach (DES) was proposed by Spalart et al. in 1997^[16]. The main theme of the DES scheme was to combine the strengths of the RANS scheme near the solid or wall boundaries and of LES elsewhere. The natural implementation was intended to simulate the entire boundary layer using the RANS and separated region with the LES. It was aimed primarily for the cases in which the flow develops a sharp unsteadiness due to a blunt body or sharp edge, increasing the large scales of flow separation being generated (LES content), independent of upstream turbulence history. In 1999, DES simulation on NACA 0012 at very high angle of attack was presented^[17]. It followed the simulation of flow around a cylinder^[18] and around a sphere^[19]. All these simulations showed very promising results. All previous mentioned work on the DES scheme was developed based on the structured mesh codes. The first application of the DES on an unstructured mesh code was done by Forsythe^[20] in which the DES was applied to study the supersonic flow separation in shock induced boundary layer and supersonic flow behind a base.

The widespread applicability and success of this approach led to its implementation at different full size aircrafts by the U.S. Department of Defence under Project titled “Multidisciplinary Applications of Detached-Eddy Simulations of Separated Flows at High Reynolds Numbers”. Some of its outcome have been published^[21,22,23,24,25] and have shown promising results.

A good beginning reference for DES is “Young Person’s Guide to Detached Eddy Simulation Grids” by Spalart^[46]. It has described the process of grid generation with particular emphasis on different regions of a grid and their required resolution and grid quality. It also points out the inherent advantage of unstructured grids in clustering more points in the regions of interest and coarsening away from it. It also stresses the need of isotropic cells in the LES region.

Due to the fact that the DES scheme involves the RANS turbulence model as its integral part, it does share the pros and cons associated with it. In short, although DES is not a perfect simulation tool, it provides good approximation for highly separated turbulent flows at competitive computational cost.

Despite the fundamental differences from RANS, LES share the same form of its resolvable equations with RANS, in which the SGS stresses corresponds to the Reynolds stresses of RANS. DES was originally proposed by modifying the S-A turbulence model^[16]. Further Travin^[42] and Strelets^[43] also proposed a Menter’s SST model based DES formulation to demonstrate the idea of DES method.

The original DES proposed combines the RANS and LES in a non-zonal manner. DES is based on the Spalart-Allmaras one equation turbulence model^[39]. Length scale, d , generally taken as the shortest distance at any point to the closest wall in RANS mode, is replaced as the minimum between the distance to the wall and a length proportional to the local grid spacing. It is represented mathematically as

$$d_{DES} = \min(d, C_{DES} \nabla) \quad (1.37)$$

where, C_{DES} represents a model constant taken as 0.65 in different studies^[17]. ∇ is the local grid spacing. For structured grids, it is the maximum grid spacing over all three directions. For unstructured grids, it is generally taken as the maximum edge length connecting the centroids of the adjacent cells. In the boundary layer regions, ∇ far exceeds the distance to the wall, d , and standard Spalart-Allmaras RANS turbulence model^[39] is recovered. However, away from the boundaries, the distance to the closest wall exceeds $C_{DES} \nabla$ and the model becomes a simple one-equation sub-grid-scale (SGS) model with mixing length proportional to the grid spacing. Length scales are highly mesh

dependant in the DES. Where it serves good for an isotropic grid, length scale must be redefined for anisotropic or stretched grids for better results. Therefore, the DES scheme is expected to perform best with the isotropic grids (this particular aspect is to become evident in Chapter 6). The concentration of the grid points is expected to be high in the region of high gradients of flow or regions of massively separated flows. The modification from RANS to DES is quite simple. The only change lies in the length scale, d . For RANS, d is the wall distance which plays as a factor of destruction of eddy viscosity. Δ is based on the largest dimension of the local grid cell or local grid spacing $\Delta = \max(\Delta x, \Delta y, \Delta z)$.

The above definition of Δ is directly implemented for the structured grid but for unstructured the grid data has to be manipulated. In this study, a generalized representation of grid spacing is employed,

$\Delta_i = \max_{j \in N_i} |\Delta r_{ij}|$. Another point to note is that this switching is purely based on the geometric or mesh characteristic based. Which means for cell i , the local grid spacing Δ_i is the maximum distance from its centroid to its neighbour cell's, where N_i denotes all the neighbouring cells of i and Δr_{ij} is displacement vector from i 's centroid to j 's. Equation 1.37 divides the whole domain into RANS and LES regions. At a stage with $d \leq C_{des} \Delta$, it corresponds to the RANS region and the model performs similar to the original S-A model. When $d > C_{des} \Delta$, it corresponds to the LES region and the model at the equilibrium state behaves as the Smagorinsky's SGS LES model. Recalling the production and destruction terms in equation 1.28, since it is in equilibrium state, the production term balances the destruction term $c_{b1} \tilde{S} \tilde{v} \sim c_{w1} f_w \left(\frac{\tilde{v}}{\tilde{d}} \right)^2$

i.e, $\tilde{v} \propto \tilde{S} \tilde{d}^2$. It is exactly the same as Smagorinsky's SGS model, where the Smagorinsky eddy viscosity is proportional to the square of grid spacing and the "resolved strain rate". With this new length scale, \tilde{d} , one single model functions as the corresponding RANS/LES model in the respective region with two advantages. Firstly, the grid refinement extends the energy cascade, which enables the solver to capture smaller eddies and on the other hand, DES is capable of treating an entire boundary layer or free shear layer through RANS, which is difficult for most of the wall-model LES solvers. The original S-A model generates too much dissipation near the vortex core, eliminating the vortex breakdown phenomenon observed in the experiments^[41].

In this study, the Dacles-Mariani^[45] version of correction is employed, which modifies the production term by adding one extra term in equation 1.18.

$$\tilde{S} = S + \frac{\tilde{\nu}}{\kappa^2 \tilde{d}^2} f_{v2} - C_{vor} \max(0, S - |S|) \quad (1.38)$$

where $|S|$ is the magnitude of strain-rate tensor and C_{vor} is an user specified constant, which is 2.0 ~ 4.0 for all the calculations. It is evident that last term used is to limit the production of eddy viscosity. When the strain-rate magnitude $|S|$ falls down to less than $\frac{C_{vor} - 1}{C_{vor}}$ of S , the vorticity will no longer generate positive contributions to the production of eddy viscosity. Squires et al^[44] made a review of recent efforts in DES with very promising results.

1.4.4.2 Delayed Detached eddy simulation (DDES)

With the widespread usage and expansion in CFD community using DES, some of the weaknesses of DES were observed. For original DES, it is imperative to use mesh which is in conjunction with natural DES architecture. For instance, for a simulation over an aerofoil, if whole of the boundary layer is to be treated with using RANS, then the mesh should not be extremely fine at leading or trailing edge to confuse the code to assume it as the LES region with in the boundary layer. It means that the chordwise distribution still should be much larger than the surface normal direction distribution. Some applications areas, in which the natural theme of DES is difficult to maintain, were pointed out to cause malfunctioning of the DES simulation. Noticeably, the flow conditions involving thick boundary layer may be difficult to be tackled just on the basis of distance parameter, d , only. It may cause the code to switch to the LES part in the outer boundary layer region, causing sudden decrease in the modelled stress giving rise to separation which is not physical but due to the grid. This problem is termed as the Grid Induced Separation (GIS) and this erratic phenomenon is termed as modelled stress depletion (MSD). Menter and Kuntz [126] were the first to highlight this problem. This issue was addressed by proposing a fix to this problem in the form of DDES, similar to the Menter's scaling functions in his SST turbulence model. It will be discussed in the next chapter with the detailed formulations. The proponents of the DES scheme renamed original DES to DES97 to indicate the initial DES scheme proposed in 1997.

The original DES, termed now as DES97, has an inherent shortcoming of switching from RANS to LES mode within the boundary layer for thick boundary layer cases or with cases in which the increased grid density e.g., near leading or trailing edge of an aerofoil;

confuses the solver to treat that region in the LES model. This problem was highlighted by Menter and Kuntz ^[126] for their study over Ahmad's model car.

The main idea of DDES is to include the molecular and turbulent viscosity information into the switching mechanism to delay this switching in boundary layers.

$$\tilde{d} \equiv d - f_d \max(0, d - C_{DES} \Delta) \quad (1.39)$$

$$f_d \equiv \tanh([8r_d]^3) \quad (1.40)$$

$$r_d \equiv \frac{v_t + \nu}{\sqrt{U_{i,j}U_{i,j}}\kappa^2 d^2} \quad (1.41)$$

The details of this modification are presented in Ref [61]. Some of the fundamental details are presented here. It is evident that $f_d = 0$ provides $\tilde{d} \equiv d$, which is the original RANS formulation. $f_d = 1$ provides $\tilde{d} \equiv d - \max(0, d - C_{DES} \Delta)$ which is the same as DES97 i.e., $\tilde{d} \equiv \min(d, C_{des} \Delta)$. In RANS, the parameter 'r' is of special importance. This parameter has a value of 1 in the logarithmic layer, decreasing gradually to '0' towards the edge of the boundary layer. Hence, the dissipation is suddenly reduced in the outer edge of boundary layer. In the DDES, a similar parameter r_d is used. $r_d \approx 1$ in the RANS region and $r_d \ll 1$ in the LES region. In order to avoid $r_d = 0$, in the region away from wall ($v_t \approx 0$), ν is added to the numerator. The function $f_d = f(r_d)$ is designed to produce '1' for the LES region and '0' elsewhere. Tanh() makes sure that it is insensitive to result $f_d = 0$ for very large input r_d values, typical where it is very close to the wall. The constants value 8 and []³ in $f_d \equiv \tanh([8r_d]^3)$ are based on shape requirements for f_d to perform as per requirements in the RANS and the LES regions and on results from tests on the flat plate boundary layer.

1.5 Turbulent Reynolds Stresses

1.5.1 Derivation of the Modelled Reynolds Stress formula (based on Bradshaw's Formulation^[93])

In 1877, Boussinesq provided a solution for turbulence closure. This approximation assumes that the principal axes of the Reynolds stress tensor are coincident with the mean strain-rate tensor throughout the domain on all points. He assumed that the turbulence stresses are directly proportional to the velocity gradient with eddy viscosity (μ_t) as the constant of proportionality and only unknown value. This value further can be calculated using different turbulence models.

From Boussinesq hypothesis [7], the eddy viscosity is linearly related with Reynolds turbulent stresses. Although, the assumption of μ_t as an isotropic scalar quantity in the Boussinesq hypothesis may not be strictly true. Other option is to go for more computationally expensive Reynolds stress transport equations. S-A model used in this study utilizes the Boussinesq hypothesis.

The basic relationship is drawn from analogy with molecular transport of momentum

$$\overline{u'_i u'_j} = \frac{2}{3}(k)\delta_{ij} - \nu_t \left(\frac{\partial U_i}{\partial x_j} + \frac{\partial U_j}{\partial x_i} \right) \quad (1.42)$$

It provides the following normal and shear stress components for Reynolds stresses:

$$\overline{u'u'} = \frac{2}{3}(k) - \nu_t \left(\frac{\partial U}{\partial x} + \frac{\partial U}{\partial x} \right)$$

$$\overline{v'v'} = \frac{2}{3}(k) - \nu_t \left(\frac{\partial V}{\partial y} + \frac{\partial V}{\partial y} \right)$$

$$\overline{u'v'} = -\nu_t \left(\frac{\partial U}{\partial y} + \frac{\partial V}{\partial x} \right)$$

Where U and V are the mean velocity components. For two-equation turbulence models using turbulent kinetic energy (k) as a variable in the equation, k is calculated from solution of those equations. However, in 1 equation S-A turbulence model, k is not explicitly calculated. Hence, it is to be approximated using Bradshaw's hypothesis [93].

The turbulent energy equation for a two-dimensional incompressible mean flow, outside the viscous sublayer, is (Townsend 1956)[94]

$$q^2 = u'^2 + v'^2 + w'^2 = 2k \quad (1.43)$$

$$\tau = -\rho \overline{u'v'}$$

$$\underbrace{\frac{1}{2}\rho \left(U \frac{\partial q^2}{\partial x} + V \frac{\partial q^2}{\partial y} \right)}_{\text{advection}} - \underbrace{\tau \frac{\partial U}{\partial y}}_{\text{Production}} + \underbrace{\frac{\partial}{\partial y} \left(\overline{pv} + \frac{1}{2} \rho \overline{q^2 v} \right)}_{\text{diffusion}} + \underbrace{\rho \varepsilon}_{\text{dissipation}} = 0 \quad (1.44)$$

$$\text{And } \varepsilon = \nu \left(\frac{\partial u_i}{\partial x_j} \right)^2$$

It can be regarded as an equation for the advection or rate of change of turbulent kinetic energy along a mean streamline through a point if all the other terms as known at that point, just as the boundary-layer momentum equation,

$$\rho \left[U \frac{\partial U}{\partial x} + V \frac{\partial U}{\partial y} \right] = \rho U_1 \frac{dU_1}{dx} + \frac{\partial \tau}{\partial y} \quad (1.45)$$

It can be regarded as an equation for the rate of change of mean-flow momentum ρU .

By defining:

$$a1 \equiv \frac{\tau}{\rho q^2}, L \equiv \frac{\left(\frac{\tau}{\rho}\right)^{\frac{3}{2}}}{\varepsilon}$$

$$G \equiv \frac{\left(\frac{\overline{pv}}{\rho} + \frac{1}{2}\overline{q^2v}\right)}{\left(\frac{\tau_{\max}}{\rho}\right)^{\frac{1}{2}} \frac{\tau}{\rho}}$$

The choice of empirical functions (Page 599, Ref. [93]):

$$a1 \equiv \frac{\tau}{\rho q^2} = 0.15 \quad (1.46)$$

$$a1 = \frac{-\rho \overline{uv}}{\rho(\overline{u'^2} + \overline{v'^2} + \overline{w'^2})}$$

$$a1 = \frac{\tau}{\frac{1}{2}\rho q^2} = 0.3 \quad (\text{by using equation 1.43})$$

$$a1 = \frac{\tau}{k} = 0.3$$

Considering a 2D log law boundary layer, put $a1 = \sqrt{C_\mu}$
 $(\Rightarrow C_\mu = 0.09)$

$$\frac{\tau}{k} = \sqrt{C_\mu}$$

$$k = \frac{\tau}{\sqrt{C_\mu}} \quad \therefore \tau = -\rho \overline{uv} \quad (1.47)$$

Using Boussinesq hypothesis:

$$k = \frac{v_t \left| \frac{\partial u}{\partial y} \right|}{\sqrt{C_\mu}} = \frac{v_t S^*}{\sqrt{C_\mu}} \quad \therefore S^* = \sqrt{2S_y S_{y'}} \quad (1.48)$$

$$S_y = \frac{1}{2} \left(\frac{\partial U_x}{\partial x_j} + \frac{\partial U_j}{\partial x_x} \right)$$

Similar approximations have been used in Ref.[95] and found to produce good results.

1.5.2 Resolved Turbulent Reynolds Stresses

Resolved stresses are computed in the code after establishing that the solution is mature (after sufficient shedding cycles, the vortex shedding establishes a more regularized pattern). A parameter, 'rssavfr' representing Reynolds stresses saving frequency, is defined in the initialization file to describe the number of iterations after which the data is accumulated for calculation of the Reynolds stresses. Two other recording parameters tr1 and tr2 are specified in the initialization file which corresponds to the start and end time of this data recording. It is imperative to make sure that this time is sufficient enough for recording of the Reynolds stresses. In all the simulations, at least 20 shedding cycles are taken for recording of the Reynolds stresses and the values are sampled at each iteration. The symbol $\langle \rangle$ represents the variable averaged values over the specified number of iterations.

$$\begin{aligned}\overline{u'u'} &= \langle uu \rangle - \langle u \rangle^2 \\ \overline{v'v'} &= \langle vv \rangle - \langle v \rangle^2 \\ \overline{u'v'} &= \langle uv \rangle - \langle u \rangle \langle v \rangle\end{aligned}\tag{1.49}$$

1.6 A brief description of the present research work:

1.6.1 Work related to the programming - Contributions to the solver development

As a part of this research, different enhancements have been made in the in-house code DG-DES^[1]. Some of the important contributions are described as follows:

The pre-processing part of the code was written in Fortran (initially was in C language). The code can now read in the Gridgen software input as well, in addition to the original Gambit software. The numerical accuracy of the in-house solver has been upgraded to a double precision (with a possibility of switching back to the single precision with a single line program change). It now includes the mechanism to locate and record readings at different probe locations in the domain. The capability to plot Delaunay triangulation and surface Y+ value is implemented. It can also compute the resolved and modelled stresses in the flow with the required recording frequencies. Two more inviscid flux calculation schemes (HLLC and AUSM) have been added.

DGDES solver has different versions for 2D (Laminar) and 3D (parallel) flow simulations. A serial version for 3D is extracted from the 3D parallel version which is very useful for some quick experimentation avoiding the complications of MPI. Delaunay Graph based mesh deformation scheme is implemented in all these codes.

1.5.2 Scientific research contributions

This research is primarily focused on the original DES and DDES with static and moving mesh simulations. As a first step, in order to validate the changes made in the DG-DES, steady state transonic flow simulations over the RAE2822 and ONERA M6 wing were carried out. A good agreement of results with the experimental data was achieved using different solver option with single and double precision.

The Aerospatiale A-airfoil was simulated at stall conditions ($\alpha=13.3^\circ$, $Re= 2 \times 10^6$). The results from the DES simulation (using the Roe scheme for the inviscid flux calculation) and the URANS were compared with the experimental data. The DES cases were further simulated using AUSM and HLLC schemes. A further in-depth analysis was done to analyse the DES results. It was revealed that the DES in this case switches prematurely to the LES mode within the boundary layer increasing the modelled stress depletion. As a remedy, the DDES was implemented and found to solve this problem. A detailed analysis was carried out to investigate the effect of the modelled stress depletion on the modelled stresses at different suction side locations. The comparison of different turbulence parameters calculated by using the RANS, DES and DDES was done with the available experimental data and reasonable agreements were obtained.

As a natural DES case, high Reynolds number flows over circular cylinder is discussed in detail at different Reynolds number of 1.4×10^5 , 3.6×10^6 and 8×10^6 . Resolved stresses at Reynolds number 1.4×10^5 are compared with experimental data and encouraging results are obtained.

2D simulations are done with the moving mesh at low Reynolds numbers using the Delaunay Graph method. A potential problem of the grid clustering with the original method for flapping wings case was observed and it was suggested that keeping the initial Delaunay Graph the same for complete flapping cycle may avoid this problem ^[75]. Implementation of the Delaunay graph is done in three dimensional space and the initial results are presented.

2 Mathematical Formulations of Governing Equations

This chapter contains the flow governing equations used in the DG-DES solver. It comprises three parts. The first part includes the general Reynolds averaged Navier-Stokes equation, their preconditioning form and its dual time stepping application. The second part comprises the ALE formulation to account for unsteady flow problems with moving boundaries. The third part covers the implementation of one equation S-A turbulence model for the Unsteady Reynolds Average Navier-Stokes equation (URANS) and its manipulation to represent the corresponding DES formulation. The main idea of its inviscid dual time step formulation is similar to the Reference [26].

2.1 Introduction

The fluid flow regimes are classified in terms of their respective Mach numbers as a measure of their flow speed. Generally, if flow speed is less than Mach number 0.3, then it is graded as subsonic and incompressible, flow speed around Mach number 0.8 is called transonic, flow speed above Mach number 1.0 is called supersonic and Mach number greater than 4 comes under hypersonic classification. There are situations when the Mach number of the flow is very small but it is compressible. e.g., strong wall heating or cooling may cause the density to change significantly. Also in MEMS, the pressure in some micro devices changes strongly because of viscous effects even at Mach number less than 0.3. Corresponding to this pressure change are the strong density changes that must be taken into account when writing the continuum equations of motion^[66].

Historically, pressure based methods are used for subsonic flows^[27] and density based methods are used for other high speed flows^[28]. Due to wide area of application of CFD in industry, academia and research, the numerical code developed are expected to cover the vast range of problems covering all flow regimes. It is, therefore, a natural preference to have a single code capable to handle these problems. To cater for this, pressure based methods have been extended to solve the compressible flow range^[29] and similarly density based methods have been extended to solve low speed incompressible domain^[30,31].

Before going further to describe the mathematical form of URANS, it is imperative to present the underlying assumptions used in the numerical solver

The fundamental principles as (described in section 1.1) are applied to a suitable model of flowfield and mathematical equations governing the fluid flow are obtained. Generally the governing equations are obtained in the conservation form for the stationary model of the flow and in the non-conservative form if it is moving with the flow ^[67]. If it is implemented on a finite domain, integral form is obtained. Where as, if it is implemented on an infinitesimal small element in a fluid, differential form is obtained. The integral form of the equations allows for the presence of discontinuities such as shock waves inside the control volume (fixed in space); there is no inherent mathematical reason to assume otherwise. However, the differential form of the governing equation assumes flow properties are differentiable; hence, continuous flow properties are required. Due to this reason, integral form is considered as more fundamental.

DG-DES solver uses conservation form to solve the governing equations. It is very important to maintain the conservation of the governing flow equations for any fluid flow simulation. By solving equations in conservation form, the conservation of mass, momentum and energy is automatically ensured. The conservation form of the governing equations provides a numerical and computer programming convenience as continuity, momentum and energy equations can all be expressed by the same generic equation. Another reason to choose conservation form is that although the primitive variables become discontinuous across the shock wave, the conservative variables do not. For instance, in one dimensional flow, although the density ρ is discontinuous across the shock wave but ρu & $\rho u^2 + p$ remains continuous ^[67].

The fluid motions under consideration are non-relativistic; the characteristic velocities of the fluids under consideration are much small in comparison with the speed of light. It makes the mass and energy non-interchangeable and they can be represented separately in conserved equation form. The fluid is assumed to be a continuum. It will ensure that the derivatives of all the dependant variables exist and represent the fluid characteristics in a reasonable way. It allows the primitive variables of the flow such as pressure, velocity, temperature, density etc. (which describe the basic properties of the fluid) to be described with the differential calculus. The differential calculus is applied on the elements which are large in comparison with the microscopic structure but reasonably small in comparison with the macroscopic phenomenon. It presents the approximate representation of a real domain of infinite detail plausible, by discretizing it numerically

to a finite collection of elements. The continuum assumptions ensure that the matter is continuous and indefinitely divisible.

The assumption of continuum is justified if the real life fluid flow statistics are considered. There are usually more than 1 million molecules in the smallest volume in which appreciable macroscopic changes takes place ^[66]. The length and time scales of molecular motion are extremely small compared with human scales. Taking air under atmospheric conditions as an example, the average spacing between molecules is 3×10^{-9} m, the mean free path, λ , is 6×10^{-8} m, and the mean time between successive collision of molecule is 10^{-10} s. In comparison, the smallest geometric length scale in a flow, l , is seldom less than $0.1 \text{ mm} = 10^{-4} \text{ m}$, which for flow velocities up to 100 m/sec , yields a flow timescale larger than 10^{-6} s. Thus, even for this example of a flow with small length and time scales, these flow scales exceed the molecular scales by three or more orders of magnitude ^[2].

The fluid media is assumed to be Newtonian, isotropic, Fourier and compressible. Newtonian implies that the stress tensor is linearly related with the symmetric part of the deformation tensor (rate of strain). The isotropy assumption reduces the 81 constants of proportionality in that linear relation to two constants ^[2]. Fourier fluid is the one for which the conduction part of the fluid is linearly related to the temperature gradient. Isotropy implies that the constant of proportionality in this relation is a single scalar. The Stokes hypothesis relates the first and second coefficient of viscosity.

For turbulent flows, the dependant variables are random functions of space and time. No straight forward numerical method is capable of obtaining stochastic solutions of these nonlinear partial differential equations. And this has been the biggest bottleneck in conquering the fortress of turbulence.

The fluid media has a Knudsen number much less than unity to satisfy continuum. Knudsen number is the ratio of the mean free path to the characteristic length. It simply represents that how much distance a molecule will travel on average before hitting another molecule. Problems with Knudsen numbers close to unity are preferred for statistical mechanics (Lagrangian approach) instead of continuum mechanics (Eulerian approach) ^[66].

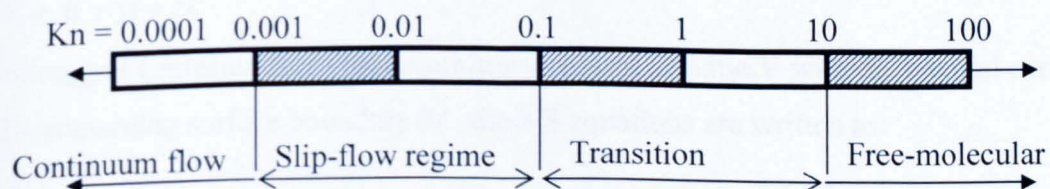


Figure 2.1 Knudsen number regimes (Reproduced from Reference [66])

Knudsen Number	Equations applied	Degree of rarefaction
$Kn \rightarrow 0$ ($Re \rightarrow \infty$)	Euler equations (neglect molecular diffusion)	Ordinary density levels
$Kn \leq 10^{-2}$	Navier-Stokes equations (No-slip boundary conditions)	
$10^{-2} \leq Kn \leq 10^{-1}$	Navier-Stokes equations (Slip boundary conditions)	Slightly rarefied
$10^{-2} \leq Kn \leq 10^{-1}$	Transition regime	Moderately rarefied
$Kn > 10$	Free-molecular flow	Highly rarefied

Table 2.1 *Different numerical approaches for Knudsen number regimes (based on data from Reference [66])*

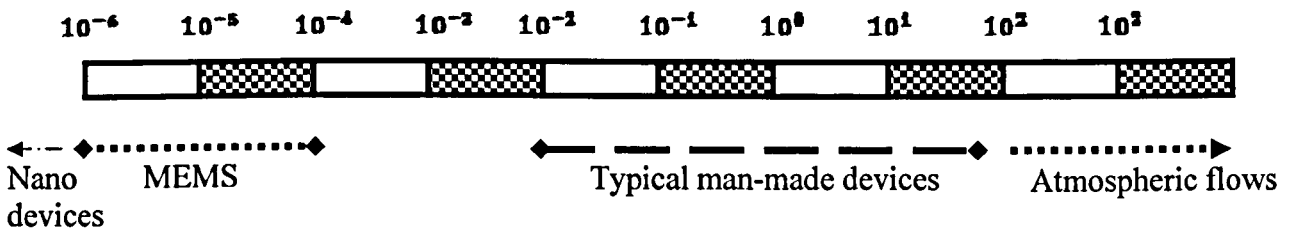


Figure 2.2 *Size in meters of different objects and flow domains under CFD simulation- based on Reference [66]*

With this overview, the Navier-Stokes equations are presented next.

2.2 Discretization of governing equations

Navier-Stokes equations form a coupled system of nonlinear PDE's describing the conservation of mass, momentum and energy. They describe the viscous flow of a continuum Newtonian fluid. For a Newtonian fluid in three dimensional space with no source term involved, the governing equations can be written in differential form as:

$$\frac{\partial \mathbf{W}}{\partial t} + \frac{\partial [\mathbf{F} - \mathbf{G}]}{\partial \mathbf{X}} = 0 \quad (2.1)$$

where,

$$\mathbf{X} = x\hat{i} + y\hat{j} + z\hat{k}$$

In integral Cartesian form for an arbitrary control volume V with differential surface area dA containing surface boundary ∂A , the NS equations are written as:

$$\frac{\partial}{\partial t} \iiint_V \underbrace{\mathbf{W}}_{\text{Conservative variables}} dV + \iint_{\partial A} \left[\underbrace{\mathbf{F}}_{\text{inviscid flux}} - \underbrace{\mathbf{G}}_{\text{viscous flux}} \right] \cdot d\mathbf{A} = 0 \quad (2.2)$$

where,

$$W = \begin{Bmatrix} \rho \\ \rho u \\ \rho v \\ \rho w \\ \rho E \end{Bmatrix}, \quad F = \begin{Bmatrix} F_x \\ F_y \\ F_z \end{Bmatrix}, \quad G = \begin{Bmatrix} G_x \\ G_y \\ G_z \end{Bmatrix}$$

$$\begin{aligned}
 F_x &= \begin{Bmatrix} \rho u \\ \rho uu + p \\ \rho uv \\ \rho uw \\ \rho uE + pu \end{Bmatrix}, & G_x &= \begin{Bmatrix} 0 \\ \tau_{xx} \\ \tau_{xy} \\ \tau_{xz} \\ u\tau_{xx} + v\tau_{xy} + w\tau_{xz} - q_x \end{Bmatrix} \\
 F_y &= \begin{Bmatrix} \rho v \\ \rho vu \\ \rho vv + p \\ \rho vw \\ \rho vE + pv \end{Bmatrix}, & G_y &= \begin{Bmatrix} 0 \\ \tau_{yx} \\ \tau_{yy} \\ \tau_{yz} \\ u\tau_{yx} + v\tau_{yy} + w\tau_{yz} - q_y \end{Bmatrix} \\
 F_z &= \begin{Bmatrix} \rho w \\ \rho wu \\ \rho wv \\ \rho ww + p \\ \rho wE + pw \end{Bmatrix}, & G_z &= \begin{Bmatrix} 0 \\ \tau_{zx} \\ \tau_{zy} \\ \tau_{zz} \\ u\tau_{zx} + v\tau_{zy} + w\tau_{zz} - q_z \end{Bmatrix}
 \end{aligned} \tag{2.3}$$

By observing the inviscid fluxes F , it can be seen that they comprise of convection and pressure terms.

$$\begin{aligned}
 F_x &= \begin{Bmatrix} \rho u \\ \rho uu + p \\ \rho uv \\ \rho uw \\ \rho uE + pu \end{Bmatrix} = \underbrace{\rho u \begin{Bmatrix} 1 \\ u \\ v \\ w \\ E \end{Bmatrix}}_{\text{Convective terms}} + \underbrace{p \begin{Bmatrix} 0 \\ 1 \\ 0 \\ 0 \\ u \end{Bmatrix}}_{\text{Pressure terms}} \\
 F_y &= \begin{Bmatrix} \rho v \\ \rho vu \\ \rho vv + p \\ \rho vw \\ \rho vE + pv \end{Bmatrix} = \underbrace{\rho v \begin{Bmatrix} 1 \\ u \\ v \\ w \\ E \end{Bmatrix}}_{\text{Convective terms}} + \underbrace{p \begin{Bmatrix} 0 \\ 0 \\ 1 \\ 0 \\ v \end{Bmatrix}}_{\text{Pressure terms}}
 \end{aligned} \tag{2.4}$$

$$F_z = \begin{Bmatrix} \rho w \\ \rho w u \\ \rho w v \\ \rho w w + p \\ \rho w E + p w \end{Bmatrix} = \underbrace{\rho w \begin{Bmatrix} 1 \\ u \\ v \\ w \\ E \end{Bmatrix}}_{\text{Convective terms}} + \underbrace{p \begin{Bmatrix} 0 \\ 0 \\ 0 \\ 1 \\ w \end{Bmatrix}}_{\text{Pressure terms}}$$

$$E = H - \frac{P}{\rho}$$

$$H = h + \frac{|V|^2}{2}$$

$$H = C_p T + \frac{1}{2}(u^2 + v^2 + w^2)$$

$$E = C_p T + \frac{1}{2}(u^2 + v^2 + w^2) - \frac{P}{\rho}$$

It can be written as:

$$E = C_v T + \frac{1}{2}(u^2 + v^2 + w^2) \quad \therefore C_p T - \frac{P}{\rho} = C_v T$$

$$S_{ij} = \begin{bmatrix} \tau_{xx} & \tau_{xy} & \tau_{xz} \\ \tau_{yx} & \tau_{yy} & \tau_{yz} \\ \tau_{zx} & \tau_{zy} & \tau_{zz} \end{bmatrix}$$

$$\tau_{xx} = 2\mu \frac{\partial u}{\partial x} + \lambda \left(\frac{\partial u}{\partial x} + \frac{\partial v}{\partial y} + \frac{\partial w}{\partial z} \right)$$

$$\tau_{yy} = 2\mu \frac{\partial v}{\partial y} + \lambda \left(\frac{\partial u}{\partial x} + \frac{\partial v}{\partial y} + \frac{\partial w}{\partial z} \right)$$

$$\tau_{zz} = 2\mu \frac{\partial w}{\partial z} + \lambda \left(\frac{\partial u}{\partial x} + \frac{\partial v}{\partial y} + \frac{\partial w}{\partial z} \right)$$

$$\tau_{xy} = \tau_{yx} = \mu \left(\frac{\partial u}{\partial y} + \frac{\partial v}{\partial x} \right)$$

$$\tau_{yz} = \tau_{zy} = \mu \left(\frac{\partial v}{\partial z} + \frac{\partial w}{\partial y} \right)$$

$$\tau_{zx} = \tau_{xz} = \mu \left(\frac{\partial w}{\partial x} + \frac{\partial u}{\partial z} \right)$$

Stokes Hypothesis provides:

$$\lambda = -\frac{2}{3}\mu$$

Sutherland's Law:

$$\frac{\mu}{\mu_0} = \left(\frac{T}{T_0}\right)^{\frac{3}{2}} \frac{T_0 + 110.4}{T + 110.4} \quad (2.7)$$

q is heat flux vector

$$q_x = -\kappa \frac{\partial T}{\partial x} \quad (2.8)$$

$$q_x = -\kappa \frac{\partial T}{\partial x}$$

$$q_z = -\kappa \frac{\partial T}{\partial z}$$

The thermal conductivity κ is represented in terms of Prandtl number.

$$\text{Pr} = \frac{\mu C_p}{\kappa} \quad (2.9)$$

It is beneficial to transform the conservation equation in terms of primitive variables. The choice of primitive variable vector Q as dependant variable is desirable due to following reasons^[26]:

1. It is a natural choice for incompressible flows
2. Q is reconstructed rather than W to obtain higher order spatial reconstruction, to obtain more accurate velocity and temperature gradients in viscous fluxes and pressure gradients in inviscid fluxes.
3. Pressure as dependant variable allows the propagation of acoustic waves in the system to be singled out.

Therefore, transforming the NS equations from previous conservative form to its primitive form:

$$\frac{\partial W}{\partial Q} \frac{\partial}{\partial t} \iiint_V Q dV + \iint_A [F - G].dA = 0 \quad (2.10)$$

where primitive variable matrix Q is presented as,

$$Q = \begin{pmatrix} p \\ u \\ v \\ w \\ T \end{pmatrix}$$

where $\frac{\partial W}{\partial Q}$ is the Jacobian matrix and is presented as

$$\frac{\partial W}{\partial Q} = \begin{bmatrix} \frac{\partial W(1)}{\partial Q(1)} & \frac{\partial W(1)}{\partial Q(2)} & \frac{\partial W(1)}{\partial Q(3)} & \frac{\partial W(1)}{\partial Q(4)} & \frac{\partial W(1)}{\partial Q(5)} \\ \frac{\partial W(2)}{\partial Q(1)} & \frac{\partial W(2)}{\partial Q(2)} & \frac{\partial W(2)}{\partial Q(3)} & \frac{\partial W(2)}{\partial Q(4)} & \frac{\partial W(2)}{\partial Q(5)} \\ \frac{\partial W(3)}{\partial Q(1)} & \frac{\partial W(3)}{\partial Q(2)} & \frac{\partial W(3)}{\partial Q(3)} & \frac{\partial W(3)}{\partial Q(4)} & \frac{\partial W(3)}{\partial Q(5)} \\ \frac{\partial W(4)}{\partial Q(1)} & \frac{\partial W(4)}{\partial Q(2)} & \frac{\partial W(4)}{\partial Q(3)} & \frac{\partial W(4)}{\partial Q(4)} & \frac{\partial W(4)}{\partial Q(5)} \\ \frac{\partial W(5)}{\partial Q(1)} & \frac{\partial W(5)}{\partial Q(2)} & \frac{\partial W(5)}{\partial Q(3)} & \frac{\partial W(5)}{\partial Q(4)} & \frac{\partial W(5)}{\partial Q(5)} \end{bmatrix} \quad (2.11)$$

A single term of the above Jacobian matrix for description is as follows:

$$\begin{aligned} \frac{\partial W(5)}{\partial Q(5)} &= \frac{\partial}{\partial T}(\rho E) \\ \frac{\partial(\rho E)}{\partial T} &= \frac{\partial}{\partial T}(\rho H - P) \\ &= \rho_T H + \rho \frac{\partial(H)}{\partial T} - \frac{\partial}{\partial T}(P) \quad \therefore \text{differentiating } \rho H \text{ by parts} \end{aligned}$$

Similarly, the resultant Jacobian matrix is represented by

$$\frac{\partial W}{\partial Q} = \begin{bmatrix} \rho_\rho & 0 & 0 & 0 & \rho_T \\ \rho_p u & \rho & 0 & 0 & \rho_T u \\ \rho_p v & 0 & \rho & 0 & \rho_T v \\ \rho_p w & 0 & 0 & \rho & \rho_T w \\ \rho_p H - 1 & \rho u & \rho v & \rho w & \rho_T H + \rho C_p \end{bmatrix} \quad (2.12)$$

where ρ_p and ρ_T are calculated from equation of state as

$$P = \rho RT$$

$$\rho_p = \left. \frac{\partial \rho}{\partial p} \right|_T = \frac{1}{RT}$$

$$\rho_T = \left. \frac{\partial \rho}{\partial T} \right|_p = -\frac{P}{RT^2}$$

The reason of representing in terms of Jacobian is that the derivatives of the dependent variables appear linearly, hence the quasi-linear form is obtained. The mathematical nature of such equations is dictated by the eigen-values of the Jacobian matrices. For instance, for the Euler equations, the eigen values come out as $u, u-c, u+c$. Due to the fact that these values are real and distinct, the equation displays hyperbolic nature. The

eigen values of the jacobian provide the direction and velocities of the propagation of information throughout the flow [67].

2.3 Pre-conditioning

Generally the numerical algorithms for the solution of Euler and Navier-Stokes equations are classified as either pressure-based or density based algorithms. Pressure based methods were originally developed based on pressure correction techniques and were well suited for incompressible flows. They generally use staggered grid and solve the governing equation in a segregated manner. On the other hand, the density based methods are coupled, solve the governing equations using time marching and are better suited for compressible flows.

The time marching schemes provide good stability and convergence at transonic and supersonic compressible flows. At subsonic speeds due to the large amount of difference between particle and acoustic speeds, the convergence rate deteriorates. Therefore, the system of equations needs to have eigen values (combination of particle and acoustic speed) of the similar order for better convergence providing the condition number of unity. Its solution is proposed by normalizing the governing set of equations with the time-derivative preconditioning [32-34] and has shown good results by enhancing the convergence of the low speed flow cases. Also, at subsonic speeds the governing system of equations for incompressible flow is not fully hyperbolic and pressure can not be updated from the equation of state. This deficiency is overcome by employing an artificial-compressibility approach [30,31]. This approach introduces a pressure time derivative to the continuity equation. This derivative is further normalized by a square of pseudo acoustic speed. The pseudo acoustic speed is set to about twice the local velocity producing pseudo Mach number of half and increasing the optimal convergence. This artificial pressure terms serves to make the governing system of equations hyperbolic and means to update pressure are achieved. Multiplying the above equation with \mathbf{K} to achieve the non-conservation form:

$$\left(\mathbf{K} \frac{\partial \mathbf{W}}{\partial \mathbf{Q}} \right) \frac{\partial}{\partial t} \iiint_V \mathbf{Q} dV + \mathbf{K} \iint_A [\mathbf{F} - \mathbf{G}] dA = 0 \quad (2.13)$$

$\frac{\partial \mathbf{W}}{\partial \mathbf{Q}}$ is represented by equation 2.12

$$\mathbf{K} = \begin{bmatrix} 1 & 0 & 0 & 0 & 0 \\ -u & 1 & 0 & 0 & 0 \\ -v & 0 & 1 & 0 & 0 \\ -w & 0 & 0 & 1 & 0 \\ -(H - (u^2 + v^2 + w^2)) & -u & -v & -w & 1 \end{bmatrix} \quad (2.14)$$

$$\Gamma_{nc} = \mathbf{K} \frac{\partial \mathbf{W}}{\partial \mathbf{Q}}$$

$$\mathbf{K} \frac{\partial \mathbf{W}}{\partial \mathbf{Q}} = \begin{bmatrix} \rho_p & 0 & 0 & 0 & \rho_T \\ 0 & \rho & 0 & 0 & 0 \\ 0 & 0 & \rho & 0 & 0 \\ 0 & 0 & 0 & \rho & 0 \\ -1 & 0 & 0 & 0 & \rho C_p \end{bmatrix} \quad (2.15)$$

It is observed that the term ρ_p that multiplies the pressure time derivative in the continuity equation controls the speed of propagation of acoustic waves in the system. It is interesting to note that, for an ideal gas, $\rho_p = \frac{1}{RT} = \frac{\gamma}{c^2}$, where c is acoustic velocity (speed of sound) and $\gamma = \frac{C_p}{C_v}$, while for constant density flows $\rho_p = 0$, consistent with the notion of infinite wave speeds in the incompressible fluids. Thus if this term is replaced with one proportional to the inverse of the local velocity squared, the eigen value of the system are controlled such that they all are of the same order.

$$\Gamma_{nc} = \begin{bmatrix} \Theta & 0 & 0 & \rho_T \\ 0 & \rho & 0 & 0 \\ 0 & 0 & \rho & 0 \\ 0 & 0 & 0 & \rho \\ -1 & 0 & 0 & \rho C_p \end{bmatrix} \quad (2.16)$$

$$\Theta = \left(\frac{1}{U_r^2} - \frac{\rho_T}{\rho C_p} \right)$$

Here U_r is the reference velocity and for an ideal gas is presented as:

$$U_r = \begin{cases} \varepsilon c, & \text{if } |v| < \varepsilon c \\ |v|, & \text{if } \varepsilon c < |v| < c \\ c, & \text{if } |v| > c \end{cases}$$

ε is a small number ($\sim 10^{-5}$) included to prevent the singularities at stagnation points. For an ideal gas, as $U_r \rightarrow c$, Θ reduces to:

$$\begin{aligned}\Theta &= \frac{1}{c^2} - \frac{\rho_T}{\rho Cp} \\ &= \frac{1}{\gamma RT} - \frac{-\rho}{T(\rho Cp)} = \frac{\gamma}{\gamma RT} \text{ or } \frac{\gamma}{c^2}\end{aligned}$$

It is consistent with equation 2.15. ρ_T is retained in Γ_{nc} . The choice for Θ simplifies the expressions for the resultant system eigen values compared with what they would be if ρ_p is replaced with the $\frac{1}{U_r^2}$. For viscous flows U_r is further restricted such that it does

not become smaller than the local diffusion velocity $\frac{v}{\Delta x}$. Thus having computed U_r from equation above, an additional restriction is placed as follows:

$$U_r = \max\left(U_r, \frac{v}{\Delta x}\right) \quad (2.17)$$

Δx is the inter-cell length scale over which the diffusion occurs. This additional limitation on U_r has the effect of pseudo acoustic speed according to the diffusive time scales. Limiting U_r in this way is necessary in regions where diffusion effects dominate and grid spacing is small, typically in boundary and shear layers.

The preconditioned system in conservation form is obtained by substituting the equation (2.16) for equation (2.15) in equation (2.13) and multiplying with \mathbf{K}^{-1} .

The whole equation is multiplied with \mathbf{K}^{-1} to obtain the conservation form of the system of equations:

$$\mathbf{K}^{-1}\Gamma_{nc} * \frac{\partial}{\partial t} \iiint_V \mathbf{Q} dV = -\mathbf{K}^{-1}\mathbf{K} * \iint_A [\mathbf{F} - \mathbf{G}] dA \quad (2.18)$$

$$\Gamma \frac{\partial}{\partial t} \iiint_V \mathbf{Q} dV = - \iint_A [\mathbf{F} - \mathbf{G}] dA \quad (2.19)$$

where,

$\Gamma = (\mathbf{K}^{-1}\Gamma_{nc})$, with

$$\mathbf{K} = \begin{bmatrix} 1 & 0 & 0 & 0 & 0 \\ -u & 1 & 0 & 0 & 0 \\ -v & 0 & 1 & 0 & 0 \\ -w & 0 & 0 & 1 & 0 \\ -(H - (u^2 + v^2 + w^2)) & -u & -v & -w & 1 \end{bmatrix}$$

The \mathbf{K}^{-1} is defined as $\mathbf{K}^{-1} = \frac{[Co-factor(\mathbf{K})]^T}{|\mathbf{K}|}$

Co-factor(K)= a_{ij}

$$a_{ij} = \begin{bmatrix} 1 & u & v & w & H \\ 0 & 1 & 0 & 0 & u \\ 0 & 0 & 1 & 0 & v \\ 0 & 0 & 0 & 1 & w \\ 0 & 0 & 0 & 0 & 1 \end{bmatrix}$$

$|\mathbf{K}|=1$

$$\mathbf{K}^{-1} = \begin{bmatrix} 1 & 0 & 0 & 0 & 0 \\ u & 1 & 0 & 0 & 0 \\ v & 0 & 1 & 0 & 0 \\ w & 0 & 0 & 1 & 0 \\ H & u & v & w & 1 \end{bmatrix}$$

$$\Gamma = (\mathbf{K}^{-1}\Gamma_{nc}) = \begin{bmatrix} 1 & 0 & 0 & 0 & 0 \\ u & 1 & 0 & 0 & 0 \\ v & 0 & 1 & 0 & 0 \\ w & 0 & 0 & 1 & 0 \\ H & u & v & w & 1 \end{bmatrix} \begin{bmatrix} \Theta & 0 & 0 & \rho_T \\ 0 & \rho & 0 & 0 \\ 0 & 0 & \rho & 0 \\ 0 & 0 & 0 & \rho \\ -1 & 0 & 0 & \rho C_p \end{bmatrix}$$

$$= \begin{bmatrix} \Theta & 0 & 0 & 0 & \rho_T \\ \Theta u & \rho & 0 & 0 & \rho_T u \\ \Theta v & 0 & \rho & 0 & \rho_T v \\ \Theta w & 0 & 0 & \rho & \rho_T w \\ \Theta H - 1 & \rho u & \rho v & \rho w & \rho \end{bmatrix} \quad (2.20)$$

As pointed out in reference [26], although equation 2.19 is conservative in the steady state, it is not conservative for time dependant flows. It is not a problem, however, since the preconditioning has already destroyed the time accuracy of the equations, and will not be employed them in this form for unsteady flows.

Thus, when $U_r = c$, (at sonic speeds and above), $\alpha = 0$, and the eigen values of the preconditioned system take their traditional form $u \pm c$. At low speed, however, as

$U_r \rightarrow 0, \alpha \rightarrow \frac{1}{2}$, and all eigen values become of the same order as u . Thus eigen values of the system remain well conditioned at all speeds.

2.4 Dual time stepping procedure

Preconditioning destroys the time accuracy of the equation and it can not be used in this form for time dependant flows. In order to extend its capability for time dependant unsteady flows, the original physical time term is kept and preconditioning time as a pseudo time is introduced in the equation. Figure 2.3 represents the structure of dual time stepping methodology. The main idea in the dual time stepping is to achieve the steady state in pseudo time as shown in the inner box of the figure 2.3. It is done by using multistage Runge-Kutta scheme. The physical time marching is done in the outer loop using the backward Euler scheme. The maximum number of iterations and convergence criteria in pseudo time loop are specified in the initialization file. If the solution does not converge below the convergence criteria within the specified pseudo time iterations, the solver advances to the next physical time. However, it is important to ensure that the number of maximum pseudo time iterations for a single physical time is sufficient enough to converge to a satisfactory level. The convergence will indicate that a steady state is achieved for that particular physical time step. It is important to note that while the slave nodes are doing iterations in the inner pseudo time loop (main solver part), the master node remains idle.

In case of the moving mesh case, the 'master node' moves the mesh, calculates the new mesh parameters and broadcasts them to the 'slave nodes' for each physical time. As described above that the master node remains idle during the pseudo time iterations in main solver part being run by the slave nodes. Thus, this not necessarily causes the bottleneck in the solution. It, in effect, provides better load balancing in the code. However, there is an additional penalty of transferring the new mesh parameters to all the slave nodes. In addition to this, the master node collects the L2-Norm of the residual from all the slaves and prints out the residual of the solution. It also periodically stores the solution data by gathering the corresponding flow variables from slave nodes. At the stage when maximum number of physical time iterations has reached, the solver ends the program.

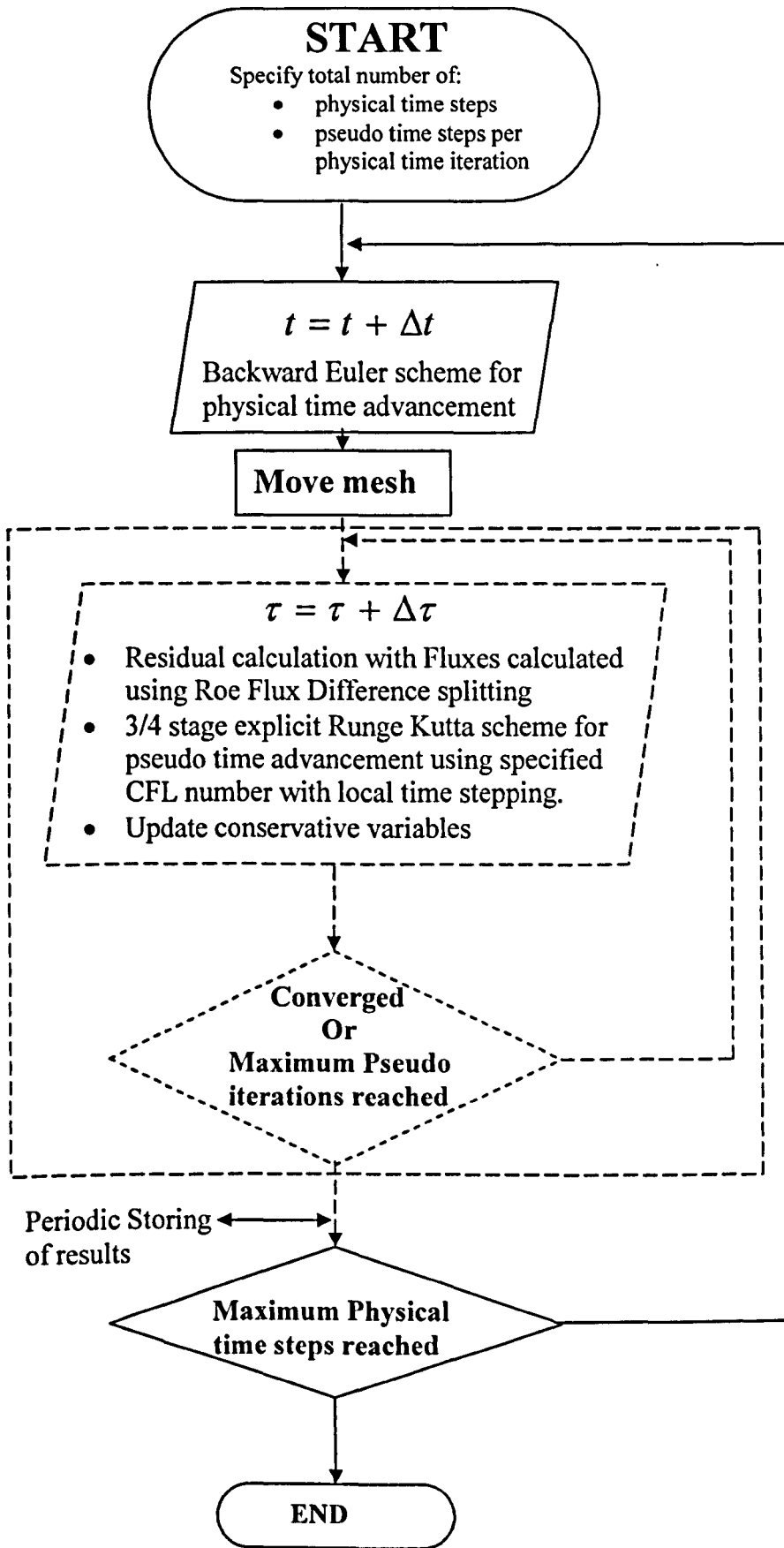


Figure 2.3 *Flow chart of dual time stepping*

It leads to the following equation:

$$\underbrace{\mathbf{K}^{-1}\mathbf{K} * \frac{\partial}{\partial t} \iiint_V \mathbf{W} dV}_{\text{Physical time term}} + \underbrace{\mathbf{K}^{-1}\Gamma_{nc} \frac{\partial}{\partial \tau} \iiint_V \mathbf{Q} dV}_{\text{Pseudo time term}} = - \underbrace{\iint_A [\mathbf{F} - \mathbf{G}] dA}_{\text{Flux Residual term}} \quad (2.21)$$

$$\underbrace{\frac{\partial}{\partial t} \iiint_V \mathbf{W} dV}_{\text{Physical timeterm}} + \underbrace{\Gamma \frac{\partial}{\partial \tau} \iiint_V \mathbf{Q} dV}_{\text{Pseudotimeterm}} = - \mathbf{K}^{-1}\mathbf{K} * \iint_A [\mathbf{F} - \mathbf{G}] dA$$

where $\Gamma = \mathbf{K}^{-1}\Gamma_{nc}$

The right hand side of the equation 2.21 accounts for the net residue \mathfrak{R} of all the flux terms passing through the faces with area dA of the control volume. These fluxes are evaluated by first dividing the cell surface into discrete faces and introducing the discrete flux vector \mathbf{F} and \mathbf{G} . These fluxes are assumed to be constant over each face as the surface integration is performed piecewise by face.

$$\underbrace{\Gamma \frac{\partial}{\partial \tau} \iiint_V \mathbf{Q} dV}_{\text{Pseudotimeterm}} = - \mathbf{K}^{-1}\mathbf{K} * \iint_A [\mathbf{F} - \mathbf{G}] dA - \underbrace{\frac{\partial}{\partial t} \iiint_V \mathbf{W} dV}_{\text{Physical timeterm}} \quad (2.22 a)$$

Applying first order Euler's backward difference on time terms,

$$\Gamma^{n,m-1} V^n \frac{\mathbf{Q}^{n,m} - \mathbf{Q}^{n,m-1}}{\Delta \tau} = - \mathfrak{R}^{n,m-1} - \frac{(\mathbf{W}^{n,m} V^n - \mathbf{W}^{n-1} V^{n-1})}{\Delta t} \quad (2.22 b)$$

where superscript m and $m-1$ are the current and previous inner iteration step in pseudo time and n , $n-1$ represent the current and previous physical time. The term $\mathbf{W}^{n,m}$ is actually an implicit treatment.^[26, 38] The stability analysis in Reference [38] indicates that this implicit treatment can remedy the numerical instability when small physical time step, Δt , is specified due to the time accuracy requirement. In this study, a further linearization is applied to $\mathbf{W}^{n,m}$

$$\mathbf{W}^{n,m} = \mathbf{W}^{n,m} + \frac{\partial \mathbf{W}}{\partial \mathbf{Q}} \Delta \mathbf{Q}^m \quad (2.23)$$

where $\Delta \mathbf{Q}^m = \mathbf{Q}^{n,m} - \mathbf{Q}^{n,m-1}$

For ease of understanding, the superscript n can be dropped when m or $m-1$ is present.

By substituting this value back:

$$\Gamma^{m-1} V^n \left(\frac{\partial \mathbf{Q}}{\partial \tau} \right)^n = - \left[\mathfrak{R}^m + \frac{\mathbf{W}^m V^n}{\Delta t} - \frac{\mathbf{W}^{n-1} V^{n-1}}{\Delta t} \right]$$

$$\Gamma^{m-1} V^n \frac{\Delta Q^m}{\Delta \tau} = - \left[\mathfrak{R}^{m-1} + \frac{1}{\Delta t} \left(W^{m-1} + \frac{\partial W}{\partial Q} \Delta Q^m \right) V^n - \frac{W^{n-1} V^{n-1}}{\Delta t} \right] \quad (2.24 a)$$

After rearrangement,

$$\begin{aligned} \left(\Gamma^{m-1} + \frac{\Delta \tau}{\Delta t} \frac{\partial W}{\partial Q} \right) V^n \frac{\Delta Q^m}{\Delta \tau} &= - \left[\mathfrak{R}^{m-1} + \frac{W^{m-1} V^n - W^{n-1} V^{n-1}}{\Delta t} \right] \\ \frac{\Delta Q^m}{\Delta \tau} &= - \left[\mathfrak{R}^{m-1} + \frac{W^{m-1} V^n - W^{n-1} V^{n-1}}{\Delta t} \right] \frac{1}{V^n} \left(\Gamma^{m-1} + \frac{\Delta \tau}{\Delta t} \frac{\partial W}{\partial Q} \right)^{-1} \\ \frac{Q^m - Q^{m-1}}{\Delta \tau} &= - \frac{1}{V^n} \left(\Gamma^{m-1} + \frac{\Delta \tau}{\Delta t} \frac{\partial W}{\partial Q} \right)^{-1} \left[\mathfrak{R}^{m-1} + \frac{W^{m-1} V^n - W^{n-1} V^{n-1}}{\Delta t} \right] \\ \frac{Q^m - Q^{m-1}}{\Delta \tau} &= - \frac{1}{V^n} [\Gamma^*]^{-1} \left[\mathfrak{R}^{m-1} + \frac{W^{m-1} V^n - W^{n-1} V^{n-1}}{\Delta t} \right] \end{aligned} \quad (2.24 b)$$

where $\Gamma^* = \Gamma^{m-1} + \frac{\Delta \tau}{\Delta t} \frac{\partial W}{\partial Q}$; $k_t = \varepsilon_0 \frac{\Delta \tau}{\Delta t}$

$$\Gamma = \begin{bmatrix} \Theta & 0 & 0 & 0 & \rho_T \\ \Theta u & \rho & 0 & 0 & \rho_T u \\ \Theta v & 0 & \rho & 0 & \rho_T v \\ \Theta w & 0 & 0 & \rho & \rho_T w \\ \Theta H - 1 & \rho u & \rho v & \rho w & \rho_T H + \rho C_p \end{bmatrix} ;$$

$$\frac{\partial W}{\partial Q} = \begin{bmatrix} \rho_p & 0 & 0 & 0 & \rho_T \\ \rho_p u & \rho & 0 & 0 & \rho_T u \\ \rho_p v & 0 & \rho & 0 & \rho_T v \\ \rho_p w & 0 & 0 & \rho & \rho_T w \\ \rho_p H - 1 & \rho u & \rho v & \rho w & \rho_T H + \rho C_p \end{bmatrix}$$

Matrix Γ^* is presented as:

$$\Gamma^* = \begin{bmatrix} \Theta + k_t \rho_p & 0 & 0 & 0 & 0 \\ (\Theta + k_t \rho_p) u & \rho(1+k_t) & 0 & 0 & \rho_T u(1+k_t) \\ (\Theta + k_t \rho_p) v & 0 & \rho(1+k_t) & 0 & \rho_T v(1+k_t) \\ (\Theta + k_t \rho_p) w & 0 & 0 & \rho(1+k_t) & \rho_T w(1+k_t) \\ (\Theta + k_t \rho_p) H - k_t - 1 & \rho u(1+k_t) & \rho v(1+k_t) & \rho w(1+k_t) & (\rho C_p + \rho_T H)(1+k_t) \end{bmatrix}$$

Putting $\tilde{\Theta} = \Theta + k_t \rho_p$ and $1+k_t = k_{t1}$

$$\Gamma^* = \begin{bmatrix} \tilde{\Theta} & 0 & 0 & 0 & 0 \\ \tilde{\Theta}u & \rho k_{i1} & 0 & 0 & \rho_T u k_{i1} \\ \tilde{\Theta}v & 0 & \rho k_{i1} & 0 & \rho_T v k_{i1} \\ \tilde{\Theta}w & 0 & 0 & \rho k_{i1} & \rho_T w k_{i1} \\ \tilde{\Theta}H - k_{i1} & \rho u k_{i1} & \rho v k_{i1} & \rho w k_{i1} & (\rho C_p + \rho_T H) k_{i1} \end{bmatrix}$$

It includes the inverse matrix of the precondition matrix and is presented as:

$$[\Gamma^*]^{-1} = \begin{bmatrix} \frac{\rho C_p + \rho_T (H - |V|^2)}{\Psi} & \frac{u \rho_T}{\Psi} & \frac{v \rho_T}{\Psi} & \frac{w \rho_T}{\Psi} & \frac{-\rho_T}{\Psi} \\ -\frac{u}{\rho k_{i1}} & \frac{1}{\rho k_{i1}} & 0 & 0 & 0 \\ -\frac{v}{\rho k_{i1}} & 0 & \frac{1}{\rho k_{i1}} & 0 & 0 \\ -\frac{w}{\rho k_{i1}} & 0 & 0 & \frac{1}{\rho k_{i1}} & 0 \\ \frac{k_{i1} - (H - |V|^2)(\Theta + k_i \rho_p)}{k_{i1} \Psi} & \frac{-u(\Theta + k_i \rho_p)}{k_{i1} \Psi} & \frac{-v(\Theta + k_i \rho_p)}{k_{i1} \Psi} & \frac{-w(\Theta + k_i \rho_p)}{k_{i1} \Psi} & \frac{(\Theta + k_i \rho_p)}{k_{i1} \Psi} \end{bmatrix}$$

where, $\Psi = [\rho(\Theta + k_i \rho_p) C_p + \rho_T k_{i1}]$. Its derivation is added in the appendix A.

It is of the general form $\frac{dQ}{d\tau} = -\mathfrak{R}(Q)$. It can be solved using an explicit time

It removes the instability caused by the small time step and a general form $\frac{dQ}{d\tau} = -\mathfrak{R}(Q)$

is obtained. It can be solved explicitly using any time iterative scheme. The term

$\frac{dQ}{d\tau} = -\mathfrak{R}(Q)$ can be solved using an explicit time stepping scheme such as Runge-Kutta

etc. as discussed in next section.

$$Q^m = Q^{m-1} - \alpha_m \frac{\Delta\tau}{V^n} [\Gamma^*]^{-1} \left[\mathfrak{R}^{m-1} + \frac{W^{m-1} V^n - W^{n-1} V^{n-1}}{\Delta t} \right]$$

for physical time 't', it can be written in general form as:

$$Q^m = Q^{m-1} - \alpha_m \frac{\Delta\tau}{V^n} [\Gamma^*]^{-1} \left[\mathfrak{R}^{m-1} + \frac{\varepsilon_0 W^{m-1} V^n - \varepsilon_1 W^{m,n} V^{m,n} + \varepsilon_2 W^{n-1} V^{n-1}}{\Delta t} \right]$$

Order of accuracy	ε_0	ε_1	ε_2
1 st order time accuracy	1	0	1

2 nd order time accuracy	$\frac{3}{2}$	2	$\frac{1}{2}$
-------------------------------------	---------------	---	---------------

Table 2.2 Selection of parameters for 1st and 2nd order temporal accuracy

Time marching in ‘physical time’ domain is done with simple back-ward facing Euler scheme. Time marching in ‘pseudo time’ domain is done using multi-stage explicit Runge-Kutta scheme.

2.5 Runge-Kutta time stepping scheme

Further to solve the explicit scheme obtained, a multi-stage Runge-Kutta scheme can be applied to increase the pseudo time step size. The standard Runge-Kutta scheme for an ordinary equation system $\frac{dQ}{d\tau} = -\mathfrak{R}(Q)$ is presented as:

$$\begin{aligned}
 Q^{(0)} &= Q_r \\
 &\dots \\
 Q^{(i)} &= Q^{(0)} - \alpha_i \Delta \tau \mathfrak{R}^{(i-1)} \\
 Q_{r+\Delta \tau} &= Q^{(p)}
 \end{aligned} \tag{2.25}$$

where $i=1,2, \dots,p$ is the stage counter for the p -stage Runge-Kutta scheme and α_i is the multi-stage coefficient for the i -th stage, which, according to the stability analysis of the linear model equation^[76] is defined by:

$$\alpha_i = \frac{1}{p-i+1}$$

Therefore, the resultant full discretisation with 1st order temporal accuracy in physical time becomes:

$$\begin{aligned}
 Q^{(0)} &= Q^{m-1} \\
 &\dots \\
 Q^{(i)} &= Q^{(0)} - \alpha_i \frac{\Delta \tau}{\Delta V^n} [\Gamma^*]^{-1} \times \left[\mathfrak{R}^{m-1} + \frac{1}{\Delta t} (W^{m-1} V^n - W^{n-1} V^{n-1}) \right] \\
 &\dots \\
 Q^m &= Q^{(p)}
 \end{aligned} \tag{2.26}$$

where $\Gamma^{m-1}, \frac{\partial W}{\partial Q}, \mathfrak{R}^{m-1}$ and W^{m-1} are functions of Q^{m-1} .

2.6 Reconstruction of the solution variables

In order to compute the residual \mathfrak{R} for turbulent flows, viscous fluxes are required at the cell centre. In order to compute these fluxes, the solution vector \mathbf{Q} is required at the faces of the cells to allow the use of divergence theorem. $\mathbf{Q}_{face\ centre}$ can be approximated as the same value in the cell centre (piecewise constant) or can be evaluated using a multidimensional linear reconstruction approach. In this approach, higher order accuracy is achieved at cell faces through a Taylor series expansion of the cell-averaged solution vector about the cell centroid. The piecewise linear interpolation is represented as

$$\mathbf{Q}_{face\ centre} = \mathbf{Q}_{cell\ centre} + \nabla \mathbf{Q}_{face\ centre} \cdot \Delta \mathbf{x} \quad (2.27)$$

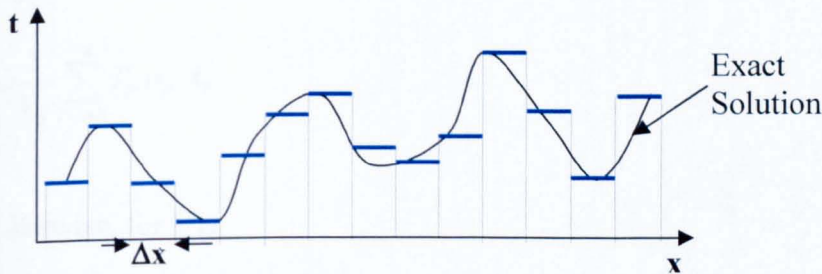
$\Delta \mathbf{x}$ is the displacement vector from the cell centroid to the face centroid. This formulation requires the solution gradient $\nabla \mathbf{Q}_{face\ centre}$ for each face. For a face, having C_0 as a cell on its left side and C_1 as a cell on its right side, $\nabla \mathbf{Q}_{face\ centre}$ is described as:

$$\nabla \mathbf{Q}_{face\ centre} = \frac{\nabla \mathbf{Q}_{cell\ centre_C_0} + \nabla \mathbf{Q}_{cell\ centre_C_1}}{2}$$

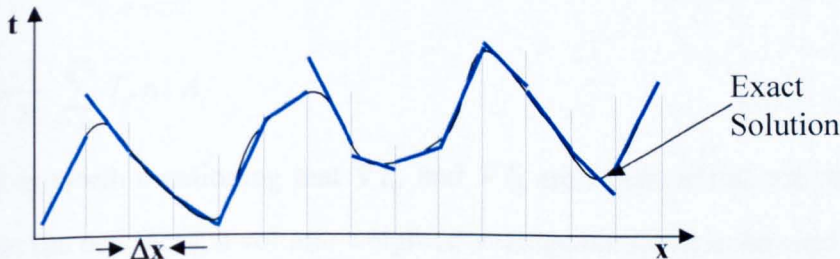
This gradient is computed using the divergence theorem, which in discrete form is written as:

$$\nabla \mathbf{Q}_{cell\ centre} = \frac{1}{V} \sum_{faces} \mathbf{Q}_{face_average} \cdot \mathbf{A}$$

It is further explained in the next section 2.4.1.



(a) 1st Order piece-wise Constant approximation (Lower Order reconstruction)



(b) Piece-wise linear approximation (Higher Order reconstruction)

Figure 2.4 Representation of effect of lower and higher order reconstruction

Finally, the gradients $\nabla Q_{face\ center}$ are limited to ensure that they do not introduce new maxima or minima into the reconstructed data.

2.6.1 Evaluation of the Gradient at the face centre

Assume that calculation of the gradient for temperature variable 'T' is required.

Step 1: Calculate the Integral

The cell averaged gradient, ∇T_0 is obtained for C0,

$$\nabla T_0 = \frac{1}{V_0} \oint_{ABCA} T \mathbf{n} dA$$

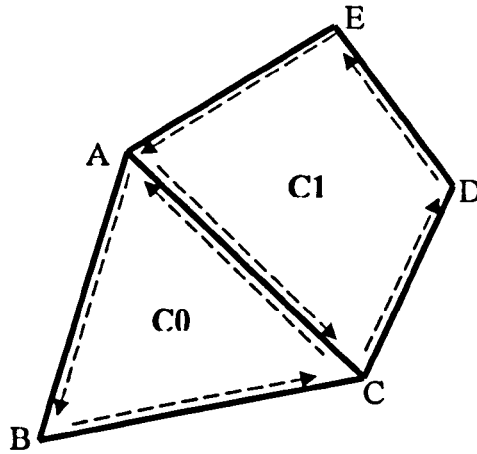


Figure 2.5 A simple 2d domain with 2 cells and 6 faces for evaluation of gradient

$$= \frac{1}{V_0} (T_{AB} n_{AB} A_{AB} + T_{BC} n_{BC} A_{BC} + T_{CA} n_{CA} A_{CA})$$

$$= \frac{1}{V_0} \sum_{P=AB}^{CA} T_P n_P A_P$$

Likewise, for C1,

$$\nabla T_1 = \frac{1}{V_1} \oint_{ACDEA} T \mathbf{n} dA$$

$$= \frac{1}{V_1} \sum_{P=AC}^{EA} T_P n_P A_P$$

It is worth mentioning that ∇T_0 and ∇T_1 are values at the cell centre. To compute values on the cell faces, a volume weighted average method can be used

$$\nabla T_{AC} = \frac{V_0 \nabla T_0 + V_1 \nabla T_1}{V_0 + V_1}$$

$$= \frac{V_0}{V_0+V_1} \nabla T_0 + \frac{V_1}{V_0+V_1} \nabla T_1$$

$$= \eta_0 \nabla T_0 + \eta_1 \nabla T_1$$

These convex weighting coefficients are taken as equal ($\eta_0 = 0.5$ and $\eta_1 = 0.5$) for neutral or zero biasing. It is obvious that $\eta_0 + \eta_1 = 1.0$ and $\eta_0 \eta_1 \leq 1.0$ where $\eta_0, \eta_1 \geq 0$

2.7 Calculation of the Inviscid Fluxes

2.7.1 Roe's flux-difference splitting scheme:

Roe's flux-difference splitting scheme^[35] or also known as Roe's approximate Riemann solver, is a method which solves the linearised Riemann problem directly. This scheme is widely used in CFD community^[26,36,37].

The discrete, inviscid flux vectors appearing in equation 2.21 above are evaluated by flux difference splitting. In terms of conserved quantities W , the value of F at each face is described as:

$$F = \frac{1}{2}(F_L + F_R) - \frac{1}{2}|A| \Delta W \quad (2.28)$$

where, $\Delta W = W_R - W_L$, F_L and F_R are fluxes computed using the reconstructed solution vectors W_L and W_R on each side (left and right) of the face. By using the reconstructed solution, discretization scheme becomes formally second order accurate. In this form, the above equation can be viewed as a second order central difference plus an added dissipation term.

The matrix A is the Jacobian $\frac{\partial F}{\partial W}$ and $|A|$ is defined by

$$|A| = M|\Lambda|M^{-1}$$

where $\Lambda = \text{diag}(u, u, u, u+c, u-c)$ and M is the modal matrix that diagonalizes the matrix A in the non-preconditioned system.

To be compatible with the preconditioned system, the flux difference splitting scheme is adapted accordingly. Here the system's modified, preconditioned eigenvalues are used and recast equation above in terms of primitive variables Q . The fluxes F_L and F_R are readily computed from the reconstructed primitive variables Q_L and Q_R on either side of the face. The second term on the right hand side $|A| \Delta W$ is rewritten as:

$$\begin{aligned}
|\Lambda| \Delta W &= \left| \frac{\partial F_n}{\partial W} \right| \Delta W = \left| \frac{\partial F_n}{\partial Q} \frac{\partial Q}{\partial W} \right| \frac{\partial W}{\partial Q} \Delta Q = \left| \frac{\partial F_n}{\partial Q} \Gamma^{-1} \right| \Gamma \Delta Q \\
&= \left| \Gamma \Gamma^{-1} \frac{\partial F_n}{\partial Q} \Gamma^{-1} \right| \Gamma \Delta Q = \Gamma \left| \Gamma^{-1} \frac{\partial F_n}{\partial Q} \right| \Gamma^{-1} \Gamma \Delta Q = \Gamma \left| \Gamma^{-1} \frac{\partial F_n}{\partial Q} \right| \Delta Q
\end{aligned} \tag{2.29}$$

where, $\Gamma^{-1} \frac{\partial F_n}{\partial Q}$ is denoted by the preconditioned Jacobian, Λ_Γ , which can be diagonalized

by M_Γ , i.e.,

$$|\Lambda_\Gamma| = M_\Gamma |\Lambda_\Gamma| M_\Gamma^{-1}$$

And

$$\Lambda_\Gamma = \text{diag}(v_n, v_n, v_n, v'_n + c', v'_n - c')$$

Values of above terms can be seen as the resultant eigen values of the preconditioned system are described as:

$$\lambda \left(\Gamma^{-1} \frac{\partial F}{\partial Q} \right) = u, u, u, u' + c', u' - c'$$

where,

$$u = v \cdot \hat{n}$$

$$u' = u(1 - \alpha)$$

$$c' = \sqrt{\alpha^2 u^2 + U_r^2}$$

$$\alpha = \frac{(1 - \beta U_r^2)}{2}$$

$$\beta = \left(\rho_p + \frac{\rho_\tau}{\rho C_p} \right)$$

$$\text{For an ideal gas, } \beta = \frac{1}{\gamma RT} = \frac{1}{c^2}$$

After rearranging terms, the resultant flux splitting can be expressed in the following form:

$$\Gamma^{-1} |\Lambda_\Gamma| \Delta Q = |v_n| \left\{ \begin{array}{c} \Delta(\rho) \\ \Delta(\rho u) \\ \Delta(\rho v) \\ \Delta(\rho w) \\ \Delta(\rho E) \end{array} \right\} + \delta v_n \left\{ \begin{array}{c} \rho \\ \rho u \\ \rho v \\ \rho w \\ \rho H \end{array} \right\} + \delta p \begin{pmatrix} 0 \\ \mathbf{n} \\ v \cdot \mathbf{n} \end{pmatrix} \tag{2.30}$$

where,

$$\delta v_n = M^* \Delta v_n + [c^* - (1-2\alpha)|v_n| - \alpha v_n M^*] \frac{\Delta p}{\rho U_r^2}$$

$$\delta p = M^* \Delta p + [c^* - |v_n| + \alpha v_n M^*] \rho \Delta v_n$$

$$c^* = \frac{|v'_n + c'| + |v'_n - c'|}{2}$$

$$M^* = \frac{|v'_n + c'| - |v'_n - c'|}{2}$$

When the splitting is written in this form, rather than the more common in terms of eigen values $|u|, |u+c|$ and $|u-c|$, the physical significance of the various added dissipation terms become clear. The three terms above represent the interpolation to the cell face of the convected variables, the flux velocity, and the pressure, respectively. The first term v_n has the effect of upwinding the convected variables. The second term δv_n is the modification to the convective velocity at the face. Here the term $M^* \Delta v_n$ causes the flux velocity to be upwinding when the normal velocity exceeds the pseudo-acoustic speed.

For low speed flows, the $c^* \frac{\Delta p}{\rho U_R^2}$ term is the added pressure dissipation, which becomes

less significant in high speed flows where ρU_R^2 become much greater than local pressure differences. The third term, δp , is a modification to the pressure at the face, where $M^* \Delta p$ results in pressure upwinding when the normal velocity becomes supersonic. In equation above the variables on the interface are the Roe-averaged values, defined by

$$\rho = \sqrt{\rho_L \rho_R}$$

$$\mathbf{v} = \frac{\rho_L \mathbf{v}_L + \rho_R \mathbf{v}_R}{\sqrt{\rho_L} + \sqrt{\rho_R}}$$

$$\mathbf{H} = \frac{\rho_L \mathbf{H}_L + \rho_R \mathbf{H}_R}{\sqrt{\rho_L} + \sqrt{\rho_R}}$$

$$c^2 = (\gamma - 1) \left(\mathbf{H} - \frac{|\mathbf{v}|^2}{2} \right)$$

It is clear that when the preconditioning is switched off, the $\alpha = 0$, $U_R = c$, $c' = c$ and $v'_n = v_n$, the equation reduces to the standard Roe's scheme.

2.7.1.1 Dissipation control through upwinding parameter

The central difference schemes such as McCormic scheme etc. require extra dissipation to be added to their flux calculations for numerical stability. Upwind schemes, on the other hand, inherently possess the needed dissipation (arguably more than needed for numerical stability) to control these numerical instabilities. An important consideration that must be taken into account when solving viscous flows with upwind schemes is the numerical dissipation that will be produced. It may be excessive enough to destroy the unsteadiness in the flow. Roe's FDS scheme generates too much dissipation for turbulent flow in fully upwinding mode^[43, 62, 63, 64, 65] dissipating the small scale turbulence. It is pointed in Ref [63] that “.. During the LES, it was found that the full Roe FDS term is too dissipative, and incorrect levels of turbulent velocity fluctuations are obtained when the normal Roe FDS term is used in turbulent simulations.” However this dissipation can be reduced as presented in the Ref [63]. This approach represents the computed fluxes through upwinding scheme as a sum of fluxes computed using central differencing from left and right state of cell boundary, with an added Roe upwinding dissipation term, which can be modulated using a dissipation parameter ε_{dissip} .

Equation 2.28 can be written as:

$$\mathbf{F} = \underbrace{\frac{1}{2}(\mathbf{F}_L + \mathbf{F}_R)}_{\text{Central Differencing part}} - \underbrace{\frac{1}{2}|\mathbf{A}| \Delta \mathbf{W}}_{\text{Upwinding Dissipation}} \quad (2.31)$$

ROE FDS (Pure Upwinding Scheme)

Adding the dissipation parameter ε_{dissip} provides

$$\mathbf{F} = \underbrace{\frac{1}{2}(\mathbf{F}_L + \mathbf{F}_R)}_{\text{Central Differencing part}} - \varepsilon_{dissip} \underbrace{\frac{1}{2}|\mathbf{A}| \Delta \mathbf{W}}_{\text{Upwinding Dissipation}}$$

It can be re-arranged as follows

$$\mathbf{F} = \underbrace{\frac{1}{2}(\mathbf{F}_L + \mathbf{F}_R)}_{\text{Central Differencing part}} - \varepsilon_{dissip} \underbrace{\frac{1}{2}(\mathbf{F}_L + \mathbf{F}_R)}_{\text{Central Differencing part}} + \varepsilon_{dissip} \underbrace{\frac{1}{2}(\mathbf{F}_L + \mathbf{F}_R)}_{\text{Central Differencing part}} - \varepsilon_{dissip} \underbrace{\frac{1}{2}|\mathbf{A}| \Delta \mathbf{W}}_{\text{Upwinding Dissipation}}$$

$$\mathbf{F} = (1 - \varepsilon_{dissip}) \underbrace{\frac{1}{2}(\mathbf{F}_L + \mathbf{F}_R)}_{\text{Central Differencing part}} + \varepsilon_{dissip} \left[\underbrace{\frac{1}{2}(\mathbf{F}_L + \mathbf{F}_R)}_{\text{Central Differencing part}} - \underbrace{\frac{1}{2}|\mathbf{A}| \Delta \mathbf{W}}_{\text{Upwinding Dissipation}} \right] \quad (2.32)$$

ROE FDS (Pure Upwinding Scheme)

$\varepsilon_{dissip} = 0$ corresponds to central differencing only and $\varepsilon_{dissip} = 1$ corresponds to full Roe FDS. In Ref [65], Lin et al., found that with the same approach to control excessive dissipation of Roe FDS, $\varepsilon_{dissip} = 0.1$ gave good results for acoustics applications.

2.7.2 AUSM flux splitting scheme for all speeds:

Advection Upstream Splitting Method (AUSM) is numerical scheme for inviscid flux computation of a general system of conservation. It is based on general upwind scheme concept and was presented by Liou and Steffen^[79] as an alternate to other upwind schemes. Its main idea is to split the inviscid flux into convective and pressure fluxes. The convective flux depends on flow speed (advection of the flow) and pressure flux with acoustic speed of the system. This method has been extended for all speeds from its initial application of compressible flows^[80,81]. It different variants have been proposed^[82,83].

For simplicity, only considering the inviscid fluxes from equation 2.19

$$\Gamma \frac{\partial Q}{\partial \tau} = - \sum_{i=1}^n \mathbf{F}_i \cdot \mathbf{n}_i A_i$$

General representation is done by splitting into convective and pressure fluxes:

$$\mathbf{F}_i \cdot \mathbf{n} = \rho (\mathbf{v} - \mathbf{v}_g) \cdot \mathbf{n} \begin{pmatrix} 1 \\ u \\ v \\ w \\ H \end{pmatrix} + p \begin{pmatrix} 0 \\ \mathbf{n} \\ 0 \end{pmatrix} \triangleq m' \bar{\psi} + p\phi \quad (2.33)$$

where, $m' = \rho (\mathbf{v} - \mathbf{v}_g)$ is a scalar quantity.

It is possible to write a numerical flux, mimicking the expression at the continuum level in terms of a common mass flux at interface as:

$$\mathbf{f}_{1/2} = m'_{1/2} \psi_{L/R} + p_{1/2} \phi$$

where $\psi_{L/R}$ is defined in an upwind fashion as

$$\bar{\psi}_{L/R} = \begin{cases} \bar{\psi}_L & \text{if } m'_{1/2} > 0 \\ \bar{\psi}_R & \text{otherwise,} \end{cases}$$

$$\mathbf{f}_{1/2} = m'_{1/2} \begin{pmatrix} 1 \\ u \\ v \\ w \\ H \end{pmatrix}_{j/j+1} + p_{1/2} \begin{pmatrix} 0 \\ \mathbf{n} \\ 0 \end{pmatrix} \triangleq m'_{1/2} \psi + p_{1/2} \phi \quad (2.34)$$

It can be represented as:

$$f_{1/2} = m'_{1/2} \begin{cases} \psi_L & \text{if } m'_{1/2} > 0, \\ \psi_R & \text{otherwise,} \end{cases} + p_{1/2} \phi$$

2.7.2.1 Mass flux

$m'_{1/2}$ is further defined as

$$m'_{1/2} = c_{1/2} M_{1/2} \begin{cases} \rho_L, & \text{if } M_{1/2} > 0 \\ \rho_R, & \text{otherwise} \end{cases} \quad (2.35)$$

$c_{1/2}$ is the speed of sound at the interface. It is taken as the average of left and right state.

$M_{1/2}$ is the splitting Mach number and $p_{1/2}$ is splitting pressure.

$M_{1/2} = M_{(m)}^*(M_L) + M_{(m)}^-(M_R) + M_p$ $m=4$ for 4th order polynomial

M_p is the pressure diffusion term and is used to enhance calculations of low Mach number or multiphase flow.

It is defined as

$$M_p = -\frac{K_p}{f_a} \max(1 - \sigma \bar{M}^2, 0) \frac{p_R - p_L}{\rho_{1/2} a_{1/2}^2}, \sigma \leq 1, \rho_{1/2} = \frac{\rho_L + \rho_R}{2}$$

$$\bar{M}^2 = \frac{u_L^2 + u_R^2}{2a_{1/2}^2}$$

$$M_o^2 = \min(1, \max(\bar{M}^2, M_o^2)) \in [0, 1]$$

$$f_a(M_o) = M_o(2 - M_o) \in [0, 1]$$

$0 \leq K_p \leq 1$. The factor $\max(1 - \sigma \bar{M}^2, 0)$ is introduced to replace a similar function ΔM used in previous formulations.

2.7.2.2 Pressure flux

The general formula in AUSM scheme for the calculation of interface pressure is:

$$p_{1/2} = P_{(s)}^*(M_L) p_L + P_{(s)}^-(M_R) p_R + P_u \quad (2.36)$$

where P_u is described as:

$$P_u = -K_u P_{(s)}^*(M_L) P_{(s)}^-(M_R) (\rho_L + \rho_R) (f_a a_{1/2}) (u_R - u_L),$$

And $0 \leq K_u \leq 1$

$$\begin{cases} M_L = \frac{v_L \cdot \mathbf{n}}{c_{1/2}} \\ M_R = \frac{v_R \cdot \mathbf{n}}{c_{1/2}} \end{cases}$$

Next step is to define the polynomial functions, $M_{(m)}^\pm$ of degree m ($=1,2,4$) and $P_{(n)}^\pm$ of degree n ($=5$). 5th degree polynomial is preferred because of better accuracy.

$$M_{(1)}^\pm(M) = \frac{1}{2}(M \pm |M|)$$

$$M_{(2)}^\pm(M) = \pm \frac{1}{2}(M \pm 1)^2$$

$$M_{(4)}^\pm(M) = \begin{cases} M_{(1)}^\pm, & \text{if } |M| \geq 1; \\ M_{(2)}^\pm(1 \mp 16\beta M_{(2)}^\mp), & \text{otherwise} \end{cases} \quad (2.37)$$

$$P_{(5)}^\pm(M) = \begin{cases} \frac{1}{M} M_{(1)}^\pm, & \text{if } |M| \geq 1; \\ M_{(2)}^\pm[(\pm 2 - M) \mp 16\alpha M M_{(2)}^\mp], & \text{otherwise} \end{cases}$$

$$\alpha = \frac{3}{16}(-4 + 5f_a^2) \in \left[-\frac{3}{4}, \frac{3}{16}\right] \text{ and } \beta = \frac{1}{8}$$

This scheme inherits the simplicity of flux vector splitting schemes yet provides excellent shock capturing capabilities similar to Roe scheme.

2.7.3 HLLC flux splitting scheme^[78]:

Original HLLC scheme developed by Harten et al.^[84] is simple and robust for density based methods. Its simplicity; primarily due to reducing the exact Riemann problem to two pressure waves and neglecting the contact surface, seriously limits its application for simulations with shock wave regions with expansion waves. Toro et. al^[85] proposed a modification with 3 wave solver named as HLLC. Ref. [78] further extended it to all speed flows.

For simplicity, only considering the inviscid fluxes from equation 2.19

$$\Gamma \frac{\partial \mathbf{Q}}{\partial \tau} = - \sum_{i=1}^n \mathbf{F}_i \cdot \mathbf{n}_i \mathcal{A}_i$$

The inviscid interface fluxes are calculated based on the signal velocities.

$$F_{LR}^{HLLC} = \begin{cases} F_L, & \text{if } S_L > 0 \\ F(U_L^*), & \text{if } S_L \leq 0 < S_M \\ F(U_R^*), & \text{if } S_M \leq 0 < S_R \\ F_R, & \text{if } S_R < 0 \end{cases} \quad (2.38)$$

where,

$$U_L^* = \begin{pmatrix} \rho_L^* \\ (\rho u)_L^* \\ (\rho v)_L^* \\ (\rho w)_L^* \\ (\rho E)_L^* \end{pmatrix}$$

$$= \frac{1}{S_L - S_M} \begin{pmatrix} (S_L - v_{n_L})\rho_L \\ (S_L - v_{n_L})(\rho u)_L + (p^* - p_L)n_x \\ (S_L - v_{n_L})(\rho v)_L + (p^* - p_L)n_y \\ (S_L - v_{n_L})(\rho w)_L + (p^* - p_L)n_z \\ (S_L - v_{n_L})(\rho E)_L - p_L v_{n_L} + p^* S_M \end{pmatrix} \quad (2.39 a)$$

$$U_R^* = \begin{pmatrix} \rho_R^* \\ (\rho u)_R^* \\ (\rho v)_R^* \\ (\rho w)_R^* \\ (\rho E)_R^* \end{pmatrix}$$

$$= \frac{1}{S_R - S_M} \begin{pmatrix} (S_R - v_{n_R})\rho_R \\ (S_R - v_{n_R})(\rho u)_R + (p^* - p_R)n_x \\ (S_R - v_{n_R})(\rho v)_R + (p^* - p_R)n_y \\ (S_R - v_{n_R})(\rho w)_R + (p^* - p_R)n_z \\ (S_R - v_{n_R})(\rho E)_R - p_R v_{n_R} + p^* S_M \end{pmatrix} \quad (2.39 b)$$

$$F_L^* \equiv F(U_L^*) = \begin{bmatrix} S_M \rho_L^* \\ S_M (\rho u)_L^* + p^* n_x \\ S_M (\rho v)_L^* + p^* n_y \\ S_M (\rho w)_L^* + p^* n_z \\ S_M (\rho E)_L^* + p^* \end{bmatrix}$$

$$F_R^* \equiv F(U_R^*) = \begin{bmatrix} S_M \rho_R^* \\ S_M (\rho u)_R^* + p^* n_x \\ S_M (\rho v)_R^* + p^* n_y \\ S_M (\rho w)_R^* + p^* n_z \\ S_M (\rho E)_R^* + p^* \end{bmatrix}$$

$$\begin{aligned} p^* &= \rho_L (v_{n_L} - S_L)(v_{n_L} - S_M) + p_L \\ &= \rho_R (v_{n_R} - S_R)(v_{n_R} - S_M) + p_R \end{aligned}$$

And S_M is defined as

$$S_M = \frac{\rho_R v_{n_R} (S_R - v_{n_R}) - \rho_L v_{n_L} (S_L - v_{n_L}) + p_L - p_R}{\rho_R (S_R - v_{n_R}) - \rho_L (S_L - v_{n_L})} \quad (2.40)$$

Signal velocities S_R and S_L are defined as

$$\begin{aligned} S_L &= \min(v_L^* - c_L^*, \hat{v}^* - \hat{c}^*) \\ S_R &= \max(v_R^* + c_R^*, \hat{v}^* + \hat{c}^*) \end{aligned}$$

where, \hat{v}^* and \hat{c}^* are Roe's average variables for preconditioned velocity and speed of sound.

2.11 Moving mesh with arbitrary Lagrangian-Eulerian formulation

Arbitrary Lagrangian-Eulerian equations (ALE) are a set of equations representing Eulerian, Lagrangian or any intermediate stage field. Historically, the ALE has been widely applied in fluid and structural dynamics with deforming domain. General Eulerian formulation can be represented similar to equation 2.1 as:

$$\frac{\partial W}{\partial t} + \frac{\partial F}{\partial X} = 0$$

where

$$\mathbf{X} = x\hat{i} + y\hat{j} + z\hat{k}$$

Following the Eulerian system of equations is written to describe the mean flow properties, in integral Cartesian form for an arbitrary control volume V with differential surface area dA .

$$\frac{\partial}{\partial t} \iiint_V W dV + \iint_{\partial A} \mathbf{F} \cdot d\mathbf{A} = 0 \quad (2.41)$$

$$W = \begin{Bmatrix} \rho \\ \rho u \\ \rho v \\ \rho w \\ \rho E \end{Bmatrix} \quad F = \begin{pmatrix} F_x \\ F_y \\ F_z \end{pmatrix}$$

$$F_x = \begin{Bmatrix} \rho u \\ \rho uu + p \\ \rho uv \\ \rho uw \\ \rho uE + pu \end{Bmatrix}, \quad F_y = \begin{Bmatrix} \rho v \\ \rho vu \\ \rho vv + p \\ \rho vw \\ \rho vE + pv \end{Bmatrix}, \quad F_z = \begin{Bmatrix} \rho w \\ \rho wu \\ \rho wv \\ \rho ww + p \\ \rho wE + pw \end{Bmatrix}$$

It is clear that the inviscid terms comprise convection and pressure terms.

$$F_x = \begin{Bmatrix} \rho u \\ \rho uu + p \\ \rho uv \\ \rho uw \\ \rho uE + pu \end{Bmatrix} = \underbrace{\rho u \begin{Bmatrix} 1 \\ u \\ v \\ w \\ E \end{Bmatrix}}_{\text{Convective terms}} + \underbrace{p \begin{Bmatrix} 0 \\ 1 \\ 0 \\ 0 \\ u \end{Bmatrix}}_{\text{Pressure terms}}$$

$$F_y = \begin{Bmatrix} \rho v \\ \rho vu \\ \rho vv + p \\ \rho vw \\ \rho vE + pv \end{Bmatrix} = \underbrace{\rho v \begin{Bmatrix} 1 \\ u \\ v \\ w \\ E \end{Bmatrix}}_{\text{Convective terms}} + \underbrace{p \begin{Bmatrix} 0 \\ 0 \\ 1 \\ 0 \\ v \end{Bmatrix}}_{\text{Pressure terms}}$$

(2.41-a)

$$F_z = \begin{Bmatrix} \rho w \\ \rho wu \\ \rho wv \\ \rho ww + p \\ \rho wE + pw \end{Bmatrix} = \underbrace{\rho w \begin{Bmatrix} 1 \\ u \\ v \\ w \\ E \end{Bmatrix}}_{\text{Convective terms}} + \underbrace{p \begin{Bmatrix} 0 \\ 0 \\ 0 \\ 1 \\ w \end{Bmatrix}}_{\text{Pressure terms}}$$

The word “arbitrary” in ALE indicates that it could be both “Lagrangian” and “Eulerian” or anywhere in between them. Therefore, the control volume $V(t)$ and the control area $\partial A(t)$ are the function of time now. For the velocity of the moving control surface $\partial A(t)$ as \mathbf{v}_g , where

$$\mathbf{v}_g = \begin{bmatrix} u_g \\ v_g \\ w_g \end{bmatrix},$$

The resulting ALE formulation becomes:

$$\frac{\partial}{\partial t} \iiint_{V(t)} \mathbf{W} dV + \iint_{\partial A(t)} \mathbf{F} \cdot d\mathbf{A} = 0 \quad (2.42)$$

$$\mathbf{F}_x = \underbrace{\rho(u-u_g) \begin{bmatrix} 1 \\ u \\ v \\ w \\ E \end{bmatrix}}_{\text{Convective terms}} + p \underbrace{\begin{bmatrix} 0 \\ 1 \\ 0 \\ 0 \\ u \end{bmatrix}}_{\text{Pressure terms}}$$

$$\mathbf{F}_y = \underbrace{\rho(v-v_g) \begin{bmatrix} 1 \\ u \\ v \\ w \\ E \end{bmatrix}}_{\text{Convective terms}} + p \underbrace{\begin{bmatrix} 0 \\ 0 \\ 1 \\ 0 \\ v \end{bmatrix}}_{\text{Pressure terms}} \quad (2.43)$$

$$\mathbf{F}_z = \underbrace{\rho(w-w_g) \begin{bmatrix} 1 \\ u \\ v \\ w \\ E \end{bmatrix}}_{\text{Convective terms}} + p \underbrace{\begin{bmatrix} 0 \\ 0 \\ 0 \\ 1 \\ w \end{bmatrix}}_{\text{Pressure terms}}$$

By replacing these inviscid terms with the inviscid flux terms of NS equations, the complete set of NS equations for ALE formulation is obtained.

2.12 Spring tension analogy

The main idea in spring tension analogy is to treat the central node as joined with the surrounding nodes through springs. The original tension model was proposed by Batina^[48,49]. The idea is to apply reciprocal of the intermediate distance between any two nodes as a stiffness parameter between them. Therefore,, when the nodes come closer, the stiffness increases. However, this model is not very efficient and leads to cross over of the mesh points and different enhancements have been suggested^[50,51].

2.13 Delaunay graph mapping

The performance of the enhanced spring tension analogy model is eclipsed by the fast non-iterative Delaunay Graph method^[52]. It can be few orders faster than the spring tension analogy and allows larger boundary movements. It will be explained further in chapter 6.

2.14 Geometric conservation law (GCL)

Geometric Conservation Law^[47] or GCL ensures the conservation of fundamental flow parameters during dynamic grid motion.

$$\frac{\partial V}{\partial t} + \iint_{\partial V(t)} (\mathbf{v} - \mathbf{v}_g) \cdot \mathbf{n} dA = 0 \quad (2.44)$$

where, $\partial V(t)$ is the time dependant boundary of the cell surface. To apply the uniform velocity condition, since surface $\partial V(t)$ is closed,

$$\frac{\partial V}{\partial t} - \iint_{\partial V(t)} \mathbf{v}_g \cdot \mathbf{n} dA = 0 \quad (2.45)$$

The discrete form of this equation should hold at all time steps for whole discretised domain. It is the essence of GCL. GCL must be solved numerically using the same scheme that is used to integrate the conservation laws of the fluid to provide a self-consistent solution for the local cell volumes.

A backward Euler scheme or a three-point difference is used to discretise the fluid equations. Therefore,,

$$\begin{aligned} \frac{V^n - V^{n-1}}{\Delta t} &= \sum_{j=1}^{nface} (\mathbf{v}_g)_j^n \cdot \mathbf{n}_j^n A_j \\ V^n &= V^{n-1} + \Delta t \sum_{j=1}^{nface} (\mathbf{v}_g)_j^n \cdot \mathbf{n}_j^n A_j \end{aligned} \quad (2.46)$$

where, $(\mathbf{v}_g)_j^n$ is the averaged mesh moving velocity of face jj at time step n , \mathbf{n}_j^n and A_j are the face normal and face are at time step n , respectively. The face normal and area are determined from the instant mesh positions. The face velocity is represented by the velocity of the face centroid by discretising the position vector with the same temporal scheme as above

$$(\mathbf{v}_g)_j^n = \frac{(X_c)_j^n - (X_c)_j^{n-1}}{\Delta t} \quad (2.47)$$

where, $(X_c)_j^n$ is the position vector of the face centroid. It can be obtained by taking average of present node positions of the centroid.

3. Preliminary Validation for Steady-state Cases

The simulation results of two of the most widely used cases by the CFD community for validation; RAE2822 aerofoil and ONERA M6 wing are presented in this chapter. The aim of these simulations is two-fold; firstly: to validate the results from the double precision solver and other changes done in the DG-DES as stated in section 1.5.1. secondly: to lay a foundation of the next study in the chapter 4 of Aerospatiale A-airfoil. The bottom line of the simulations done in this chapter depict that for an attached boundary layer the solution based on the DES or DDES and pure RANS should be similar, provided that the RANS simulation is switched within the boundary layer region and the LES away from it;.

3.1 RAE2822 aerofoil

The main features of this simulation are the presence of a shock wave on the suction side of the aerofoil. All the cases are run using double precision solver. The steady state simulations were carried out by two different ways. Firstly, the infinite physical time step was used in the dual time stepping scheme giving directly the steady state solver. Secondly, the finite physical time was used with large number of physical time iterations to reach steady-state in physical time. Both methods give similar results. It is a transonic speed case with a thin boundary layer attached to the aerofoil surface. The flow separation is not expected. In this particular case, the results are expected to be primarily dictated by the RANS solver. For the DES and DDES, the simulation should present results very similar to the RANS simulation; because they will have only RANS part operational in the thin boundary layer.

Mach Number	Angle of Attack	T (°K)	P (Pa)	Reynolds Number
0.729	2.31	300	101325	6.5×10^6

Table3.1 Operating conditions for simulation of RAE2822

The mesh used in this case is a two dimensional structured mesh with 1 cell extruded in

Number of cells	Number of Nodes	Type of cells
17440	35398	Hexahedral

Table3.2 Mesh statistics for simulation of RAE2822

z-direction with unit length. The solution L2-Norm converged to 4th order. Mesh parameters are as follows:

This case was simulated using DES, DDES, RANS (1st order), RANS(AUSM) and RANS(HLLC) schemes for their validation. Figure 3.1 (Left) indicates the basic parameters as Y^+ values on the surface which is under 1.0 as preferred for transonic speed flows. Right side figure show the switching region from RANS to LES for DES and DDES. Both DDES and DES have similar regions and it is evident that the RANS is being implemented by all the methods in the near wall region.

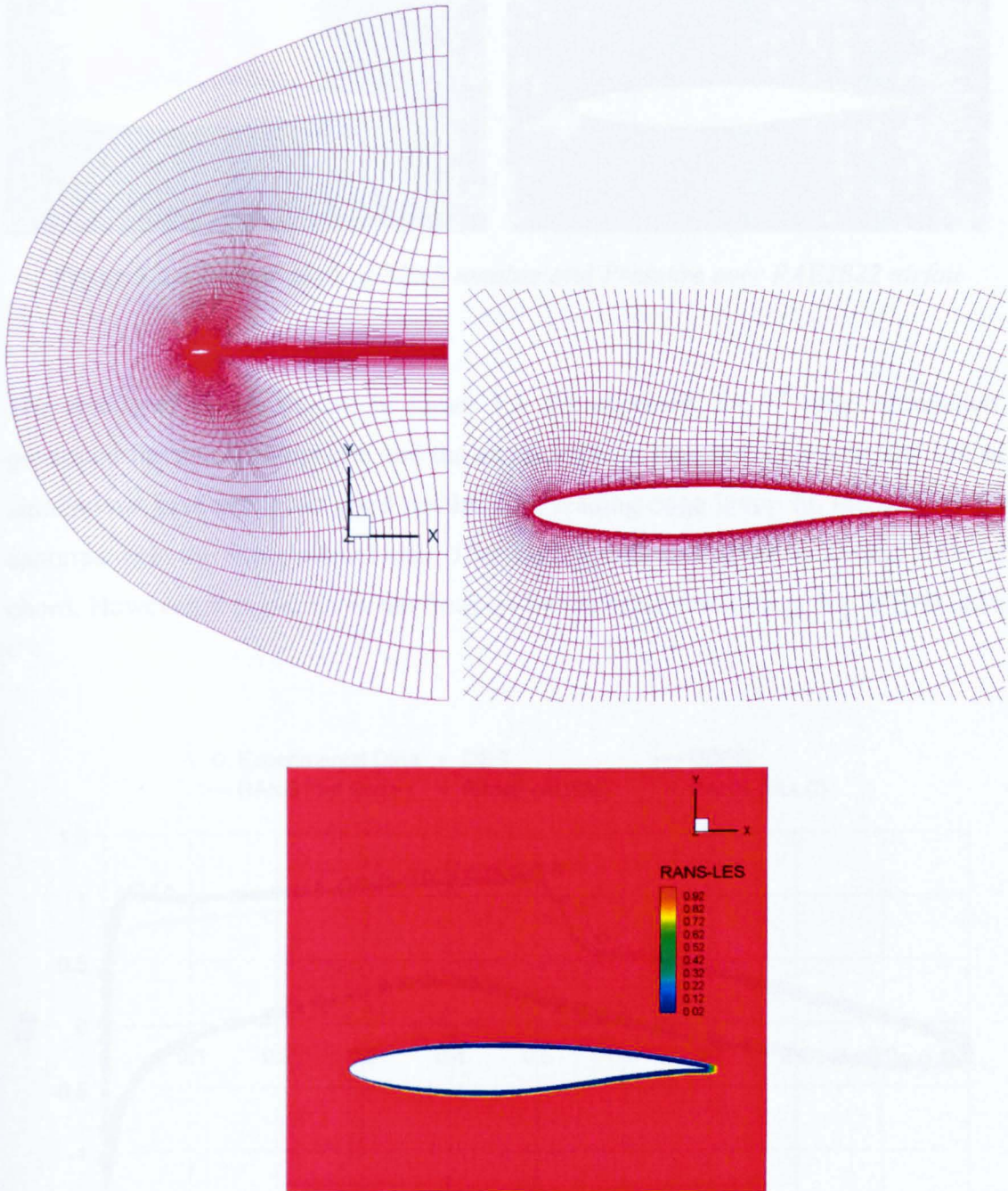


Figure 3.1 Top(Left): Domain with mesh Top(right) Zoom view of RAE2822 aerofoil mesh
Bottom: RANS-LES switching

The resultant plots of static pressure and Mach number by all the simulations (except RANS 1st order) are similar as presented in figure 3.2. The shock region on the suction side is clear from both Mach number and static pressure plots.

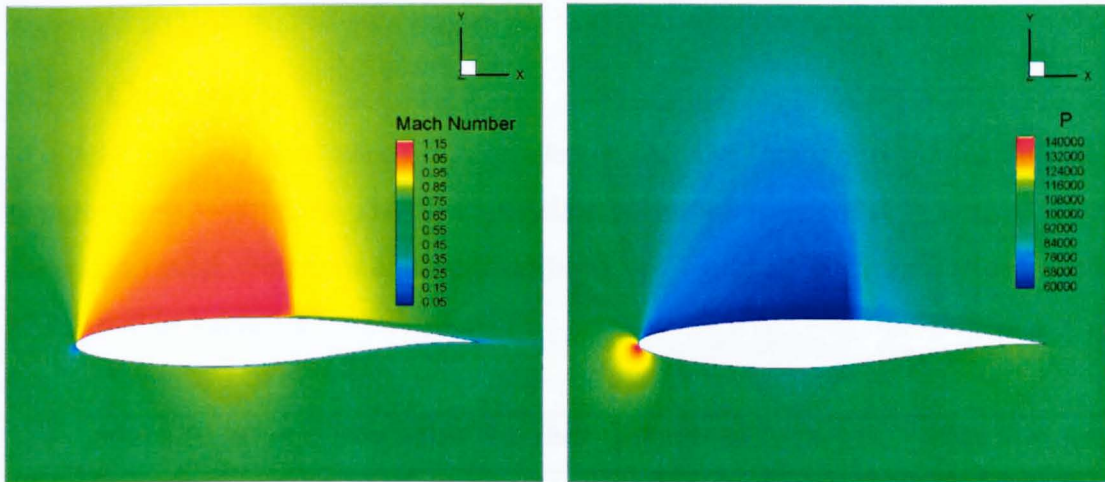


Figure 3.2 Contour plots of Mach number and Pressure over RAE2822 airfoil

The results of C_p are plotted in figure 3.3. As expected, the 1st order simulation has generated too much dissipation and the shock wave is smeared. However, the rest of the simulations have produced good results. The leading edge hump on the suction side is captured as in the experimental data. The shock location is offset by around 1.8% of the chord. However, it is similar to the findings by the other studies e.g., by WIND cfd code [77].

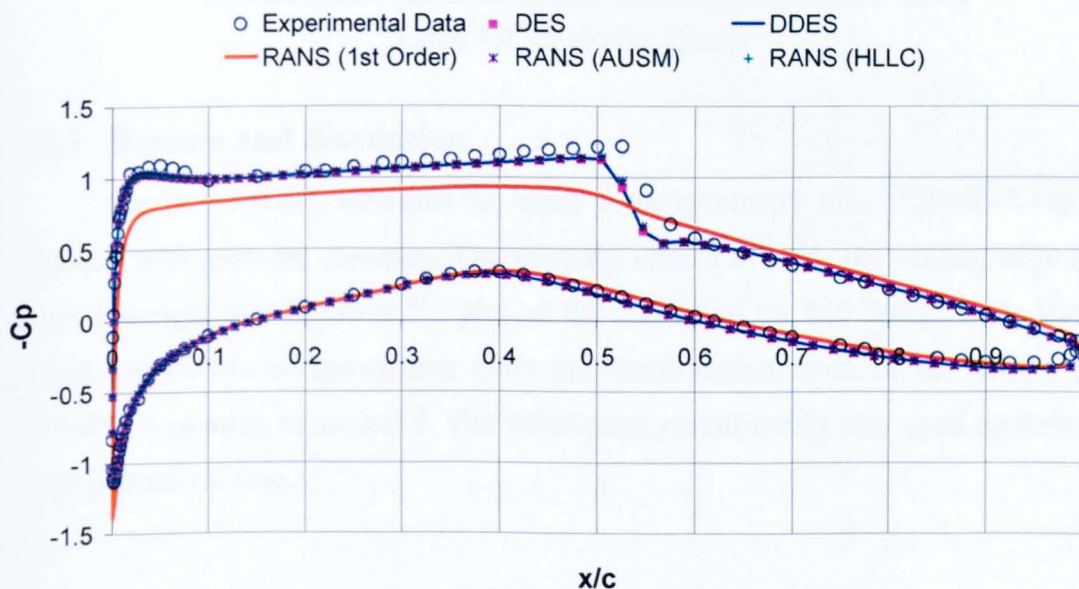


Figure3.3 Comparison of pressure coefficient using RANS (1st order, AUSM, HLLC), DES and DDES with experimental data

3.2 ONERA M6 Wing at Transonic Mach Number

The second test case is of ONERA M6 wing at transonic Mach number is a classical validation case. It has been archived by NPARC Alliance as the CFD Validation case^[53]. The ONERA M6 wing is a swept, semi-span wing with no twist.

3.2.1 Case setup

Only half of the wing is considered for the numerical simulation to save computational resources. The Spalart-Allmaras turbulence model^[39] is used for steady state simulation. Freestream flow conditions are assumed with further case details as mentioned in Table 3.1.

Mach Number	Reynolds Number	Angle of Attack	Side Slip Angle
0.8395	11.72×10^6	3.06	0.0

Table 3.3 *Case setup of Onera M6 wing at transonic speeds*

3.2.2 Mesh details

Mesh used in this validation was generated by H.Xia^[1]. This mesh has a baseline prismatic layer with tetrahedral elements on top for economizing the mesh density. It is an unstructured grid and further details are presented below in Table 3.3.

Total nodes	Total cells	Tetrahedral	Prism
621,282	1,520,491	452,651	1,067,840

Table 3.4 *Mesh size details*

3.2.3 Results and discussion

Figure 3.4 (Left) indicates the mesh at the symmetry axis with M6-Wing surface coloured with pressure contours. The wing tip effects towards the trailing edge are very clear. The right side figure is Y+ plot on the surface of the M6 Wing. Y+ is less than 1 almost everywhere on the surface. Only in a small region shock on the suction side has Y+ value increasing to around 3. The subsequent results are in very good agreement with the experimental data.

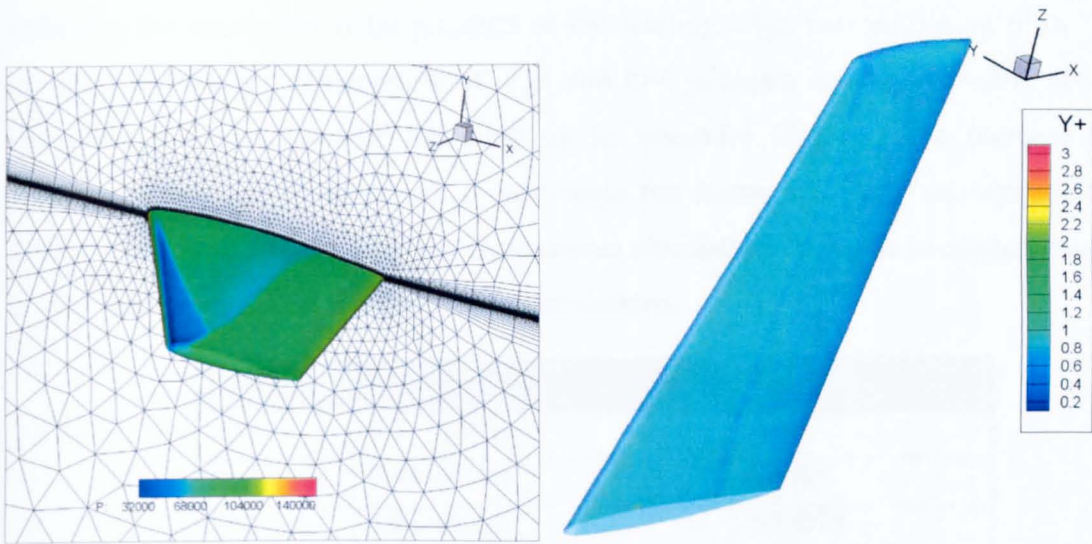


Figure 3.4 Left: Mesh along the symmetry plane with M6 Wing surface colour with pressure contour. Right: M6 Wing surface colour with Y^+ .

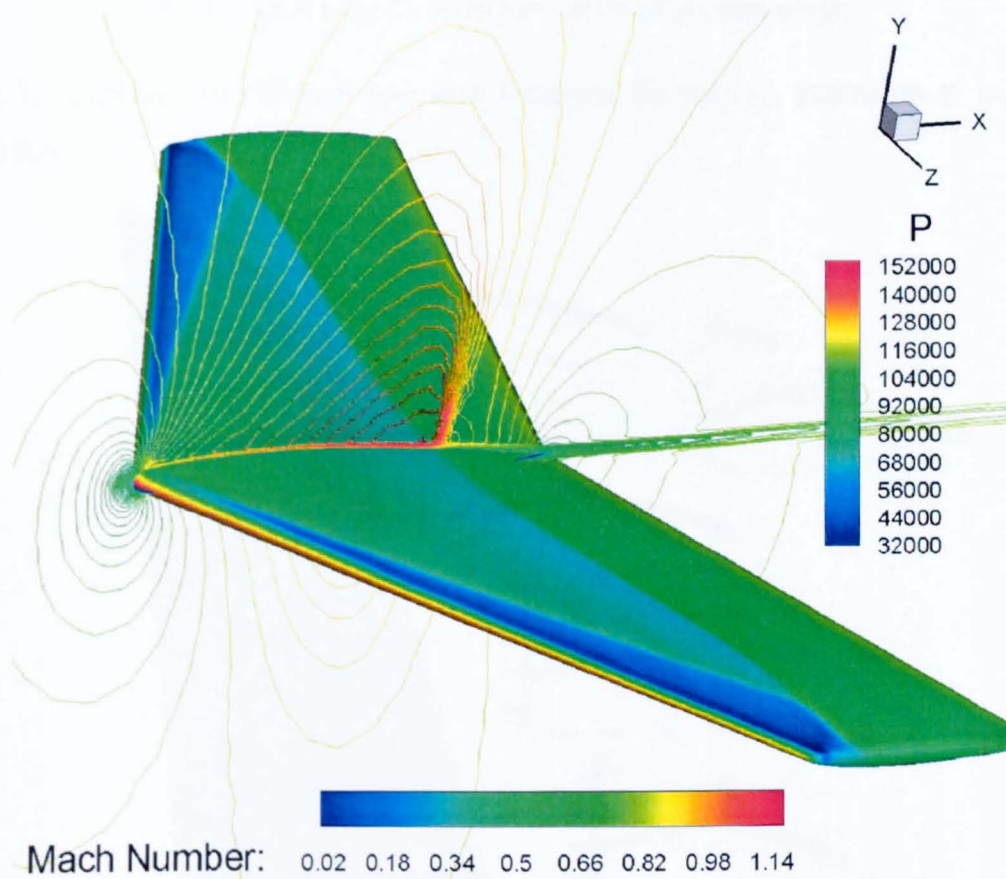


Figure 3.5 Onera M6 wing surface pressure plot (flood mode) and symmetry plane Mach number plot (line mode)

Figure 3.5 indicates the Mach number plot in line mode. The “ λ -shock”, as termed generally in literature, can be observed on the wing surface. In addition, the maximum Mach number obtained by the CFD simulation is around 1.14 which is in accordance with the experimental observations^[55] and other simulation results^[53]. The surface plot

indicates the maximum static pressure at the leading edge corresponding to stagnation pressure and a clear demarcation of high and low pressure regions is visible across the shock wave. Down towards the wing tip in spanwise direction, the increase in low pressure region can be observed. It represents the strong tip effect and spanwise three dimensional flow effects. The two dimensional simulation is unable to capture this and it is very important in real life finite span simulations.

Plot	Spanwise Location (η) y/b	Actual Height (m)
Cp1	0.2 (20%)	0.227
Cp2	0.44 (44%)	0.4994
Cp3	0.65 (65%)	0.73775
Cp4	0.8 (80%)	0.908
Cp5	0.9 (90%)	1.0215
Cp6	0.95 (95%)	1.07825

Table3.5 *Span wise location for surface Cp comparison*

Table 3.5 explains the different spanwise locations for the $-C_p$ extraction as shown in figure 3.6.

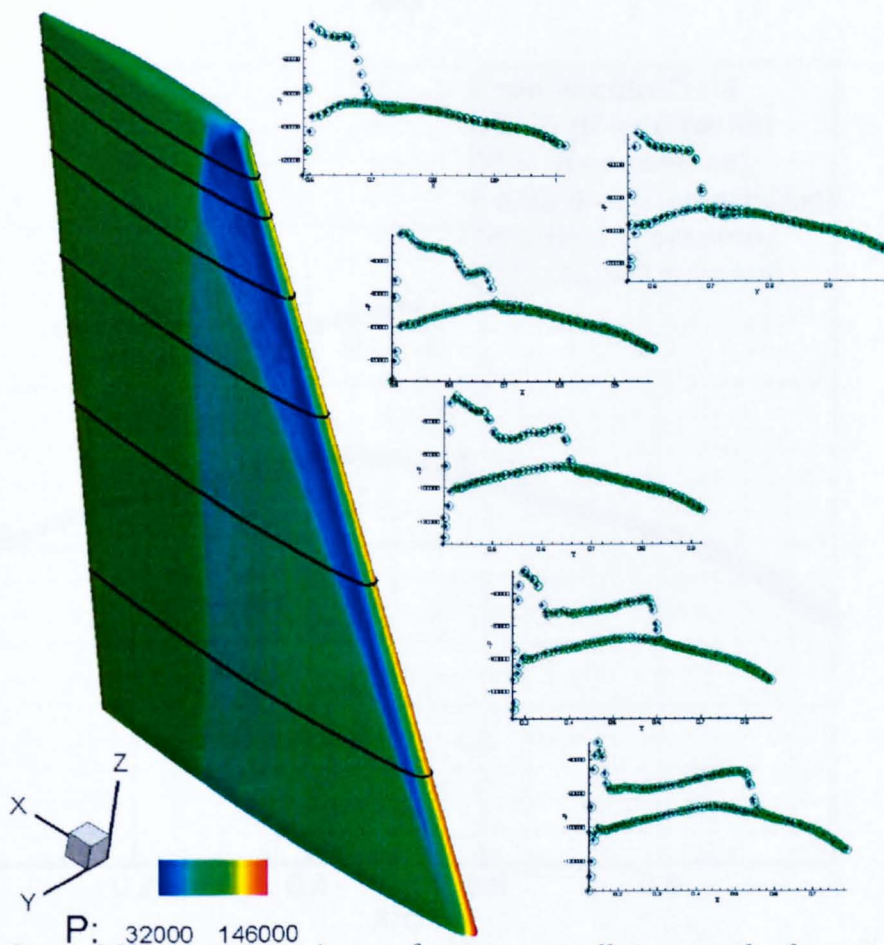
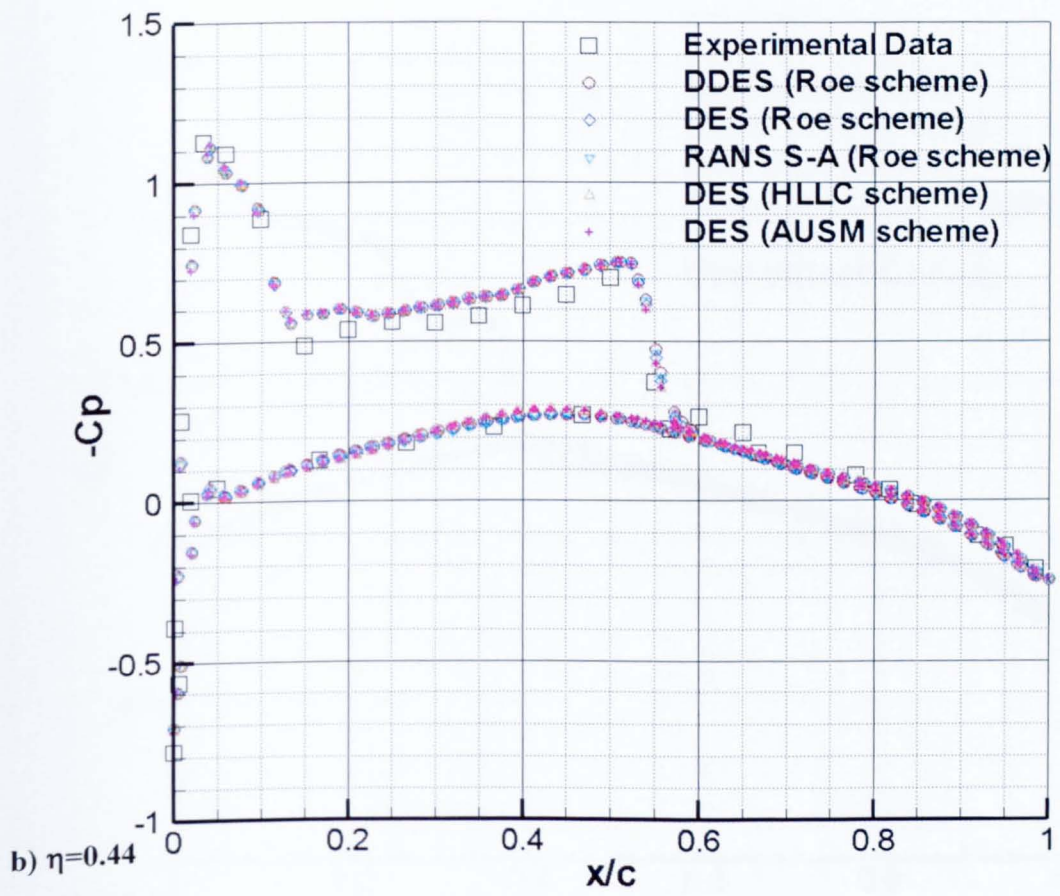
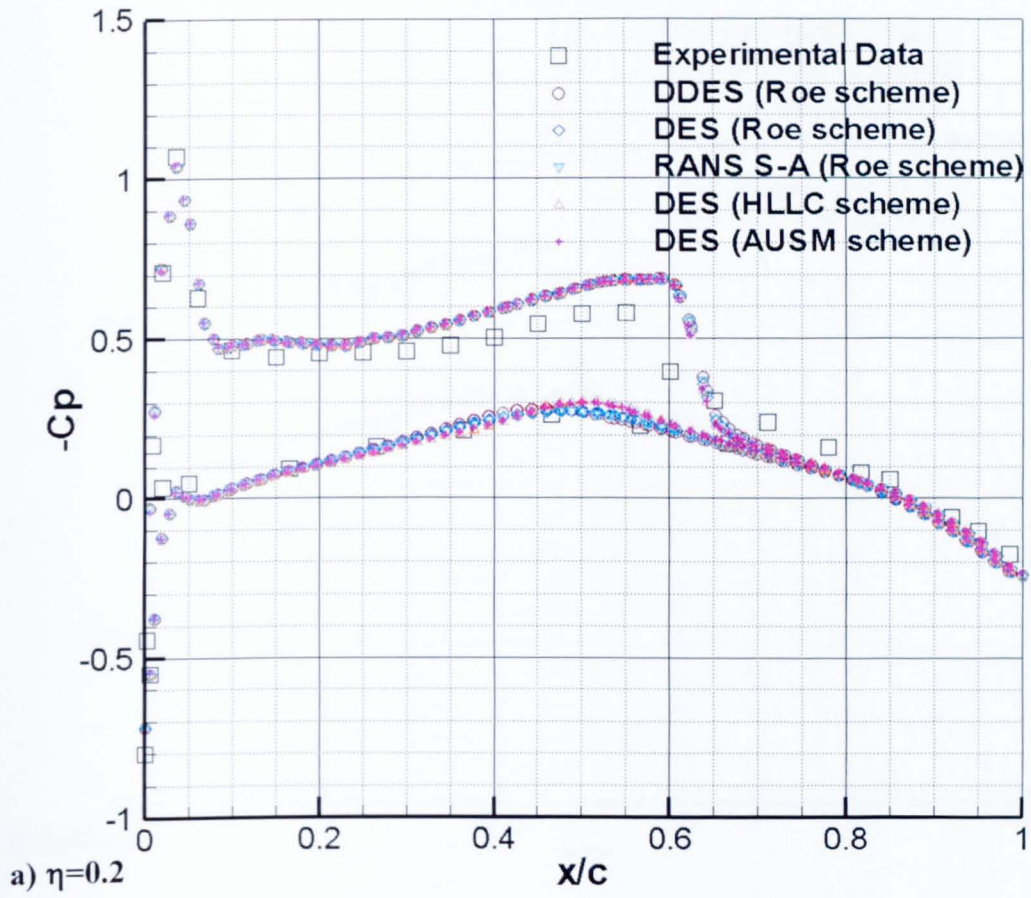
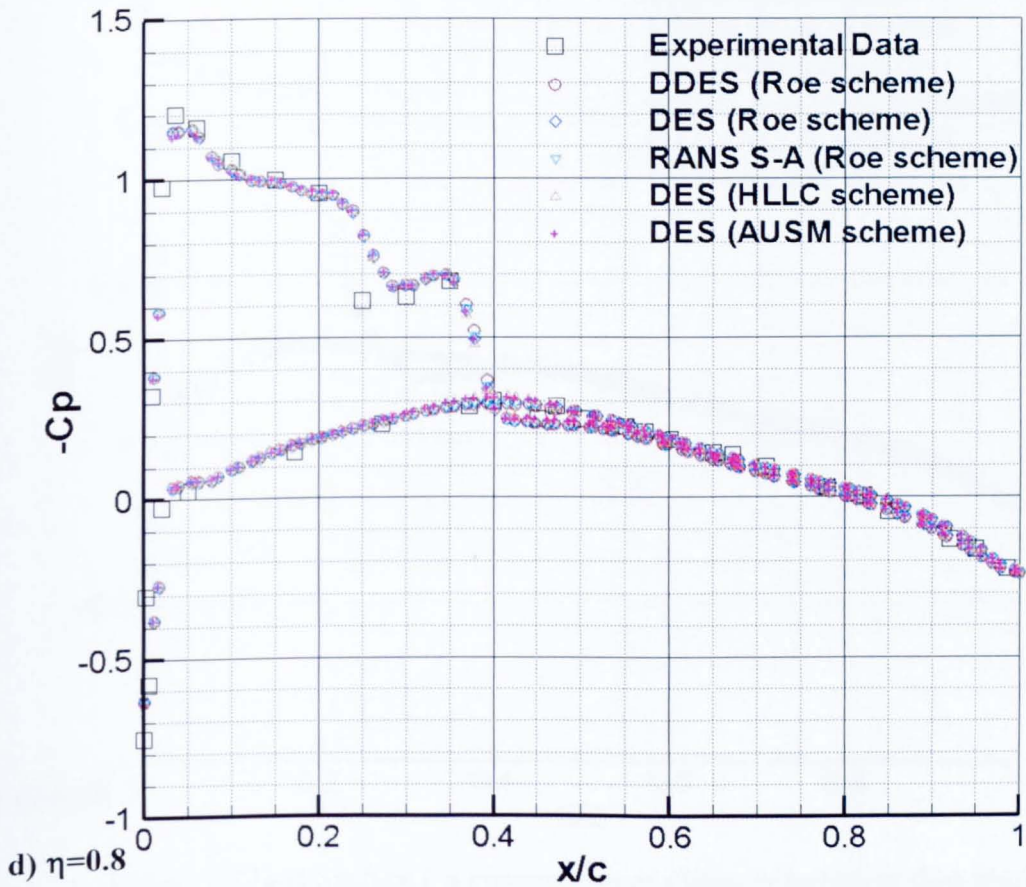
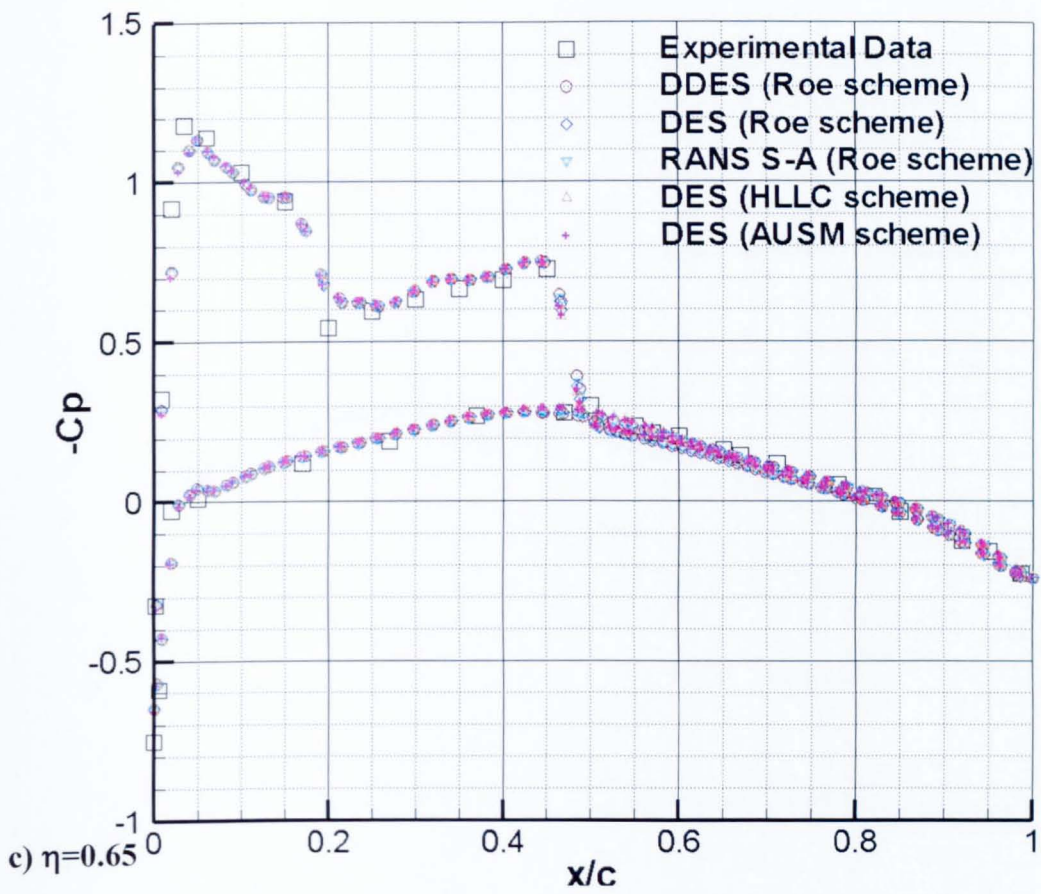


Figure3.6 *Onera M6 wing comparisons of pressure coefficient results from single and double precision solver using DES (Roe scheme based) at different spanwise locations. Single precision results are represented with “+” sign and double precision with a green colour circle.*





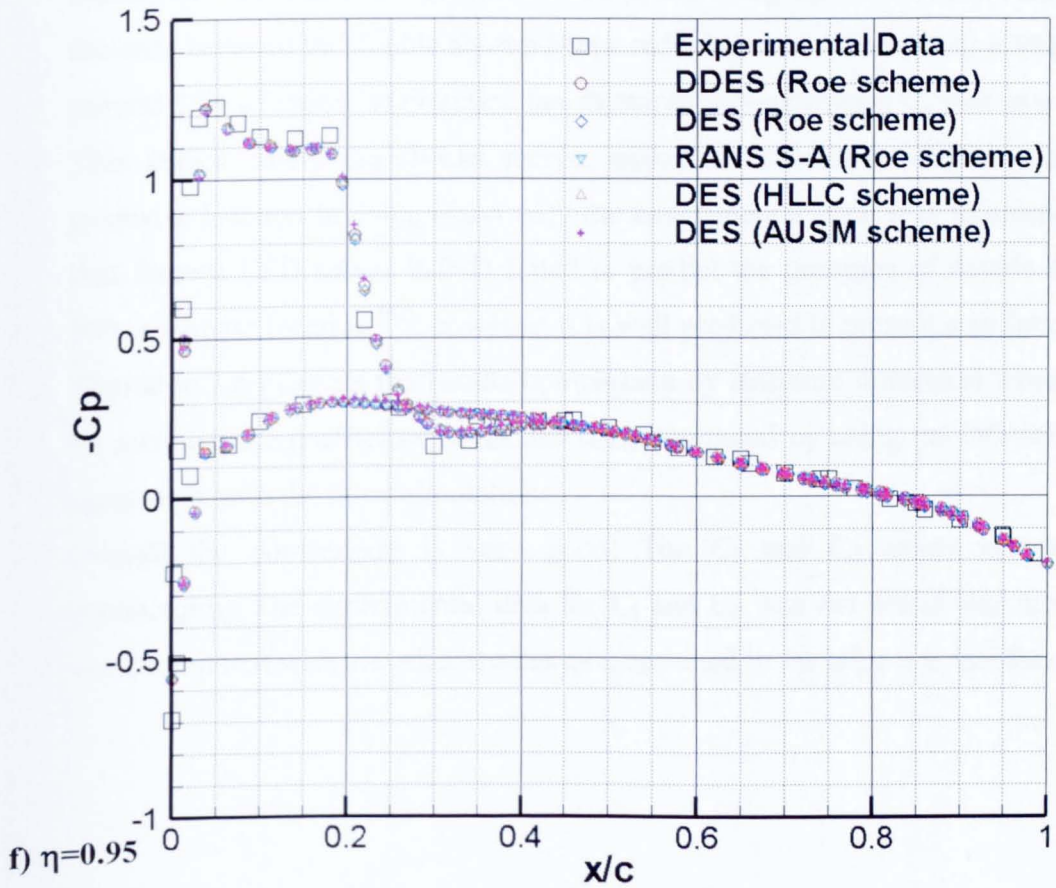
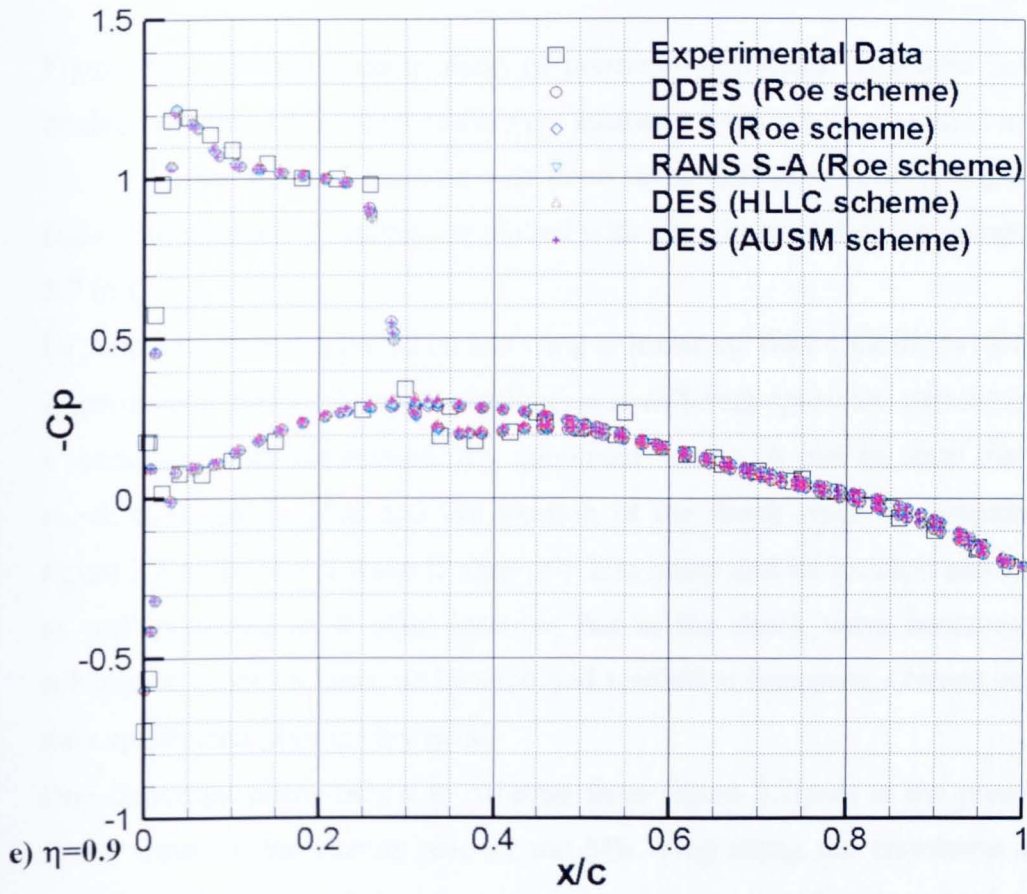


Figure 3.7 [a-f] Surface C_p comparison of different turbulent flow simulation schemes at different spanwise locations (η) with experimental data

Figure 3.6 indicates a comparison of pressure coefficient computed using single and double precision DES solver at different spanwise locations as presented in table 3.3.

Further detailed analysis was done using different options implemented in the code. The resultant C_p values are plotted with experimental data for comparison in figure 3.7 (a-f).

Experiments were conducted on M6 wing at transonic flow conditions by Schmitt et al^[55]. Experimental surface pressure distribution at different spanwise stations is available and is compared with the numerically simulated results. It can be seen that generally the shock capturing is good and the location of the shock wave is correctly predicted. In figure 3.7 a, the shock wave is relatively less sharp and its location and resolution is not as well predicted as at other location; but as the shock wave becomes steeper along subsequent cross sections, its location and resolution improves. Overall comparison with the experimental data is very good.

One important phenomenon to mention from figure 3.7(a-d) is the presence of double shock wave on the suction side of the M6 Wing along the chordwise direction. It is typical of “ λ -shock”. Going down towards the wing tip in the spanwise direction, the distance between the double shocks keeps reducing until it merges to a single shock after around 85% of spanwise direction (as shown in 90% spanwise C_p plot as a single shock). This region where the shocks merge, makes it difficult to obtain good C_p at 80% spanwise location in comparison with the experimental data. It is interesting to mention that famous CFD solver WIND failed to predict the presence of double shock wave at 80% spanwise location^[53], however, it is well predicted in present simulation.

The table 3.6 presents the results comparison by different numerical simulations. It can be seen that the coefficient of lift and drag computed by using the DG-DES are in good agreement with the other simulations.

Overall the comparison is very good. The C_l and C_d values obtained are quite encouraging. The experimental data for C_l and C_d was not found and hence the results were compared with the other studies as mentioned in the table 3.6. All these studies also

Solver	Turb. Model	Flux Scheme	Precision	Mesh Type	C_l	C_d
DG-DES	S-A	Roe	Double	Unstructured	0.2579	0.01970
DG-DES	DES	Roe	Double	Unstructured	0.2564	0.01960
DG-DES	DDES	Roe	Double	Unstructured	0.2580	0.01955
DG-DES	DES	AUSM	Double	Unstructured	0.2540	0.01910
DG-DES	DES	HLLC	Double	Unstructured	0.2550	0.01991
MERLIN ^[56]	S-A	Osher	Double	Structured	0.2697	0.01736
Neilsen et al. ^[58]	S-A	xx	xx	Unstructured	0.2530	0.01680
Lee et. al. ^[57]	SST	xx	xx	Structured	0.2622	0.01751

Table 3.6 *Comparison of different mesh parameters using DG-DES solve with different options with other studies*

compared the C_l and C_d with other numerical simulation results and only C_p values were compared with the experimental data.

3.3 Conclusions

The steady state simulations for both RAE2822 and Onera M6 wing were quite successful. The close matching of the simulation from the double precision solver and various numerical schemes (that were added to the DGDES), validated the implementation and accuracy. The good agreement of the C_p distribution at different spanwise locations with the experimental data is quite encouraging. Another important observation is that for these high speed flows with no separation, the generated boundary layer is very thin. This thin boundary layer without separation generates the results which are similar for RANS, DES and DDES. It is evident that for such type of cases, both the DES and DDES use the RANS results in the near wall region. It is to be noticed that this particular section was primarily aimed to check the accuracy of the enhancements in the solver. The strengths of DES and DDES can not be judged by steady state cases and are analysed in next forth coming chapters.

4 A-Airfoil at Maximum Lift Configuration

In this chapter, unsteady Reynolds Averaged Navier-Stokes (URANS), Detached-Eddy Simulation (DES97) and Delayed Detached-Eddy Simulation (DDES) are used to investigate the flow around the high lift Aerospatiale A-airfoil. The configuration used is at maximum lift ($\alpha=13.3^\circ$) at $Re= 2 \times 10^6$. The main idea is to analyse and highlight the merits and demerits of these schemes for mild separation cases.

The first part of this chapter focuses on CFD simulations and comparison of the results. Initially URANS and DES simulations were compared. The DES results were observed to be different with URANS at the leading and the trailing edge of the suction side. The results from different DES schemes using ROE, AUSM and HLLC schemes for flux calculation were similar and consistent. Subsequently, it was found that the boundary layer growth on the suction side of the trailing edge, as indicated by experimental displacement thickness, is not followed by the DES for its switching mechanism. This failure causes the premature switching from URANS to LES within the boundary layer reducing the modelled turbulent shear stresses. This problem is known as Modelled Stress Depletion (MSD) in DES. To address this problem, Delayed-Detached Eddy Simulation (DDES) was used and found to overcome this problem by delaying the switching to LES mode. However, the superior results at the trailing edge and the wake region presented by the DES scheme suggests that the levels of dissipation in DDES may be excessive enough to dissipate the effective levels of unsteadiness in the flow.

The second part of this chapter contains a detailed comparison of modelled turbulent stresses computed by using URANS, DES (with MSD) and DDES with the experimental data.

4.1 Introduction

Lift and Drag are two of the most important parameters in aerodynamics. The performance and efficiency of any aerodynamic object, say a wing, greatly depends on its response to a number of operating conditions it is subjected to. Some of these conditions are extremely important from the design point of view. For example, the maximum lift and drag requirement, especially at take-off and landing configuration, is achieved at high incidence angle. Analysis of flow physics at these operating conditions is of great importance in aeroplane

wing design. Flow separation and other related phenomena need to be carefully analyzed for any feasible wing design to work within the required safety margin.

LESFOIL, a European initiative to assess the feasibility of using the LES for calculating the flow around aerofoils, started in 1997 with various partners from industry and academia ^[86]. A detailed experimental data was made available for flow around the Aerospatiale A-airfoil at different angles of attack and at very high Reynolds numbers. However, the high Reynolds numbers are computationally prohibitive in the near wall region for the LES. It also motivated some groups to use hybrid schemes such as the DES to simulate these cases ^[91,92].

The case chosen for the simulation is Aerospatiale A-airfoil at an angle of attack of 13.3° (maximum lift configuration), with a chord based Reynolds number of 2×10^6 at a subsonic Mach number of 0.15. Typically it is a high lift configuration near the stall. The separation in the flow makes it a candidate for the DES scheme to be applied.

What makes this case more challenging is the presence of different flow regimes, as sketched in figure 4.1. These regimes are briefly described with reference to experimental data plotted in figure 4.2 and figure 4.3 to understand the flow complexity and diversification:

Suction side: The leading edge C_p indicates a low pressure region leading to a favourable pressure gradient which accelerates the flow, causing a thin laminar boundary layer going downstream to separate from the curved surface and form a separation bubble (laminar separation). Further downstream, the flow re-attaches and boundary layer transition leads to turbulent flow. The adverse pressure gradient causes the thickness of the attached turbulent boundary layer to increase. At 83% of the chord, a turbulent separation occurs, as seen in the C_f plot in figure 4.3.

Pressure side: The laminar boundary layer is tripped at 30% of the chord in the experiments and a transition to a thin turbulent boundary layer occurs.

Wake side (aft region of aerofoil): A mixed shear layer is formed from the thin turbulent layer emanating from the pressure side joining with the low speed flow from the separation region.

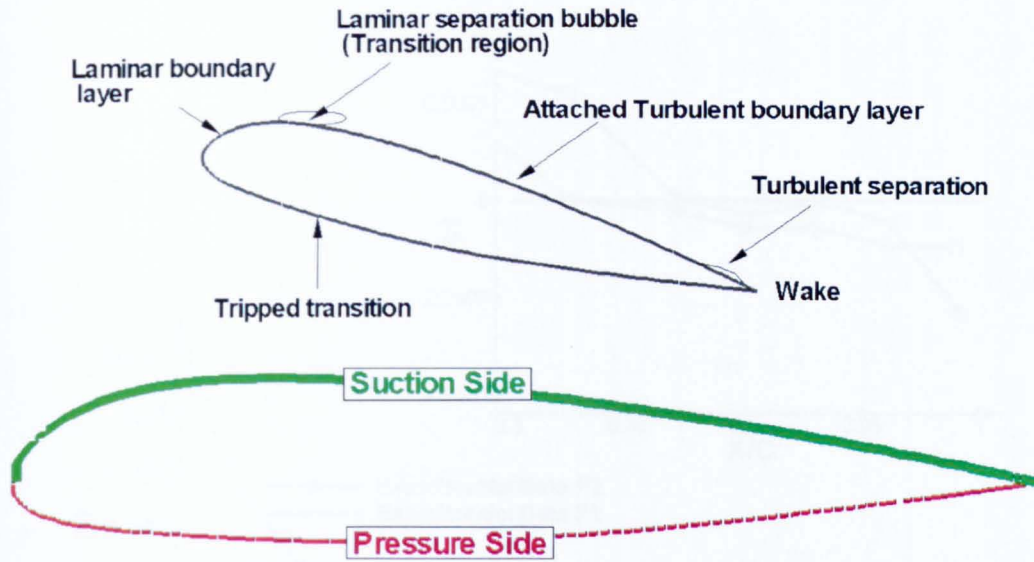


Figure 4.1 Schematics of different flow regimes on Aerospatiale A-airfoil

The experimental data is obtained from two wind tunnels, F1^[88] and F2^[89]. F1 and F2 data contains lift coefficient (C_l), drag coefficient (C_d) and skin friction coefficient (C_f) values for the test cases. F2 contains additional data for velocity profiles and Reynolds stresses at different wall normal and streamwise normal direction after the transition point ($x/c \geq 0.3$). The experimental data output from both F1 and F2 is different for the same case as shown in C_f plot in figure 4.3. Reference [90] presents a condensed synopsis of important results by seven partners in the Brite-Euram project LESFOIL^[86].

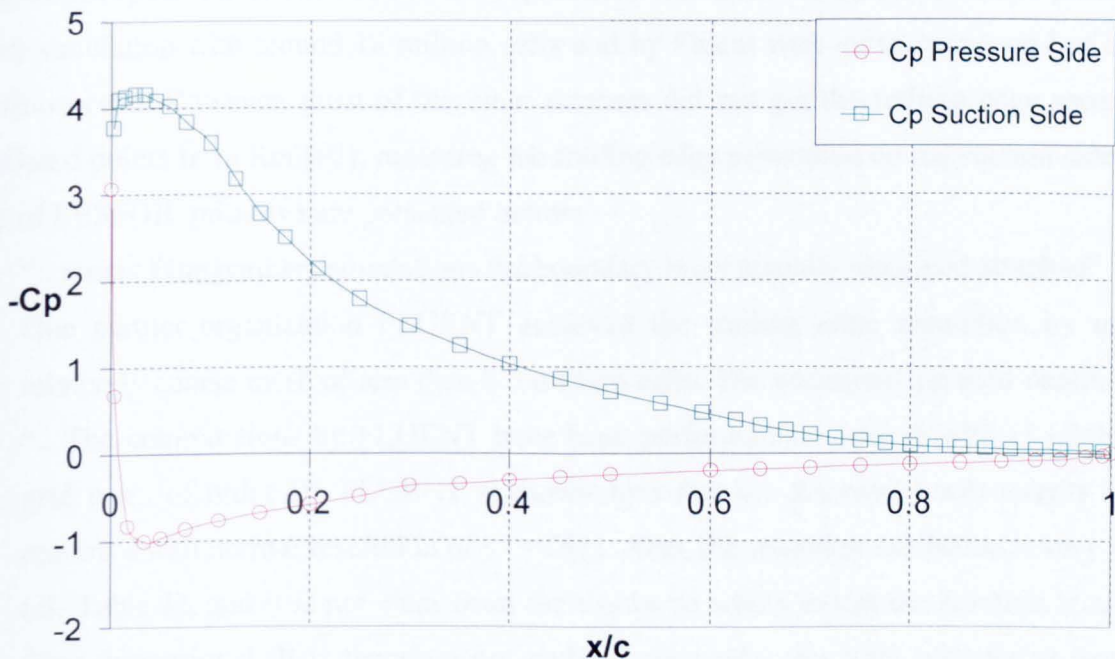


Figure 4.2 C_p plot experimental data F2

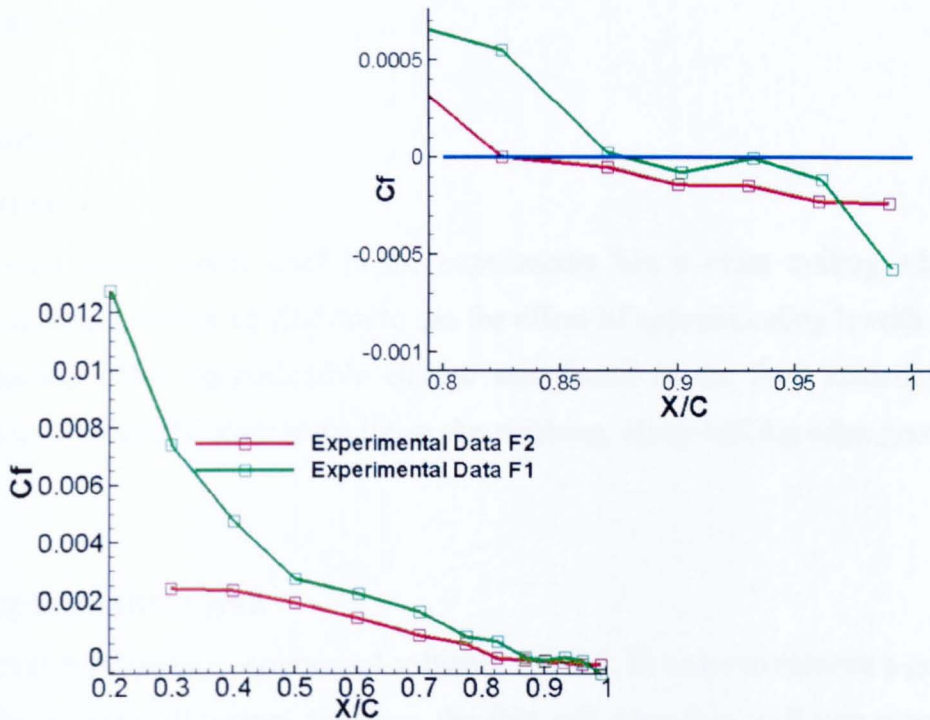


Figure 4.3 Skin friction coefficient plot for experimental data F1 and F2. Top: Zoom view showing turbulent separation around 83% of the chord on suction side near trailing edge F2 (solid blue line is at $y=0$)

The results from LESFOIL, by its different partners have been compiled and published^[90]. The trailing edge separation as observed in the experiment was achieved by the ONERA (one of the partner) simulation with around 18 million cells and by Fluent with quite coarse grid of around 0.4 million cells. However, most of the other partners did not get the trailing edge separation. Two related points from Ref [90], regarding the trailing edge separation on the suction side, from results of LESFOIL initiative are presented below:

1. “.. most of the partners simulations the boundary layer actually remained attached”
2. One partner organization FLUENT achieved the trailing edge separation by using a relatively coarse mesh of less than 0.5 million cells. The comments on their results were: “.. The computations by FLUENT have been performed on a mesh with y^+ of the first grid point of order 10. FLUENT acknowledges that the SA model will usually in fact require a wall normal resolution of $y^+ = O(1)$. Also, the spanwise resolution is very coarse (cf. Table 1), and it is not clear from the results to which extent the solution is actually three-dimensional. It is therefore not entirely clear why this DES calculation has been

able to capture the trailing edge separation while using a mesh much coarser than those of all other partners.”

4.2 CFD simulation

4.2.1 Geometry

The wind tunnel model used in the experiments has a blunt trailing edge. Ref [90], describes the different studies carried out to see the effect of approximating it with sharp trailing edge and concluded that no noticeable change was found in the flow statistics due to this geometric simplification. In order to facilitate the meshing, sharp trailing edge geometry is used in this study.

4.2.2 Computational mesh

The mesh was created using a commercial software Gambit. In order to achieve a good boundary layer resolution in the wall normal direction, the first cell normal to wall was placed at $6 \times 10^{-6}c$ which results in an overall $\Delta y^+ < 1$ on the aerofoil from the solution. The mesh details are as follows:

Type	Cells	Nodes	N_z	L_z/c	Δy^+
Structured	1936000	2004080	40	0.25	<1

Table 4.1 *Mesh details of the mesh used in present study*

The mesh size is very coarse (roughly an order less) in comparison with what is generally required for the LES to simulate similar size domain at this Reynolds number. Only the wall normal direction is resolved as required by the URANS. Typical Δy^+ for all the simulations were less than 1 for all simulations. It is accepted as a pre-requisite for proper functioning of the S-A model as mentioned above in point 2 and in Ref [91]. It is pointed out in ref. [90] that the spanwise extent for this test case should be at least $L_z/c=0.12$ to allow the growth of vortical structures. $L_z/c=0.25$ is chosen for this simulation. The mesh size is far less that what is required for the LES simulation for the same case. The spanwise grid is also much coarser and is typical of the RANS grid in the near wall region.

Figure 4.4 indicates the mesh domain with the 120 partitions each represented with different colour.

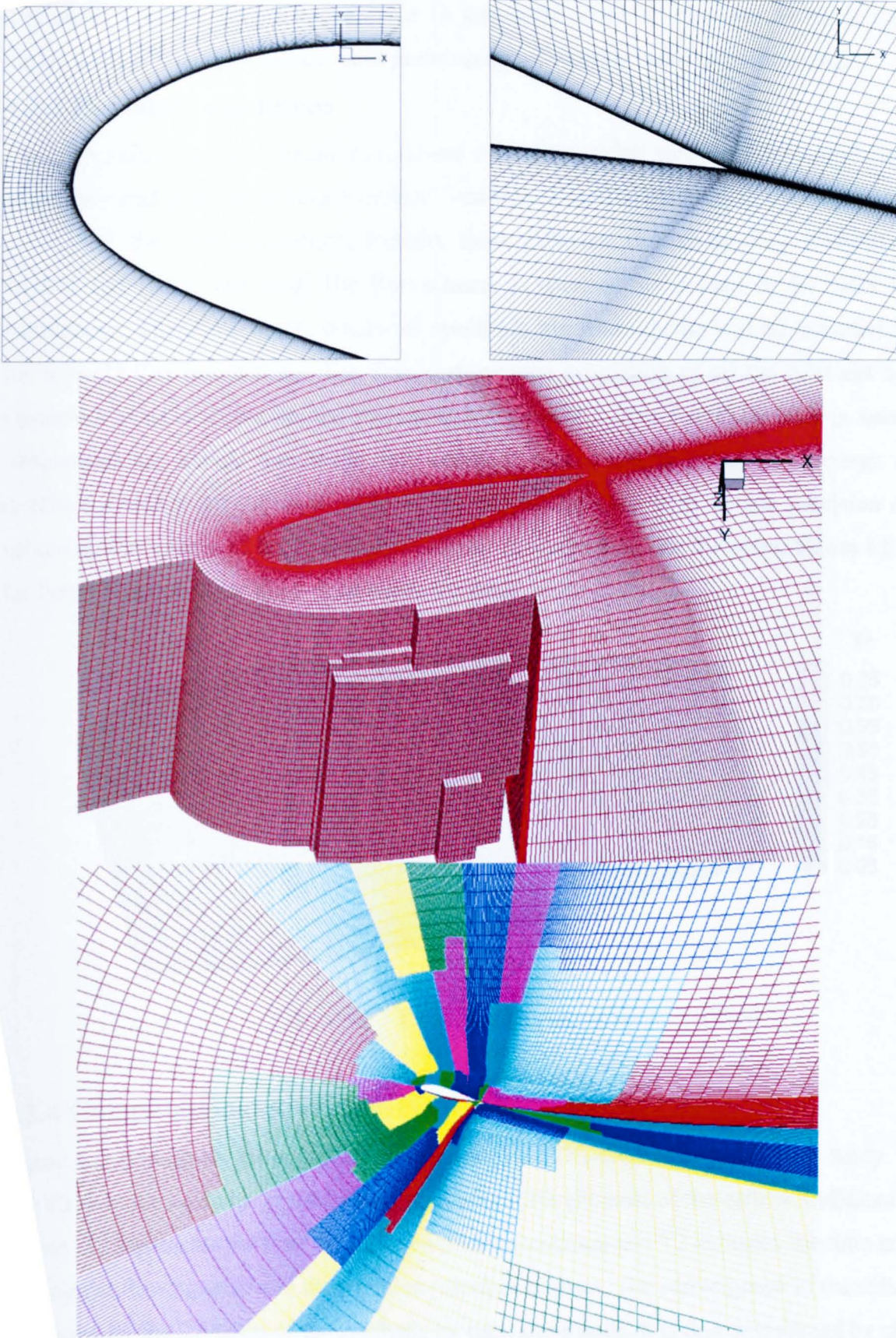


Figure 4.4 *Bottom: Domain mesh with 120 partitions with different colours
 Middle: 3D breakdown of the mesh
 Top: Zoomed view of leading and trailing edge in black colour*

The mesh is c-type with a domain size 16 times the chord at inlet and 24 times the chord at outlet. Metis^[60], an open source mesh partitioning software is used for partitioning.

4.2.3 Boundary conditions

No slip boundary conditions are used over the aerofoil surface. Side boundaries are kept as periodic and pressure farfield boundary condition is used around rest of the domain.

For the DES simulations, initially three different flux computing schemes; the Roe, AUSM and HLLC are used. The Roe scheme is used as the default in the DES for all the simulations. Therefore, unless otherwise specified, the Roe scheme will be assumed by default for inviscid flux calculations. The time performance evaluation of all the different schemes is presented in table 2. No special treatment for transition (trip functions etc.) is used and the simulations are carried out in the full turbulent mode. Lift and drag coefficients of all the different schemes are shown in table 3. The solver DG-DES is in double precision mode. Y^+ values on the surface of the A-airfoil are shown in figure 4.5. The Y^+ value below 1.0 is sought for better functioning of the S-A turbulence model.

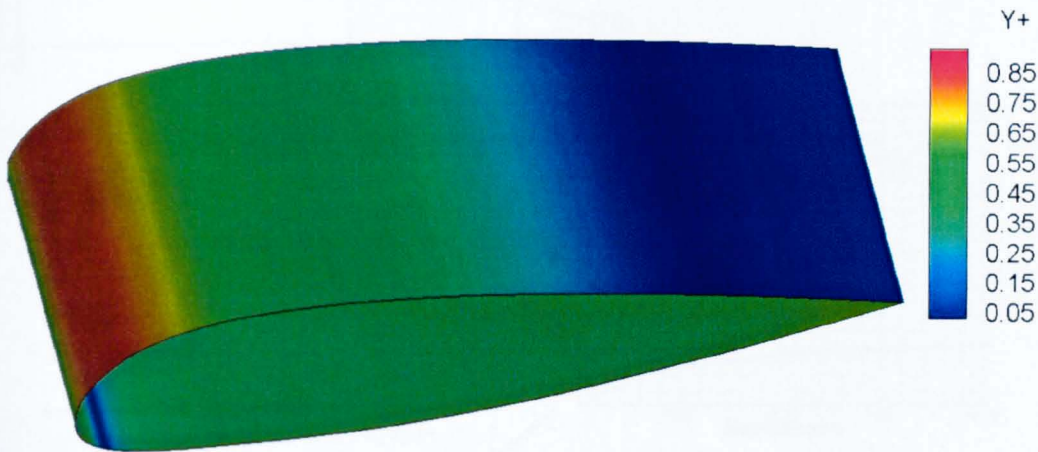


Figure 4.5 : Y^+ values on Aerospatiale A-airfoil

4.2.4 Computational time statistics

Figure 4.6 a) indicates the parallel performance of the DG-DES code used in this study. T1, T2 and T3 are time taken in 'seconds' for simulating different parts of the code as indicated in the legend. T1 represents the time taken for residual calculation and T2 indicates the time taken for solving the flow equations in the partition interface regions. The convergence of the solution is computed by the L2-norm of the residuals by each slave node. It is then transferred by all the slave nodes to the master for calculation of the global L2-norm. The time taken by this transfer is represented by T3.

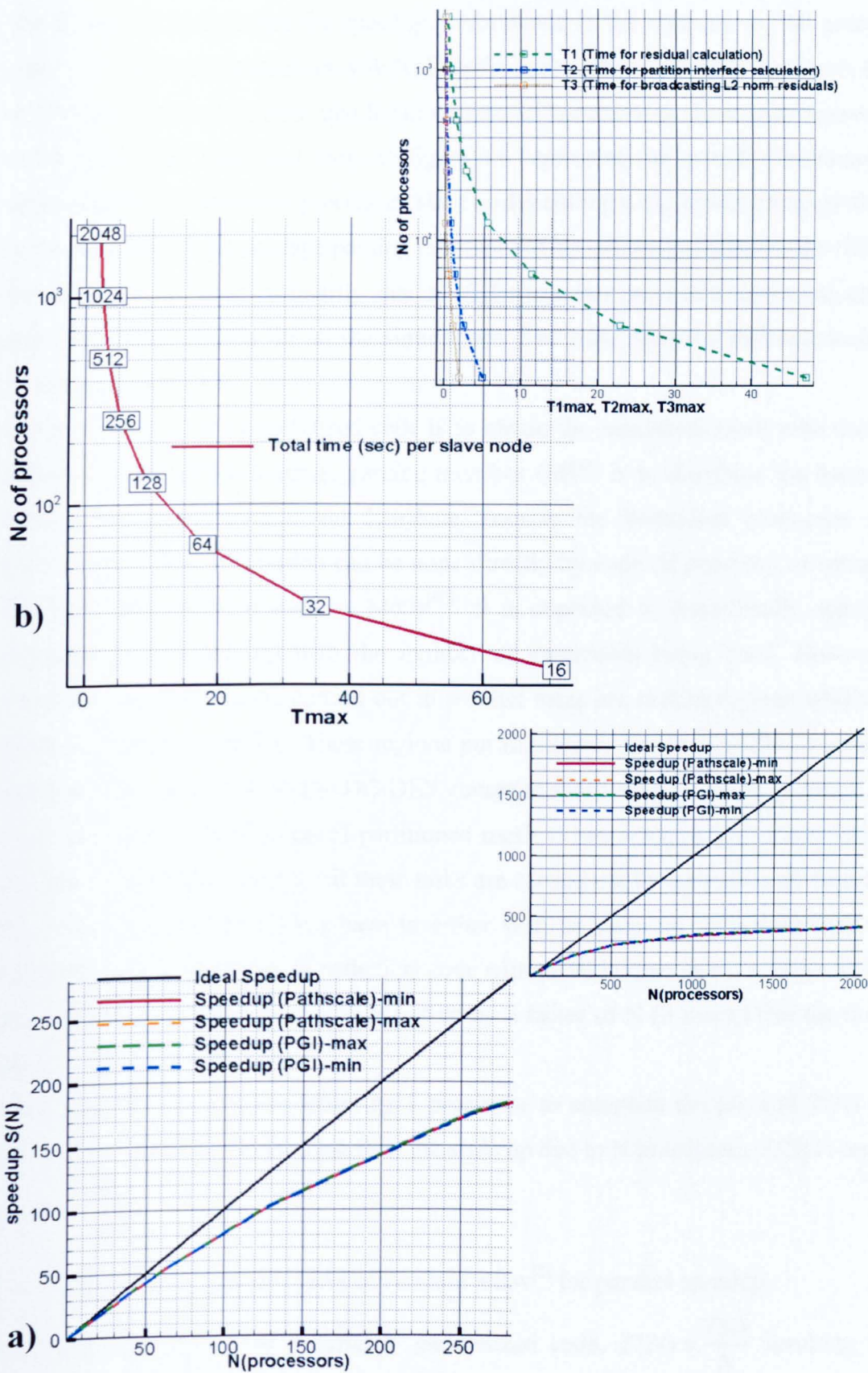


Figure 4.6 a) Parallel performance of the solver part of code with different number of processors. Inset is the time breakdown of main parts of code
 b) Parallel efficiency of the parallelizable part of code with different number of processors.

The figure 4.6 b) indicates the speedup performance in the code up to 380 processors in using ‘pgi’ and ‘pathscale’ compilers with ‘O2’ optimization flags. The inset indicates the same for up to 2048 processors. It is clear that for more than 250 processors, there is no appreciable speed-up in the code. The ‘max’ and ‘min’ in figure 4.6 represents the overall maximum and minimum time taken by an individual processor (slave node) amongst the whole group of slave nodes. Due to the structure of the message passing interface (MPI), all the processors take different times for execution of the code, primarily due to different inter-processor communication times. 120 processors were chosen for all the simulations. The time taken by different techniques will be presented in table 4.2.

The basic aim of any parallelized code is to obtain the maximum work with shortest time. The underlying idea of the message passing interface (MPI) is to distribute the huge computational domain into small chunks and distribute them to the individual processors in the parallel environment. This distribution can be done directly by code (if possible) or using some domain decomposition software such as Metis^[60]. It is expected to dramatically speed up any huge computation speeding up with the number of processors being used. However, for all the computational work being carried out in parallel there are certain regions which are inherently serial or non-parallelizable. These regions put limitations on the benefits of parallelization. For example, the serial parts in the DG-DES comprise mesh reading, mesh partition, calculation of mesh parameters, distribution of partitioned mesh to the working processors (slave nodes) and storage of simulation results. All these tasks are carried out by a single node (master node) while the other nodes (slave nodes) have to either wait or carry on with their task. In a perfectly parallelized code (an ideal/ hypothetical code with no serial part in it), a computational job that is split up among N processors, will speed-up by a factor of N (it means that the time to complete the job will scale with 1/N).

Assuming T(1) as the time taken by 1 processor to complete the job and T(N) to be the time taken by N processors to do a job then the scale up due to N processors, S(N) is represented as:

$$S(N) = \frac{T(1)}{T(N)} \quad 4.1$$

Equation 4.1 is the simplest form of Amdahl’s law^[4] for parallel speedup.

As mentioned above, for a perfectly parallelized code, $T(N) = \frac{T(1)}{N}$ resulting in a speed up S(N)=N. Apart from the serial part in the code, the inter-processor communication does not scale linearly with the increase in number of processors. In fact, for a large number of processors, the transfer time may increase if the amount of data being communicated is not very large. The

serial part (non-parallelizable portion of the code) takes 48.6 seconds for an A-airfoil case excluding the time for data save (as that involves the saving frequency and the details of data variables to be saved). The 48.6 seconds time is taken in reading the mesh, its partitioning and calculation of mesh parameters. In the scale-up study, no matter how best the whole code is parallelized, this serial part has put a lower limit on the parallelized performance. Also, it is more logical to use a much finer grid for speed-up study of up to 2048 processors. The speed up part shown in figure 4.6 is the totally parallelizable part of the code excluding the serial (non-parallelizable) part.

4.2.5 URANS and the DES simulation results

The time averaged C_p and C_f plots are shown in figure 4.7 and 4.8.

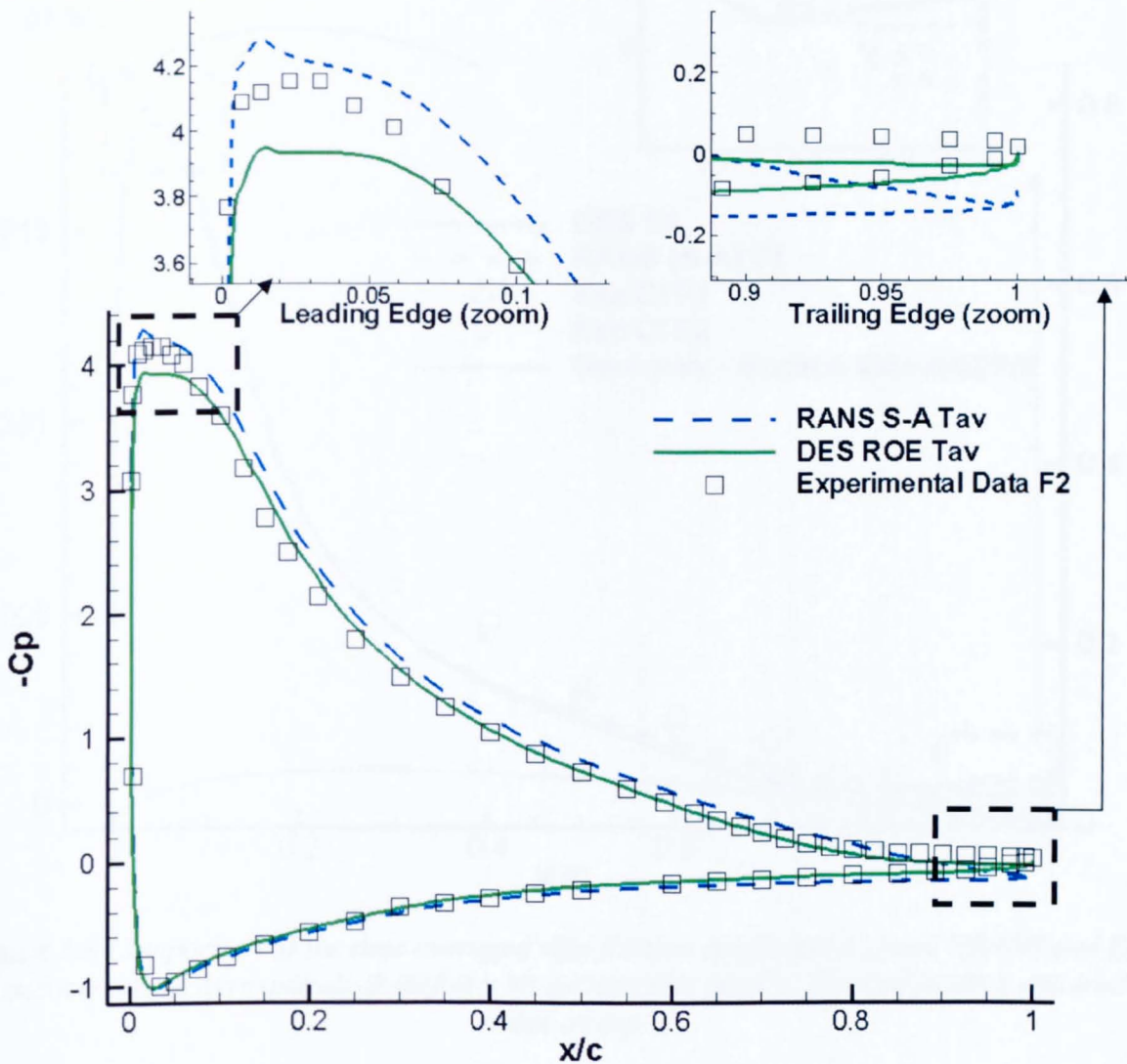


Figure 4.7 Comparison of computed time averaged (T_{av}) coefficient of lift (C_l) from URANS and DES on Aerospatiale A-airfoil with experimental data F2

In comparison with experimental data for the leading edge of the suction side, the DES predicts a relatively higher pressure region, producing lower $-C_p$ value. A close up of the leading edge as shown in figure 4.9 a) and 4.10 a) indicates that the low pressure bubble in the URANS is larger than the DES depicting a larger region of low pressure. The pressure side of the A-airfoil is generally presented well by both the URANS and the DES. Near the trailing edge, the DES simulation has a better match with experimental data in comparison with the URANS scheme.

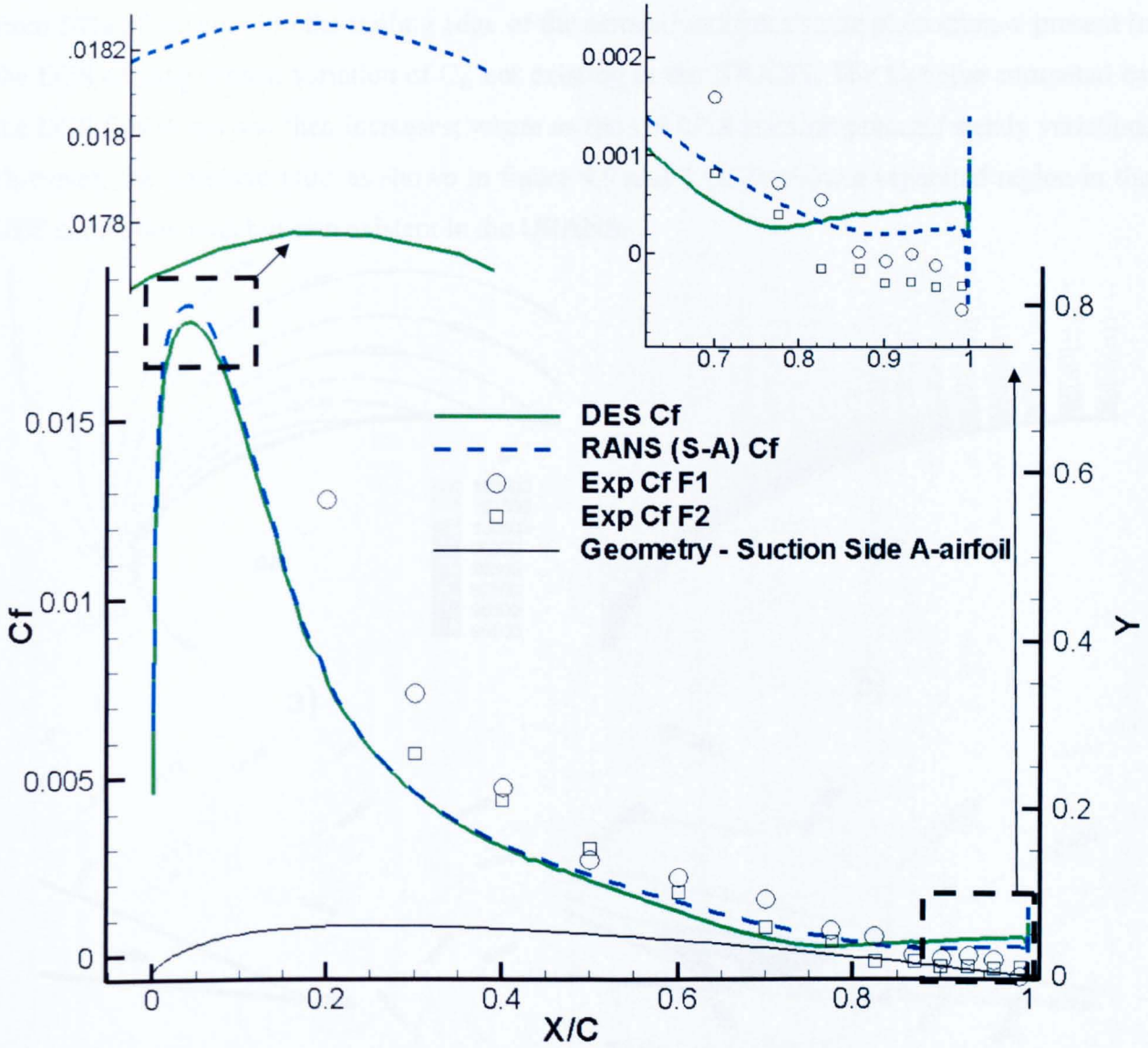


Figure 4.8 Comparison of the time averaged skin friction coefficient C_f from URANS and DES on suction side of Aerospatiale A-airfoil with suction side profile. Zoomed leading and trailing edge on top

A low pressure region is present at the leading edge of the suction side in both the URANS and the DES (see fig 4.9 and 4.10), but it does not contain any separation region. Similar results were reported in other 3D studies (for instance Ref. [91] and [92]), that is, no separation bubble at the leading edge of the suction side (no dip in the C_f values around the 30% of the chord region). Ref

[91] and [92] reported flow separation at the suction side of the trailing edge. From figure 4.8, the DES indicates a considerable lower value of skin friction coefficient on the suction side until 81% of the chord in the downstream direction. It means that the modelled shear stresses are considerably less in the DES simulation in comparison with the URANS. Near the trailing edge, the C_f in the DES simulation increases. However, the C_f for neither scheme becomes negative which would indicate the flow separation on the surface. The behaviour of C_f curve for the DES from 50% of the chord to the trailing edge of the aerofoil indicates some phenomenon present in the DES causing typical variation of C_f , not existing in the URANS. The C_f value computed by the DES first drops and then increases; whereas the URANS solution presents steady variation. However, the flowfield plots as shown in figure 4.9 and 4.10 do show a separated region in the DES simulation which is non-existent in the URANS.

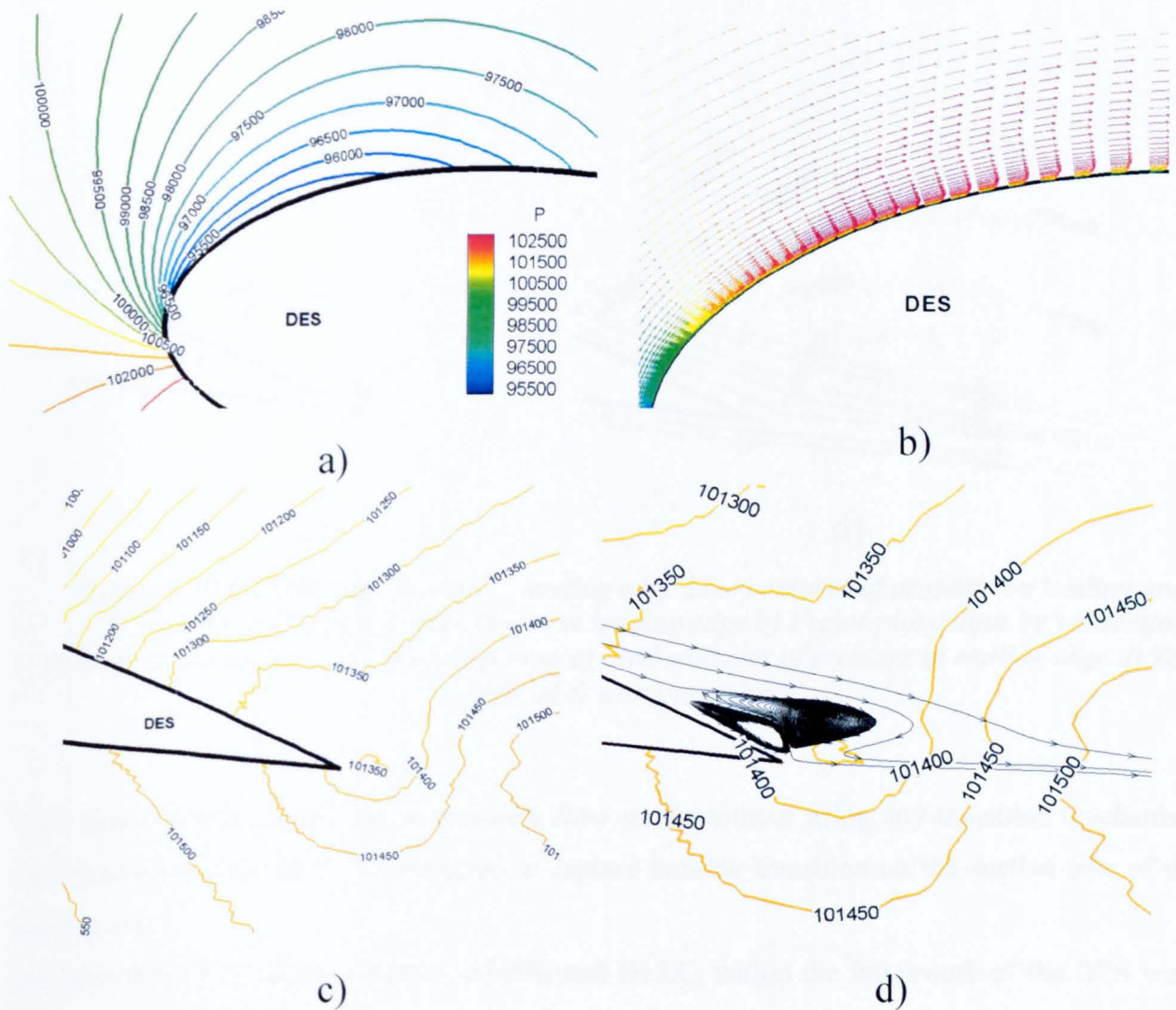


Figure 4.9 DES computation of leading edge Line contours of pressure on leading and trailing edge a) Line contours of press at leading edge b) Vector plot colour by x-direction velocity at the suction side of leading edge c) Line contours of pressure at trailing edge d) Zoom view of c) with streamlines

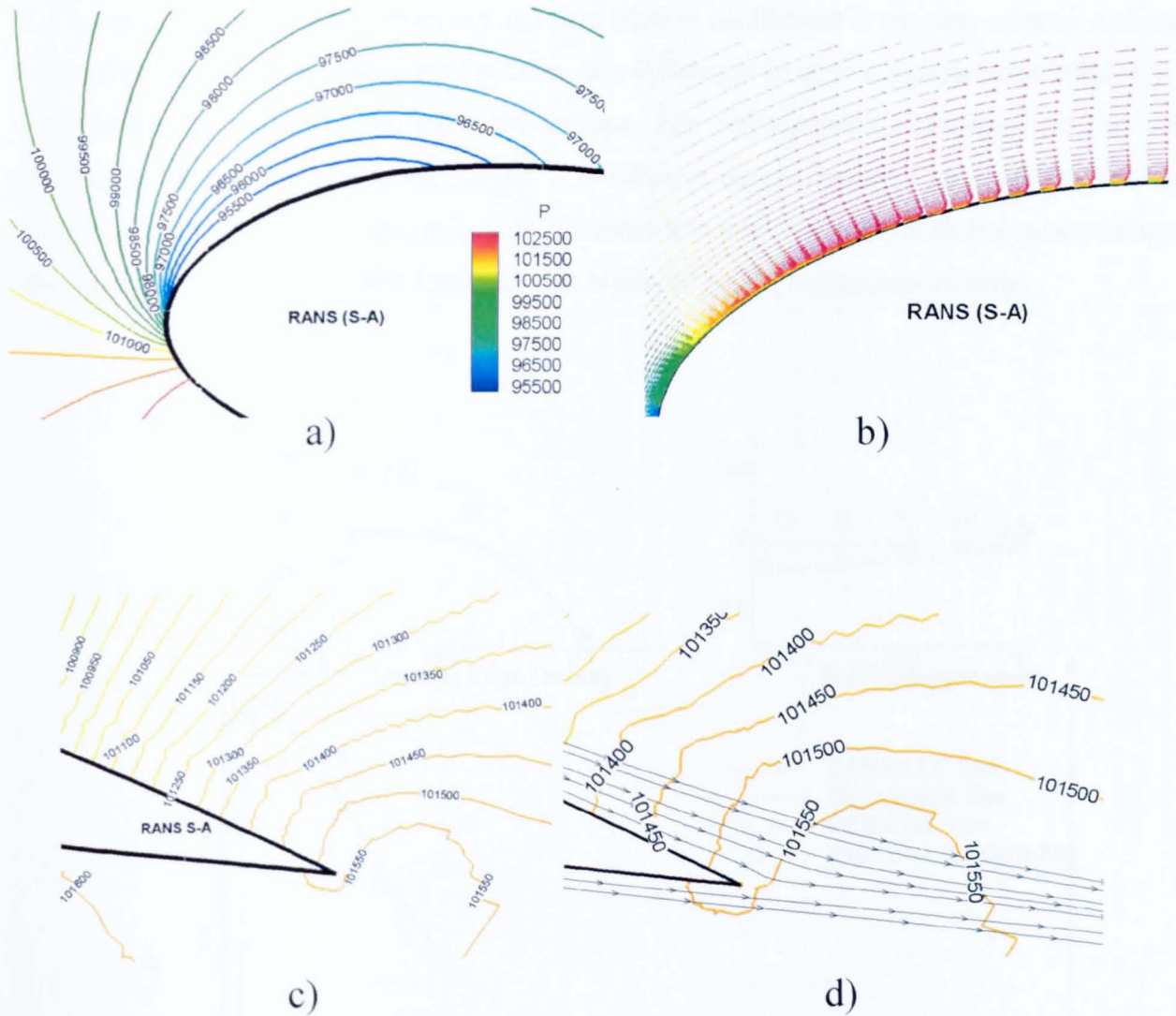


Figure 4.10 URANS computation of leading edge Line contours of pressure on leading and trailing edge a) Line contours of press at leading edge b) Vector plot colour by x-direction velocity at the suction side of leading edge c) Lind contours of pressure at trailing edge d) Zoom view of c) with streamlines

This simulation is carried out in turbulent flow mode without using any transition mechanism (trip functions etc) and is not expected to capture laminar transition on the suction side of the leading edge.

Inviscid flux computation schemes, AUSM and HLLC, within the framework of the DES were used to appreciate the role of the inviscid fluxes and ascertain the output from using Roe scheme with the DES methodology. The pressure and skin friction distribution of the DES scheme (using Roe, AUSM and HLLC flux calculation schemes), are shown in figures 4.11 and 4.12. The

difference between these schemes is barely noticeable. It is indicated from the figure that these simulations give consistent flowfield results. It is also evident that the influence of the inviscid flux computing scheme on the pressure and skin friction coefficient is not very critical. Although these schemes give very similar results, there is a difference in their computational efficiency in terms of the time taken to run these simulations. The computational efficiency, lift and drag coefficients are presented in the section 4.2.7. It indicates the performance of different turbulence modelling schemes used in this study with different inviscid flux computational methodologies. The main observation is that the dominant part is played by the turbulence scheme.

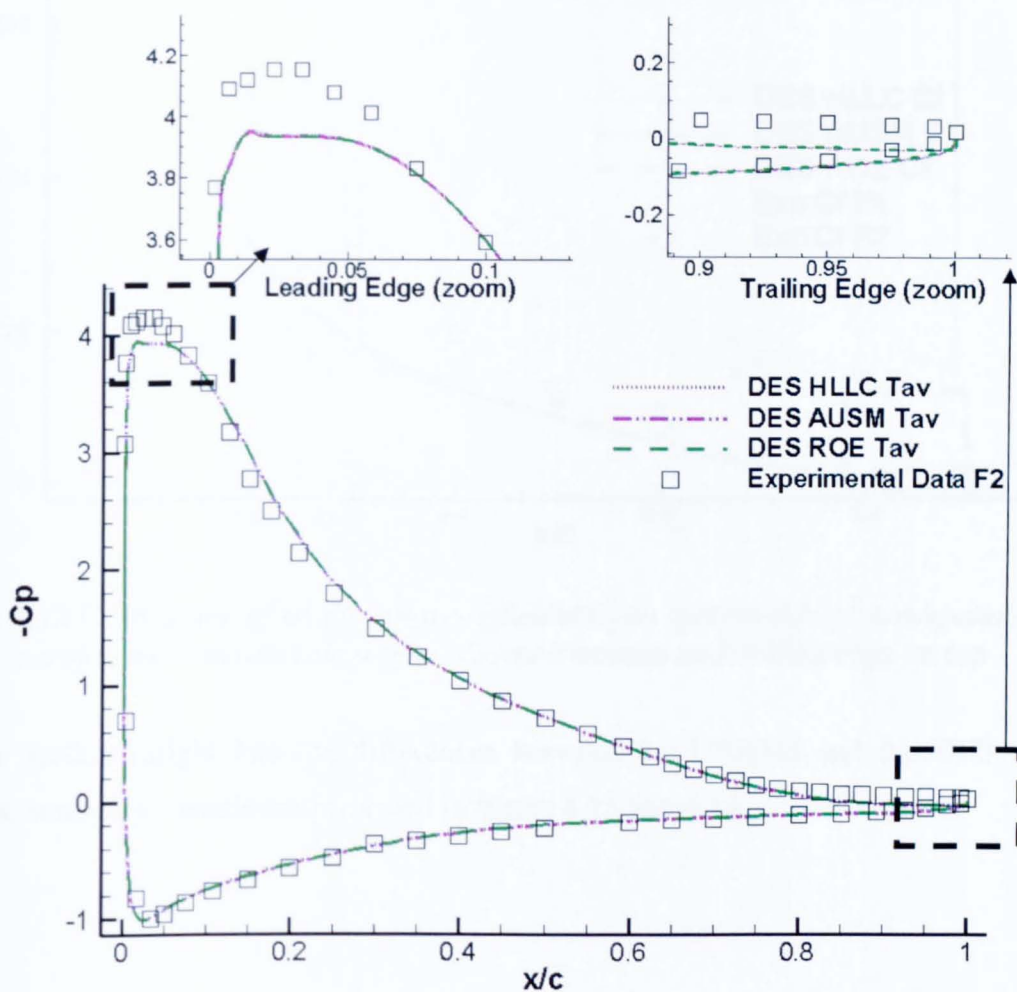


Figure 4.11 Comparison of computed time averaged (T_{av}) coefficient of lift (C_L) from the DES simulation using ROE, AUSM and HLLC inviscid flux computing schemes on Aerospatiale A-airfoil with experimental data F2

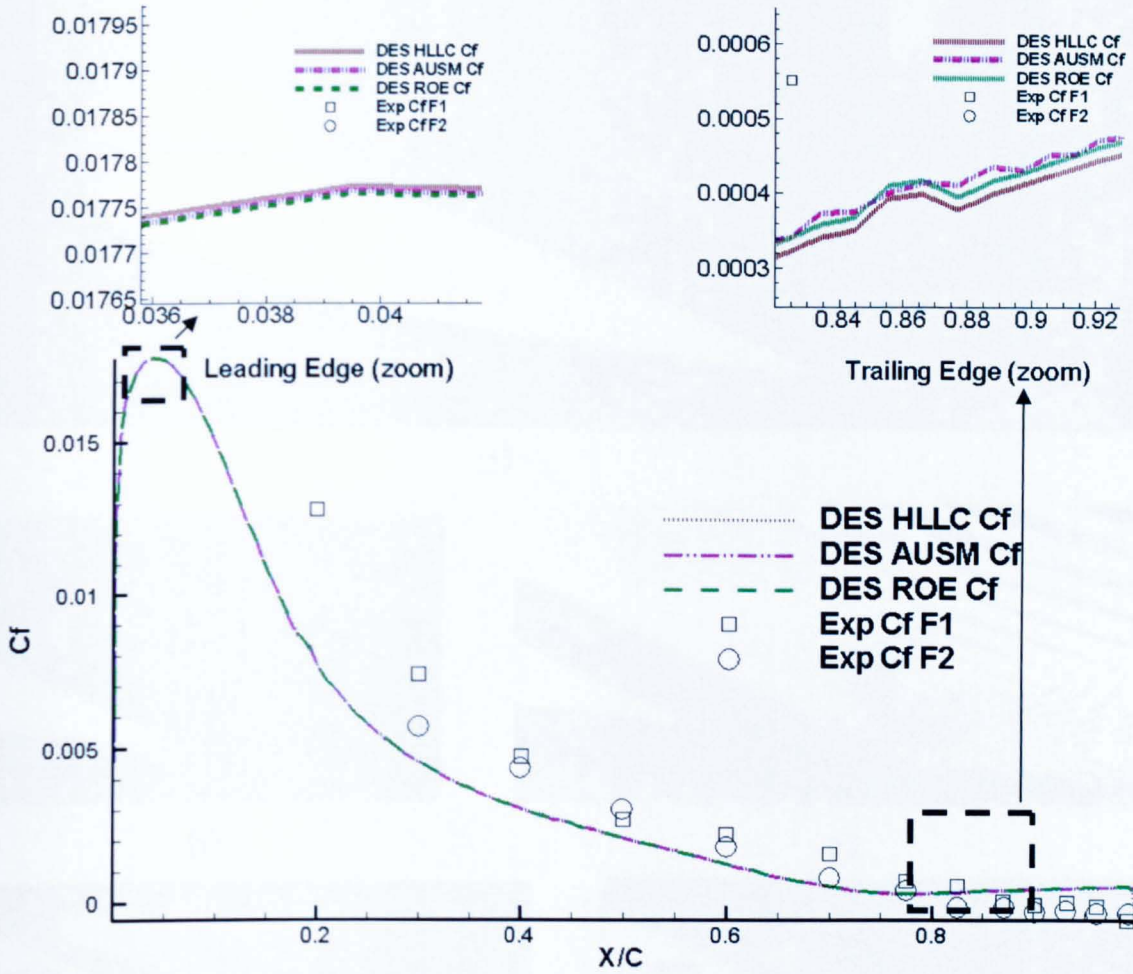
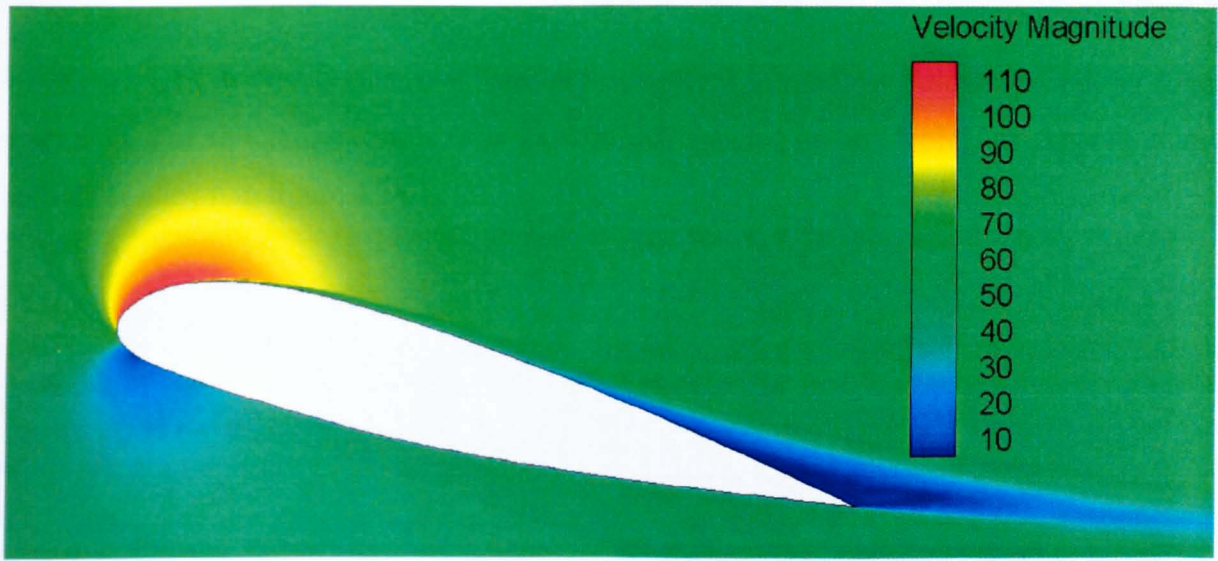
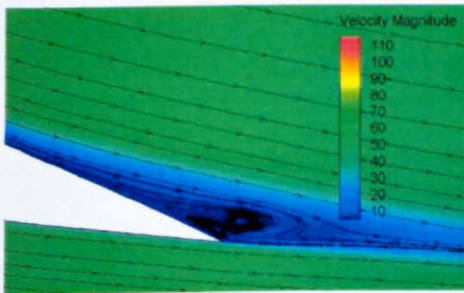


Figure 4.12 Comparison of skin friction coefficient C_f on suction side of Aerospatiale A-aerofoil with suction side profile. Zoomed leading and trailing edge on top

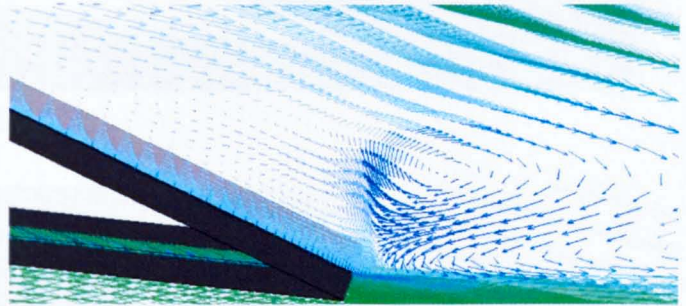
To obtain further insight into the differences between the URANS and the DES simulation flowfields, some flow details are presented in figure 4.13 and 4.14.



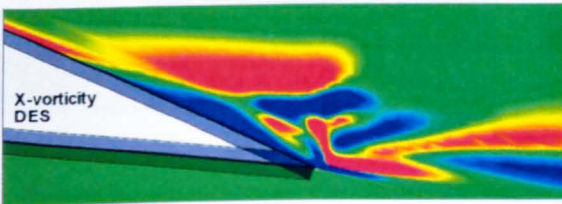
a)



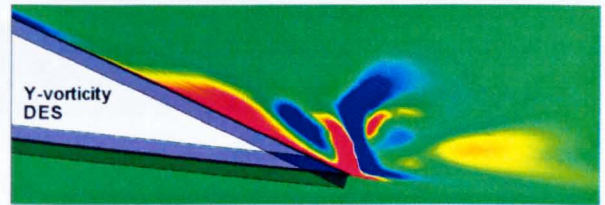
b)



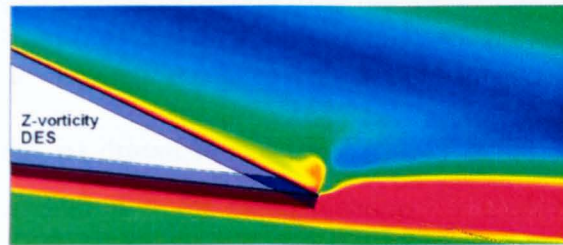
c)



d)



e)



f)

Figure 4.13 Time averaged flowfield details from the DES simulation a) Velocity magnitude contours b) Velocity magnitude contours with time mean streamlines at trailing edge c) Velocity vectors around trailing edge from mid-plane of 3D aerofoil d) x-vorticity e) y-vorticity f) z-vorticity plots

From figure 4.13 [b-f], it is clear that there is a separation in the flow field at the trailing edge of the aerofoil. The simulation results from the URANS scheme do not depict any separation in the flowfield as shown in figure 4.14.

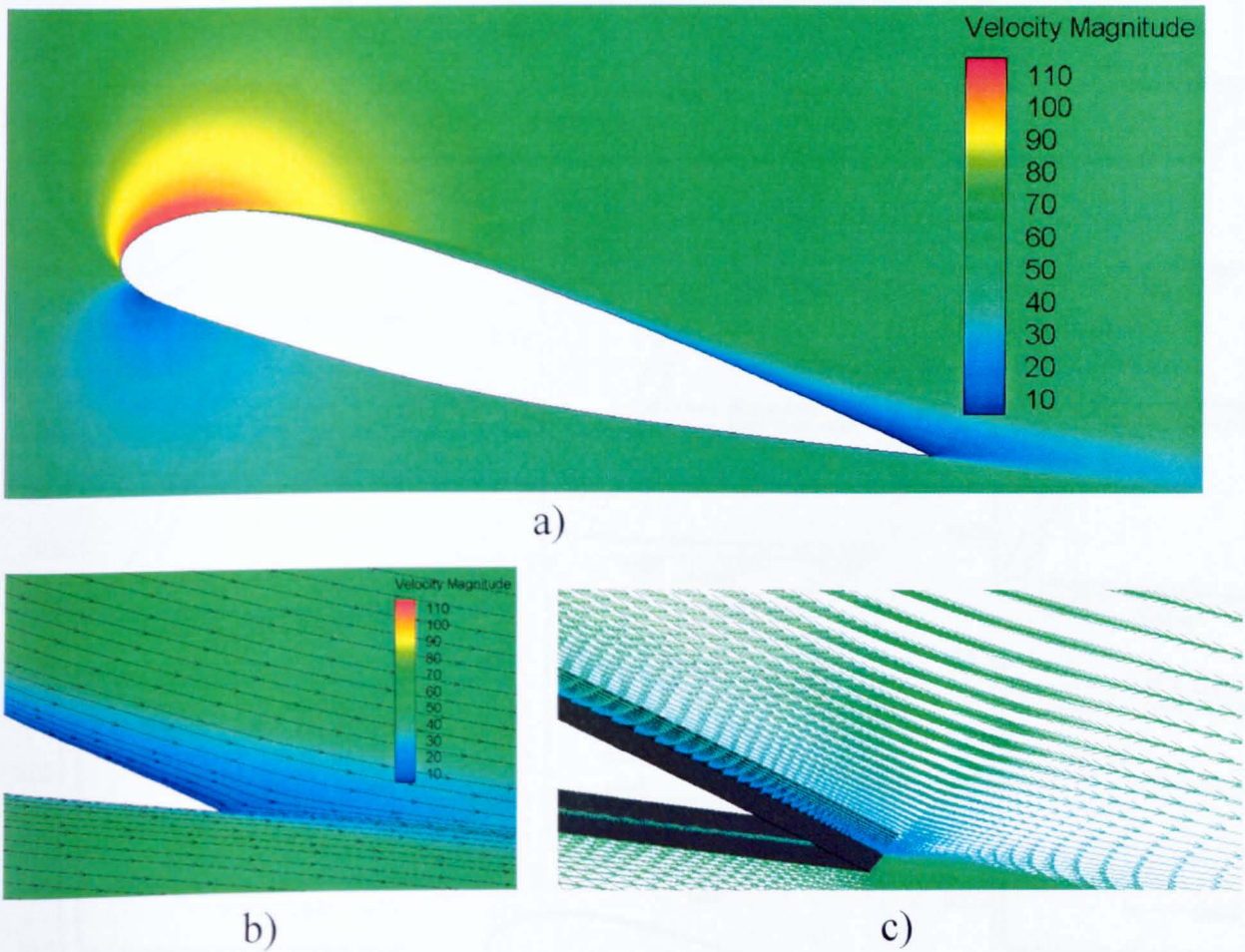


Figure 4.14 Time averaged Flowfield details from the RANS solution a) Velocity magnitude contours b) Velocity magnitude contours with the streamlines at trailing edge c) Velocity vectors around trailing edge from mid-plane of 3D aerofoil

The first conclusion that can be drawn is that the URANS is too dissipative and has failed to predict the trailing edge separation in the flow, whereas the DES has performed well and has produced better surface pressure distribution and skin friction coefficient, apart from capturing the trailing edge separation. For the leading edge, there is a dip in $-C_p$ at the suction side, in comparison with both the experimental data and the URANS, which needs to be explored. Ideally for the attached flow at the leading edge, the DES should produce similar results to the URANS simulation. The regions with maximum disparity between these two techniques are the leading and the trailing edge of the aerofoil.

The experimental data for turbulence stresses is available after the transition region ($x/c > 30\%$ of chord). To make comparison of the DES with the URANS simulation on the leading edge of the suction side, 3 probe lines are created as shown in figure 4.15.

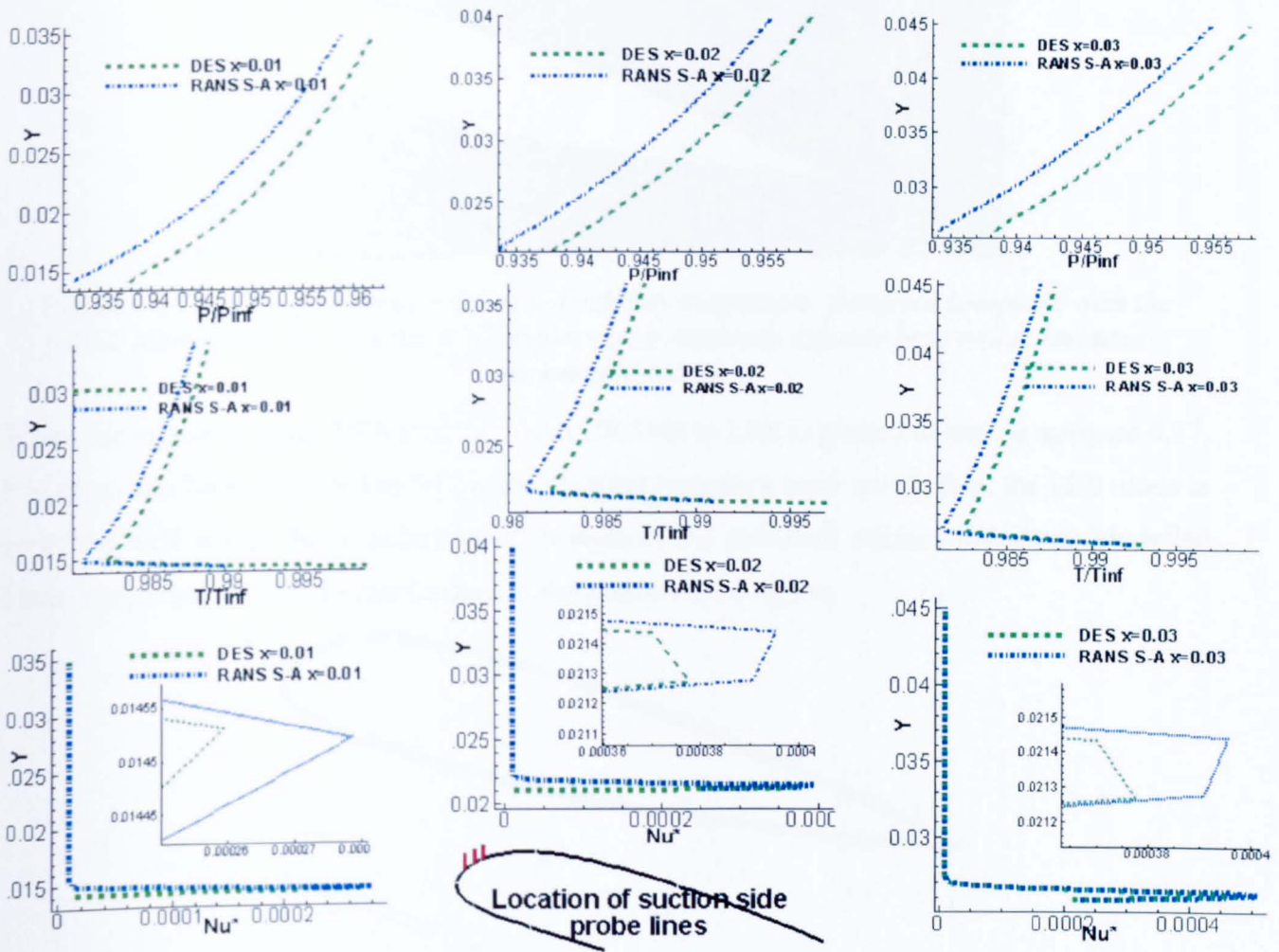


Figure 4.15 Comparison of the computed parameters from the RANS and the DES on leading edge suction side at $x=0.01$ (first column), $x=0.02$ (middle column) and $x=0.03$ (third column). Leading edge is $x=0$ and trailing edge $x=0.6$. Top row: P/P_{inf} , Middle row: T/T_{inf} , bottom row: Nu^* (working parameter of S-A model)

It is obvious that the leading edge modelled stresses are lower in the DES results than in the URANS. The prediction of pressure by the DES is higher than the URANS as well.

For DES calculations to qualify, the fundamental rule is that the entire boundary layer should be treated in URANS. If this condition is met, then the DES scheme is clearly producing better results than the URANS scheme. Another observation from the experiments is regarding the growth of the boundary layer in the downstream direction, at the trailing edge on the suction

side, as presented in figure 4.16. This data is available only after the experimental transition (>30% of the chord).

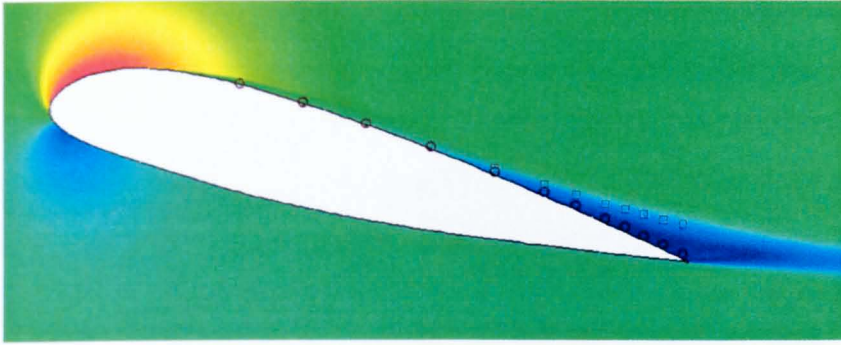


Figure 4.16 *Contours of the time averaged velocity magnitude- flowfield computed with the DES plotted with the experimental displacement thickness (square box) and momentum thickness (circles)*

When the region in which DES switches from URANS to LES is plotted as shown in figure 4.17, it is clear that DES has failed to follow the growing boundary layer and in fact, the LES mode is switched well within the boundary layer. It reduces the turbulent stresses known as Modelled Stress Depletion (MSD), further leading to separation in the region.

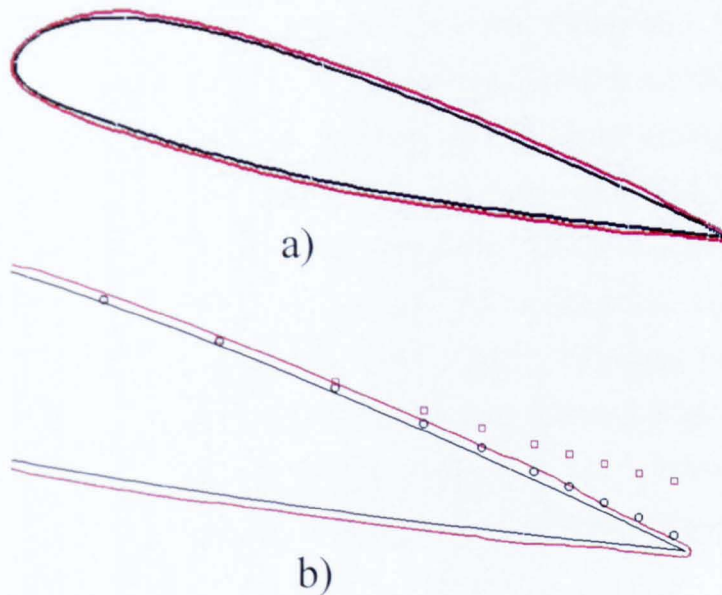


Figure 4.17 *LES-RANS switching region computed with the DES plotted with experimental displacement thickness (square box) and momentum thickness (circles)*

Also, the region near the leading edge is very thin. The reason for the relatively low $-C_p$ at the leading edge can be due to earlier switching to LES mode in this region in comparison with the complete URANS. At the trailing edge on the suction side, it is the worst affected region due to

the growth in the boundary layer or region in which the LES mode is switched on prematurely. It consequently induces a separation in the flow, as shown in figure 4.8.

It can be argued that a similar phenomenon maybe the reason for the query raised for Ref. [91] as described in point 2 at the start of this chapter. It is possible that in a similar way to this study, no negative C_f values were obtained on the suction side in Ref. [91]. The main disparity of the C_f values between the URANS and the DES at the trailing edge on the suction side is observed in the regions where the boundary layer is gradually growing. An initial decrease and then rise in the C_f values can be argued to be the consequence of a gradual increase in the region in which the wrong switching to the LES mode is being carried out, reducing the turbulent shear stress in a larger area. It leads to a stage where the separation is generated in the flow above the attached turbulent boundary layer. With the presence of a separation region, on top of the attached turbulent boundary layer, the skin friction increases again.

4.2.6 DDES simulation results

For an attached boundary layer flows, the DES may not out-perform the URANS scheme. In fact, the best expected solution for such cases in the boundary layer regions is based on the performance of the underlying URANS. With this flowfield information, the DDES is applied to compare its results. In order to perform correctly, it should delay the switching in response to the boundary layer growth. It means that the turbulent stresses in the leading edge and the trailing edge region of the suction side will be higher and closer to the URANS than the DES. It is important to know the limitations of the DES and DDES for different types of flows.

The cases where the flow quickly develops the unsteadiness such as flow separations from a blunt body or sharp edges are termed as the natural DES cases. For such cases, the DES and DDES simulations are expected to give similar results different from URANS. However, for thick boundary layer flows or the cases where the mesh is excessively refined within the boundary layer (such as at the leading and trailing edges of an aerofoil), the DES solution will be different from DDES.

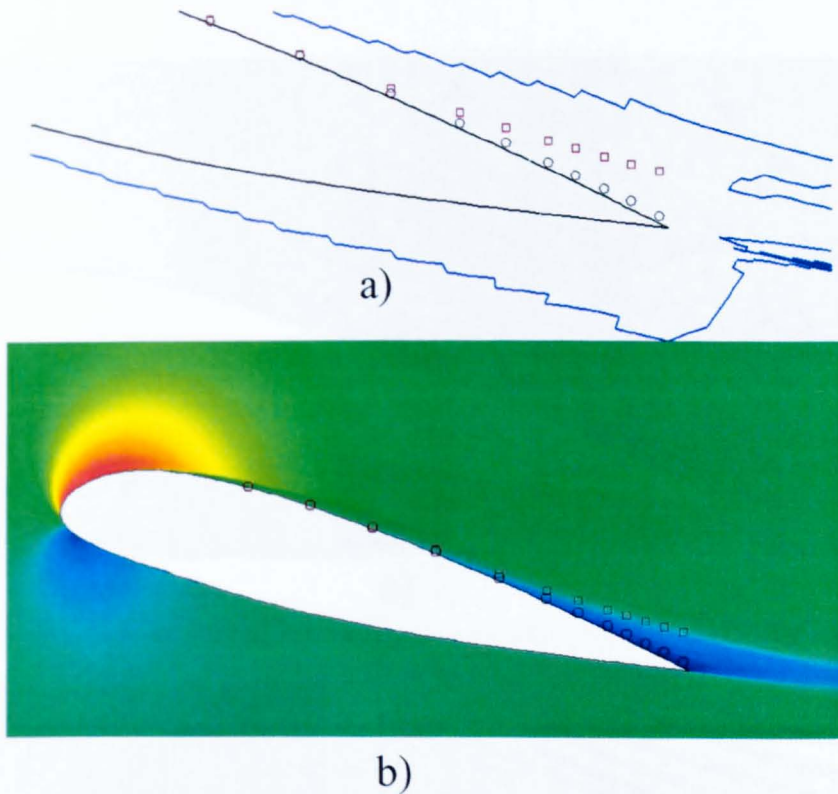


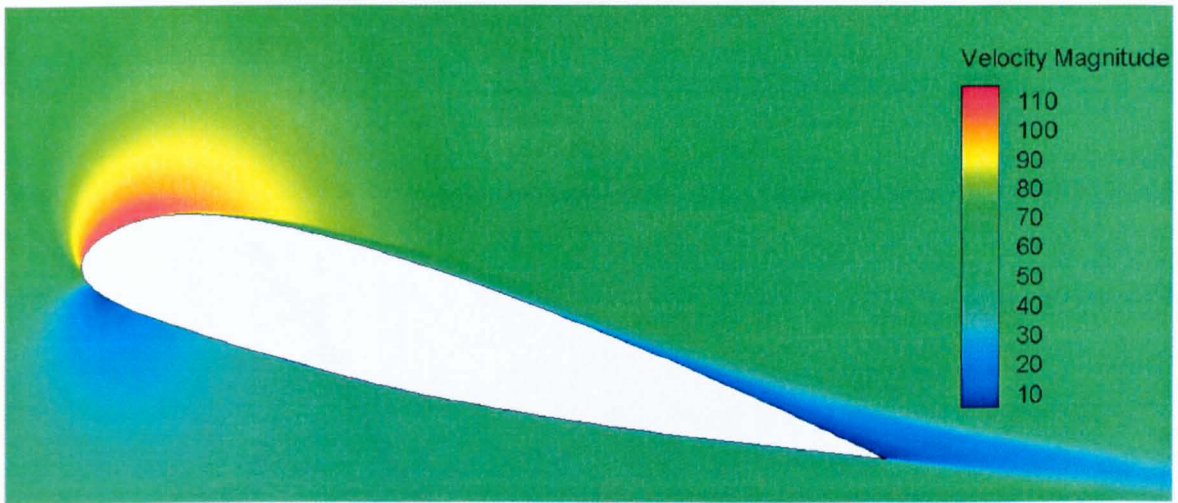
Figure 4.18 Time averaged DDES solution

a) RANS-LES region boundary around the aerofoil at the trailing edge side

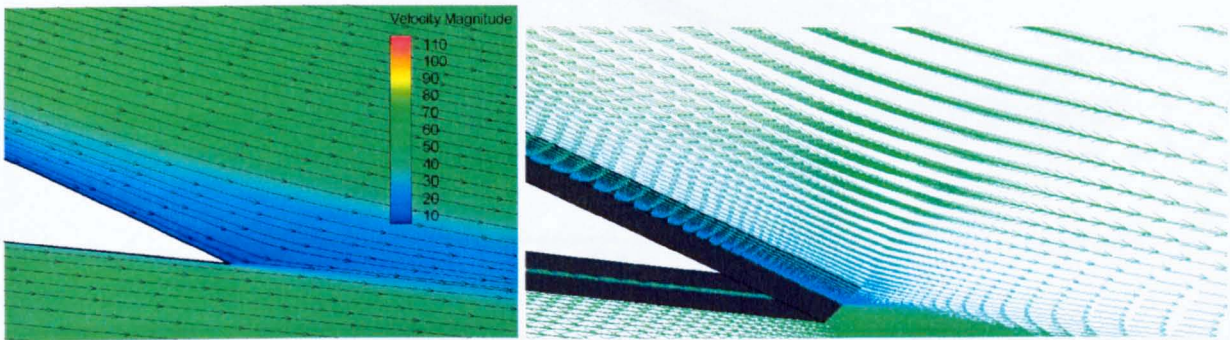
b) Velocity magnitude contours plotted with experimental displacement thickness (square box) and momentum thickness (circles)

Results from the DDES simulation are presented in figure 4.18 (a-b). The RANS-LES switching zone is presented in Figure 4.18a). In contrast with the quite thin RANS region as presented in figure 4.17, it is apparent that the DDES has actually performed well to delay the switching. It has included the boundary layer within the URANS mode region as required. It confirms that the scheme is working properly with switching in the intended regions. Now, it will be interesting to analyse the flow field to observe that the flow develops the trailing edge separation or not and how turbulent stresses compare with the original DES and the URANS. The C_f and C_p values at the leading edge on the suction side will be of interest as well. All these parameters will indicate the response of URANS, DES and DDES for the same flow.

Figure 4.19 (b-c) indicates that there is no separation in the trailing edge region on the suction side and the flowfield resembles quite well with the URANS flowfield as shown in figure 4.14.



a)



b)

c)

Figure 4.19 *Flowfield details from the time averaged DDES solution*
a) Velocity magnitude contours
b) Velocity magnitude contours with streamlines at trailing edge
c) Velocity vectors around trailing edge from mid-plane of 3D aerofoil

Although, this resulting steady flowfield is achieved from the intended switching in the solver, it does not necessarily indicate the better solution. The experimental observation of the separation in the flow at the trailing edge of the A-airfoil in the thick turbulent boundary layer region is not obtained. It also indicates that the dissipation levels in this region may have become excessive due to this delayed switching causing the flowfield to become steady.

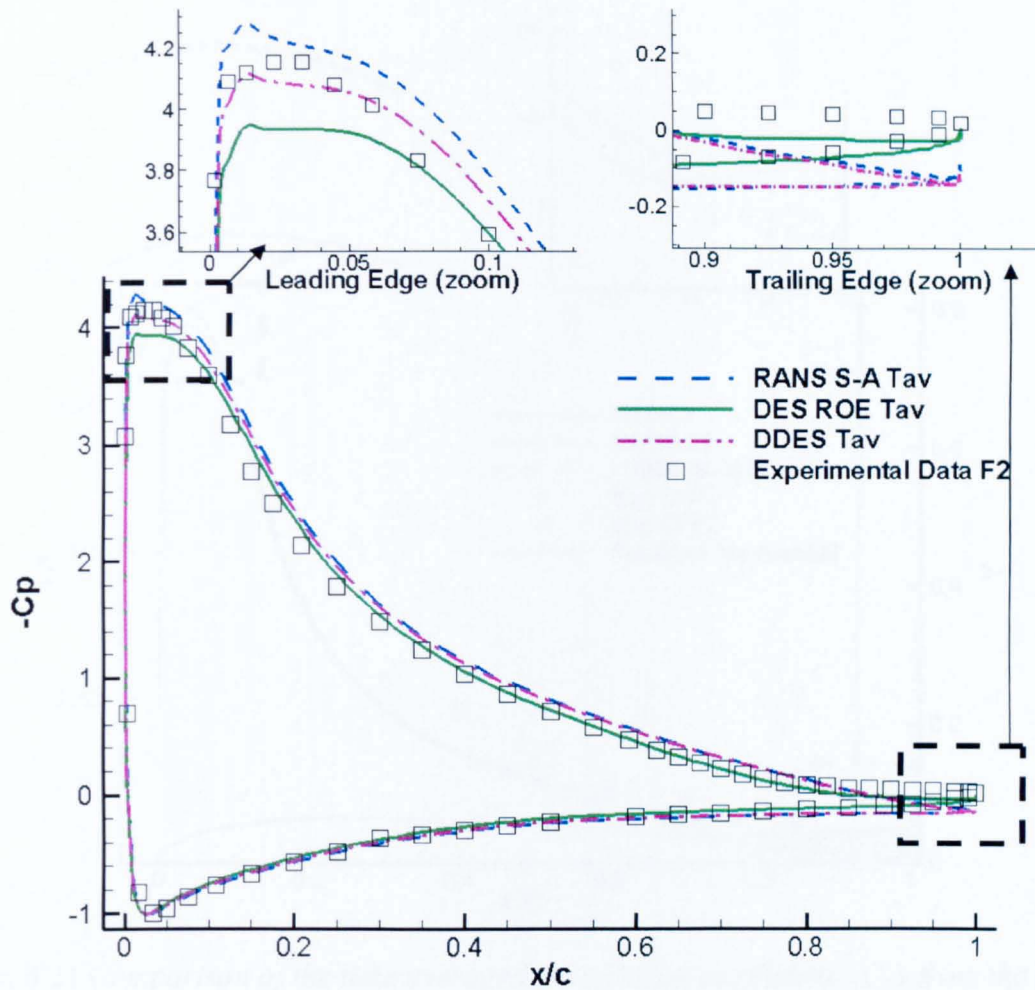


Figure 4.20 Comparison of the computed time averaged (Tav) coefficient of lift (C_L) from the RANS, DES and DDES on Aerospatiale A-airfoil with experimental data F2

$-C_p$ plot, in Fig 4.20 (zoomed view of leading edge), indicates that the initial dip in the DES and overshoot of the URANS results are balanced by the DDES simulation results. It means that the early switching of the DES in the leading edge section was the main cause of the lower $-C_p$ value. It is further augmented by the figure 4.21, which indicates that the skin friction has increased now to a similar level to those of the URANS results. Further downstream, due to the presence of the thick boundary layer, the DDES solution closely follows the URANS solution, in contrast with the DES. It is logical because the solution of the DDES in attached boundary layers is to be similar to URANS.

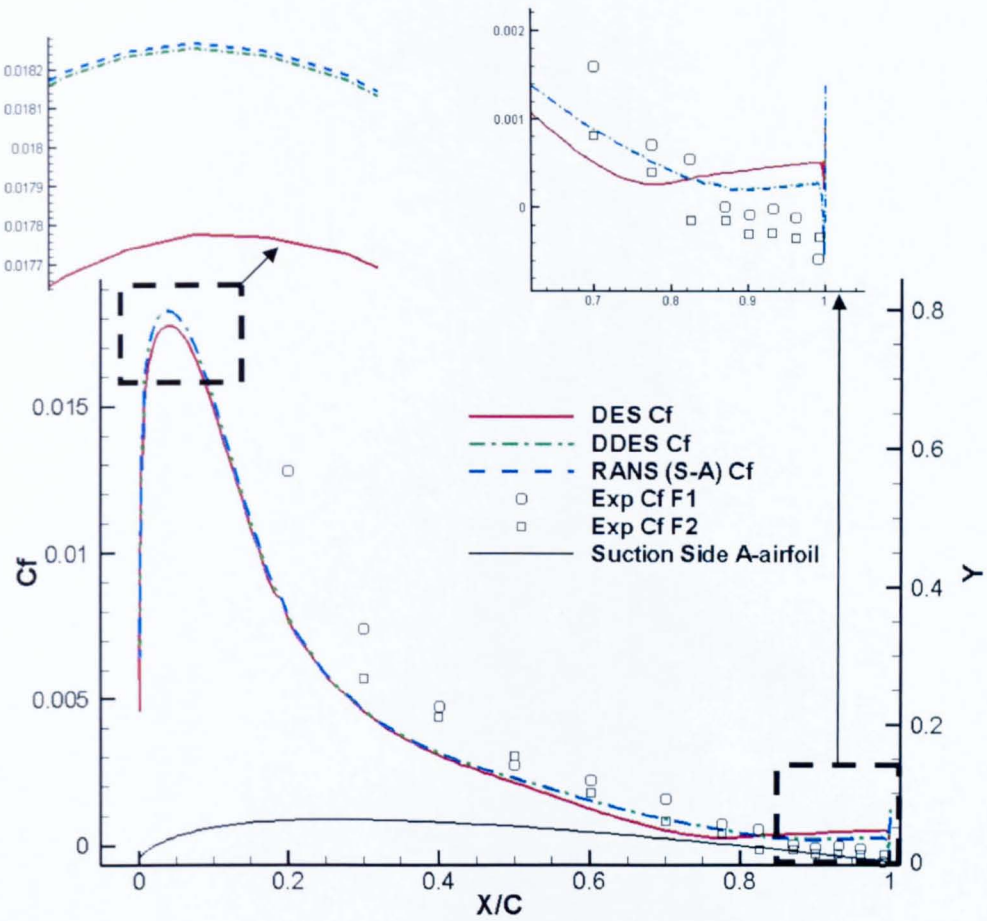


Figure 4.21 Comparison of the time averaged skin friction coefficient (C_f) from the RANS, DES and DDES simulations on suction side of Aerospatiale A-airfoil with suction side profile. Zoomed leading and trailing edge on top

A comparison of switching zones from the URANS to LES is shown in Figure 4.15, to appreciate the disparity of switching regions in the DES and DDES. It is clear that the DES is switching prematurely at the leading edge as well as at the trailing edge.

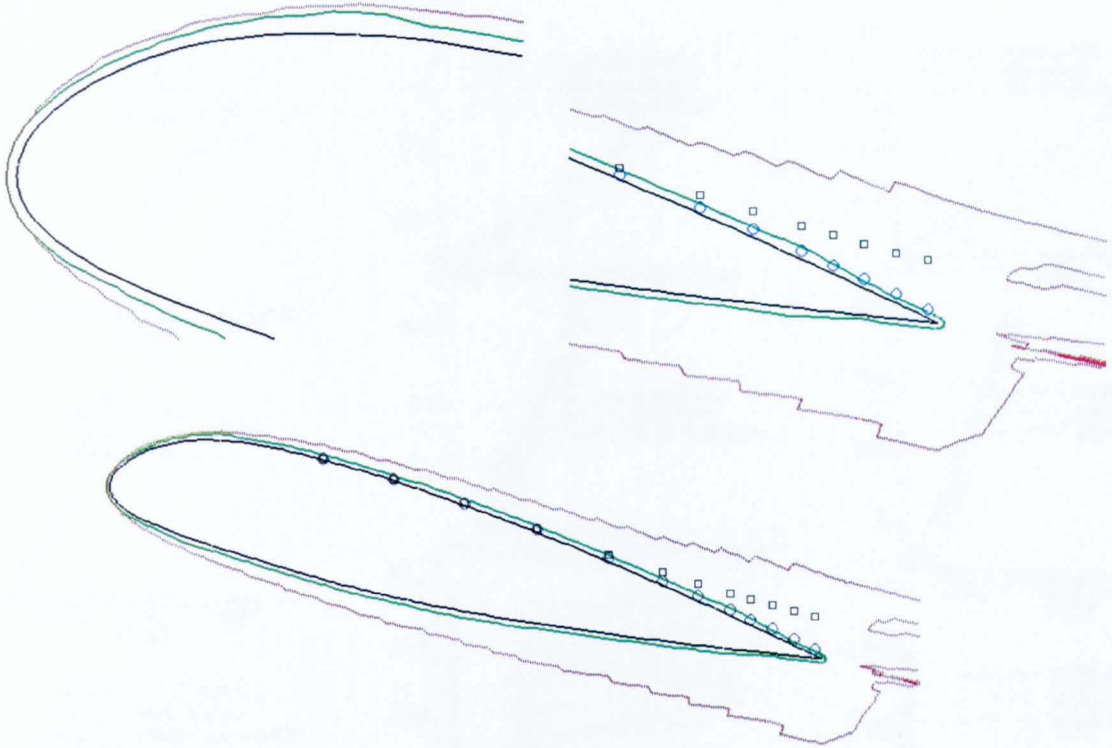


Figure 4.22 *Bottom: Comparison of the RANS to LES switching zones for the DES (inner side shown in green colour) and the DDES (outer side red colour), plotted with experimental displacement thickness (square box) and momentum thickness (circles). Top: Zoomed view at leading and trailing edge*

In order to verify the argument presented above that early switching to LES was the main reason for the dip in C_p plot at the leading edge of the suction side, the probes presented in figure 4.15 are revisited with DES. Figure 4.23 show the different parameters of DDES in comparison with DES and URANS. It can be seen that with the delayed switching, the modelled turbulent stresses have increased and pressure has decreased as well. The small difference between URANS and DDES is due to the delayed switching to LES which reduces the relative turbulence stresses by slightly increasing the static pressure.

The difference of viscosity and pressure values between the URANS and DDES solutions indicates that the effect of LES region is present in the solution despite the delayed switching. However, due to DDES operating in predominantly RANS mode, the flow variables are more close to the URANS solution. It is particularly evident from the C_p plot of over the leading edge of the A-airfoil as shown in figure 4.23.

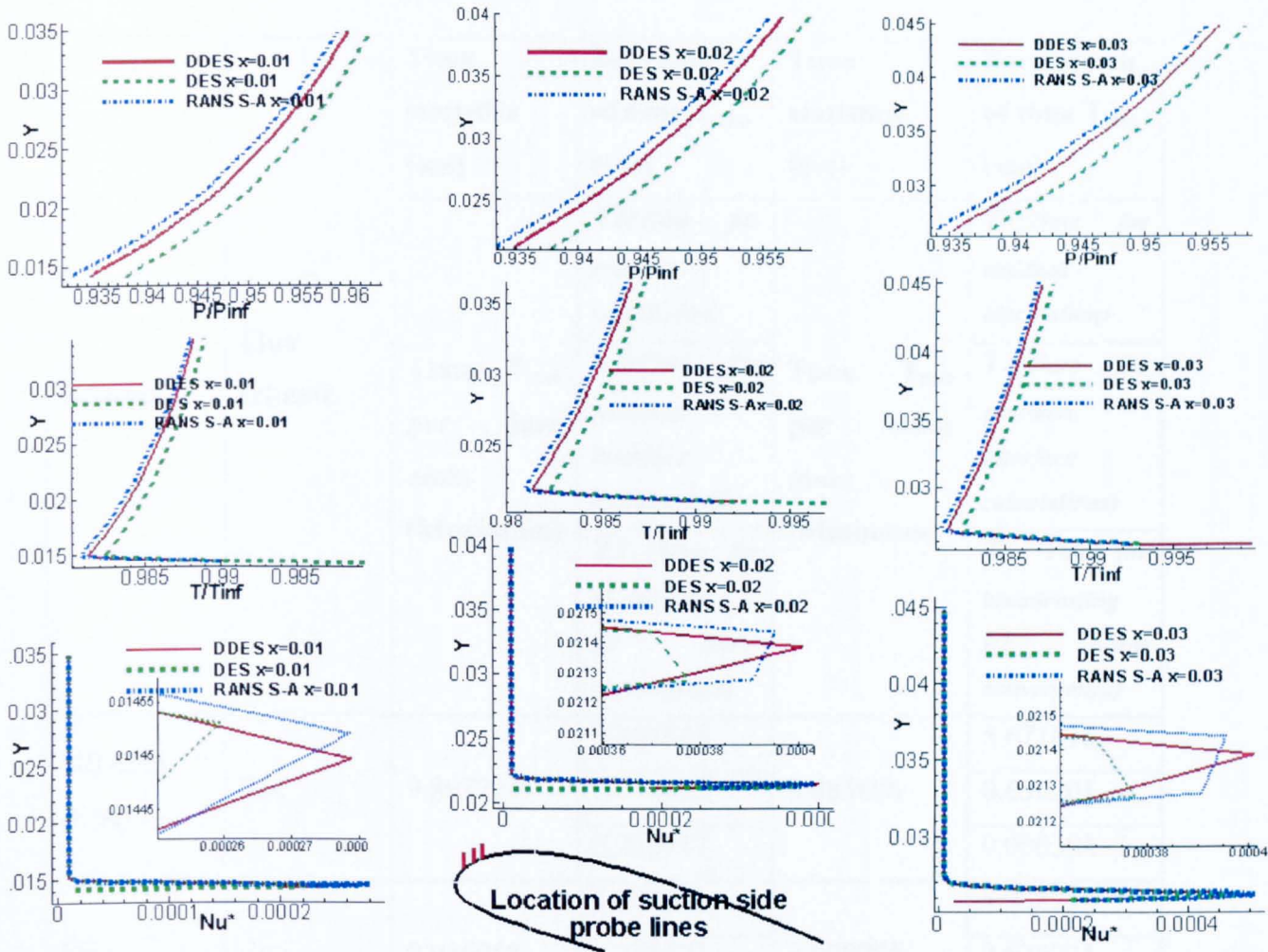


Figure 4.23 Comparison of the time averaged computed parameters from the RANS, DES and DDES on leading edge suction side at $x=0.01$ (first column), $x=0.02$ (middle column) and $x=0.03$ (third column). Leading edge is $x=0$ and trailing edge $x=0.6$. First row. Top row: P/P_{inf} , Middle row: T/T_{inf} , bottom row: Nu^* (working parameter of S-A model)

4.2.7 Time statistics of all the schemes used

Table 2 presents the time efficiency of all the schemes used in this study. This time is taken in marching one physical time step with 9 pseudo time iterations (each running 4 stage RK time stepping). AUSM is the best in time efficiency. The HLLC scheme takes more time than the Roe and the AUSM scheme. The URANS scheme takes the least time in the other Roe scheme based solutions.

Scheme	Flux scheme	Time statistics (sec)	Breakdown of time T_{max} (sec)	Time statistics (sec)	Breakdown of time T_{min} (sec)
		Time T_{max} per slave node (Maximum)	$T1$ (Time for residual calculation)	Time T_{min} per slave node (Minimum)	$T1$ (Time for residual calculation)
			$T2$ (Time for partition interface calculations)		$T2$ (Time for partition interface calculations)
			$T3$ (Time for broadcasting $L2$ norm convergence)		$T3$ (Time for broadcasting $L2$ norm convergence)
URANS (S-A)	Roe	9.897731	5.861843	9.883698	5.671815
			0.743952		0.650201
			0.235147		0.000384
DES	Roe	9.936058	5.902572	9.908985	5.738299
			0.735422		0.626721
			0.181668		0.000391
DES	AUSM	9.704097	5.652356	9.678132	5.498081
			0.740824		0.628393
			0.156002		0.000369
DES	HLLC	10.035570	5.987162	10.008942	5.828793
			0.734553		0.634423
			0.161318		0.000388
DDES	Roe	12.567045	5.947911	12.552626	5.799741
			0.748766		0.631347
			0.154455		0.000389

Table 4.2 *Time efficiency of the different simulations with 120 processors*

The extra time taken by the DDES simulation is due to the calculation of the wall distance parameter. This parameter is to be calculated during each iteration in the DDES simulation (as it

includes molecular and turbulent viscosity changing at each time step). The DES scheme, in contrast, requires this parameter to be computed once only (and is a function of mesh and geometry only).

4.2.8 Convergence of the simulations

L2-norm convergence criterion was used for density and turbulence viscosity. All the simulations were converged to at least 6th order for density and 3rd order to turbulence viscosity residuals.

4.2.9 Comparison of the lift and drag coefficients

Table 4.3 compares the lift and drag coefficient over the Aerospatiale A-airfoil from the present simulations and experimental data.

Data Type	Flux calculation Scheme	Turbulence Scheme	Angle of attack $\alpha=13.3^\circ$	
			C_l	C_d
Experiment F2	xxxx	xxxx	1.515	0.0308
Experiment F1	xxxx	xxxx	1.560	0.0204
DG-DES	Roe	URANS (S-A)	1.4812	0.03269
DG-DES	Roe	DES	1.4525	0.02565
DG-DES	AUSM	DES	1.4534	0.02539
DG-DES	HLLC	DES	1.4524	0.02562
DG-DES	Roe	DDES	1.5656	0.03155

Table 4.3 Comparison of Lift and Drag coefficients on the Aerospatiale A-airfoil

4.2.10 Observation regarding the RANS-LES region in the DDES

One observation in this study is on the RANS and LES regions of both the DES and DDES after switching. Switching in the DES is based purely on mesh and geometric parameters which provides normally the shape of the RANS-LES region in the more regular fashion as shown in the figure 4.24 a). However, with the modification in the switching mechanism, it includes turbulent and molecular viscosity as well. Due to this, although the MSD problem is sorted but the zones understandably are not very well defined (see figure 4.24 c). It, especially for the attached boundary with shear layer in the wake may produce more distorted RANS/LES regions

in the flowfield. For low order upwind solvers, this may not be a problem due to high inherent dissipation, but for high order less dissipative schemes, there may be some problems. However, this observation is totally based on the visual appearance of the region.

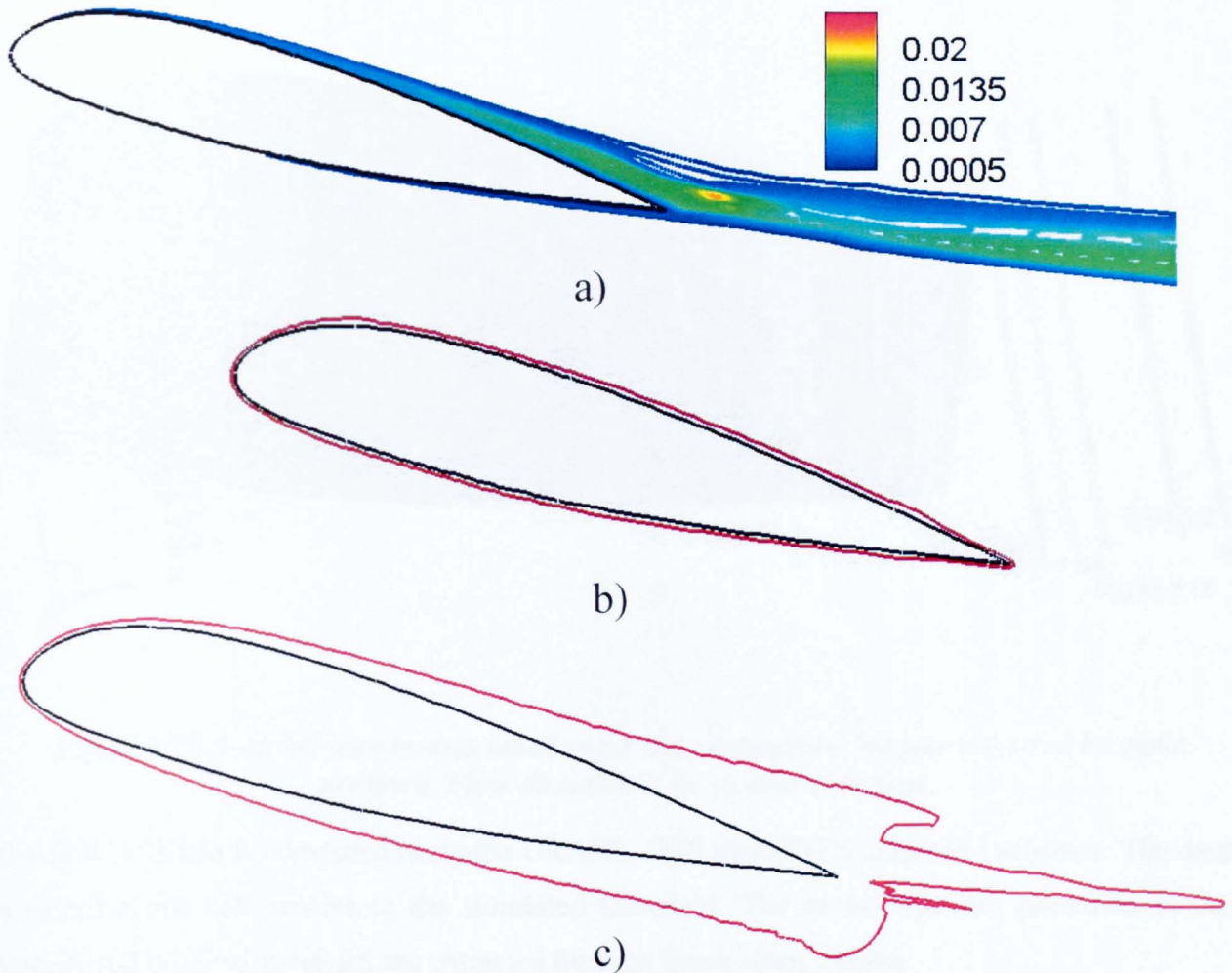


Figure 4.24 a) DDES flow field – contours of the turbulent viscosity parameter Nu^* (working parameter of S-A equation) b) RANS to LES switching zone of the DES scheme c) RANS to LES switching zone of the DDES scheme

4.3 Comparison of the Turbulent Reynolds Stresses using the RANS, DES and DDES with the experimental data

4.3.1.1 Suction side of the A-airfoil

The probe lines at different locations on the surface of the A-airfoil and in the wake region are described in figure 4.25. The field variables data is extracted along the length of these lines.

Probe lines are either normal to the aerofoil surface or normal to the free-stream flow direction as shown.

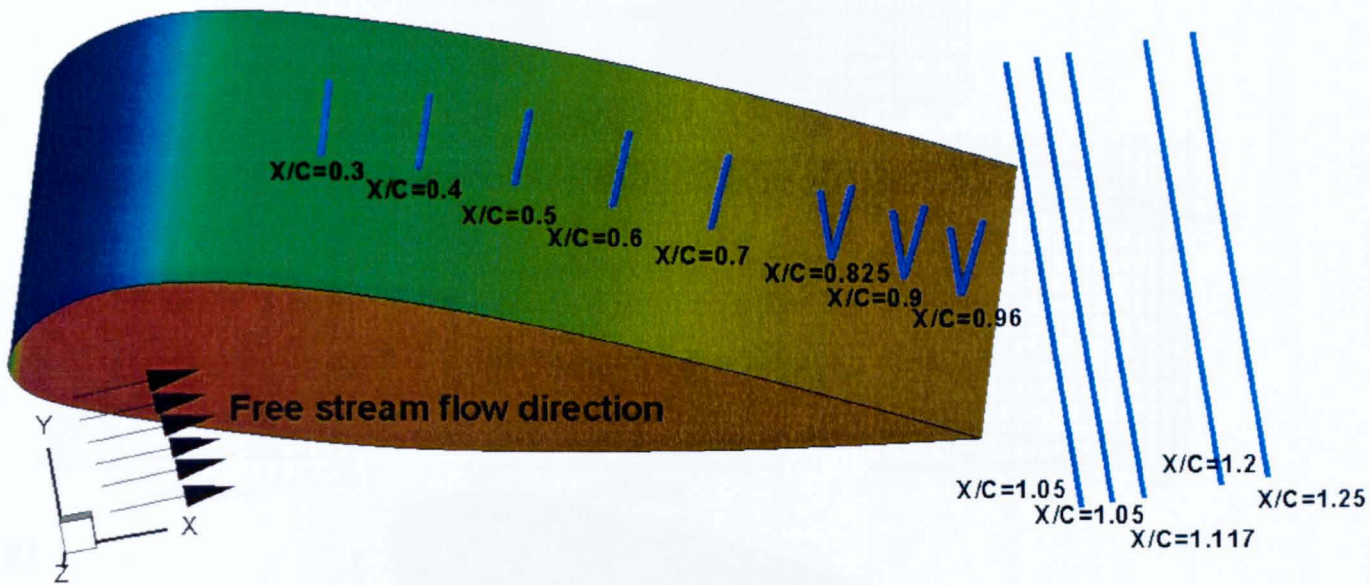
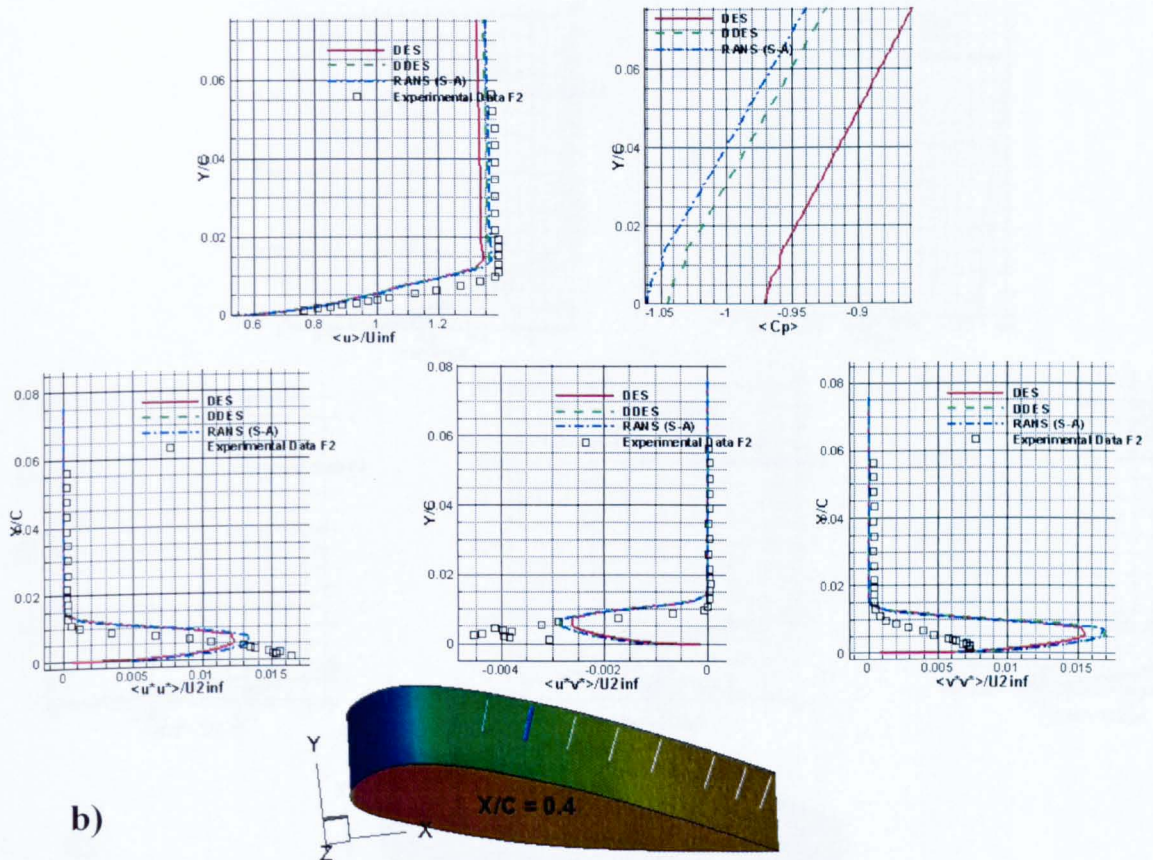
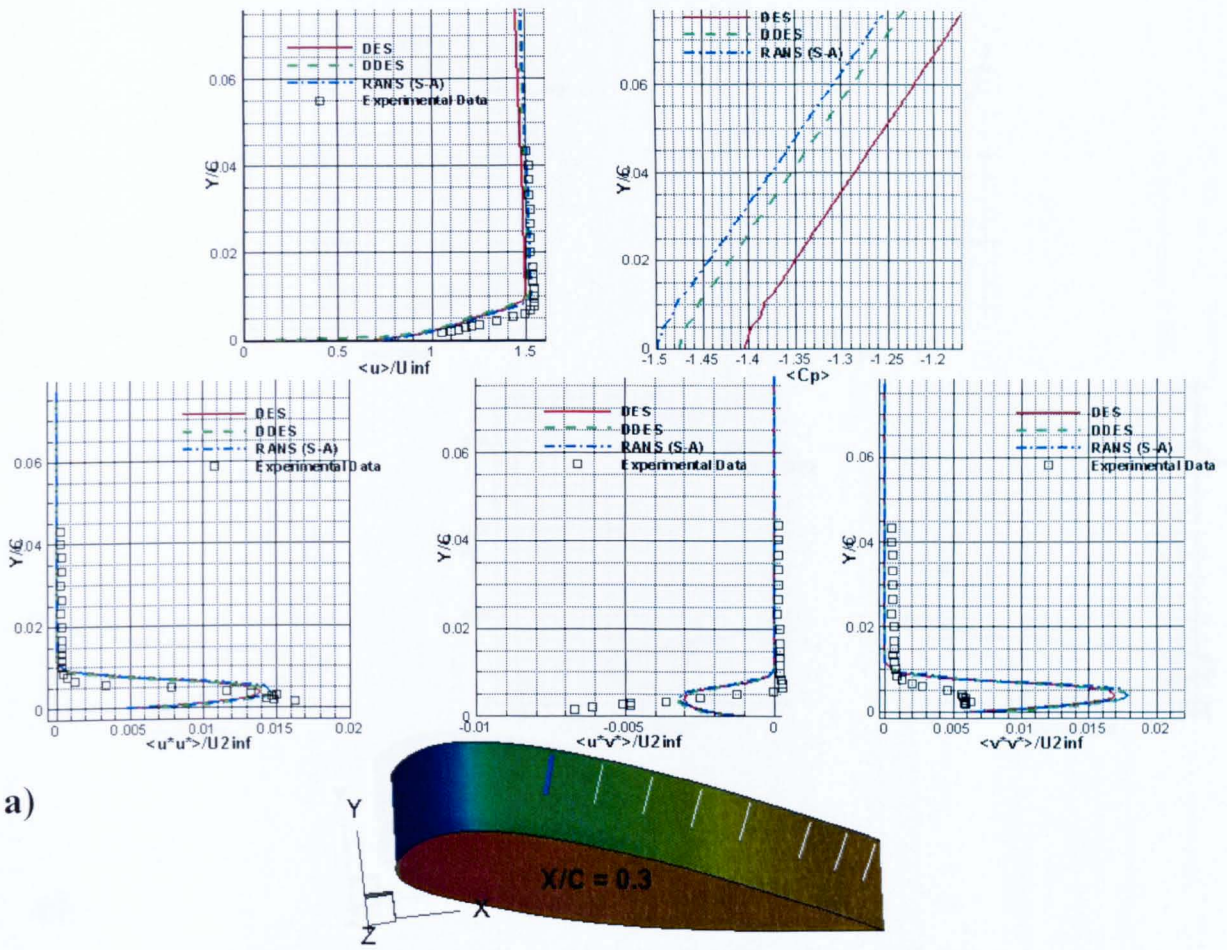
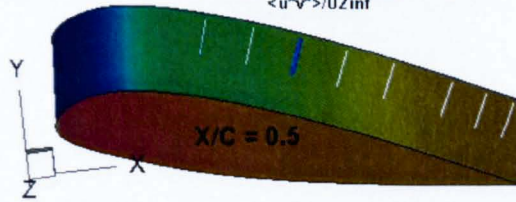
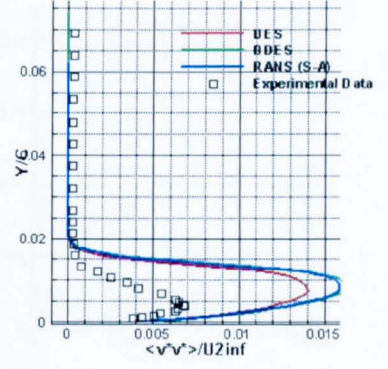
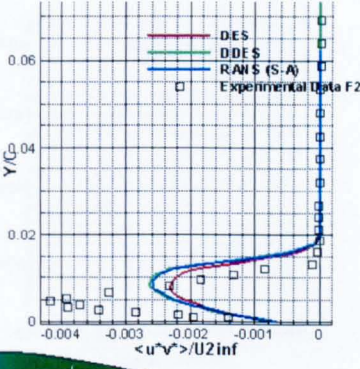
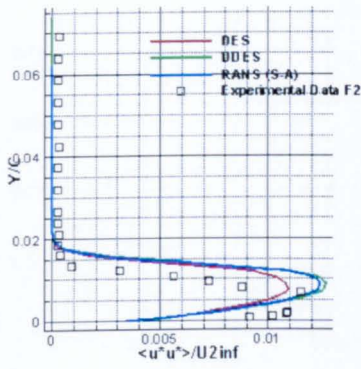
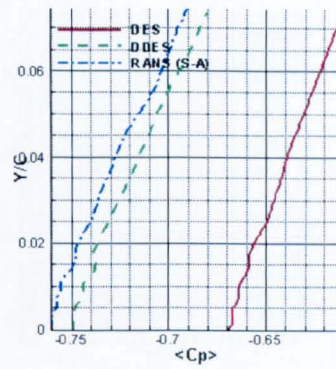
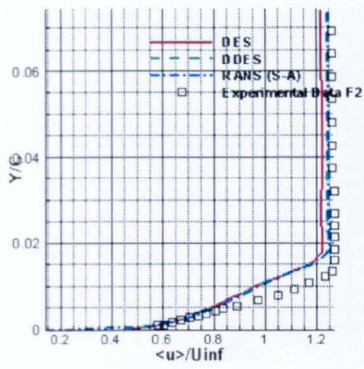


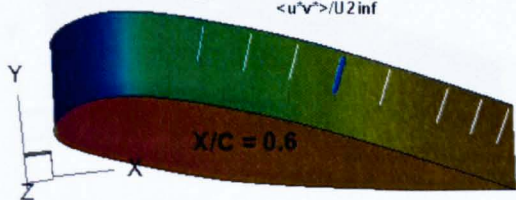
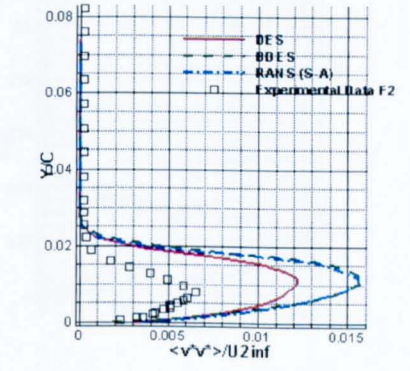
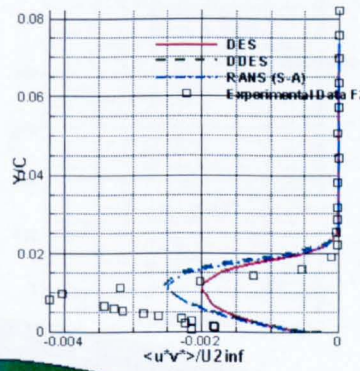
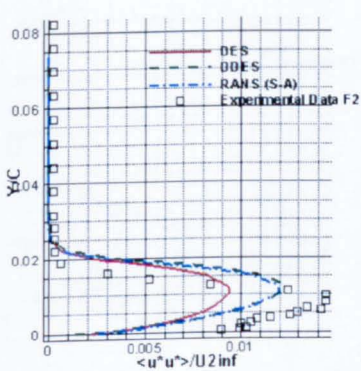
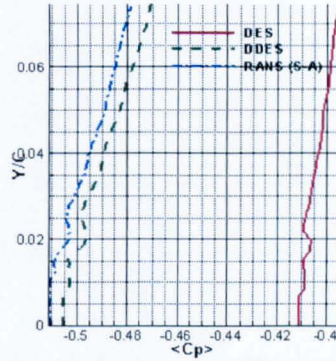
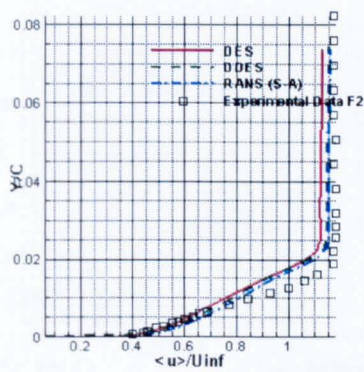
Figure 4.25 A-airfoil with probes location for data extraction. Surface coloured by static pressure. Flow direction is in +x-axis direction

The flowfield data is computed using the URANS, DES and DDES numerical schemes. The data is stored at the cell centers in the simulated flowfield. The probe lines are generated in the domain and the field variables are extracted through linear interpolation.

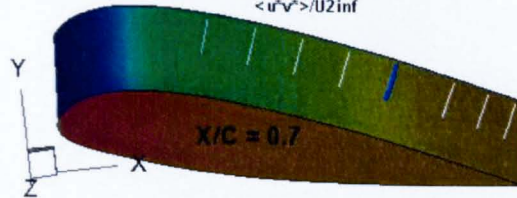
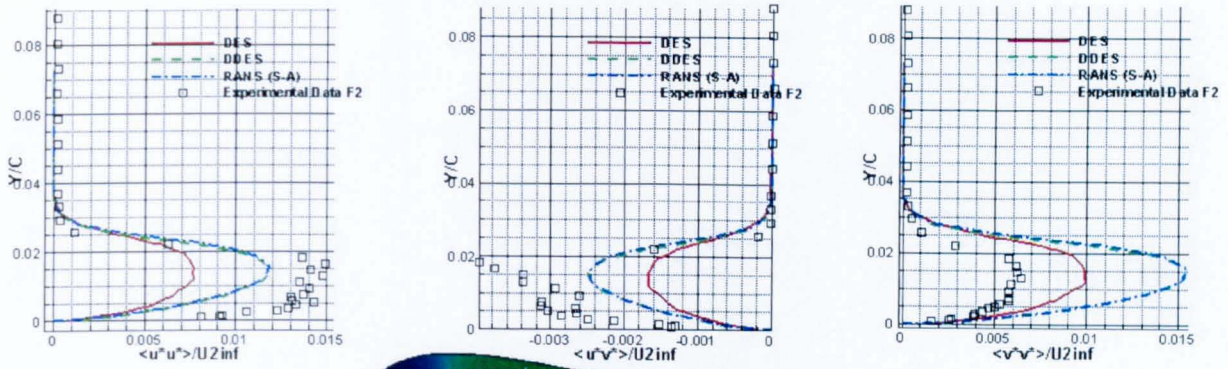
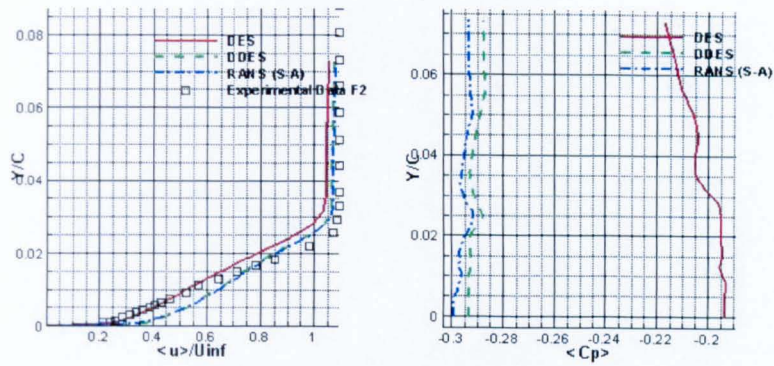




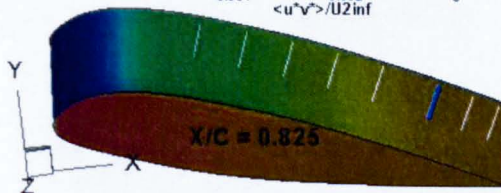
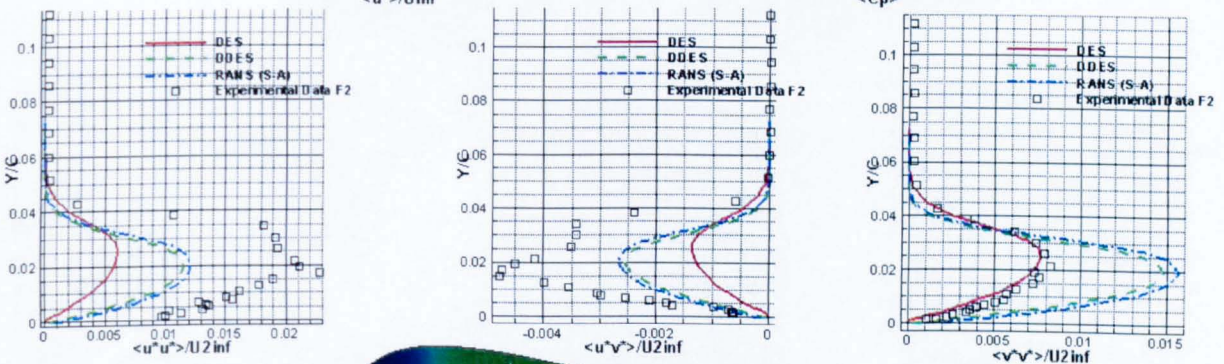
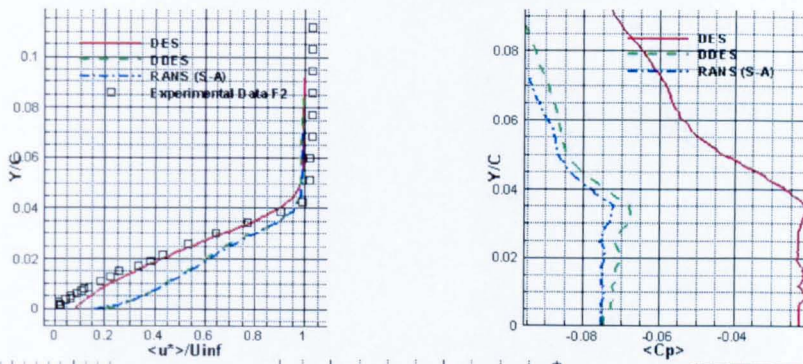
c)



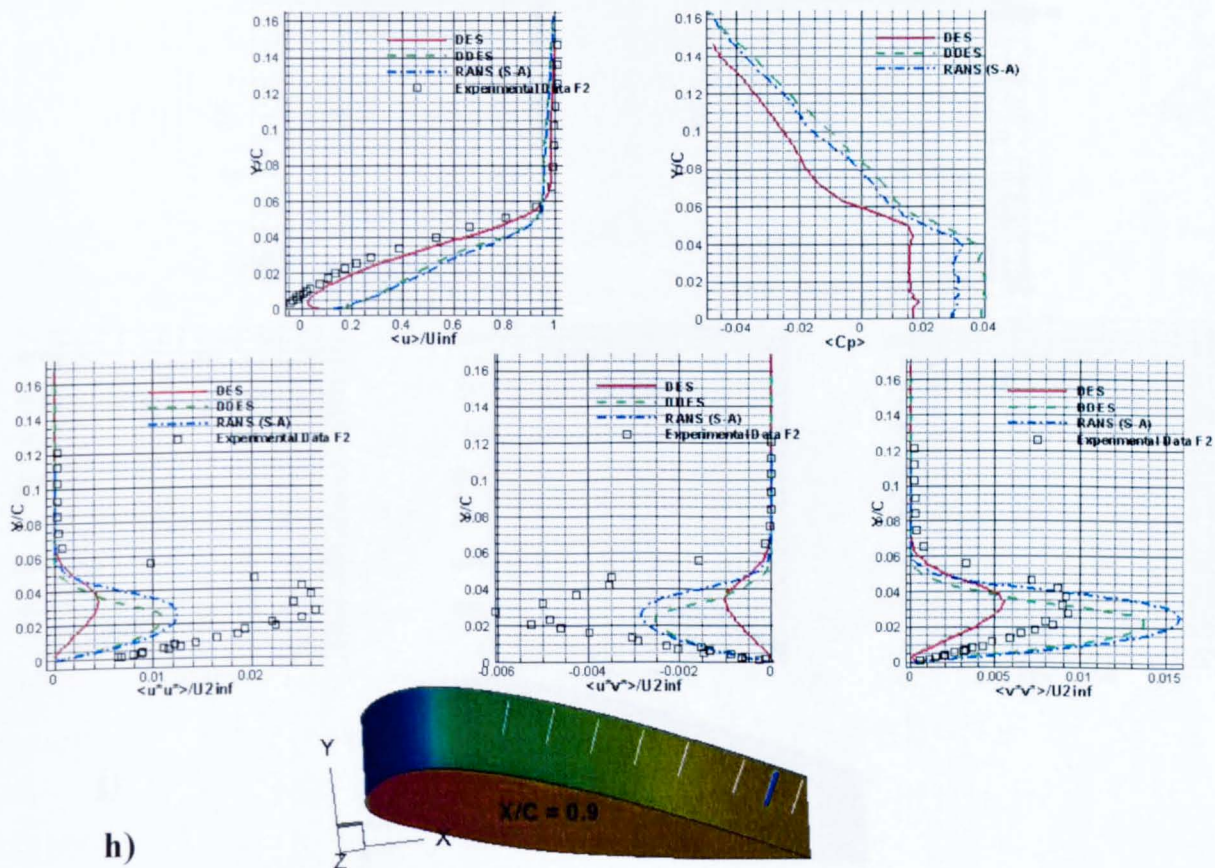
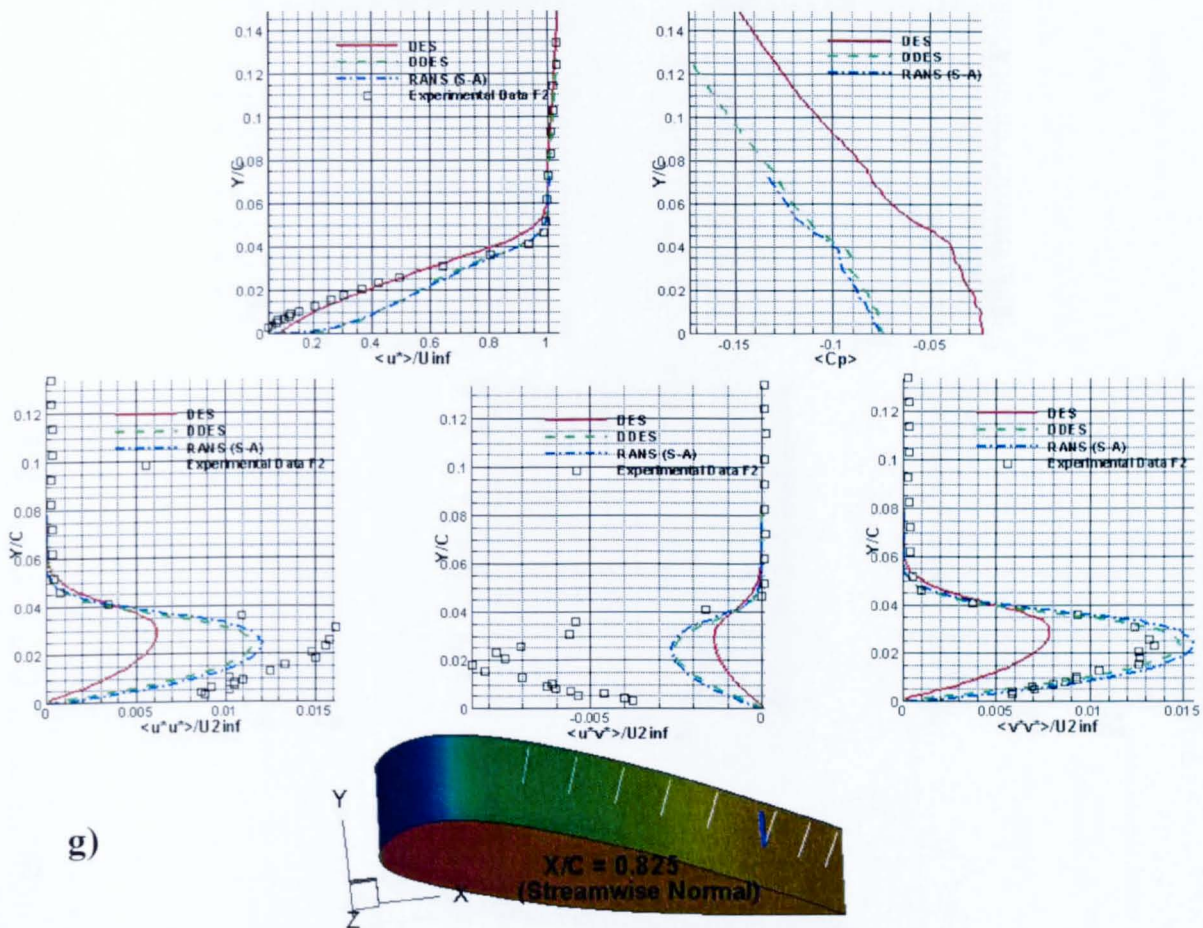
d)

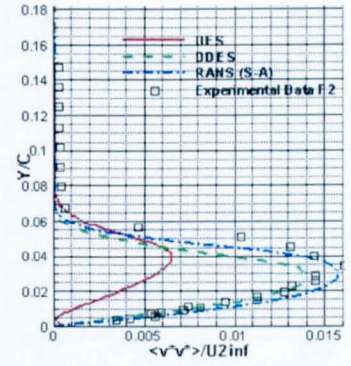
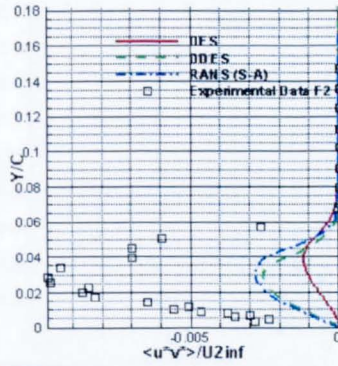
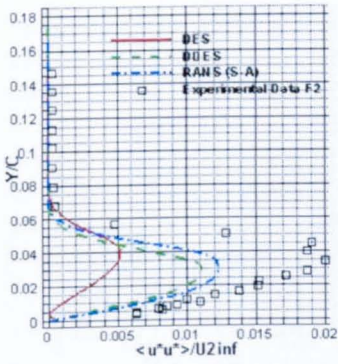
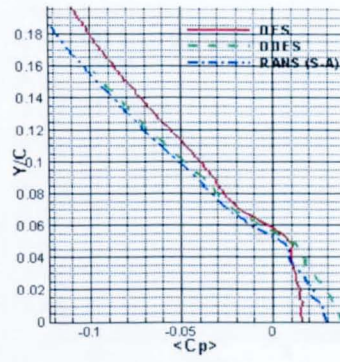
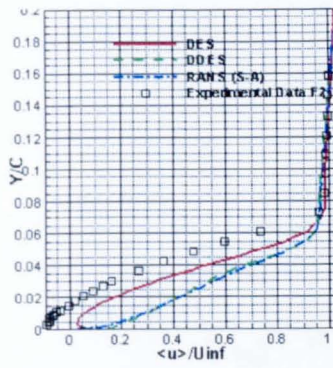


e)

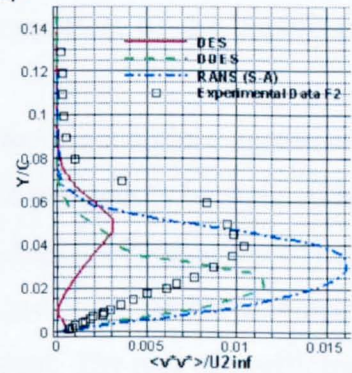
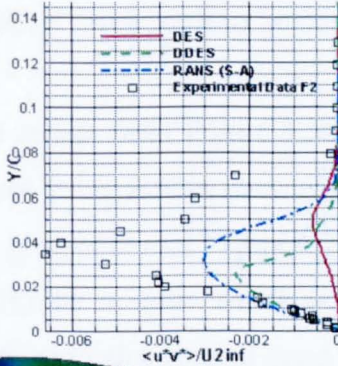
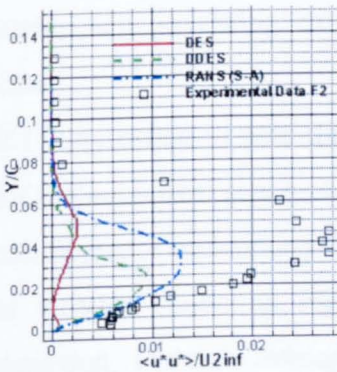
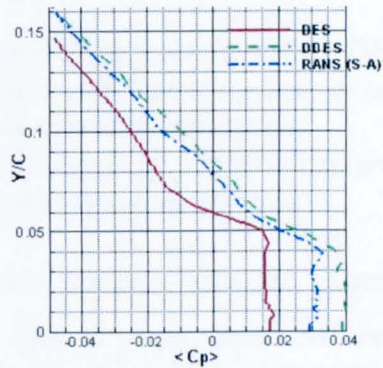
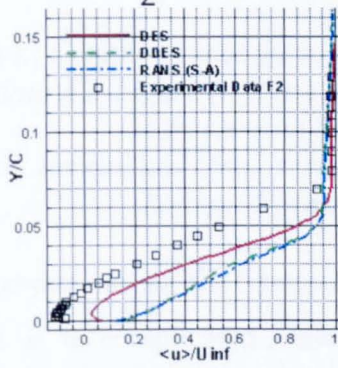
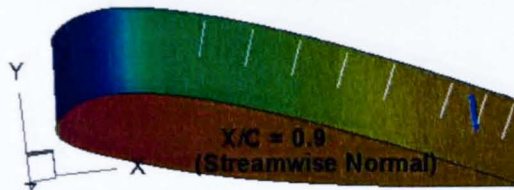


f)

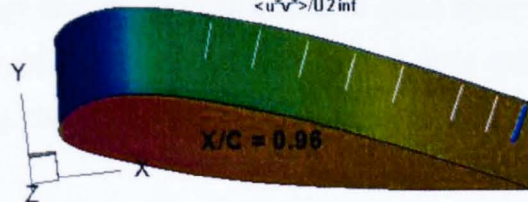




i)



j)



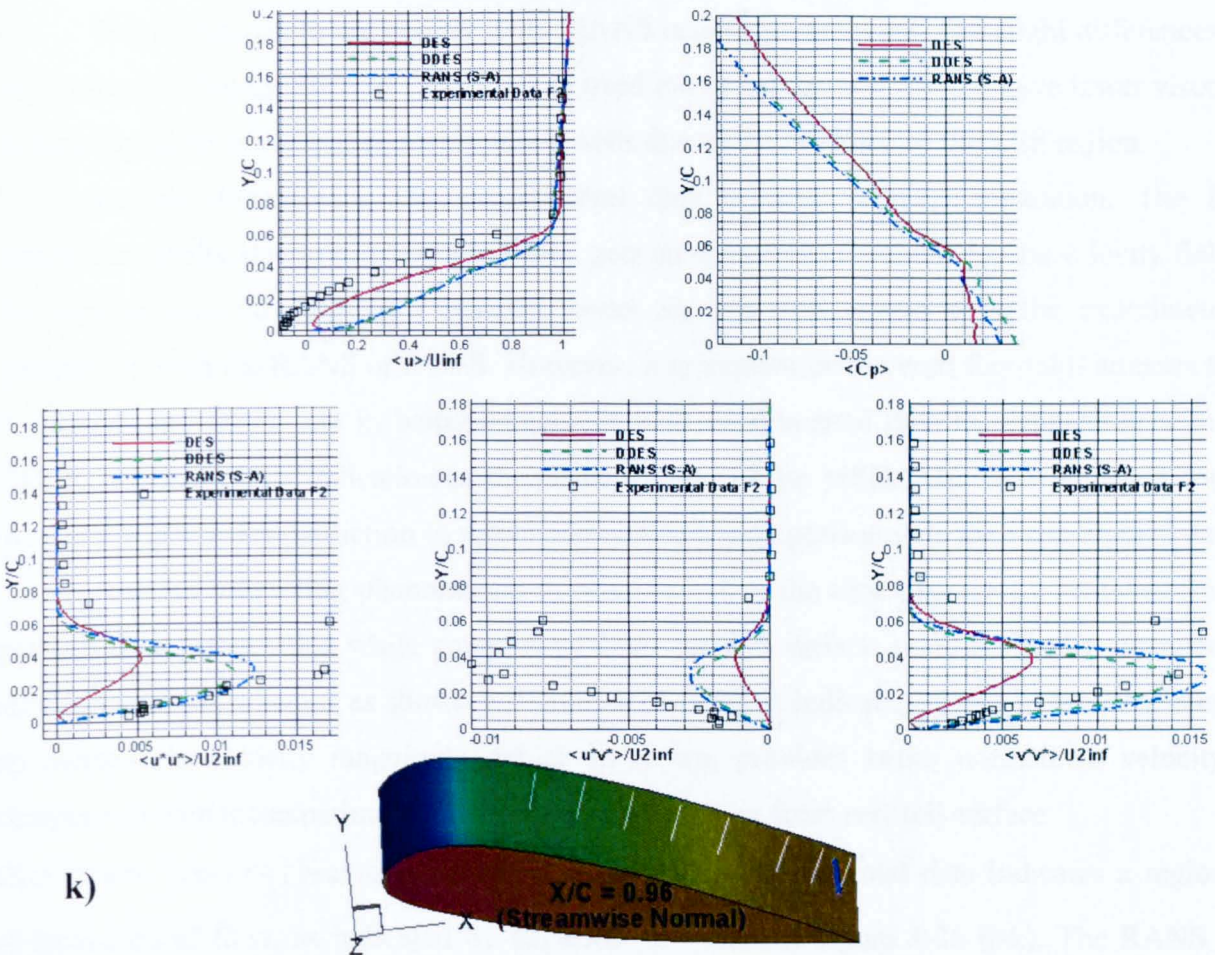


Figure 4.26 [a-k] Comparison of the turbulence parameters from the RANS, DES and DDES with experimental data F2. Figure (a-f) are computed normal to airfoil surface, g) is computed normal to freestream flow direction at specified location.

Top (left): normalized time averaged x-direction velocity (right): Pressure coefficient
 Bottom: Normalized modelled Reynolds stresses

Overall, the comparison of the computed Reynolds stresses with the experimental data is encouraging. It is a complicated flowfield and lots of approximations are made for the underlying governing equations apart from various uncertain parameters of the experimental data.

It is interesting to note that initial results from Figure 4.26 (a-b) represent a close agreement of all the numerical schemes. However going further downstream, the differences become wider. It can be better understood from the perspective of Figure 4.22. The region of premature switching at location shown in Figure 4.26(a-b) is quite small as compared with further downstream direction. The time average normalized velocity is in good agreement. The plot of coefficient of pressure is selected to highlight the flowfield pressure. It is evident that even in the locations shown in figure 4.26(a-b), there are noticeable differences in the flowfield pressure of the DES with RANS and DDES.

The DDES results are similar to the RANS results, as expected. The slight differences are due to the fact that the DES or DDES, when used in correct fashion, should have lower viscosity in their flowfield in comparison with pure RANS due to the presence of the LES region.

Further downstream, the experimental data actually predicts separation. The DES simulation results, due to its MSD problems, gets an unwarranted benefit for the velocity field as the suction side flowfield now matches better in near-wall region with the experiment in comparison with the RANS or DDES. However, it is evident that overall Reynolds stresses from the RANS and DDES are in better agreement with experimental data in comparison with the DDES. It is one major indication of the disadvantages of the MSD. Also from Figure 4.26(c-f) there is a slight under prediction in velocity observed in comparison with the experimental data.

Another interesting phenomenon to observe is that the time average C_p switches from a positive to negative value while going away from aerofoil surface along the probe, depicted by all the numerical schemes as shown in Figure 4.26 (h-k). It indicates a drop in pressure causing an increase in velocity magnitude, which in return, provides better normalized velocity in comparison with the experimental data at the regions away from aerofoil surface.

One typical trend to observe is in the $\langle u \rangle / U_{inf}$. The experimental data indicates a region of recirculation of flow, as indicated by negative $\langle u \rangle$ velocity figure 4.26 (i-k). The RANS and DDES simulations do not predict this recirculation. The DES simulation indicates a region of sudden retardation in the flow near the wall region. Figure 4.26 (i-k) shows that actually DES does not predict the reverse flow with negative $\langle u \rangle$ velocity in this region but there are certain pockets of retarded flow in this region just on top of attached turbulent boundary layer.

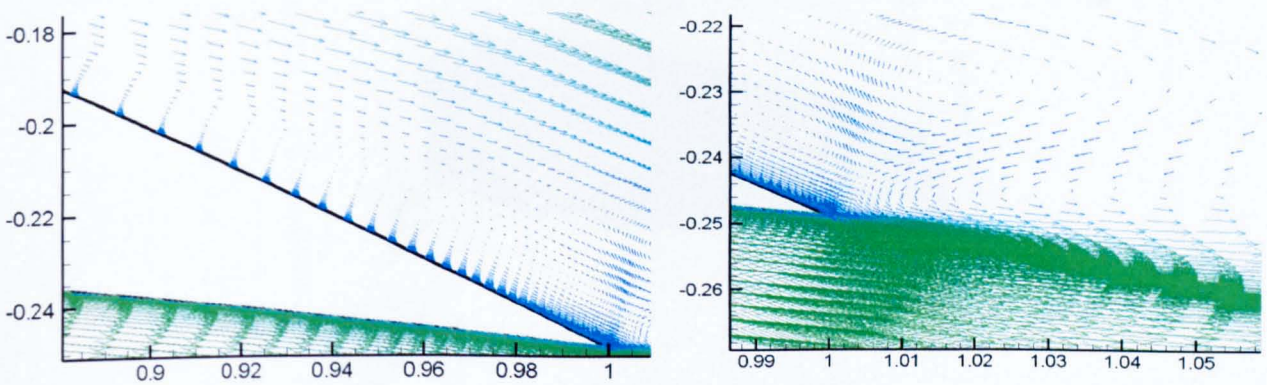


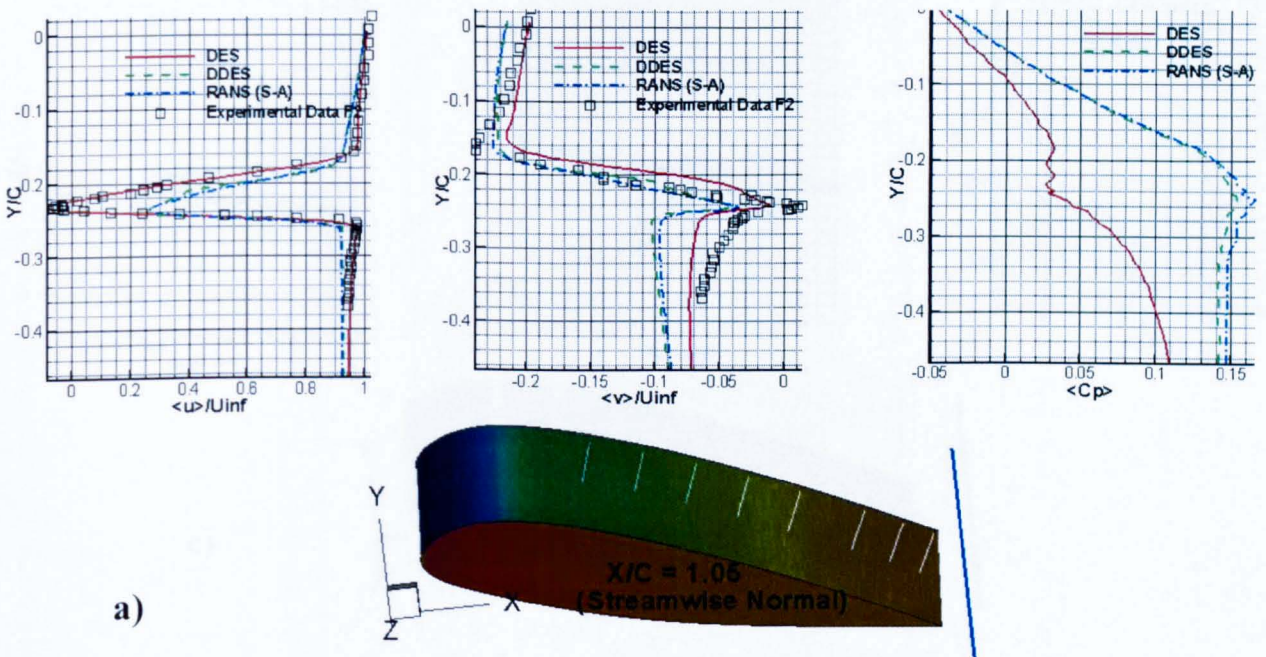
Figure 4.27 *Trailing edge of A-airfoil with time averaged velocity vectors (colour with velocity magnitude)*

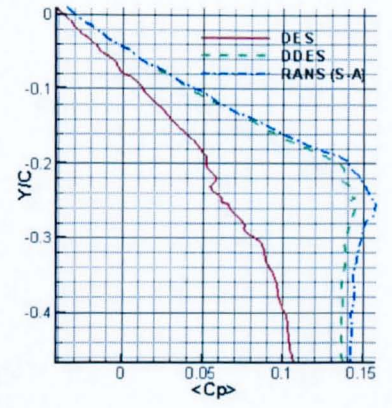
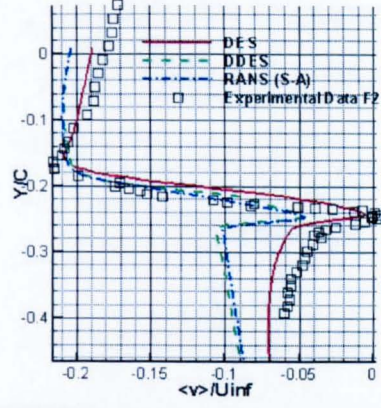
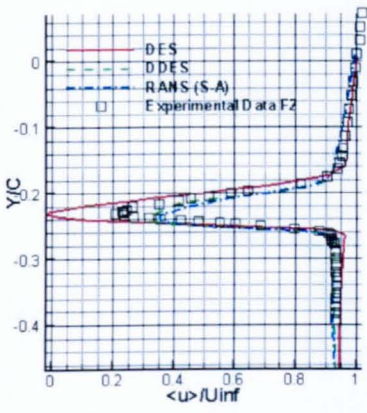
The recirculation region predicted by the DES simulation is actually at the trailing edge as shown in the flowfield of Figure 4.27.

The DES simulations from Figure 4.26 (e-k) continuously show the superior prediction of the DES for time averaged u-velocity which is under predicted by both the RANS and DDES. It opens another dimension to ponder about the results from the DDES simulation. Apparently, the premature switching to the LES in DES simulation, although incorrect from the basic working perspective of the numerical scheme, provides better flow physics. From this point of view, the performance of the DDES simulation can be improved by reducing the effective levels of the dissipation in the thick boundary layer. It can be achieved by modifying the switch to decrease its delay in switching from the RANS to LES mode.

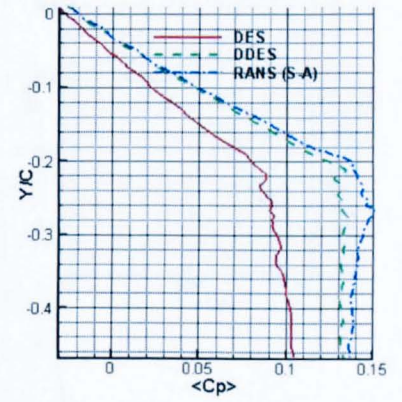
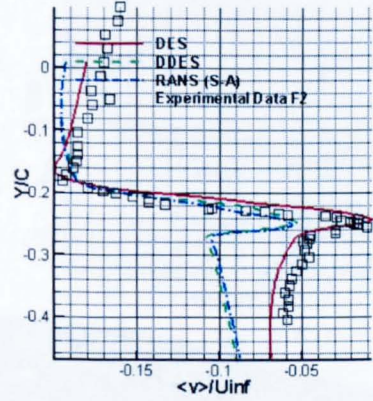
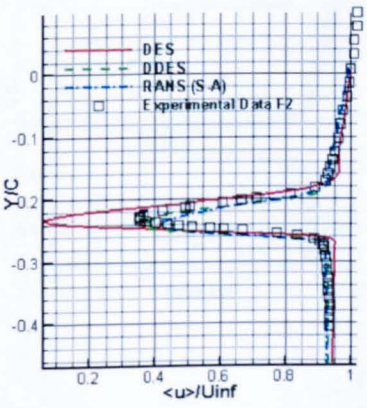
4.3.1.2 Wake region analysis

The experimental data is also available for different locations in the wake region, normal to the free stream flow.





b)



c)



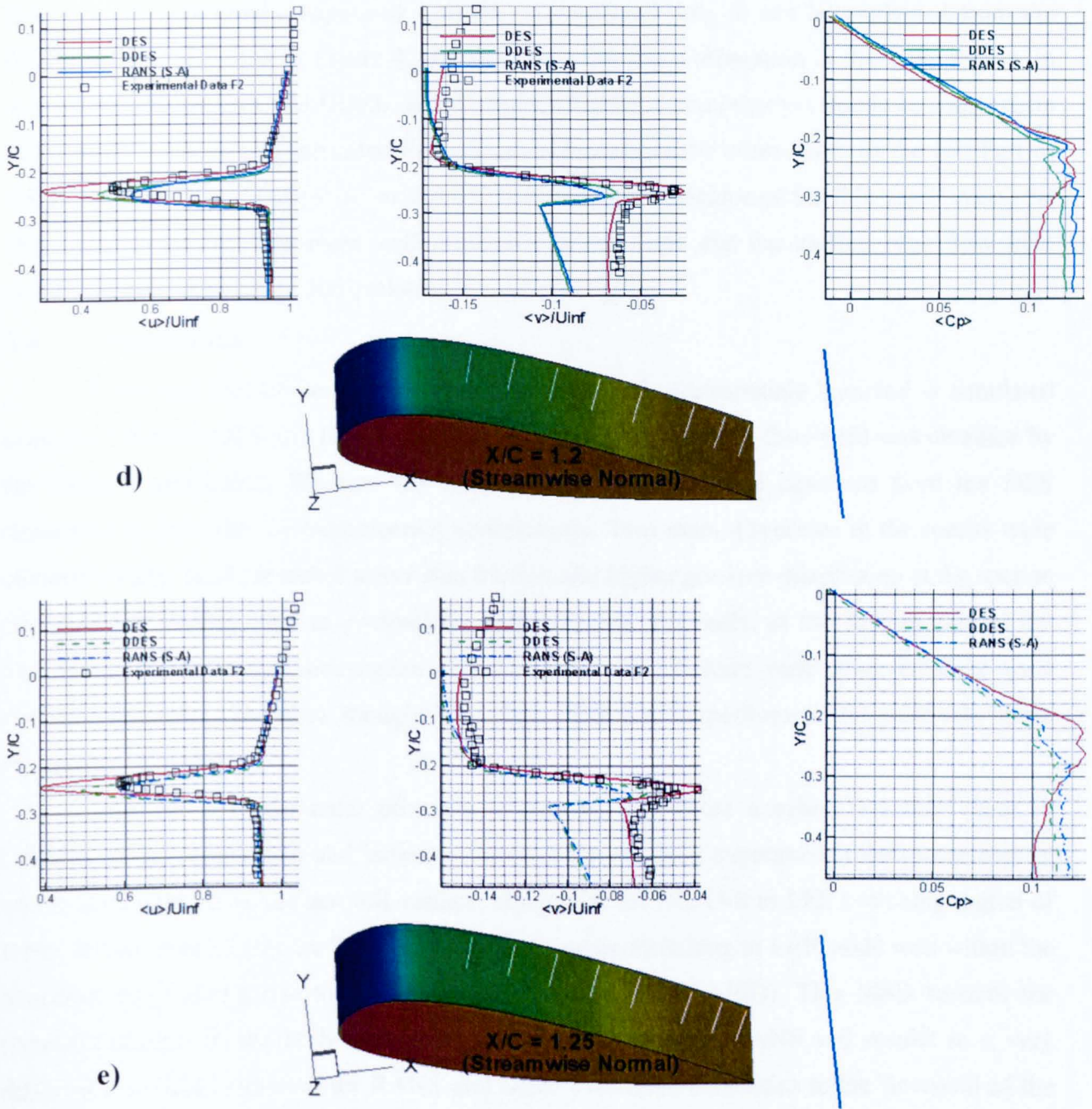


Figure 4.28 [a-e] Comparison of the flowfield parameters in the wake region from the RANS, DES and DDES with the experimental data F2. Figure 4.28(a-c) are computed normal to freestream flow direction at specified locations. Top (left): time averaged x-direction velocity (middle) time averaged y-direction velocity (right) time averaged pressure coefficient

Wake region flowfield data as presented in figure 4.28(a-e) is interesting in many ways. First thing to appreciate is that for the farthest location in the flow field (figure 4.28 (e)), the pressure field from the RANS, DES and DDES converges in the region away from aerofoil surface. It indicates that effects of premature switching are reducing as a logical consequence. The largest disparity of results of the DES with RANS and DDES are in y-axis velocity. Actually, the DES

results are in very good comparison with the experimental data. It can be explained from the DES flowfield, as shown in Figure 4.28, which develops flow separation in the wake region, in contrast with the RANS and DDES. RANS and DDES have smoother y-velocity in comparison with the DES due to non-separated flow. It again highlights the observation in the last Part of 4.3.2.1. Is DDES too dissipative to predict realistic flow simulations for this case? Also, the DES, despite the MSD problem, still presents a better wake and the trailing edge flow field picture because of its lower dissipation.

4.4 Conclusions

In the first part of the chapter, the flow around the Aerospatiale A-airfoil is simulated using the URANS, DES and DDES simulation techniques. A steady flow field was obtained by the URANS simulation. Whereas the trailing edge separation was observed from the DES simulation in line with the experimental observations. Two main disparities in the results were obvious. Firstly, DES presented lower skin friction and higher pressure distribution at the suction side near the leading edge in comparison with URANS. Secondly, at the suction side of the trailing edge, the pressure distribution and skin friction coefficients were observed to be quite different for both. The first thought was that DES has outperformed the relatively more dissipative URANS.

DES has a fundamental principle of treating the whole attached boundary layer in URANS mode. Momentum and boundary layer thickness from experimental data were plotted on the flow field above the aerofoil surface, along with the URANS to LES switching region of DES. It was revealed that the DES performs a premature switching to LES mode well within the boundary layer giving rise to the Modelled Stress Depletion (MSD). This MSD reduces the turbulent stresses in the DES simulation as compared with the RANS and results in a very different flowfield prediction for RANS and DES. Two main disparities in the flowfield of the URANS and the DES schemes were attributed to the improper switching function of the DES simulation technique.

In order to ascertain the conclusion above, the DDES scheme, which is presented as a solution to MSD in the DES scheme, was applied to the same case. The underlying idea is that if the switching is done correctly in the intended regions (treating the whole boundary layer in the URANS mode), then the DDES results should match closely with RANS; in contrast with the DES results. Firstly, the switching region was observed to work properly and then the results obtained from the DDES were analyzed. Similar to the URANS, no separation region was observed. The pressure distribution at the leading edge improved with the decrease in the

pressure distribution around the suction side of the leading edge increasing the turbulent Reynolds stresses. It was a typical outcome of delayed switching to LES mode. For the downstream region near the trailing edge, the DDES is treating the whole boundary layer in the RANS mode, resulting in the pressure and skin friction distribution much closer to URANS, as expected. It is pointed that for the thick attached boundary layers with no separation predicted by URANS (such as this study), the best solution of DDES is essentially dependant on URANS output. For mild separation cases, DDES, although it sorts the MSD problem, its RANS-LES region is observed to be more irregular. It is observed that this irregular RANS-LES switching region may cause some problems for high order less dissipative schemes.

The superior performance of the DES at the suction side of the trailing edge and in the wake region indicates that a lower level of dissipation is favourable to achieve better results in these regions. The DES scheme results, although incorrect from the switching of RANS-LES regions, represent the flowfield in a better way as compared with the URANS and DDES schemes. In contrast, the DDES although works in accordance with the basic methodology but produces excessive dissipation in the flowfield. In a nutshell, the DDES performs quite well in delaying its switching in response to the growing boundary layers; a case which arguably is not the best suited for it without flow separation.

In the second part of the chapter, the modelled stresses computed by the URANS, DES (with its premature switching) and DDES are compared with the experimental. The underlying idea is that it will highlight the extent of Modelled Stress Depletion by DES in comparison with URANS and DDES apart from its effect on the flow field. The reduction of the modelled stresses on the suction side of the leading and trailing edges of the aerofoil casts huge effect on the flowfield. For the DES, it leads to the separated flow near the suction side of the trailing edge, in line with the experimental observation. Due to this, the overall flowfield prediction by the DES simulation is better as compared with URANS and DDES results. The DDES simulation suffers from excessive dissipation due to its large delay in switching to the LES mode.

5. High Reynolds number flows over a Circular Cylinder

In this chapter, a detailed analysis of high Reynolds number flows over a circular cylinder is conducted. The selected Reynolds numbers are 1.4×10^5 , 3.6×10^6 and 8.0×10^6 . The comparison of the pressure coefficient over the surface of circular cylinder is carried out with the experimental data for these Reynolds numbers. The experimental data for Reynolds stresses is available for $Re = 1.4 \times 10^5$. Comparisons of computed Reynolds stresses are carried out with experimental data for DES and DDES. The $Re = 3.6 \times 10^6$ case presents effects of the change of velocity on the separation angle and the lift and drag coefficients. The $Re = 8 \times 10^6$ case presents a comparison of URANS, Laminar and DES simulation results. It also compares the effect of the smaller time step on the flow field quality. For massively separated flows, the resolved stresses have much bigger contribution than modelled stresses. A comparison of the modelled and resolved stresses is made at the $Re = 8 \times 10^6$ to appreciate their contribution.

5.1 Introduction

Numerical simulation of high Reynolds number turbulent flow over a circular cylinder is a common bench marking case. The production of von Karman vortex sheet with strong spanwise flow effects make it both challenging and well suited to judge the performance of the DES solver. A circular cylinder of aspect ratio $\frac{L}{D} = 2$ is taken for all the simulations consistent with study^[18]. Unfortunately, different experimental studies do not have a complete set of the data for comparison at a fixed Reynolds number. It is worth noticing that the experimental data by Achenbach^[59] for flow over a circular cylinder at Reynolds no of 3.6×10^6 is used for comparison of skin friction coefficient (Cf) for all the CFD simulations in this study, at different Reynolds numbers. Similarly, the Cp comparison of all the CFD simulations is carried out with the experimental work by Roshko^[130] and Von Nunnen^[131], in line with the other studies^[18,129]. The experimental results by Cantwell^[127] are used for the Reynolds stress comparison. The available data for each study is listed in the table 5.1. It is to be pointed out that due to this unavailability of complete set of experimental data, some of the simulation results at a particular Reynolds number are compared with different experimental Reynolds numbers, as done in other studies.

Experiment	Reynolds Number	Cp	Cf	Cd	Reynolds stresses
Achenbach ^[59]	3.6×10^6	X	√	X	X
Roshko ^[130]	8.5×10^6	√	X	√	X
Cantwell ^[127]	1.4×10^5	**	X	1.237	√
Von Nunen ^[131]	7.6×10^6	√	X	√	X

Table 5.1 *Details of different available experimental data for circular cylinder*

** Large variations in data

5.2 Reynolds Number 1.4×10^5

5.2.1 Mesh Statistics

Table 5.2 presents the mesh statistics with different cell types used in the mesh.

Number of nodes	Number of elements	Type of cells		
		Brick	Tetrahedral	Pyramid
405259	1789623	110880	1675047	3696

Table 5.2 *Mesh statistics of circular cylinder with $L/D=2$ for $Re=1.4 \times 10^5$*

Domain at the inlet and outlet is 35 times the radius of the cylinder and on top and bottom sides is 20 times the radius of the cylinder. All the meshes are generated using commercial software Gambit^[128].

5.2.2 Numerical simulation details

Table 5.3 presents the numerical simulation details and different parameters used for the CFD simulation.

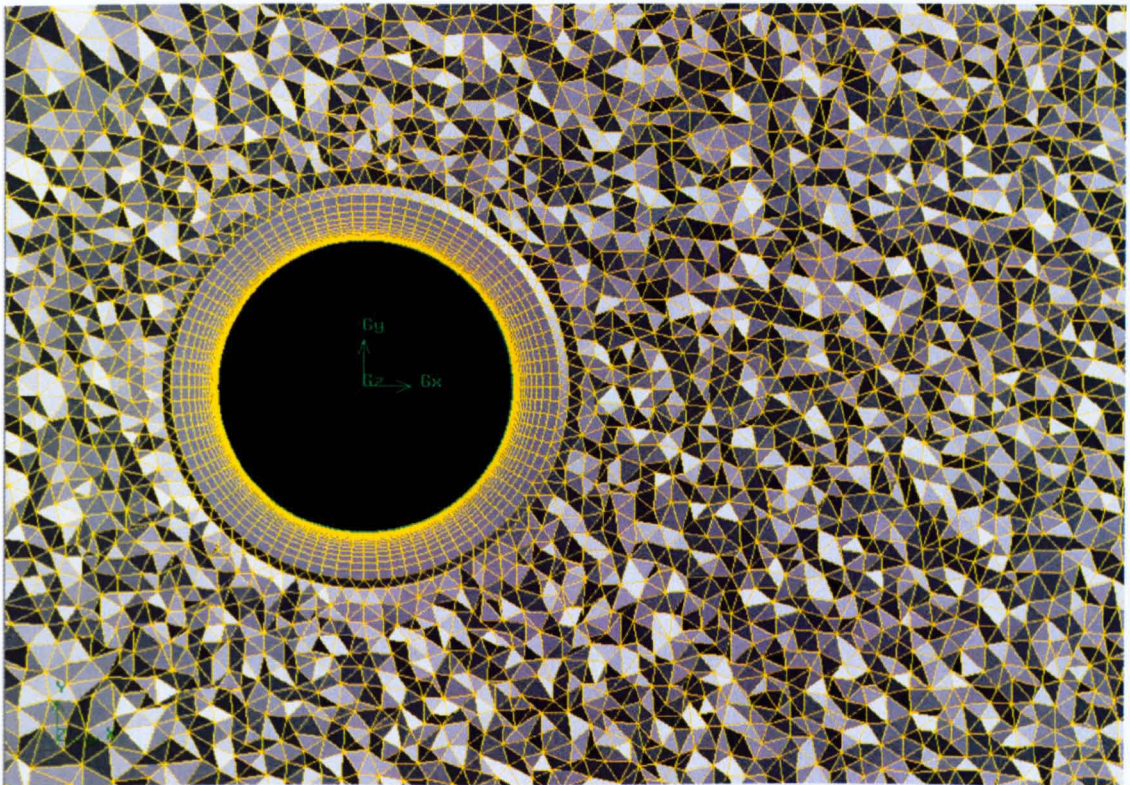
Reynolds Number	Mach Number	Velocity (m/sec)	Inviscid Flux Scheme	Turbulence Scheme
1.4×10^5	0.288	100	Roe	DES/DDES

Table 5.3 *Case details of simulation*

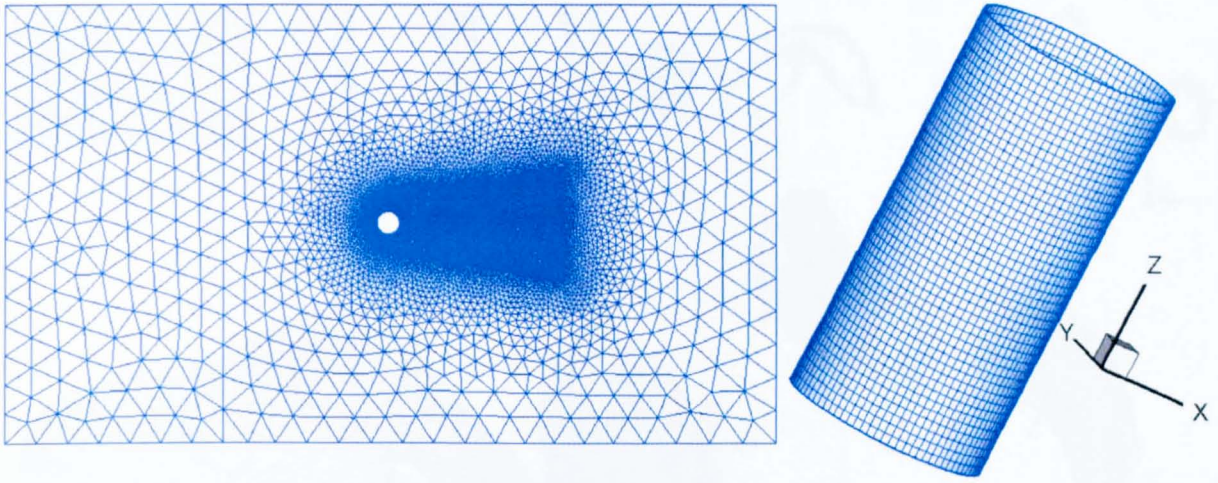
Mesh details with the surface mesh and element distribution in the near-wall and wake region are shown in figure 5.1 (a-c).



a) Overview of near cylinder domain meshing with elements



b) Zoomed top view near cylinder with mesh elements



c) Left: Top view Right: surface mesh of cylinder

Figure 5.1 Different views of Mesh over circular cylinder with $L/D=2$ for $Re=1.4 \times 10^5$

Fig. 5.2 indicates that the Y^+ value over the whole cylinder surface does not exceed 0.3. It was observed during simulations that the S-A model is quite sensitive to first cell height. For very low Y^+ value, the convergence achieved is very good and for Y^+ values over 1, the turbulence equations do not converge well. The strong dependence of S-A model on first cell height is

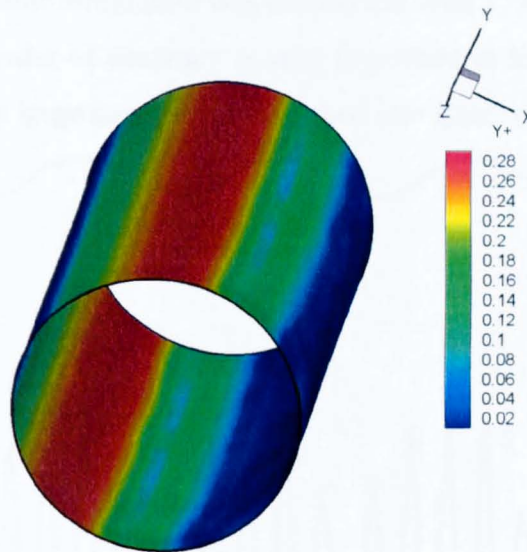


Figure 5.2 Y^+ values over the surface of circular cylinder at $Re=1.4 \times 10^5$

consistent with similar observations from other studies ^[91]. There are 44 cells along the spanwise direction on the cylinder surface resulting in $\frac{\Delta_z}{D} \approx 0.0455$.

5.2.3 Results with 1st order spatial accuracy

To understand the effect of the order of accuracy of the solver in capturing the large number of

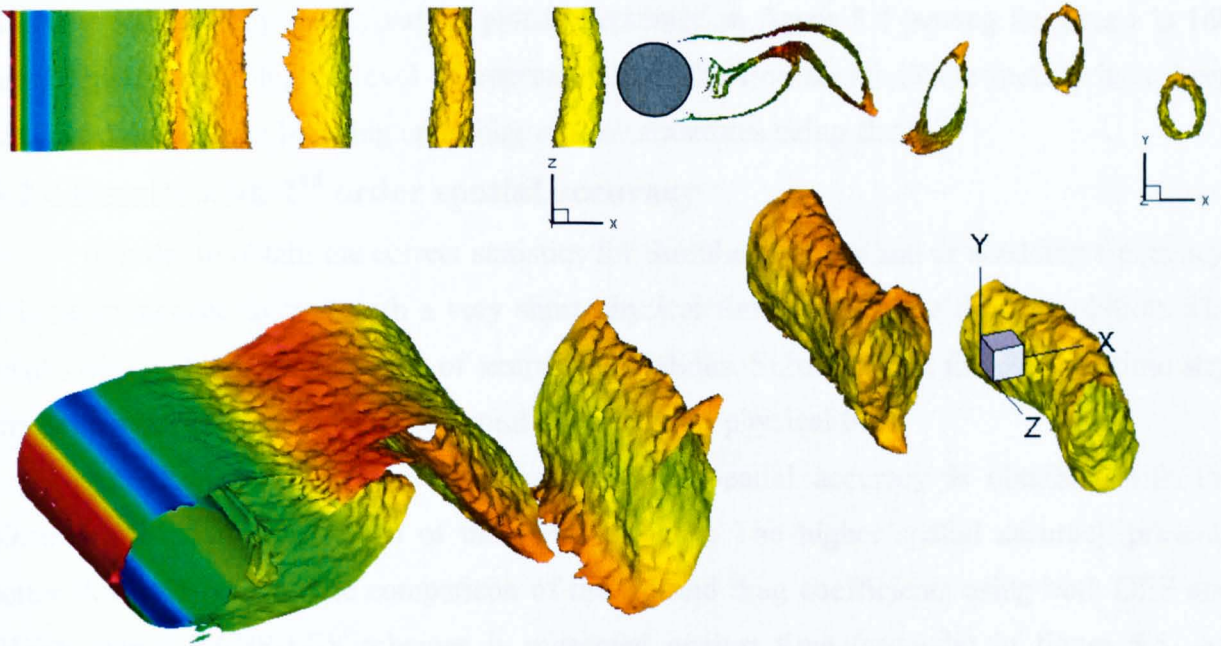


Figure 5.3 *Instantaneous Isosurface of vorticity magnitude colour by Pressure of circular cylinder at $Re=1.4 \times 10^5$ using DDES scheme with 1st order spatial accuracy. Vorticity magnitude level is 8000 and pressure range is 65000 to 102500. Physical time ≈ 2.1 sec
Top (left) : View from bottom side Top(right) View from side Bottom: Isometric View*

length scales in the flow, the same simulation was carried out with 1st order spatial accuracy. Figure 5.3 indicates that the order of accuracy is very important in turbulent flow simulation. 1st order solver fails to develop large structures being shed into small turbulent structures.

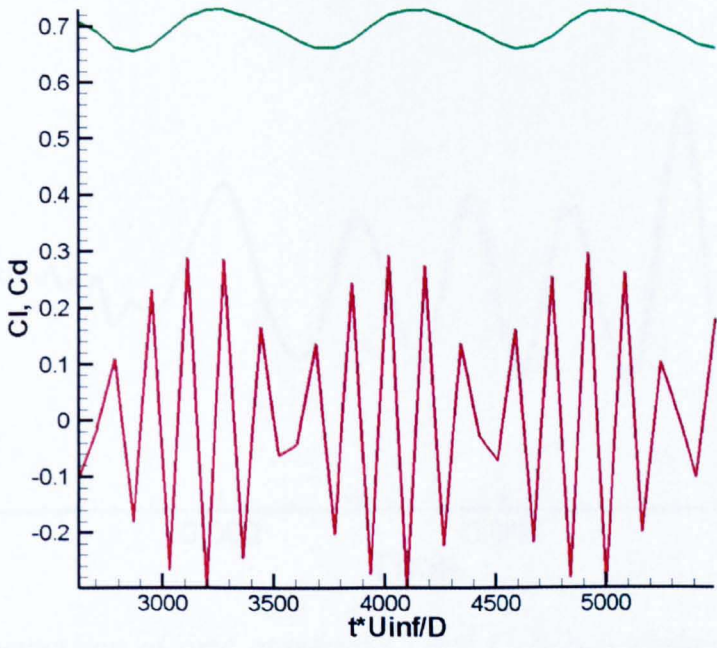


Figure 5.4 *Comparison of time averaged C_l and C_d values computed by DGDES using DES with 1st order spatial accuracy.*

It is also indicated by the C_l and C_d plot as presented in figure 5.4 (sampling frequency is 160 time steps). Due to higher level of approximation, the fine scales of the motion have been dissipated out with no breaking up of bigger flow structures being shed.

5.2.4 Results with 2nd order spatial accuracy

In order to obtain the correct statistics for Strouhal number and or shedding frequency, it is recommended to start with a very short physical time step for the flow simulation. The results obtained indicate the scale of temporal variations. Subsequently, the physical time step can be increased to obtain better temporal efficiency for physical time.

As described in Section 2.6, the 2nd order spatial accuracy is obtained with the piecewise linear reconstruction of the flow variables. The higher spatial accuracy presents better flowfield results. The comparison of the lift and drag coefficients using both DES and DDES hybrid RANS-LES schemes is presented against time (seconds) in figure 5.5. An important observation is that for this case which is termed as ‘natural DES’ case, the results

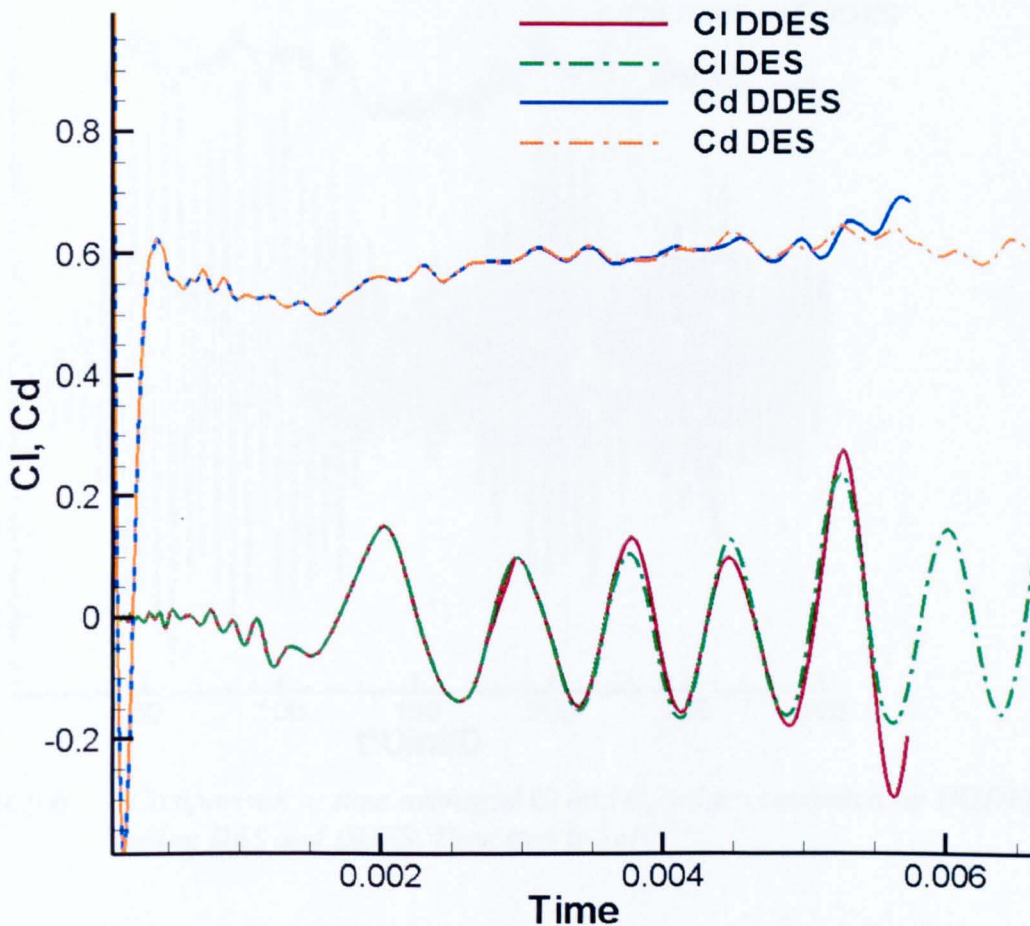


Figure 5.5 Comparison of time averaged C_l and C_d values computed by DGDES using DES and DDES. Time step is very small, 5×10^{-7} seconds with data showing around 12000 iterations data. X-axis represents physical time in seconds.

from DDES closely follow the DES results.

One shedding cycle is about 1600 iterations as plotted in figure 5.5. Idea of starting from a very small time step is to obtain the correct Strouhal number statistics. Based on this, the time step can be increased with confidence that the time accuracy will be sufficient to present correct time dependant phenomenon. The DDES and DES solutions start to differ in terms of shedding cycle and associated lift and drag values. In the next simulation, the time step is increased to 5×10^{-5} for subsequest simulations. The data input (length of data on plot figure) of DDES is shorter than DES in figure 5.5 and 5.6. It is intentionally put in this way to appreciate the extra cost associated with DDES. Both simulations were run for the same amount of time using same number of processors and compilation flags. The extra computational cost associate with the DDES scheme is due to the calculation of the switching parameter for each iteration.

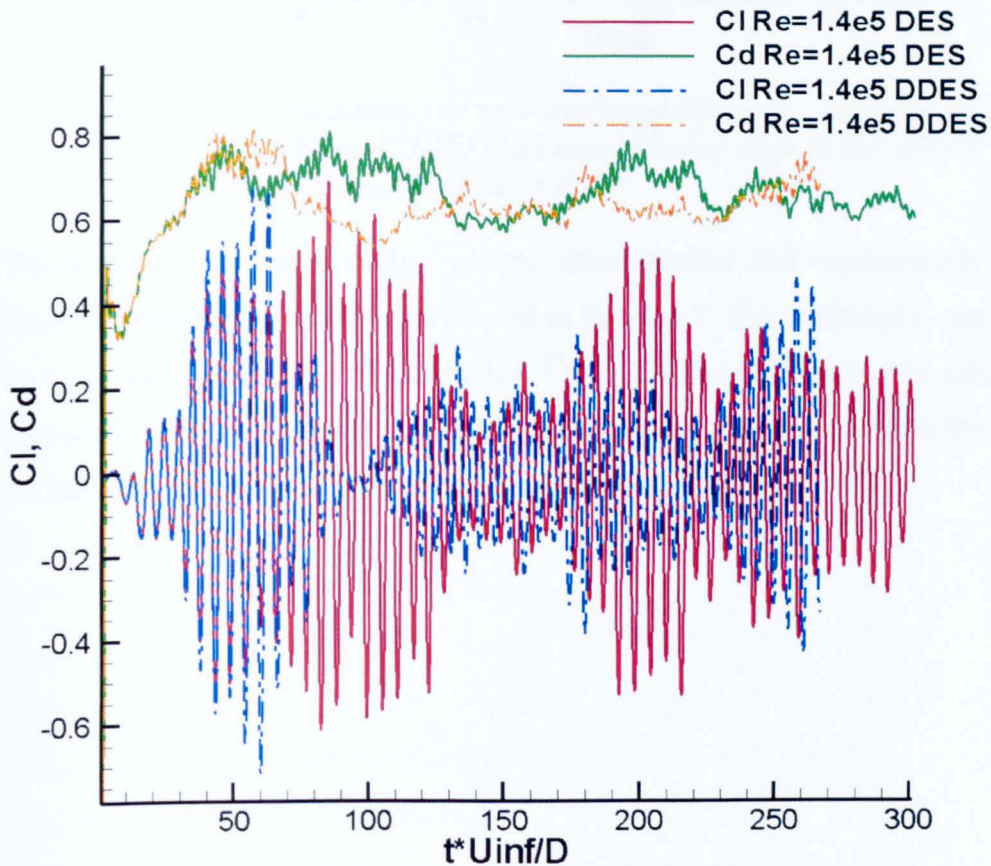


Figure 5.6 Comparison of time averaged C_l and C_d values computed by DGDES using DES and DDES. Time step is 5×10^{-5}

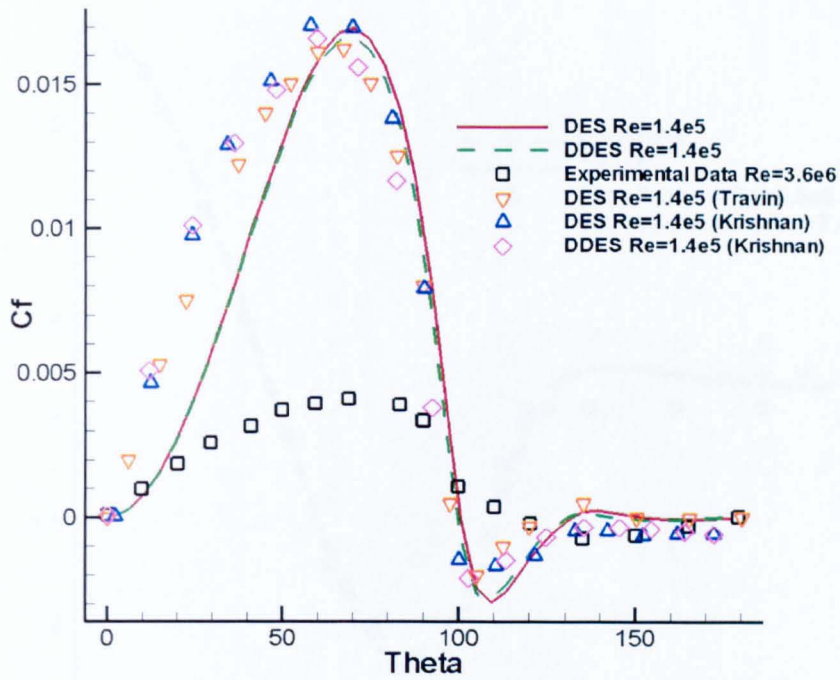


Figure 5.7 Comparison of time averaged C_f values computed by DGDES using DES and DDES with experimental data at $Re=3.6 \times 10^6$ [59] and other CFD studies at $Re=1.4 \times 10^5$

The comparison of this study with the other studies and experimental data at a different Reynolds number of 3.6×10^6 is presented in figure 5.7. The predicted C_f and separation angle is in good agreement with other studies [17,129]. The experimental C_p data for this Reynolds number has a large variation as described in table 5.1, thus it is compared with higher Reynolds number experimental data of 3.6×10^6 , similar to other studies [17,129].

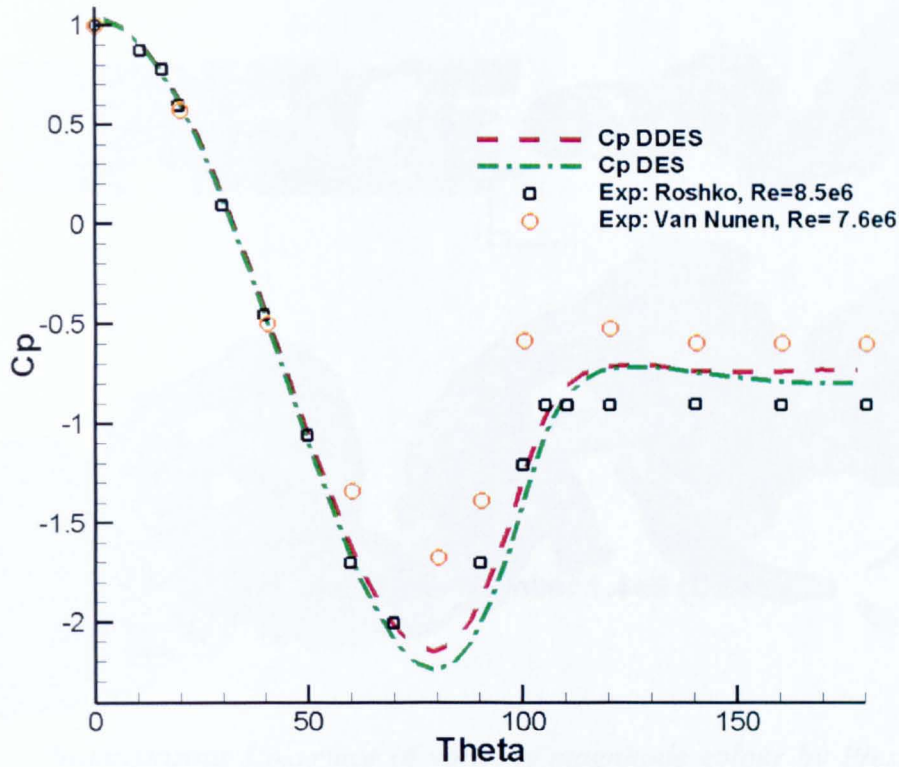


Figure 5.8 Comparison of C_p values computed by DGDES using DES and DDES with experimental data at $Re=1.4 \times 10^5$

The C_p plot from the DES simulation indicates a deeper $-C_p$ region in comparison with the DDES simulation, as presented in figure 5.8. The available experimental data results for comparison, which are at higher Reynolds number than these simulations, indicates a similar trend. 'Exp' in figure 5.8 indicates the experimental data.

Figure 5.9 and 5.10 present the different views of vorticity isosurfaces coloured with static pressure. The complexity of the flowfield and presence of large scales of flow indicate the high level of turbulence in the flowfield. DES and DDES both present the complex turbulent flow field with large number of length scales present.

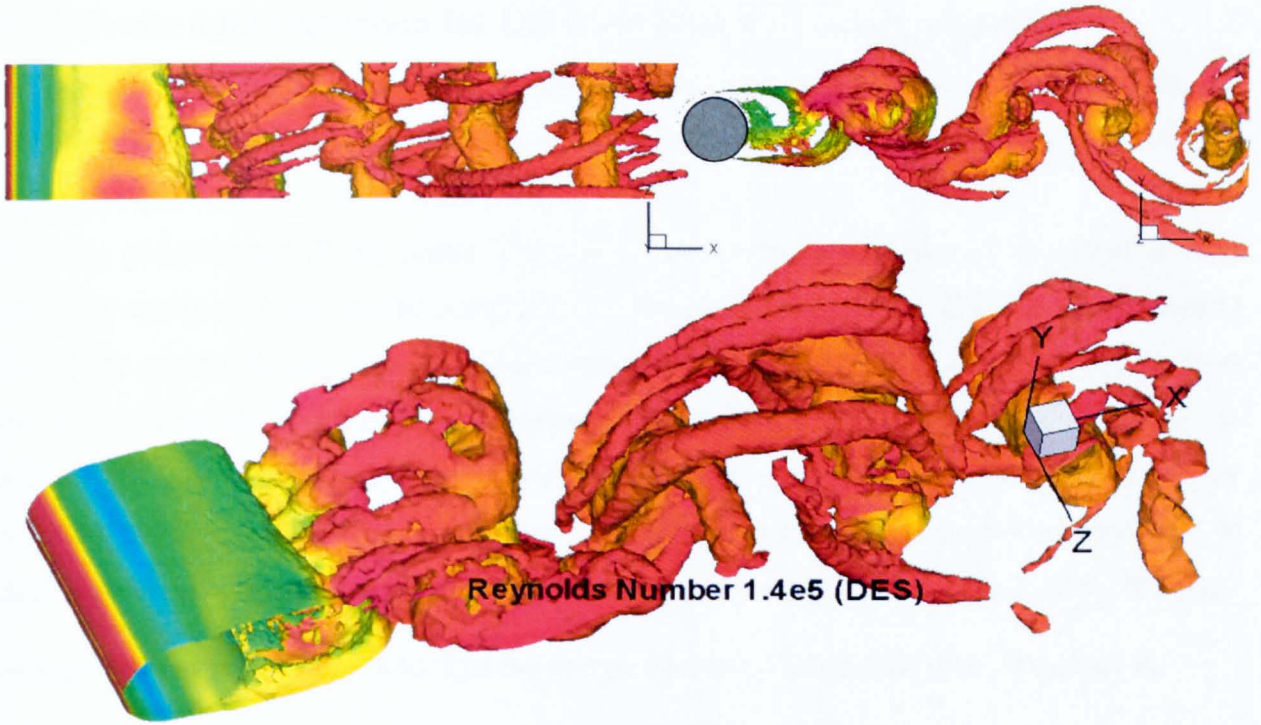


Figure 5.9 *Instantaneous Isosurface of vorticity magnitude colour by Pressure of circular cylinder at $Re=1.4 \times 10^5$ using DES scheme. Vorticity magnitude level is 8000 and pressure range is 65000 to 102500. Physical time ≈ 2.1 sec*

Top (left) : View from bottom side Top(right) View from side Bottom: Isometric View

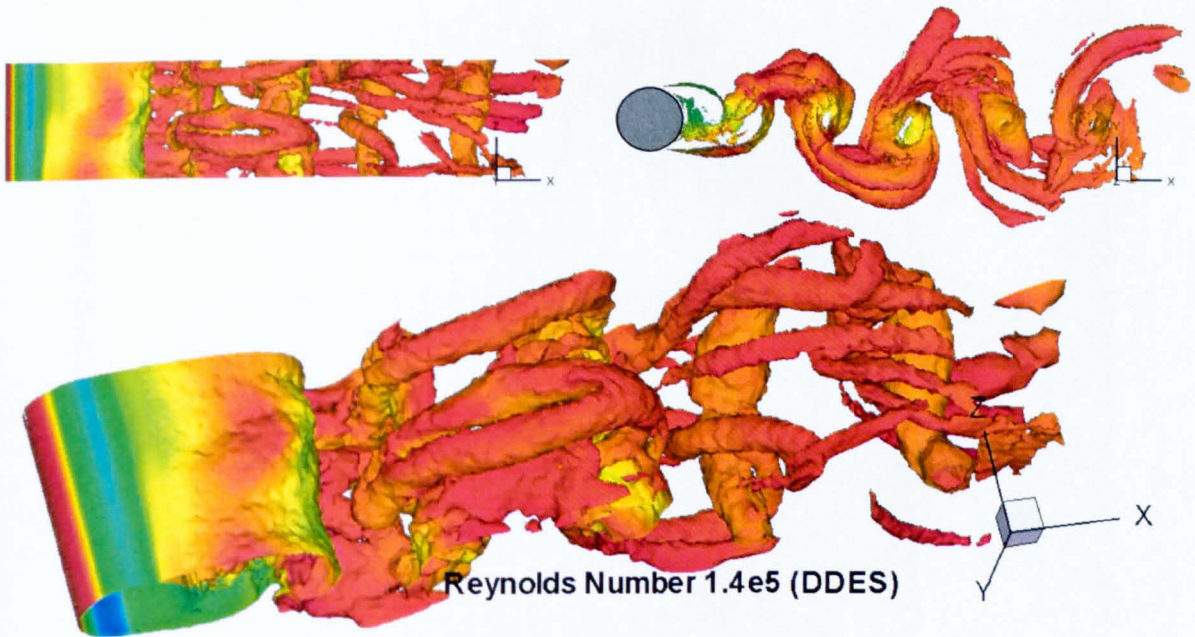


Figure 5.10 *Instantaneous Isosurface of vorticity magnitude colour by Pressure of circular cylinder at $Re=1.4 \times 10^5$ using DDES scheme. Vorticity magnitude level is 8000 and pressure range is 65000 to 102500. Physical time ≈ 2.1 sec*

Top (left) : View from bottom side Top(right) View from side Bottom: Isometric View

5.2.5 Probe data extraction for DES and DDES flowfield analysis

A subroutine was added in DG-DES which can read in the probe locations from an input file and then locate these probes in individual partitions of the mesh and subsequently extract the data to a separate output file for each probe.

A probe point located at the centre line with 2 diameters downstream of the cylinder. The recorded data is analysed for the comparison of the DES and DDES output. Fig 5.11 indicates the power spectral density plot of recorded data using the DES and DDES scheme. It is evident that energy cascade as discussed in Chapter 1 from Kolmogorov's hypothesis is occurring. X-axis of the plot is frequency and y-axis is the power spectral density in decibels. Power Spectral Density (PSD) is the frequency response of a random or periodic signal and it describes the average power distribution of the signal as a function of frequency. With the

increasing frequency from left to right the energy (y-axis) content decreases. The slope of $-\frac{5}{3}$ indicates that the energy decay is in accordance with the Kolmogorov's energy spectrum.

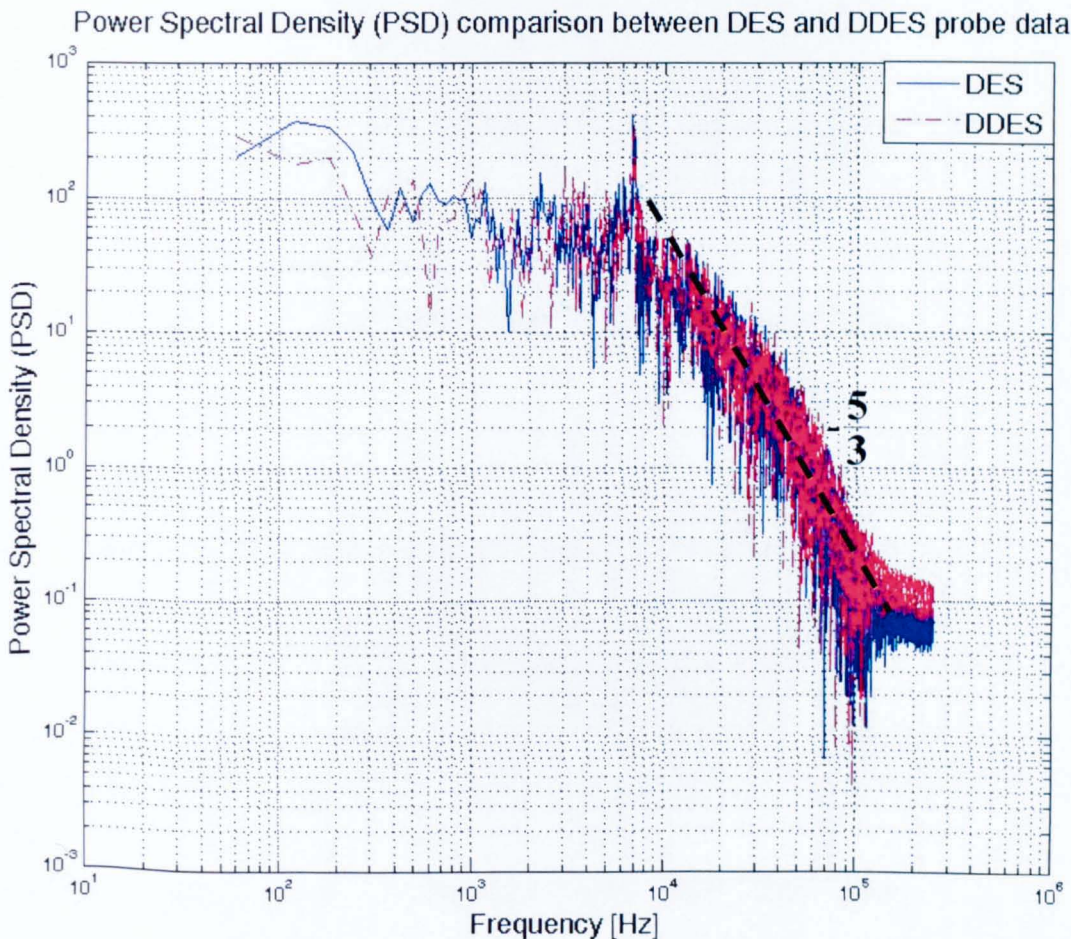


Figure 5.11

Power spectral density (PSD) estimate of pressure data stored at a probe in wake region, using the DES and DDES schemes.

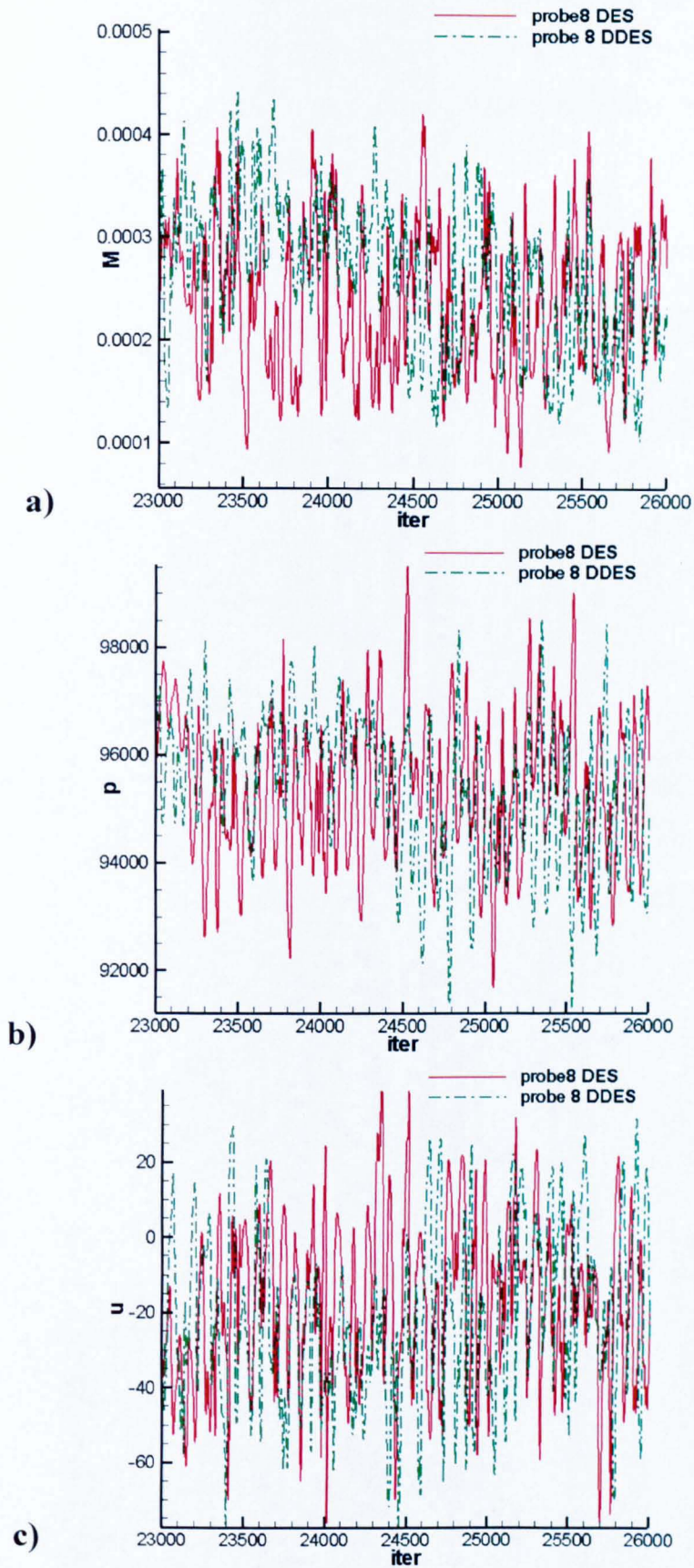


Figure 5.12(a-c)

Recorded data at different iterations probe using the DES and DDES schemes

a) Turbulent viscosity b) static pressure c) x-direction velocity

The other observation from the probes data is that the completely different flowfield variable values at the probe location with varying time are obtained, as presented in figure 5.12(a-c). It indicates that the simulation results from the DES and DDES simulation are bound to produce slightly different flow field picture.

5.2.6 Summary of the results $Re=1.4 \times 10^5$

Table 5.3 presents the overall comparison of results at $Re=1.4 \times 10^5$. It is clear that the results are quite encouraging. C_{pb} or base pressure is more negative in comparison with other studies. It may be improved by using finer mesh as used in Ref.[129]. Generally the results are satisfactory.

Case	Cd	St	$-C_{pb}$	θ_{sep}
DG-DES DES97	0.66	0.29	0.80	101°
DG-DES DDES	0.64	0.29	0.77	100°
Travin et al. ^[18]	0.65	0.28	0.70	93°
DES 97 Krishnan et al. ^[129]	0.58	0.29	0.64	98°
DDES Krishnan et al. ^[129]	0.60	0.28	0.69	99°
Roshko ^[130]	0.62-0.74	0.27	----	----

Table 5.4 Summary of results $Re=1.4 \times 10^5$

Table 5.3 presents the overall comparison of results at $Re=1.4 \times 10^5$. It is clear that the results are quite encouraging. C_{pb} or base pressure is more negative in comparison with other studies. It may be improved by using finer mesh as used in Ref.[129]. Generally the results are favourable.

5.2.7 Comparison of the velocity flowfield in the domain

Travin et. al (Ref. [18]) present the comparison of time averaged normalized velocity field in the domain with the experimental data as a measure of quality of the solution. Fig 5.13(a) is the comparison with the upper half as simulation and the lower half as the experimental data. Fig. 5.13(b) presents a comparison of time averaged centreline velocity aft of the circular cylinder with the experimental data. With the presence of different phenomenon including massive separation and vortex shedding, it is quite challenging to obtain this value correctly. The effect of mesh refinement is evident from solid and dashed line by Travin's simulations.

The overall comparison is not very good. However, the present simulation is in better agreement with the experimental data. Figure 5.13(a) is split and is separately compared with present simulation results in 5.13 (b) and (c). The simulations carried out in this study, again provides better flowfield picture.

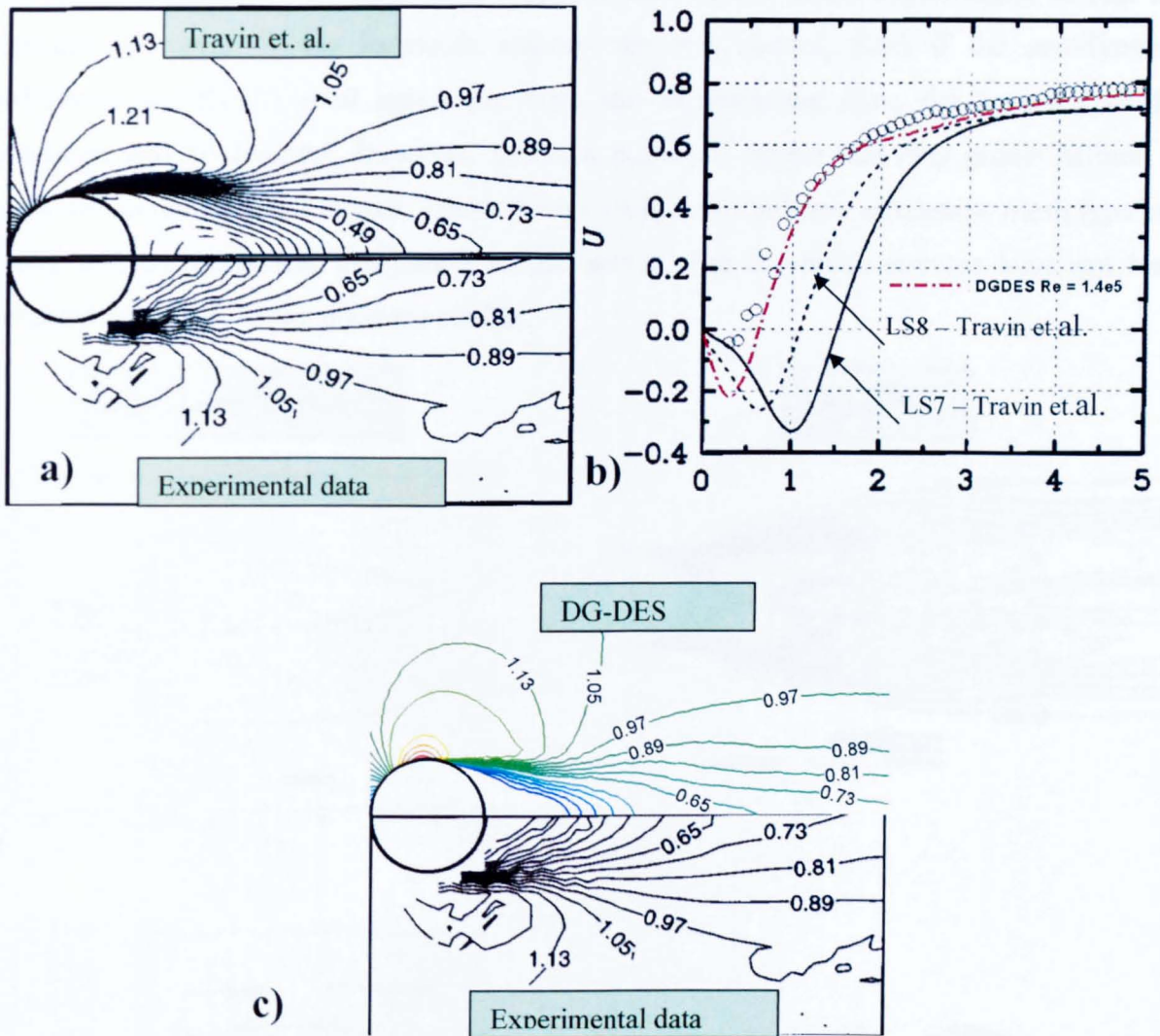
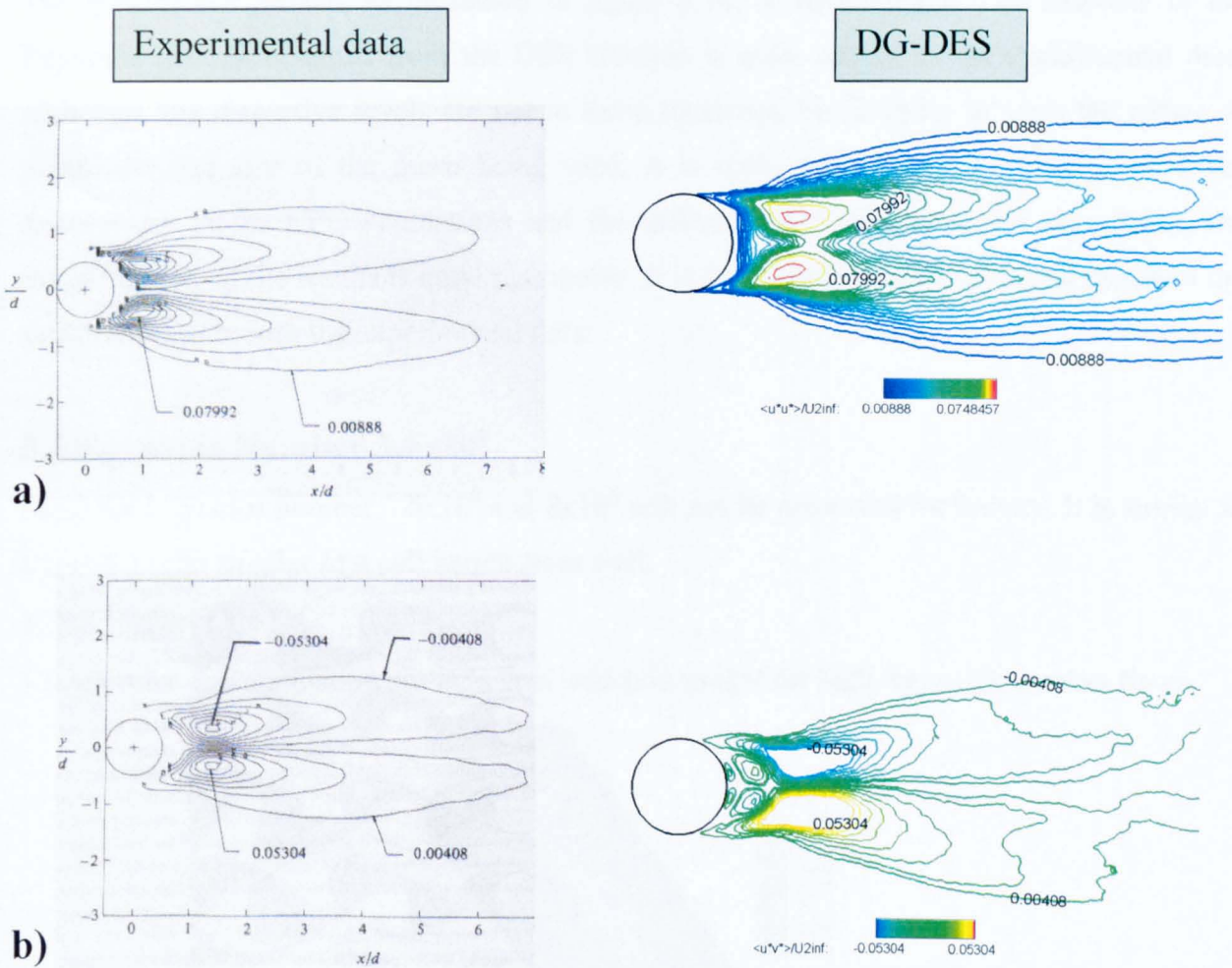


Figure 5.13 a) Comparison of time averaged normalized velocity field by Travin et. al.^[18] with experimental data^[127]. Travin et. al. results (upper side) with experiment data on lower side (picture from Ref [18]).
 b) Centre line velocity comparison downstream cylinder surface. Black solid and dashed lines are results from Travin et al. with experimental data plotted as circles
 c) Upper side DG-DES simulation lower side experimental data

5.2.8 Comparison of the Reynolds stresses from the DES simulation with the experimental data ^[127]

For any turbulent flow simulation, the comparison of the Reynolds stresses is very important but equally challenging. This comparison provides an overall resemblance of the real time flow turbulence compared with the simulation. The favourable comparison will indicate that the flow being simulated results in a good representation of the actual experimental or real life flowfield. However, if the Reynolds stresses are not correct, even if the aerodynamic coefficients are in good agreement with the experimental data, the accuracy of the simulation will be doubtful. However, this is a particular aspect that may prove difficult to match due to the different factors. These factors include the scheme efficiency, mesh type and quality and the numerical dissipation in the solver. The Reynolds stresses have not been presented frequently in the previous studies.



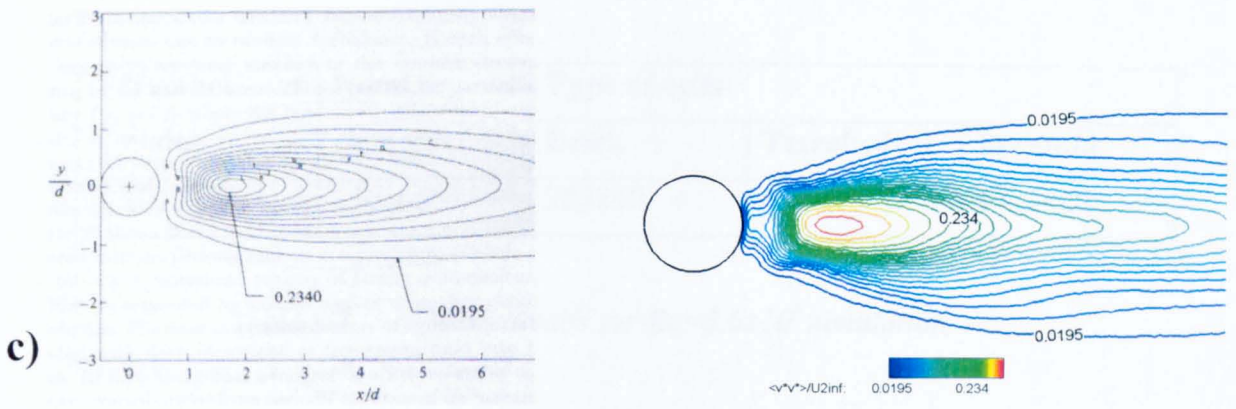


Figure 5.14 Comparison of the experimental Reynolds stresses^[127] at $Re=1.4 \times 10^5$ with the DES simulation at $Re=1.4 \times 10^5$

- a) $\langle u^* u^* \rangle / U_{inf}^2$ left: Experimental right: DES simulation
- b) $\langle u^* v^* \rangle / U_{inf}^2$ left: Experimental right: DES simulation
- c) $\langle v^* v^* \rangle / U_{inf}^2$ left: Experimental right: DES simulation

The general comparison, as presented in figure 5.14, is encouraging. The structure of the Reynolds stresses obtained from the DES solution is quite similar to the experimental data. Although, the respective levels are not at same locations, but keeping in view the nature of simulation and size of the mesh being used, it is quite satisfactory. Keeping in view the assumptions in the CFD simulations and the different uncertainties in the experiment, the overall quality of the results is quite reasonable. It is quite challenging to get good match of the simulated results with the experimental data.

5.3 Reynolds Number 3.6×10^6

Mesh for Reynolds number 3.6×10^6 and 8×10^6 will not be presented for brevity. It is similar to figure 5.1 with smaller first cell height from wall.

5.3.1 Yplus (Y+)

Y+ value for this simulation are quite low which is sought for high Reynolds number flows.

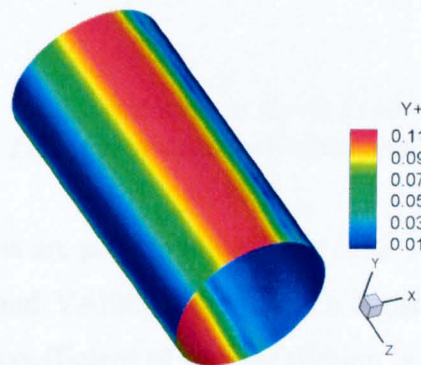


Figure 5.15 Y+ values over the surface of circular cylinder at $Re=3.6 \times 10^6$

Number of nodes	Number of elements	Type of cells		
		Brick	Tetrahedral	Pyramid
1012957	1703660	282240	0	1421420

Table 5.5 Mesh details for $Re=3.6 \times 10^6$ simulation

Reynolds Number	Mach Number	Velocity (m/sec)	Inviscid Flux Scheme	Turbulence Scheme
3.6×10^6	0.288	100	Roe	DES
3.6×10^6	0.432	150	Roe	DES

Table 5.6 Numerical scheme details

Table 5.4 provides the mesh details. Table 5.4 presents two cases which are simulated using the DES approach. Both cases have same Reynolds number but different velocity; to study the effect of Mach number on the flow simulation.

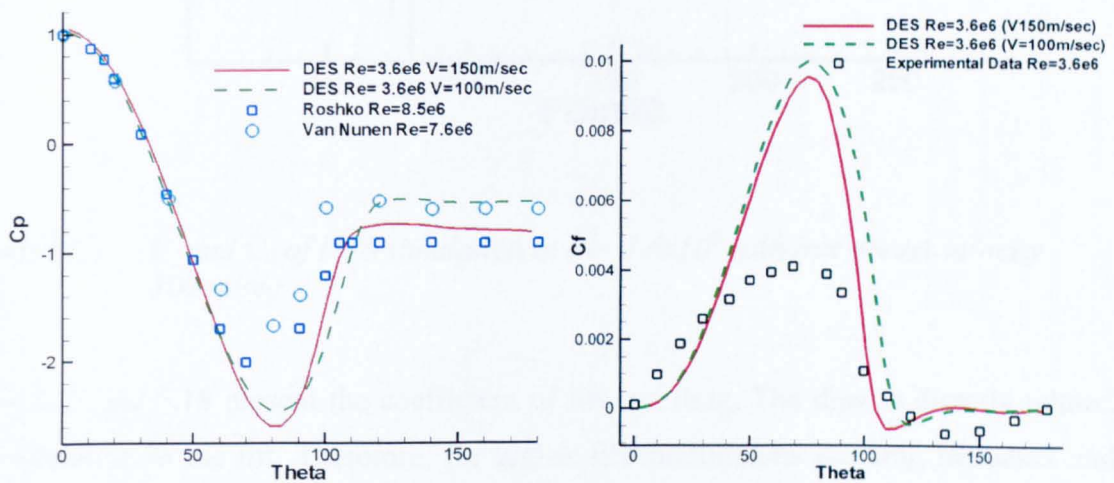


Figure 5.16 DES simulation at $Re=3.6 \times 10^6$
 Left: C_p comparison circular Right: C_f comparison

The results from the simulations are presented in figure 5.16. It is evident from the comparison of the velocity ($V=150\text{m/sec}$ and $V=100\text{m/sec}$) that the higher Mach number results in more drop in the C_p values and the coefficient of surface friction is relatively less. The skin friction at higher speeds reduces due to the boundary layer becoming thinner and that leads to

relatively early separation. It has an effect of more pressure variation along the surface in comparison with low Mach number flows. Again, the comparison of numerical C_p results is compared with higher experimental Reynolds number. It is due to limited experimental data available for comparison as stated before and presented in table 5.1.

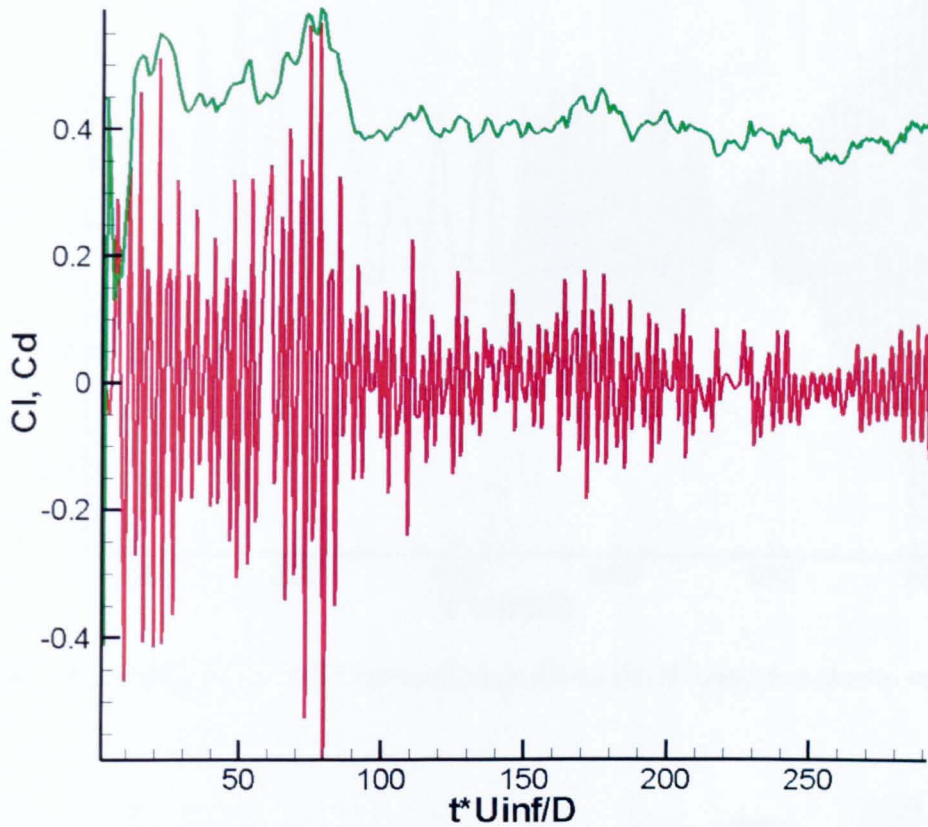


Figure 5.17 C_l and C_d of DES simulation at $Re=3.6 \times 10^6$ with freestream velocity 100 m/sec

Figure 5.17 and 5.18 present the coefficient of lift and drag. The drag is directly related with the modulation in the lift. Therefore, for higher lift modulations the drag increases and vice versa.

Figure 5.18 indicates another interesting phenomenon. The recording frequency of C_l and C_d is very important. In this figure, first half the plotted intentionally with a recording frequency of 150 time steps, while later half with recording frequency of 1. It can be seen that It filters the resultant parameter to quite a coarse shape. Care must be taken in ensuring that the sampling frequency is sufficient to predict the correct flowfield information.

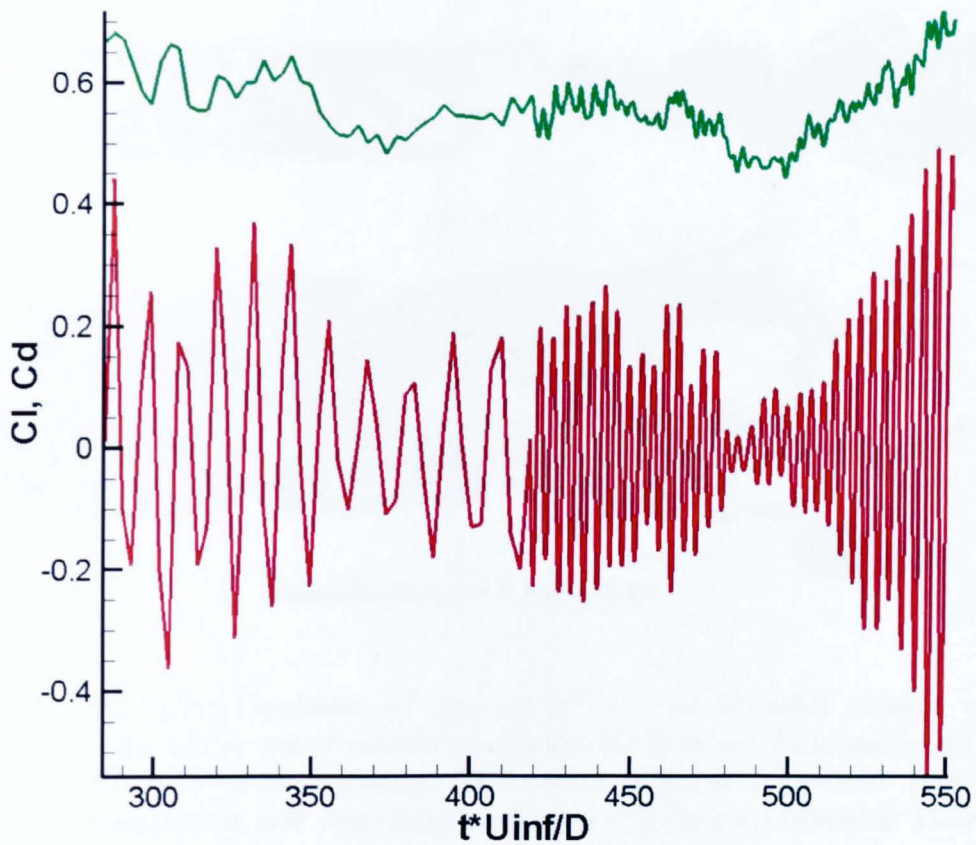
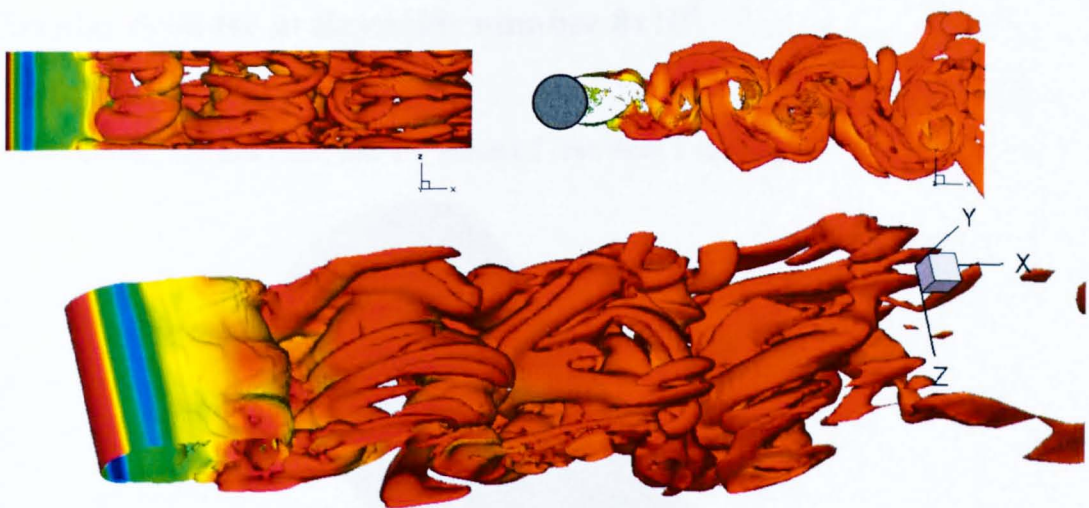


Figure 5.18 C_l and C_d of the DES simulation at $Re=3.6 \times 10^6$ with freestream velocity 150 m/sec



Reynolds Number $3.6e6$ (DES)
Velocity = 150 m/sec

Figure 5.19 DES flow simulation of circular cylinder at Reynolds number = 8×10^6 at $t=0.4575$ sec with freestream velocity of 150 m/sec. Instantaneous isosurface plot of vorticity magnitude 1000 coloured by static Pressure Top (left) : View from bottom side Top(right) View from side Bottom: Isometric View

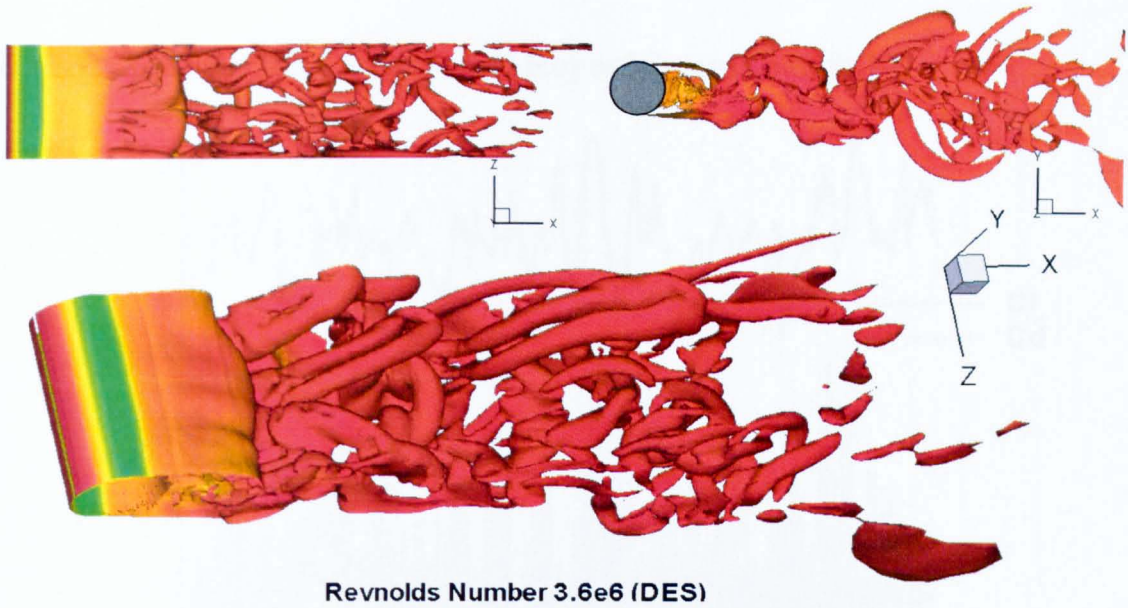


Figure 5.20 *DES flow simulation of circular cylinder at Reynolds number = 8×10^6 at $t=0.4575\text{sec}$ with freestream velocity of 100 m/sec. Instantaneous iso-surface plot of vorticity magnitude 1000 coloured by static Pressure Top (left) : View from bottom side Top(right) View from side Bottom: Isometric View*

Figure 5.19 and 5.20 presents the flowfield picture indicating a large number of scales in the flow typical of a turbulent flowfield.

5.4 Circular cylinder at Reynolds number 8×10^6

5.4.1 Yplus (Y+)

Similar to previous simulations, the Y+ value of less than 1 is sought.

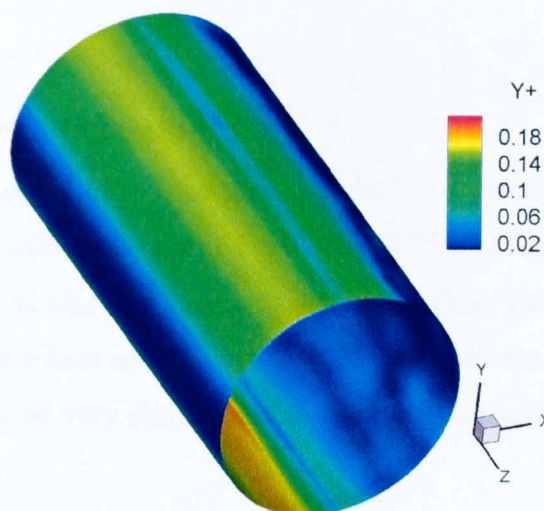


Figure 5.21 *Y+ values over the surface of circular cylinder at $Re=8 \times 10^6$*

Y+ value of well below 1 is obtained as presented in figure 5.21.

5.4.2 C_l C_d plot circular cylinder at Reynolds number 8×10^6

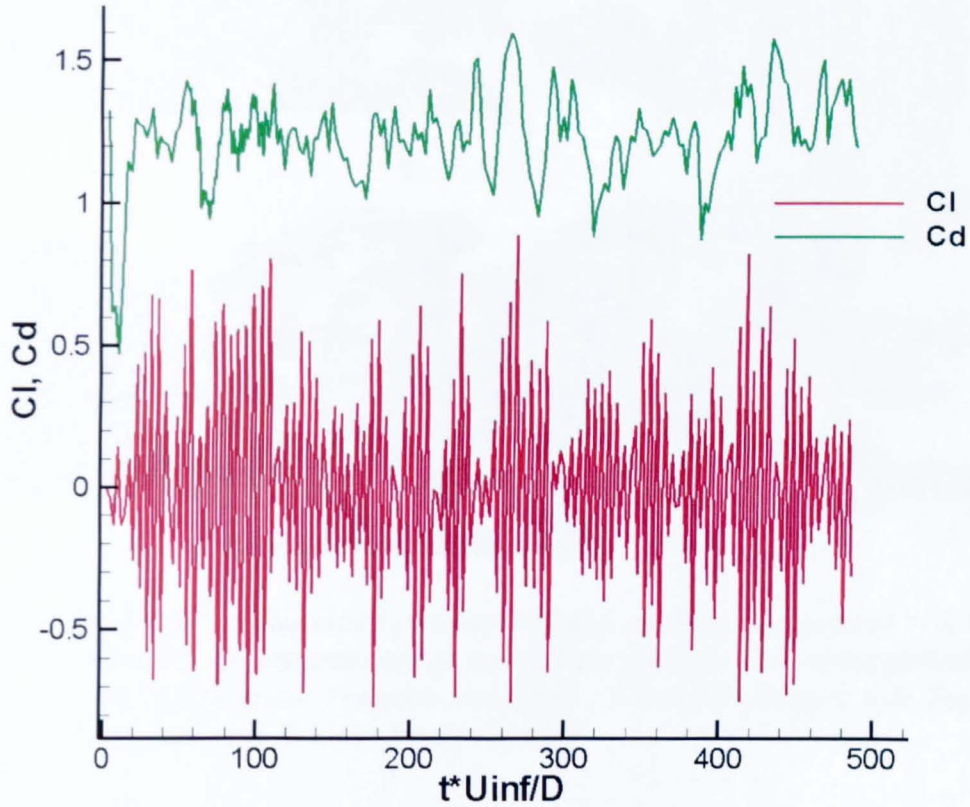


Figure 5.22 C_l and C_d of circular cylinder at $Re=8 \times 10^6$ using the DES scheme

Due to a large number of length scales of the vortices being shed from the circular cylinder, the lift and drag have varying amplitudes of modulations in their time history as presented in figure 5.22. It is typical of a massively separated flow field exerting fluctuating forces on the body of disturbance (object).

5.4.3 Vorticity magnitude contours

The short physical time step of 1×10^{-5} sec clearly indicates more detail and more length scales in the flow in comparison with time step of 5×10^{-5} (fig. 5.23 and fig. 5.24). It can be argued that certain small length scales are captured by short time step that results in the form generation of extra details which are skipped or dissipated by the large time step. Also, the solution is not expected to be very similar due to the LES dominated solver application in the flow.

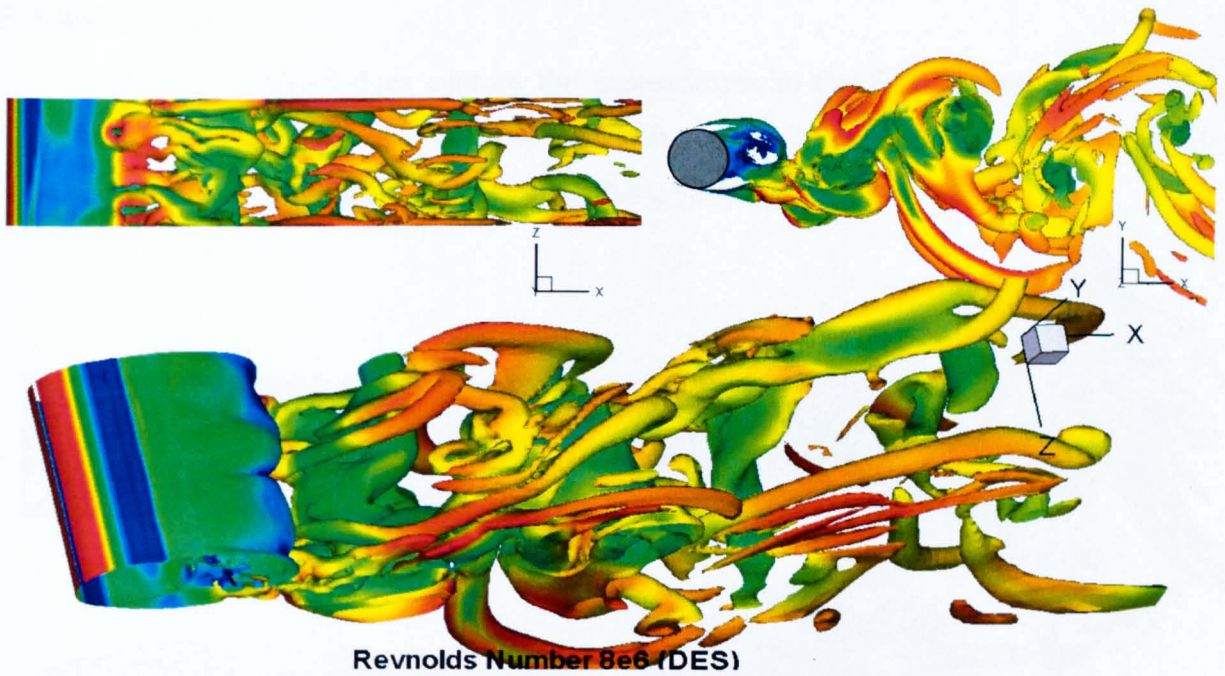


Figure 5.23 *DES flow simulation of circular cylinder at Reynolds number = 8×10^6 at $t=0.4575\text{sec}$. Instantaneous iso-surface plot of vorticity magnitude 1000 coloured by static Pressure Top (left) : View from bottom side Top(right) View from side Bottom: Isometric View*

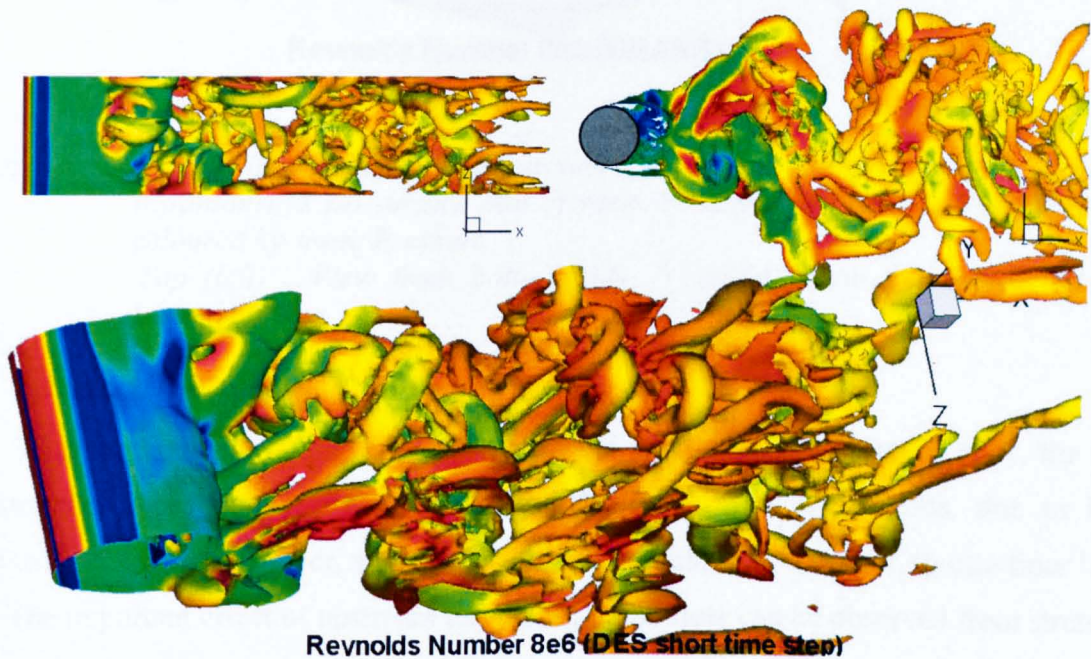


Figure 5.24 *DES flow simulation of circular cylinder at Reynolds number 8×10^6 . Instantaneous iso-surface plot of vorticity magnitude 1000 at $t=0.4575\text{sec}$., coloured by static Pressure Top (left) : View from bottom side Top(right) View from side Bottom: Isometric View*

5.4.4 URANS

Although URANS does capture the unsteadiness in the flow as presented by figure 5.25, but clearly the details of flow field are much coarser in terms of the fine scale turbulent structures. It is primarily due to the excessive dissipation by RANS.

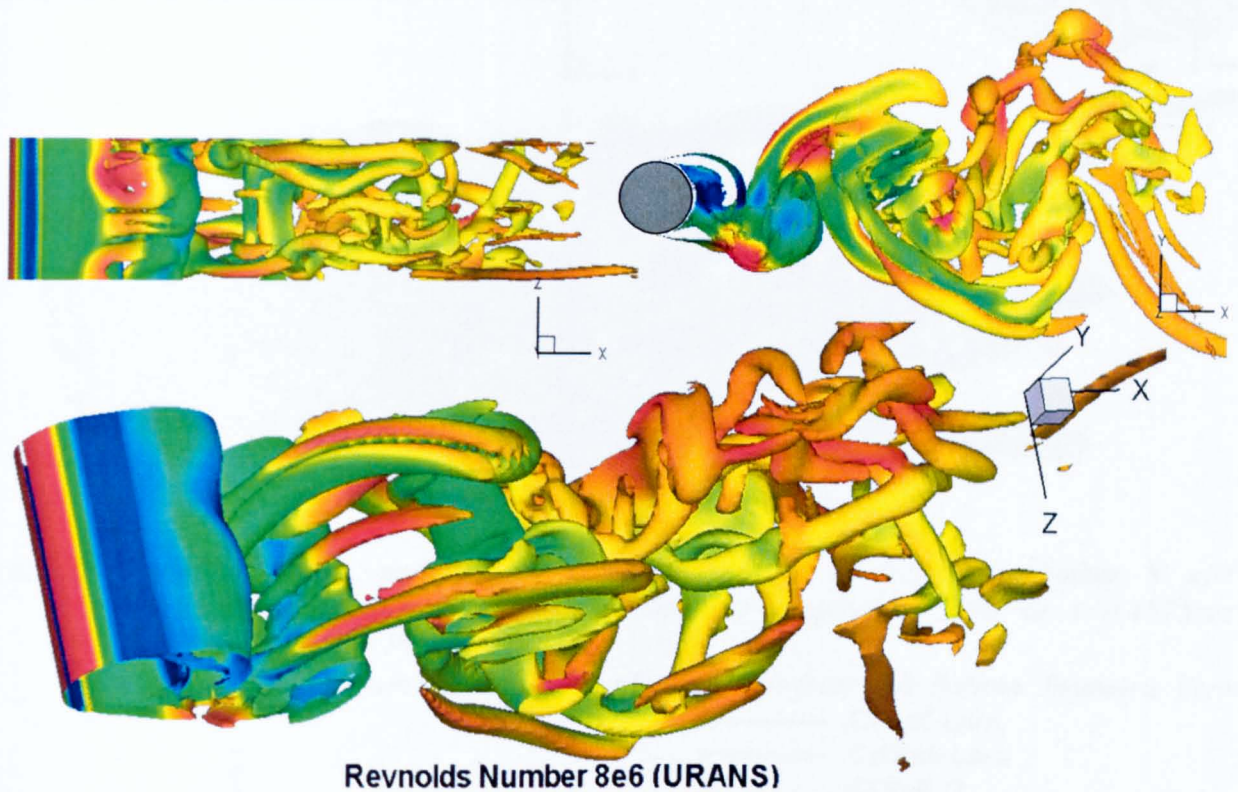
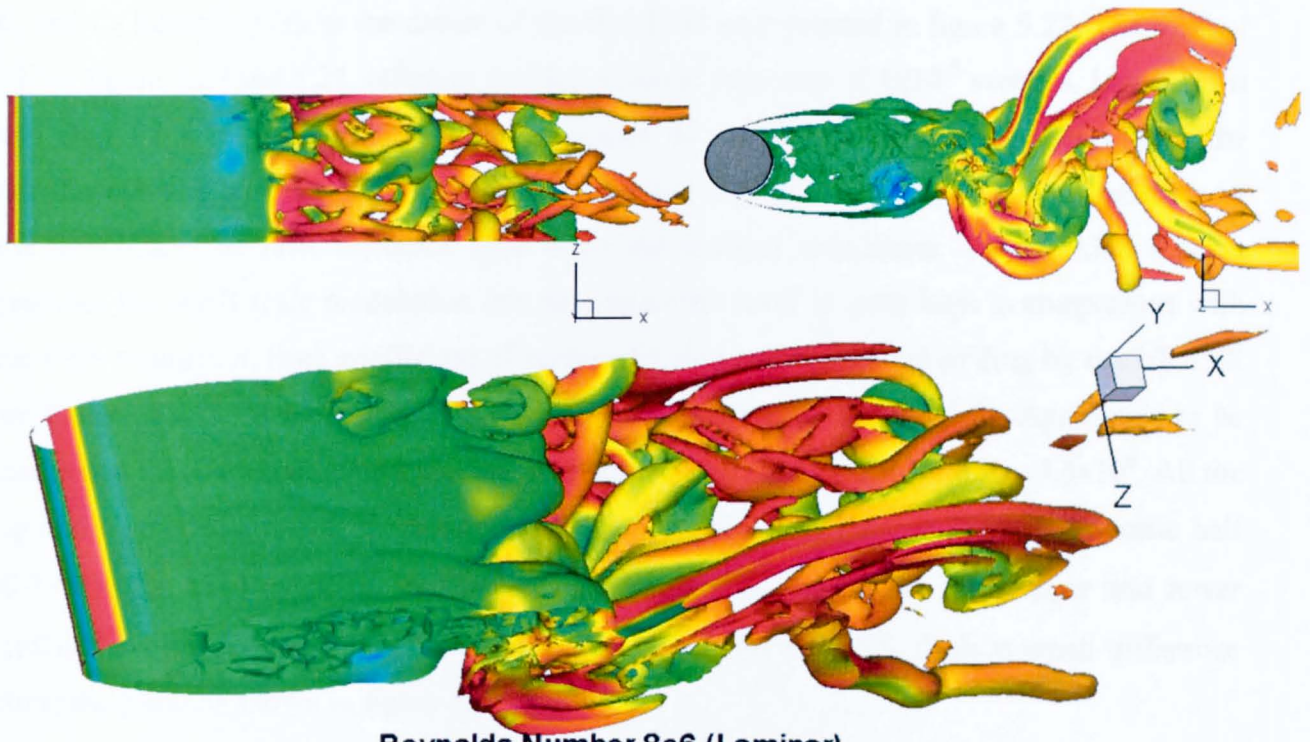


Figure 5.25 *URANS flow simulation of circular cylinder at Reynolds number 8×10^6 . Instantaneous iso-surface plot of vorticity magnitude 1000 at $t=0.4575\text{sec.}$, coloured by static Pressure
Top (left) : View from bottom side Top(right) View from side Bottom: Isometric View*

5.4.4 Laminar Flow

With the laminar solution, the flow separates early (As seen from C_f plot), the shear layer stretches more in comparison with other turbulent flow simulations, due to lesser turbulence in the flow. However, after the shear layer destabilizes, it breaks up into finer length scales. The important effect of upstream turbulence in the flow can be observed from stretching of the shear layer as presented in figure 5.26.



Reynolds Number 8e6 (Laminar)

Figure 5.26 *Laminar flow simulation of circular cylinder at Reynolds number 8×10^6 . Instantaneous iso-surface plot of vorticity magnitude 1000 at $t=0.4575\text{sec.}$, coloured by static Pressure*

Top (left) : View from bottom side Top(right) View from side Bottom: Isometric View

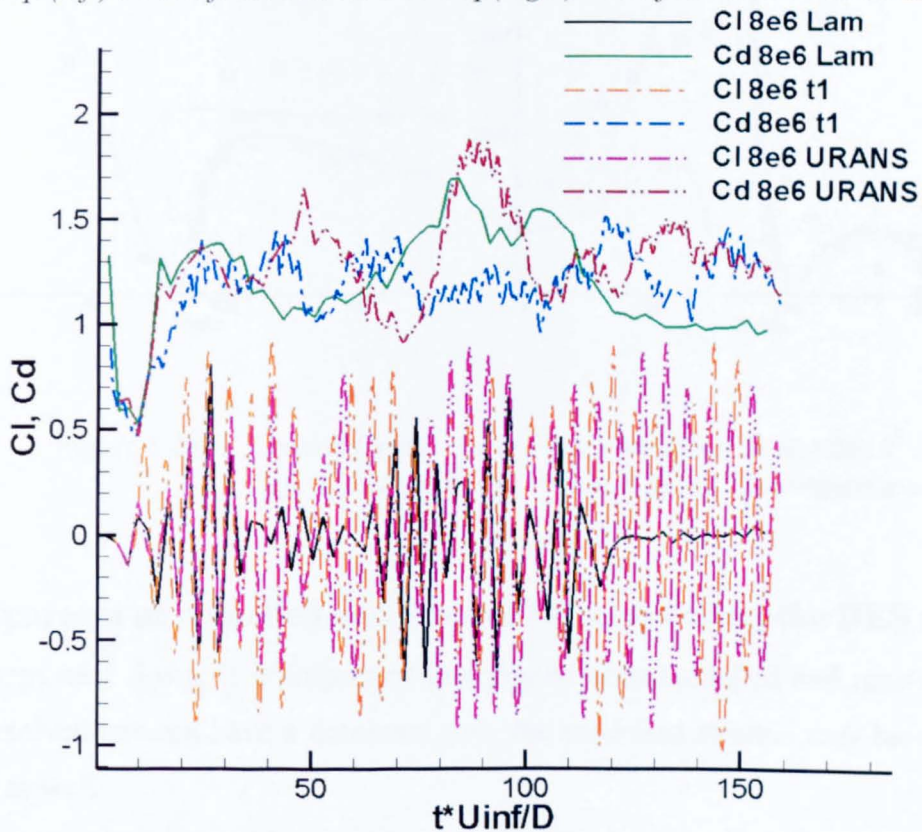


Figure 5.27 *C_l and C_d plots at $Re=8 \times 10^6$ using DES, URANS and Laminar flow*

C_l and C_d histories present the nature of the flowfield as presented in figure 5.27. The symbol ‘t1’ in figure 5.27 and 5.28, refers to smaller physical time step of 1×10^{-5} seconds. Laminar lift and drag force is lacking small scale variations due to long shear layer presence over the circular cylinder with much lesser friction as shown in figure 5.28 (right). Due to absence of the turbulence, the flow separates quite early for laminar simulation. The URANS scheme provides the small scale modulation but its dissipation level is quite high in comparison with the DES simulation. Both coefficient of surface friction and coefficient of drag by the URANS are higher than DES highlighting more dissipative nature of the flowfield. Again it is to be mentioned that the experimental C_f data available for the comparison is for $Re=3.6 \times 10^6$. All the C_p and C_f plotted are over the complete surface of circular cylinder split into symmetric half ($0-180^\circ$). For majority of the time averaged simulations, the results from upper and lower surface have been overlapping (symmetric). However, for URANS, there is small difference along the peaks as shown in figure 5.28.

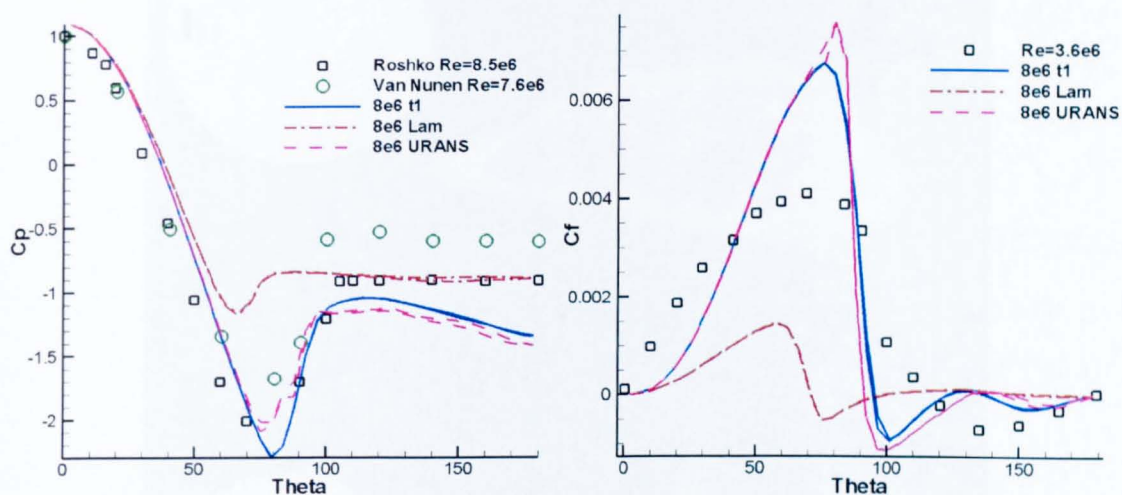


Figure 5.28 C_p and C_f plot using DES simulation at $Re=8 \times 10^6$
 Left: C_p comparison circular Right: C_f comparison

5.4.6 Comparison of modelled and resolved stresses using the DES scheme

For highly separated flows, it is important to compute both modelled and resolved stresses. Although, resolved stresses have a dominant role, the modelled stresses may have significant contribution as well.

Generally the modelled Reynolds stresses are more dominant in boundary and shear layers with relatively insignificant contribution from resolved stresses for attached flows. However,

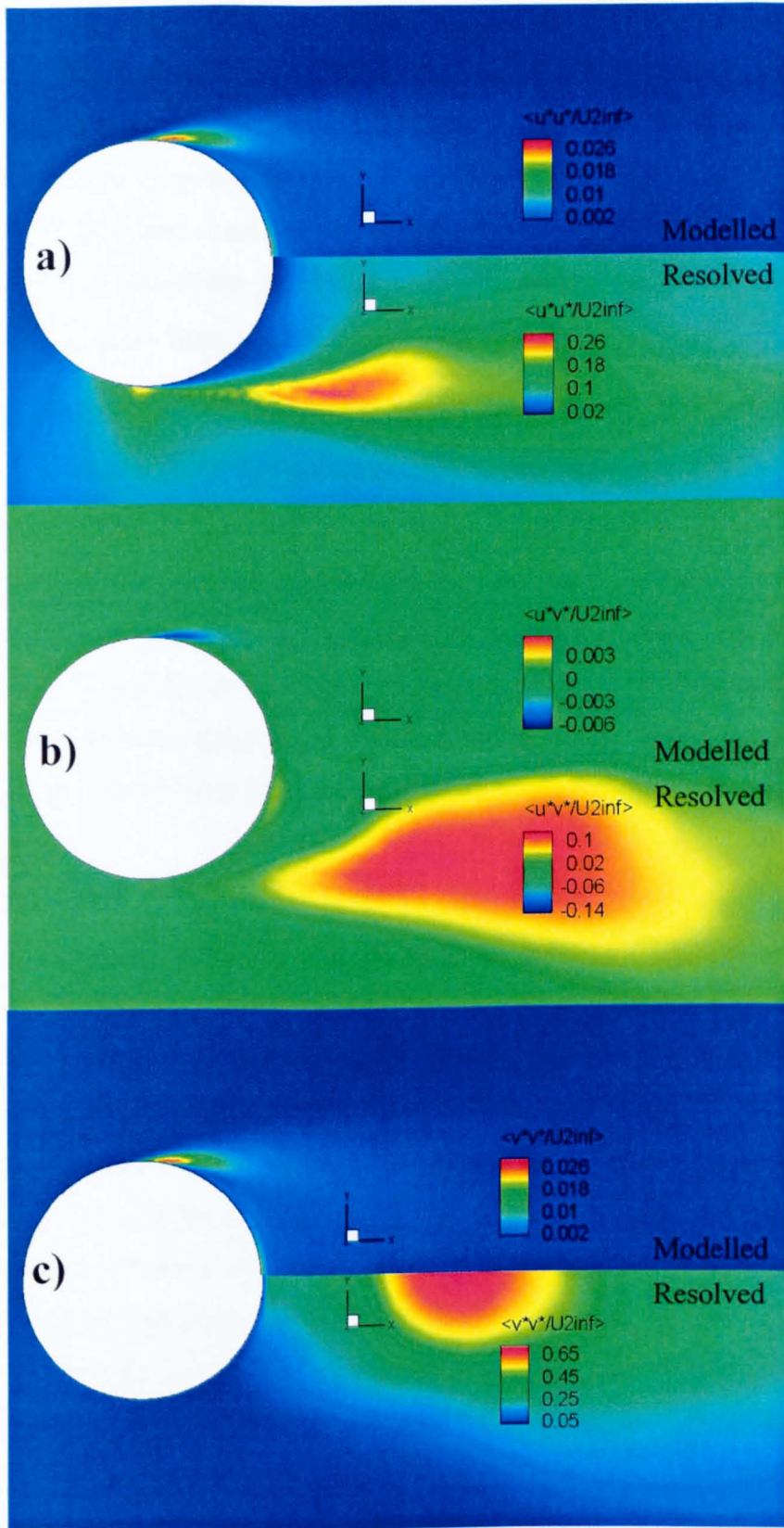


Figure 5.29 Comparison of modelled and resolved stresses using DES simulation at $Re=8 \times 10^6$. Upper half is modelled stresses and lower half is resolved stresses.
 a) $\langle u^*u^* \rangle / U_{inf}^2$ b) $\langle u^*v^* \rangle / U_{inf}^2$ c) $\langle v^*v^* \rangle / U_{inf}^2$

for massively separated flowfields, the resolved stresses play a dominant role. In hybrid schemes like DES, it is important to appreciate the contribution by both modelled and resolved stresses. Generally for mild separation, it is better to present the Reynolds stresses as a accumulative contribution by both modelled and resolved stresses. Figure 5.29 presents a comparison of modelled and resolved stresses for $Re=8 \times 10^6$. It is evident that the resolved stresses are clearly a dominant contributor of the overall Reynolds stresses. Roughly, $\langle u^* u^* \rangle / U_{inf}^2$ contribution from resolved stresses is 10 times that from the modelled one. The $\langle u^* v^* \rangle / U_{inf}^2$ contribution from resolved stress is 30 times that of the modelled stress and $\langle v^* v^* \rangle / U_{inf}^2$ contribution from the resolved stress is 25 times that of the modelled stress. It indicates that although the contribution from the modelled stresses is roughly an order of magnitude lower than the resolved stresses for this case yet the modelled stresses cannot be neglected. One point to notice is the concentration location of these stresses. The resolved stresses near the surface of the circular cylinder (boundary layer and shear layer region etc.) are negligible; however, these are the areas of maximum stress contribution by modelled stresses. Hence, to obtain an overall close proximity of the Reynolds stresses, these stresses should be added in the domain.

5.5 Conclusions

The high Reynolds number flows over circular cylinder are natural DES cases. The blunt body with high Reynolds number flows causes the massive separation and instability in the downstream direction of circular cylinder in the domain. The new turbulent viscosity generated by this phenomenon is independent of the upstream turbulent viscosity.

The three commonly reported cases for high Reynolds number flows over circular cylinder are simulated at Reynolds number of 1.4×10^5 , 3.6×10^6 and 8.0×10^6 . The overall results are very encouraging and the flowfield turbulence, vortical structures and flow parameters are well captured. The shedding frequency, pressure distribution and skin friction coefficient values of the simulated results match well with the other published studies. The computed resolved stresses also provide satisfactory comparison with the experimental data, better than one of the reported studies which is done with coarser than present grid. This particularly is very encouraging from the perspective of the applicability of the hybrid RANS-LES methodology for massively separated flow at Reynolds numbers which are still prohibited by LES simulations. The size of the grid used is roughly an order less than what is required by LES.

6 Flapping Wing with Delaunay based moving mesh

This chapter is divided into two parts. An overview of dynamic grid deformation scheme in 2D, using Delaunay graph mapping to simulate flapping aerofoil propulsion at low Reynolds numbers of 9,000 to 27,000 is presented in first part. A rigid NACA0033 aerofoil attached with different flat plates of varying stiffness values is used as a flapping aerofoil element. Different chordwise flexibility values corresponding to varying thickness flat plates are simulated at frequency ranges of 0.29-2.54 Hz with constant leading edge amplitude of 17.5mm according to the experimental work of Heathcote and Gursul, (AIAA J., vol. 45, No. 5, 2007, pp. 1066-1079).

The extension of 2d implementation to 3d MPI version of DG-DES is covered in the second part. An oscillating rigid NACA0012 wing is simulated in heave motion to validate the implementation. The 3D wing is fully rigid and the simulation is done to compare the results with the experimental work of Heathcote and Gursul, (AIAA-2006-2870). The simulation done for the rigid wing is essentially 2D. The resultant instantaneous coefficient of thrust is in good agreement with the experimental data.

6.1 Introduction

Observing natural evolution of various mechanisms in living species has been very intuitive for the human kind. Spanning over hundreds of millions of years, these mechanisms for propulsion, stability and maneuverability are arguably thought to be the most refined ones for a particular environment and operating conditions for particular specie. Owing to prevailing geo-strategic circumstances, there is a surge in desire to build micro-air vehicles (MAVs) with various roles and capabilities. One recent example of this is “MOD Grand Challenge” by MoD, UK. Various applications of such MAVs range from military usage including reconnaissance and surveillance to urban environment usage including reconnoiter large buildings or regions of interest, identification of a potential threat, assist in rescue operations. Unlike conventional propulsion methods using separate thrust, lift and control devices for stability and maneuvering, MAV’s have various constraints including size, weight, stability and maneuverability prompting for non-conventional approach.

The degree of suppleness, stability and maneuverability portrayed by various species in nature including insects, birds and fishes to name some, have revitalized interest of large section of aerodynamic community looking for non-conventional MAV's design. One distinct feature in above mentioned locomotion and propulsion is the use of single surface for lift and propulsion through flapping wing. Reynolds number is a very import aerodynamic parameter for the relative study of flapping motion of birds etc. Owing to their small size, typically in centimeters, and slow speed, the general Reynolds number range is from 10^3 - 10^5 . Ref. [96] provides a good starting point about basics of MAV's and some related research.

The ability of oscillating wing to produce thrust was first described by Knoller^[97] and Betz^[98] in 1909 and 1912 respectively in their independent studies. They observed that a wing oscillating sinusoidally in a cross-stream of flow creates an effective angle of attack leading to a force vector normal to the relative flow direction. This force vector gives both lift and thrust. This effect known as the Knoller-Betz effect was demonstrated experimentally by Katzmayr^[99]. In 1922, Birnbaum^[100,101], suggested oscillating wing as a possible 'alternate to propeller' mechanism for propulsion. The mainstream of aerodynamic community, however, concentrated on lifting forces instead of drag or propulsive forces due to its application in flutter analysis, a topic of prime interest during that period. In 1935, Theodorsen^[102] derived expressions for the unsteady lift and moment on a flat plate undergoing combined sinusoidal pitching and plunging motion. It was based on the inviscid, incompressible, oscillatory flat plate theory. Garrick^[103] further theoretically determined the thrust force and predicted that the plunging aerofoils generate thrust over the whole frequency range while pitching aerofoils do so only beyond a critical threshold frequency as a function of location of the pivoting point. In 1939, Von Karman and Burgers^[104] theoretically related the negative drag (thrust) production in conjunction with the shape and position of a double row of counter rotating wake vortices generated by bluff bodies. In 1939, Silverstein and Joyner^[105] experimentally verified Garrick's prediction while Bratt^[106] did visualization experiments to bolster what we call now von Karman vortex street generation for different wake flows. Freymuth^[107], Koochesfahani^[107], Jones^[108], Dohring and Platzer^[109] and Lai and Platzer^[110] showed experimentally the different wake structures generation based on plunge frequency and amplitude. They typically characterized wake structures as thrust producing, neutral and drag producing.

The majority of the experiments carried out in different experimental studies in the literature have used rigid bodies. However, in view of the propulsion mechanism in the natural world, all the flapping, hovering or plunging motions are done by flexible surfaces. Unfortunately, a little work has been done on flexible bodies in comparison with the rigid body experimentation. It has been reported through numerical simulations that higher efficiencies are achieved with flexible surfaces as compared with rigid bodies [111-112]. Isaac et al. [113] have done water tunnel experiments on a flapping-and-pitching thin flat plate wing of semi elliptic planform apart from studying flapping wing based MAV's [117,118]. Recent water tunnel experiments by Heathcote and Gursul [114] at low Reynolds number have shown that a degree of flexibility is beneficial for thrust supplement and better efficiency.

This study is related with the numerical simulation of the experiments done by Heathcote and Gursul [114] to get further insight of the flow physics of flapping wing unsteady aerodynamics. With the detailed unsteady flow field information, the basic aim is to understand the mechanism for thrust production in relation with the vortex shedding, plate flexibility, and the role that the leading edge induced vortices play in the process.

6.2 Case setup and Mesh Deformation

Schematic representation of the aerofoil element is shown in figure 6.1. The flapping aerofoil element consists of a rigid aerofoil section (NACA0033) and a flexible flat plate tail section. Different parameters used in this study are also presented in figure 6.1 for their clarification.

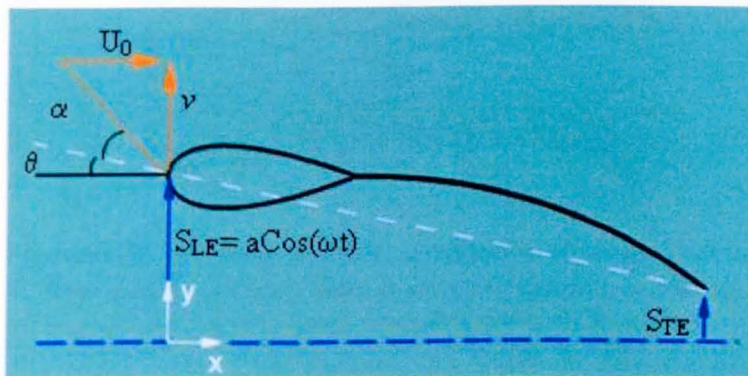


Figure 6.1 Schematic diagram of flapping aerofoil with flexible tail heaving sinusoidally in vertical (cross-flow) direction

Due to the geometric deformation occurring at each interval of time including relatively large tail movement as shown in Fig. 6.2, selection of dynamic grid technique to be used is of great importance. Two options available are either to “remesh” at each time step or “deform the mesh” by keeping the same topology. With the remesh option, the number of nodes, faces and cells change at each time step. This requires the update the mesh connectivity at each time step with a variable mesh size in terms of the number of elements and faces. The mesh temporal flowfield history is to be reconstructed for every new mesh as well. “Remesh” is not a favourite option in terms of computational time and cost so the mesh deformation becomes an obvious choice. Nevertheless, the main strength of the “remesh” tool is its extreme flexibility to adapt to the highly deformed domain. Most mesh deformation methods based on spring analogy were iterative in nature such as the one proposed by Batina et al.^[48,49]. The basic idea of this methodology was to treat the edge between two nodes as a spring with certain stiffness. Therefore, the edge can be compressed and elongated similar to springs with certain governing rules to avoid them crossing over. Following the same principle, different improvements have been proposed in the literature^[115, 50]. However, these iterative methods can drastically increase the computational cost of the grid deformation, particularly for highly stretched viscous meshes with large deformations, such as in our case during the maximum deflection of tail in up and down plunge.

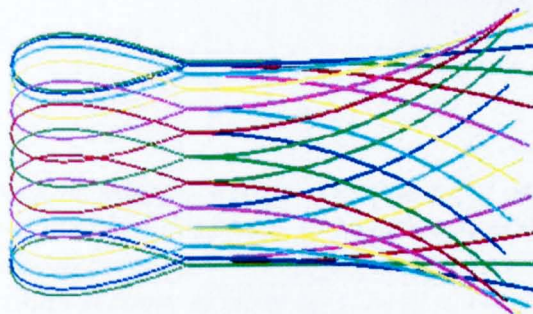


Figure 6.2 *Flapping aerofoil snapshots at different interval of time during pitching motion showing relative tail motion*

6.2.1 Mesh Details

Although different meshes including pure structured and unstructured type are generated, the baseline grid present here is of hybrid nature as shown in figure 6.3. It has 27803 node points

with 36651 triangular and quadrilateral elements. Wake size is about 3.5 times the length of aerofoil element. Domain length is 5 times aft and 8 times downstream with height of 5 times of the length of aerofoil element. The mesh was generated through commercial software “Gambit” in generic mode and then read directly by the solver.

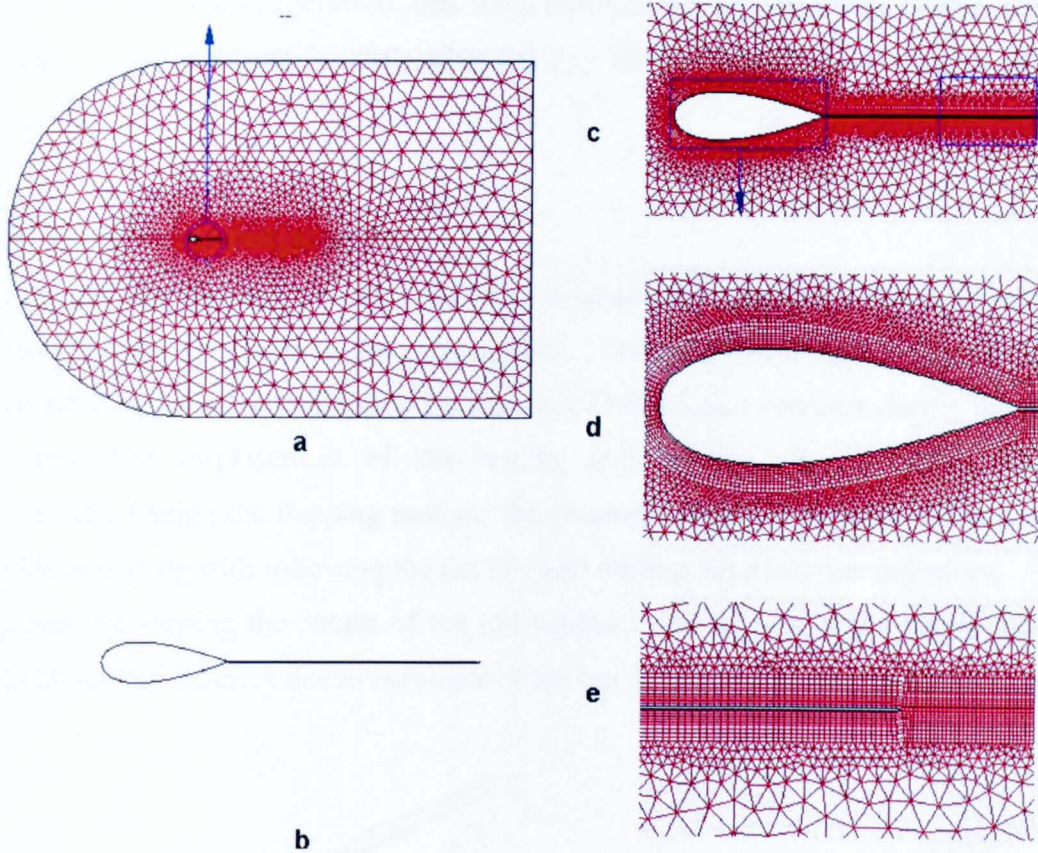


Figure 6.3 Mesh details of the flapping aerofoil comprising of aerofoil section NACA0033 and flexible tail section of attached flat plate: a) complete domain mesh; b) outline of the flapping aerofoil element; c) mesh around flapping aerofoil element; d) close-up view of aerofoil section; e) close-up view of tail section

To facilitate the meshing, the tip of flat* plate was made pointed by creating a small notch at the end. The grid near the aerofoil element and in the wake is structured with clustering towards the wall to maintain the numerical accuracy of the boundary layer and the wake resolution. Delaunay graph was generated using selected nodes of the aerofoil section and outer

* Private communication with Prof. I. Gursul

domain as shown in figure 6.7. As described earlier, the most critical grid deformation stage is when tails is at peak trailing edge amplitude in upward and downward plunging motion. A good control of the near wall mesh was achieved using Delaunay graph mesh deformation as shown in figure 6.9 and figure 6.10. Also, the fact that a single Delaunay graph was sufficient to simulate the complete flapping motion considerably reduced the computational cost of whole mesh deformation. From our own experience, this large deformation and clustered viscous near wall mesh can cause huge problems for the spring analogy based methods in robustness and mesh quality.

6.2.2 Tail motion specification

For the tail flapping, the curvature is taken as quadratic function of the elements of tail section to give a closer proximity to the experiments*. Total length of the tail is kept constant by keeping the edge length of all the meshed elements of tail section constant during the motion. The time dependant displacement of the leading and trailing edge is known from the experimental data. During the flapping motion, the quadratic shape of flapping tail and its total length are ensured along with following the leading and trailing edge location trajectory.

However, by keeping the length of the tail constant, the lengths of the upper and lower surfaces of tail will be different due to curvature at the trailing edge as shown in figure 6.3a.



Figure 6.4 *Due to finite thickness of the flapping tail, the curvature effects will cause the trailing edge to have different x-axis location for upper and lower surface with fixed length*

A small routine was written to extend the shorter surface to match the x-axis location by keeping the initial angle to the sharp trailing edge notch constant.

6.2.3 Fast Grid Deformation using Delaunay Graph Mapping

A simple, efficient and non-iterative grid deformation technique based on Delaunay Graph Mapping^[120] is used. This method gives an order of magnitude improvement in CPU time over traditional spring analogy methods^[120]. This method is divided into four main steps as follows:

a) Generate a Delaunay graph based on selected mesh points on flapping aerofoil and outer domain to encompass all the interior mesh nodes as shown in figure 6.7.

b) Locate all the mesh points in the domain with respect to generated Delaunay graph

Locating the Graph elements for all the mesh points is done by checking the area ratios of the mesh nodes with Delaunay Graph nodes. e.g., a mesh node P will be in a Delaunay Graph element ΔABC only if ΔABP , ΔBCP and ΔCAP are not negative.

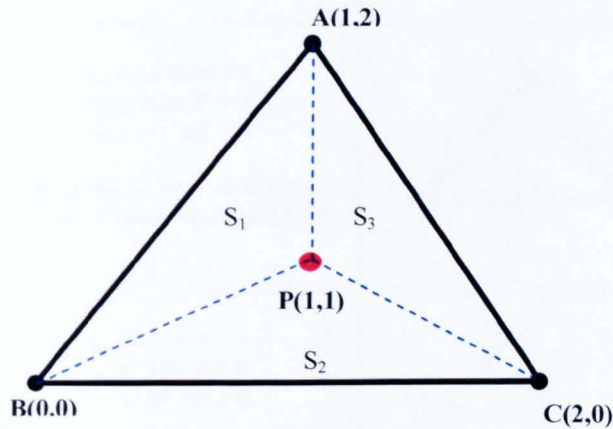


Figure 6.5 A Graph element ΔABC with a mesh node P

$$\Delta ABC \text{ or } S = \frac{1}{2} \begin{vmatrix} x_A & y_A & 1 \\ x_B & y_B & 1 \\ x_C & y_C & 1 \end{vmatrix}; \quad \Delta CAP \text{ or } S_3 = \frac{1}{2} \begin{vmatrix} x_A & y_A & 1 \\ x_P & y_P & 1 \\ x_C & y_C & 1 \end{vmatrix} \quad (6.1)$$

$$\Delta ABP \text{ or } S_1 = \frac{1}{2} \begin{vmatrix} x_A & y_A & 1 \\ x_B & y_B & 1 \\ x_P & y_P & 1 \end{vmatrix}; \quad \Delta BCP \text{ or } S_2 = \frac{1}{2} \begin{vmatrix} x_P & y_P & 1 \\ x_B & y_B & 1 \\ x_C & y_C & 1 \end{vmatrix}$$

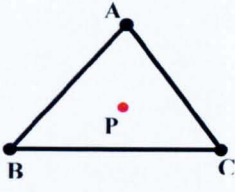
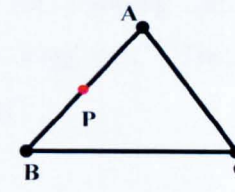
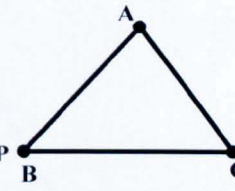
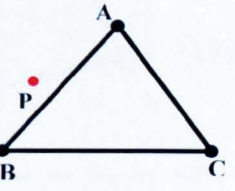
Delaunay Graph element Location for interior mesh	Schematic Description <ul style="list-style-type: none"> ● Moving Mesh node ● Delaunay Graph Element Node
S_1 or $\Delta ABP > 0$ S_2 or $\Delta BCP > 0$ S_3 or $\Delta CAP > 0$ Conclusion: Point P is located in Delaunay Graph element ΔABC	
S_1 or $\Delta ABP = 0$ S_2 or $\Delta BCP > 0$ S_3 or $\Delta CAP > 0$ Conclusion: Point P is located in Delaunay Graph element ΔABC	
S_1 or $\Delta ABP = 0$ S_2 or $\Delta BCP = 0$ S_3 or $\Delta CAP > 0$ Conclusion: Point P is located in Delaunay Graph element ΔABC	
S_1 or $\Delta ABP < 0$ S_2 or $\Delta BCP > 0$ S_3 or $\Delta CAP > 0$ Conclusion: Point P is not located in Delaunay Graph element ΔABC	

Table 6.1 Various possible situations during Graph element location of all the mesh points in the moving mesh domain

Area	Value (unit)
S or ΔABC	2
S_1 or ΔABP	0.5
S_2 or ΔBCP	1
S_3 or ΔCAP	0.5

Table 6.2 Area ratio of the different elements

$$e_i = \frac{S_i}{S}, i = 1, 2, 3 \quad (6.2)$$

$$x_P = e_1 x_C + e_2 x_A + e_3 x_B \quad (6.3)$$

$$y_P = e_1 y_C + e_2 y_A + e_3 y_B$$

$$e_1 = 0.25; e_2 = 0.5, e_3 = 0.25$$

$$x_P = 1$$

$$y_P = 1$$

c) Move the Delaunay graph according to the specified flapping aerofoil motion

The domain is deformed with point C getting relocated to C^* . Due to this deformation, the Delaunay Graph element will be deformed to ΔABC^* .

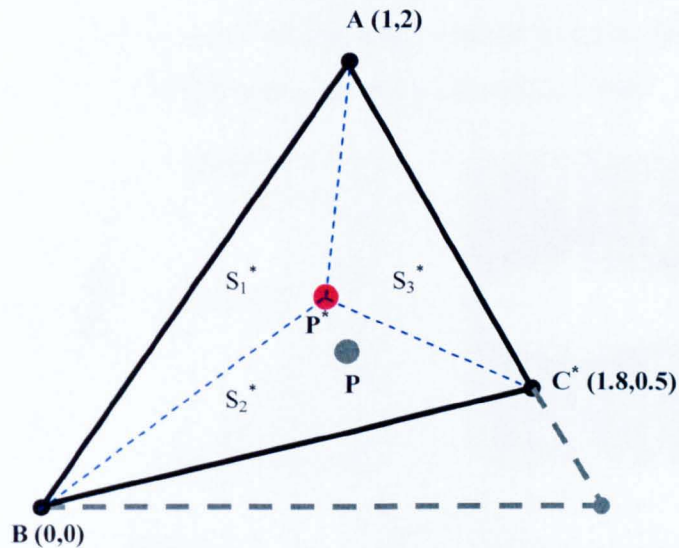


Figure 6.6 A deformed Graph element ΔABC^* with a relocated mesh node P^*

d) Relocate the interior nodes to adjust the whole domain mesh as per flapping aerofoil motion

The coordinates of moving mesh node P will be :

$$x_{P^*} = e_1 x_{C^*} + e_2 x_A + e_3 x_B$$

$$y_{P^*} = e_1 y_{C^*} + e_2 y_A + e_3 y_B$$

$$e_1 = 0.25; e_2 = 0.5, e_3 = 0.25$$

$$x_{p^*} = 0.95$$

$$y_{p^*} = 1.125$$

Note that we have used the area ratios calculated before the deformation to get the new position of moving mesh point P^* . Further in depth details are given in Ref.[75]. Due to flapping motion, the aerofoil element is simultaneously becoming convex at one side and concave on the other side. Delaunay graph is obtained by creating Delaunay triangulation of the selected points as described in step 'a' above. To improve the robustness, a modification to the graph formation has been made so that a single graph is required without repeated graph generation during the flapping motion. To achieve this, we ensure that all the graph elements have at least one node from the outer domain or aerofoil element to minimize any localized degradation effect due to convex/concave region swapping between the flap and the aerofoil junction. By doing so, some of the graph elements are no longer Delaunay but this does not affect the purpose of serving as a mesh transformation map.

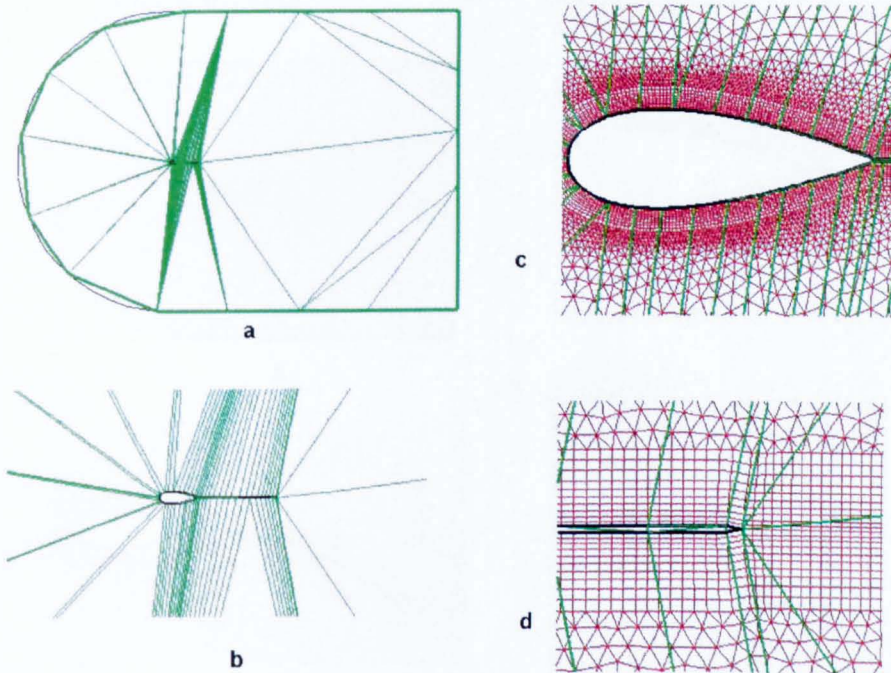


Figure 6.7 *Delaunay Graph generation over the flapping aerofoil: a) complete domain showing only Delaunay triangles; b) close up view of Delaunay triangles around flapping aerofoil element; c) close-up view of aerofoil section; d) close-up view of tail section*

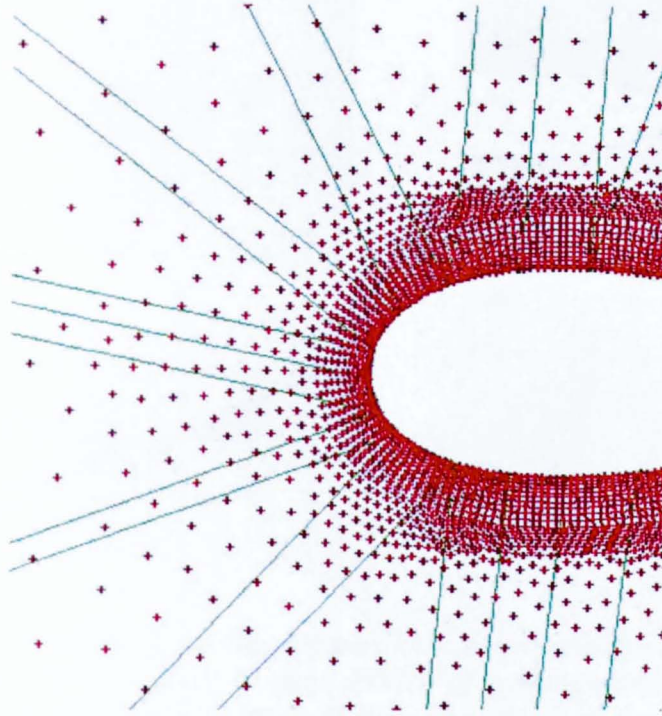


Figure 6.8 Location of all interior mesh nodes (represented by '+' symbol) through Delaunay graph

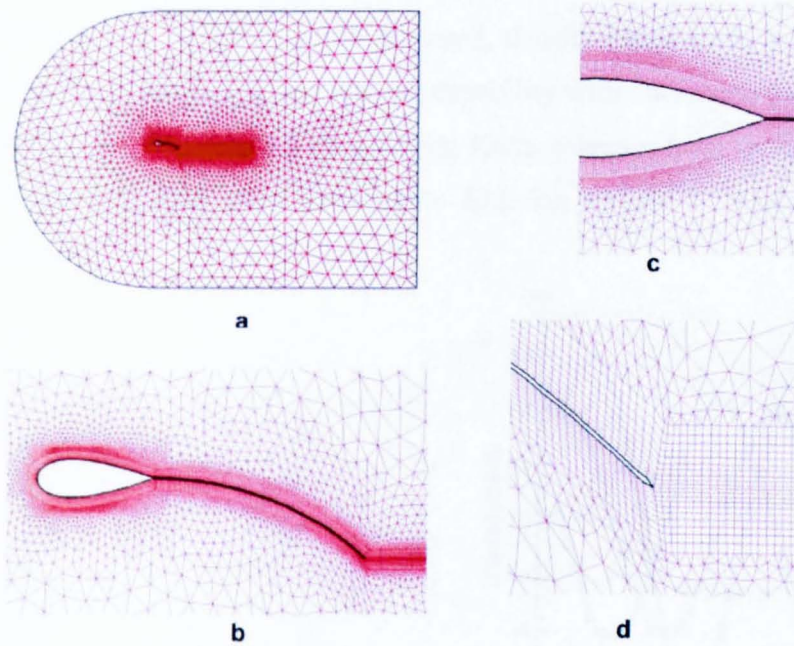


Figure 6.9 Deformed mesh over the flapping aerofoil element during maximum downward tail deflection: a) complete domain mesh; b) close up view of flapping aerofoil element; c) close up view of aerofoil section; d) close up view of tail section

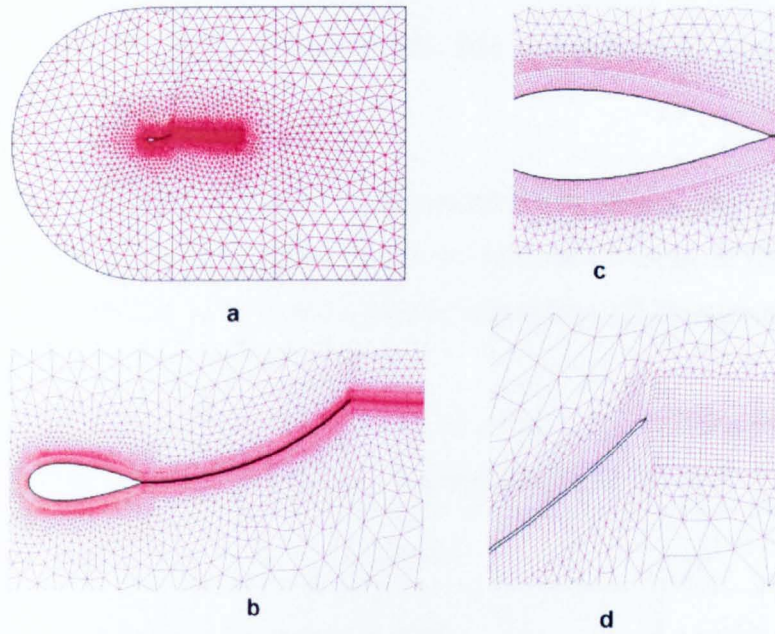


Figure 6.10 Deformed mesh over the flapping aerofoil element during maximum upward tail deflection: a) complete domain mesh; b) close up view of flapping aerofoil element; c) close up view of aerofoil section; d) close up view of tail section

6.2.4 Numerical Simulation of Flapping aerofoil

As described before, DGDES, a cell centered, density based finite volume solver is used for all the simulations. It has dual time stepping capability with outer time loop advancing in real time and inner ‘pseudo time’ using 4 step Runge Kutta scheme. Low speed preconditioning is used similar to Ref.[26]. Arbitrary Lagrangian Eulerian (ALE)^[121] formulation is used for moving mesh solution.

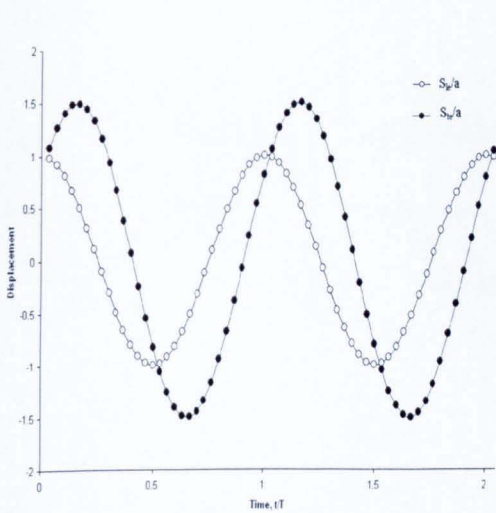


Figure 6.11-a Leading-edge and trailing-edge displacement as a function of time; $Re=9,000$, $b/c = 0.56 \times 10^{-3}$, $Sr = 0.34$

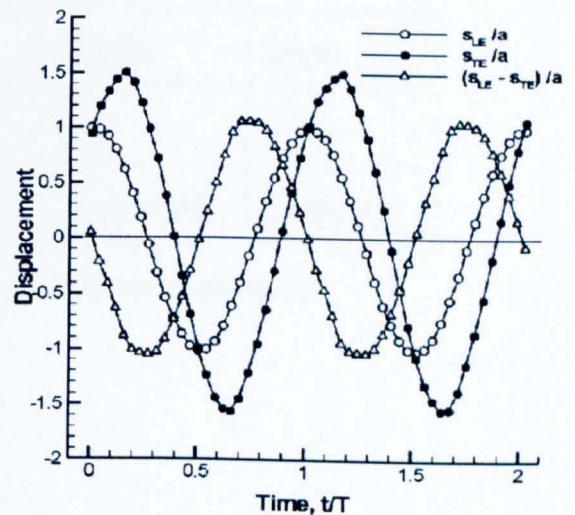


Figure 6.11-b Leading-edge displacement, trailing-edge displacement and their difference as a function of time; $Re=9,000$, $b/c = 0.56 \times 10^{-3}$, $Sr = 0.34$

6.2.5 Comparison of fluid properties for numerical simulation and the experimental data

The experimental data available ^[114] is for a water tunnel experiment. Strouhal No and Reynolds number are matched with the experiment to get the simulation input of CFD simulation using “air” as working fluid. Some Experimental and corresponding CFD parameters are tabulated in tables 6.3, 6.4, and 6.5.

Parameter Description	Units	Experimental Data ^[114]	CFD
Working fluid		Water	Air
Density (ρ)	Kg/m ³	1000	1.17666
Chord Length (c)	m	0.09	0.09
Leading Edge Amplitude (a_k)	m	0.0175	0.0175
Dynamic Viscosity (μ)	Pa.s	1.00E-03	1.84600E-05

Table 6.3 Comparison of CFD and experimental variables

		Reynolds No		
		9000	18000	27000
Experiment	Velocity (m/s)	0.1	0.2	0.3
CFD	Velocity (m/s)	1.56884742	3.13769483	4.70654225

Table 6.4 Reynolds Number of CFD and Experiment

b/c=0.56e-3; Reynolds Number 9000		
U = 1.56884742 m/sec		
Strouhal Number	Frequency	Time period (s)
9.99E-02	4.47986128	0.2232211978
1.35E-01	6.03995945	0.1655640253
2.04E-01	9.12898864	0.1095411594
2.73E-01	12.24995059	0.0816329823
3.42E-01	15.32738823	0.0652426874
4.12E-01	18.45173890	0.0541954341
4.83E-01	21.65630249	0.0461759343
5.57E-01	24.95122721	0.0400781890
6.32E-01	28.34297671	0.0352821092
7.11E-01	31.86375718	0.0313836185
7.93E-01	35.56484305	0.0281176554
8.81E-01	39.47418221	0.0253330137
9.70E-01	43.49297760	0.0229922175

Table 6.5 *Calculation of frequency from Strouhal Number*

6.2.6 Defining Stiffness of different thickness flat plates

To consider the stiffness factor, the known experimental data from Ref.[114] is used. 4 different thickness plates corresponding to different stiffness were used to determine the effect of chordwise flexibility. Experimental position of flapping aerofoil with varying stiffness tails were recorded using the position sensor as detailed in Ref.[114]. A quadratic shape is assumed to mimic the actual shape of the plate deformation by maintaining the recorded trajectories of the leading and trailing edges of the aerofoil in the experiment. Figure 6.11 shows one typical case, which is almost reproduced exactly as the experimental condition.

Plate Thickness, (b/c)	Lower Strouhal Number	Higher Strouhal Number
0.56×10^{-3}		
0.85×10^{-3}		
1.13×10^{-3}		
1.41×10^{-3}		

Table 6.6 *Effect of bending stiffness on shape*

6.2.7 Results

The results are presented for the flapping motion case shown in figure 12. It shows the instantaneous vorticity snapshot of the experiment for a similar case at the same Reynolds number. Due to flapping motion, counter rotating vortices are shed from the trailing edge downstream of the aerofoil section. These vortices are similar in magnitude but opposite in direction as shown with different colors. There is some elongation in the vortices seen in the simulation, which may be due to the small differences in the Strouhal number and flexibility of flat plates. Now that the methodology is tested to work and a closer match to the experimental cases is under way.

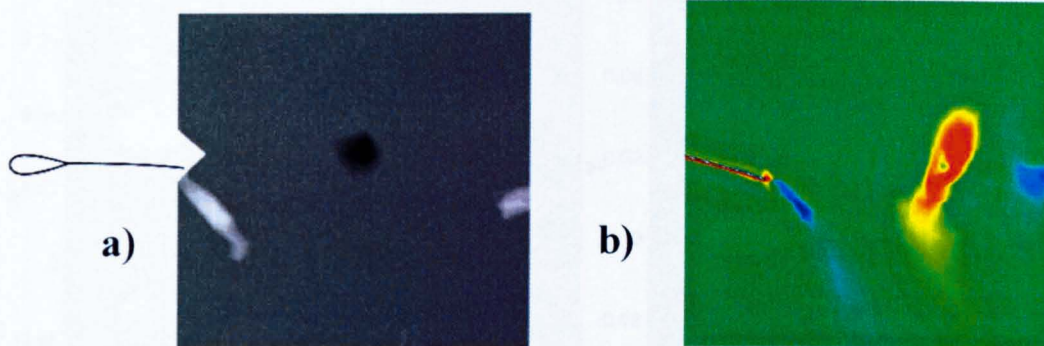
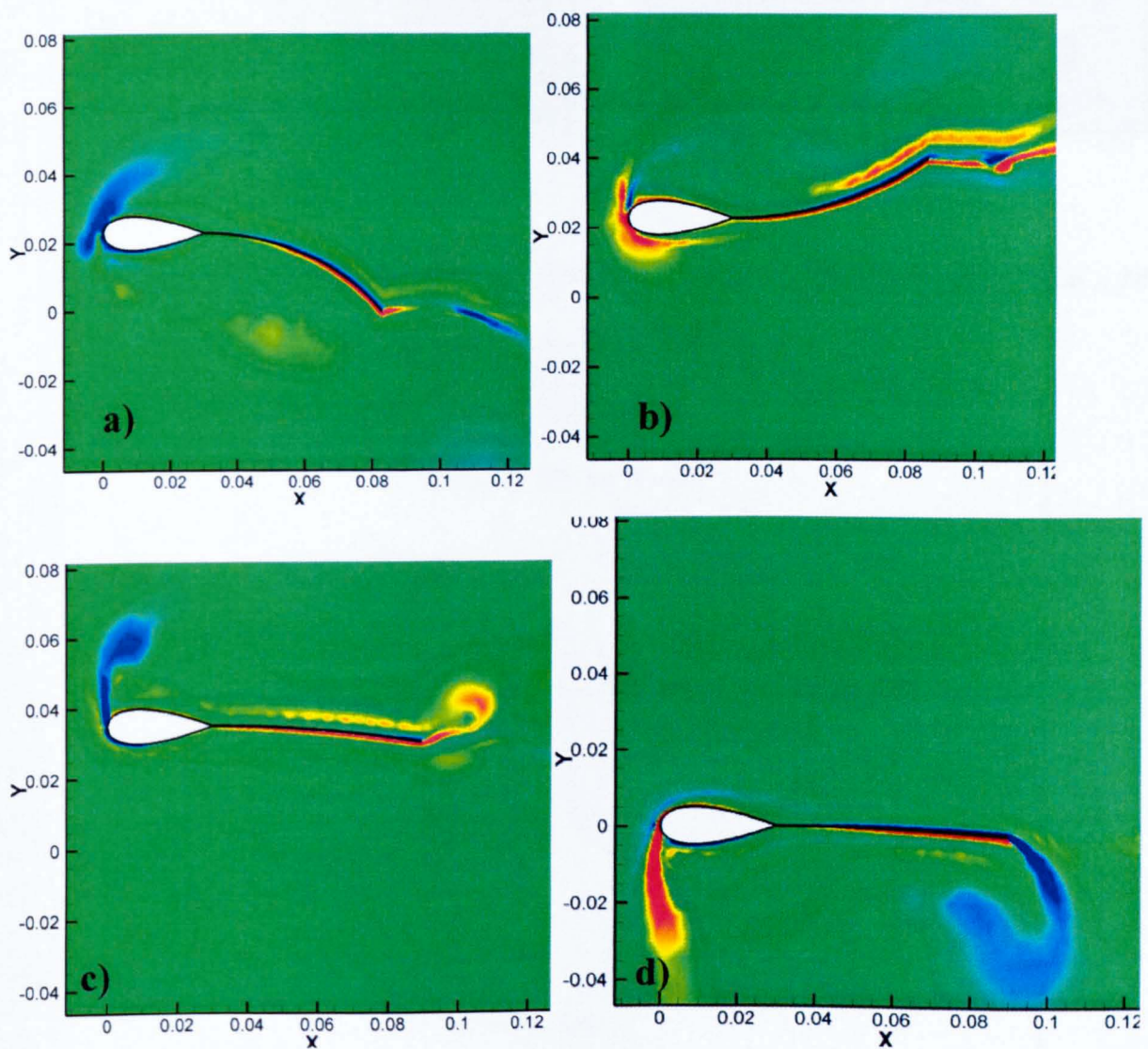


Fig. 6.12 Comparison of experimental and numerical instantaneous vorticity
a) Experiment $Re=9000$, $Sr=0.27$, $b/c=0.85 \times 10^{-3}$ b) Numerical simulation
 $Re=9000$, $Sr=0.34$, $b/c=0.56 \times 10^{-3}$

Figure 6.12 above shows a phenomena consistent with the previous observations in literature. Firstly the upward and downward direction motion is producing counter-rotating vortices. This generates the thrust producing wake as described in Ref. 14. Secondly, as observed in the simulation of Lewin and Haj Hariri^[122], leading edge vortices is also clearly shed from the leading edge as shown , with one dominant in strength. Both the upward and downward direction motions show these phenomena.

Z-vorticity from the flow field obtained during the simulation are shown below in sequence of cycle in figure 6.13.



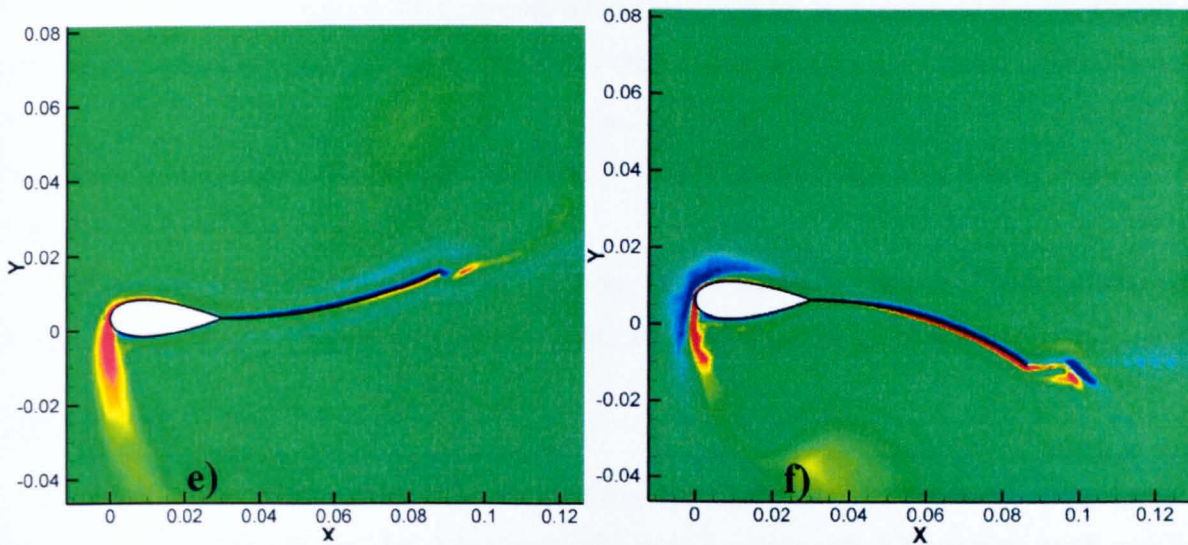


Fig. 6.13 Z-vorticity of flapping aerofoil during one cycle; $Re=9,000$, $b/c = 0.56 \times 10^{-3}$, $Sr = 0.34$

a-b Mean position while going up and coming down

c-d Top and bottom peak cycle with tail in horizontal position during flapping

e-f bottom position while flapping up and down

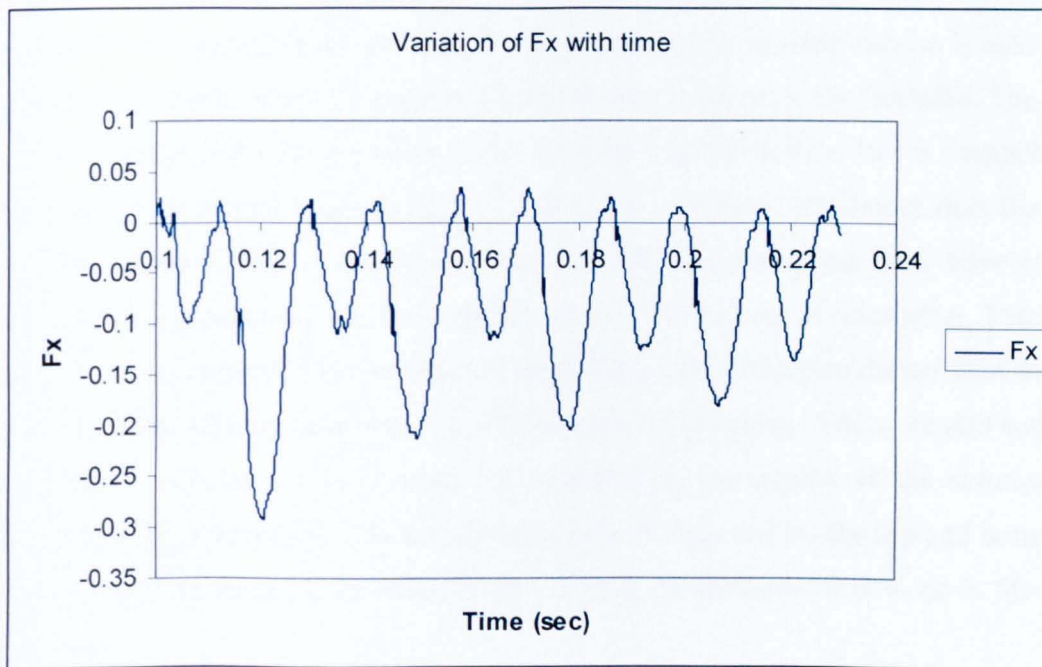


Fig. 6.14 Variation of F_x with time

The coefficient of thrust C_T obtained for baseline case of $b/c=0.56 \times 10^{-3}$ and Strouhal number of 0.34 obtained was 0.57 against the experimental value of 0.814. It is observed that the flapping aerofoil gets very high and low pressure regions during the flapping cycle in the top and bottom domain. This significantly changes the velocity along x and y axis as shown by the streamlines. The flapping frequency of the teardrop element is 15.327 for this case with leading edge amplitude of 0.0175 m.

A similar case was done by Jian Tang^[137] in which the simulation results produce more regular C_T plot. However, the comparison with the experimental data is not presented in it.

6.2.8 Conclusions

A complete cycle of flapping wing motion has been successfully simulated using a modified Delaunay graph mapping and has been very efficient. A single initial Delaunay graph was found to work for the complete flapping motion of thinnest and most flexible flat plate ($b/c = 0.56 \times 10^{-3}$), the most challenging case with regard to moving meshes. Due to the non-iterative nature of the Delaunay graph mapping, it is found to be an attractive tool for continuously deforming domains such as flapping surfaces of aerodynamic or marine interest. Average time it took for a single time step movement for this baseline case was around 0.1 second for mesh size of over 36500 elements. Vortex shedding in pairs from leading edge of the aerofoil section is observed with one dominant in strength, which is consistent with the observations in the literature. The coefficient of thrust (C_T) calculated with experiment for $Sr=0.34$ and $b/c=0.56 \times 10^{-3}$ is computed to be 0.57 against the experimental value of 0.814. This value is around 30% lower than the experimental data. There are different factors in the water tunnel experiment that may have contributed the thrust force in the experiment but are not included in the numerical simulation. The buoyancy and inertia of the water used in the experiment (being around 1000 times denser than the air which is used for simulation) may have some vital influence on the results. There are still some issues with the numerical simulations which may be deteriorating the quality of the solution. During the flapping motion, a very high and low pressure area is observed on the top and bottom side of the domain emanating from the moving aerofoil. The continuation of this work in 3D is left for the future work.

6.3 3D implementation of Delaunay Graph Mapping based mesh deformation in the DG-DES solver

This research work was motivated by the experiments on the oscillating NACA0012 wing^[139] with spanwise flexibility. As an initial task, the Delaunay graph mapping based grid deformation technique was implemented in the MPI version of the DG-DES. As an initial work, only stiff wing (no spanwise flexibility is simulated). For the Delaunay graph mapping based grid deformation, the complete oscillating motion is successfully simulated. It is observed that particularly for the three dimensional Delaunay graph based mesh deformation is sensitive to the quality of the parent Delaunay triangles. The resulting mesh may deteriorate with the number of iteration if the area ratios are calculated at each step of the mesh motion from the highly skewed parent Delaunay triangles. In this study, the preference is given to use the mesh area ratios calculated from the undeformed mesh, corresponding to the original graph. This reduces the computational time considerably by avoiding the calculation of the area ratios at each step of mesh deformation. This also ensures that the subsequent skewness in the Delaunay triangles has a minimal effect on the resulting mesh quality. However, this reduces the flexibility of this methodology. If the original Delaunay graph fails to provide the feasible mesh for the complete cycle, it is still preferred to generate another Delaunay graph after some specified number of simulation iterations instead of each mesh deformation step. The number of these steps has to be decided after observing the step during which the mesh deformation fails. Obviously, if a single Delaunay Graph suffices the complete mesh motion, the mesh deformation becomes very fast. The Delaunay elements generated at the first step are not to be generated again and their connectivity remains the same. It is to function much faster than the original Delaunay Graph that needs to be computed at each mesh deformation step.

The flexibility and accuracy of the mesh deformation increases with the increase in the number of Delaunay triangles generated at extra computational cost.

6.3.1 Oscillating NACA0012 Wing

The domain mesh for NACA0012 wing is shown in figure 6.15 a). The Delaunay graph is generated with selected input domain points as shown in figure 6.15 b). In order to display the

Delaunay graph map, figure 6.15 c) presents on the Delaunay triangulation. The zoomed view of the wing is shown in figure 6.15 d).

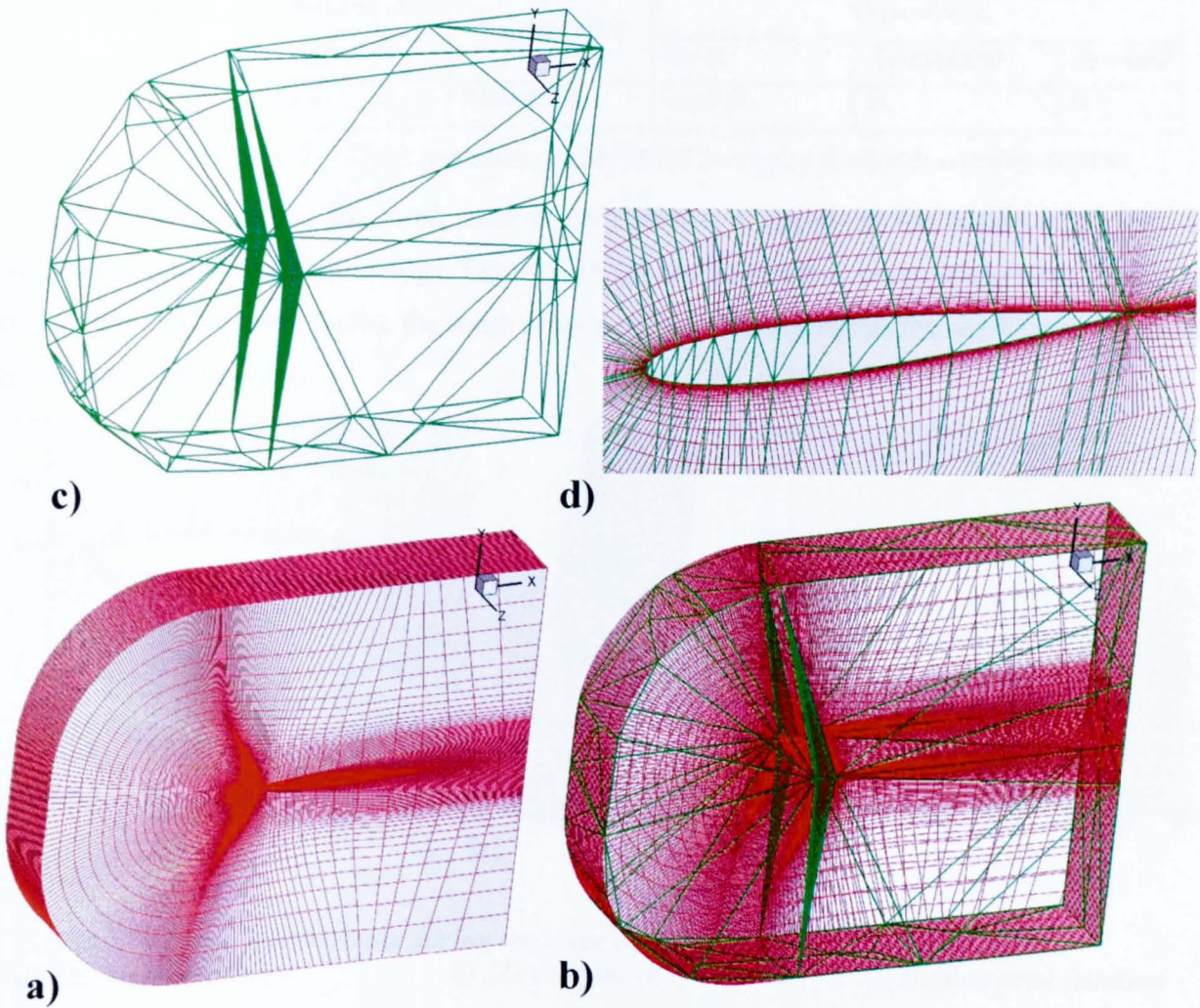


Figure 6.15 Domain and Delaunay Graph meshes

a) Mesh of the domain b) Delaunay Graph with the 3D mesh
 c) Delaunay Graph only d) Zoom view of the wing

The mesh statistics of the mesh used in this simulated are tabulated in table 6.7. It is structured mesh generated in Gambit with near wall clustering. The number of Delaunay graph elements used for this mesh deformation is 4821. It is to be ensured that all the internal mesh nodes (excluding the boundary nodes) are encompassed by the Delaunay Graph elements. The mesh

resolution especially in the LES region is less than what is generally adopted for the hybrid RANS-LES methodology.

Number of nodes	Number of elements	Nx x Ny x Nz	Type of cells		
			Brick	Tetrahedral	Pyramid
274533	255760	278x46x20	255760	0	0

Table 6.7 Mesh statistics of NACA0012 wing at Reynolds number 30,000

As mentioned before, the mesh used is very coarse to speed up the results and verify the implementation of the methodology. Figure 6.16 (a) and (c) are two instantaneous mesh images at the top and bottom peak during the mesh motion. Figure 6.16 presents the mesh over the surface of the NACA0012 wing.

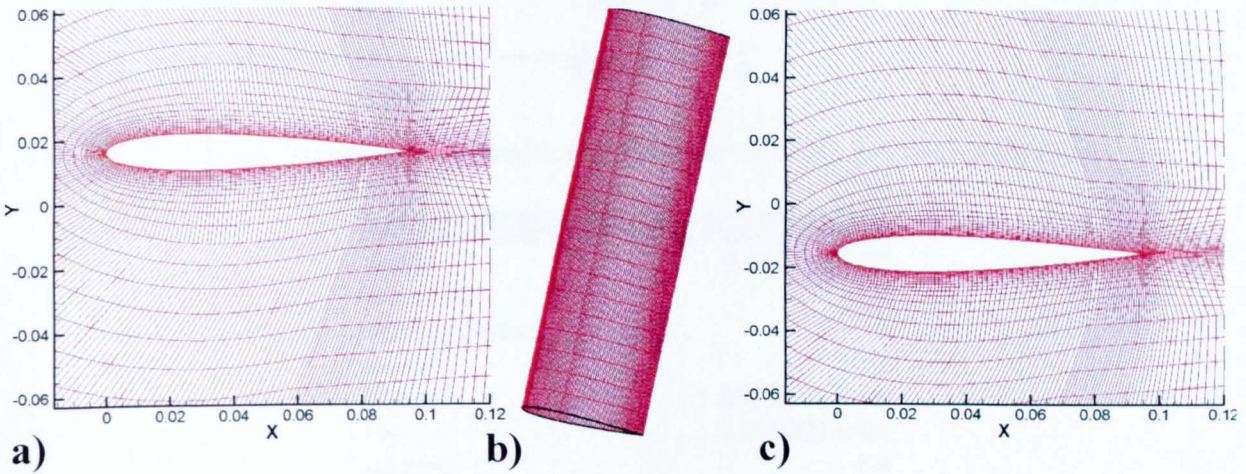


Figure 6.16 Mesh deformations during the wing oscillation with 17.5% c amplitude
 a) Top peak location b) 3D wing mesh c) Bottom peak location

6.3.2 Case details

The case simulated corresponds to the inflexible motion case as presented in the figure 6.17. However, the experimental inflexible case has a certain tip displacement due to the flexibility of the material. For the simulated case, the root and tip displacements are in zero phase lag (fully rigid body). Table 6.8 presents the different parameters from the case set up for the numerical simulation and correspond to the experimental data^[139]. The trajectory followed in this simulation is similar to the profile by the ‘Root’ as shown in figure 6.17.

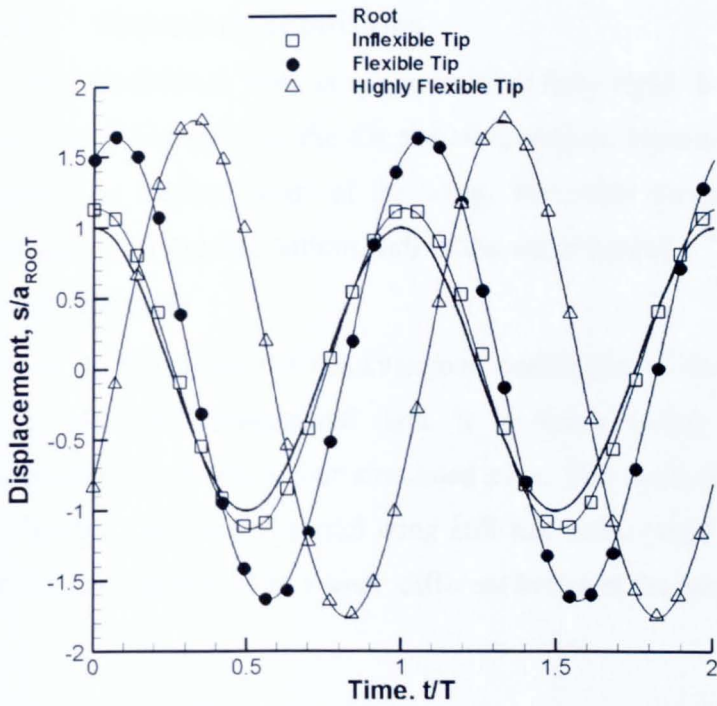


Figure 6.17 Tip displacements as a function of time, $Re=30,000$, $k_G=1.82$. Ref [139]

Re = 30000	
scale	9.413196E-02
chord (m)	1
velocity (m/sec)	5
density	1.17666
viscosity	1.84602186E-05
Re	3.000000E+04
gamma	1.4
R	287.04
T	300
c	347.212903
meu	1.84602186E-05
p	101324.545920
Mach	0.014400
meu_ref	1.789400E-05
T_ref	288.150000
C	110.4
frequency (flapping)	30.771908
Amplitude (m)	0.016473093
distance traveled by le in 1sec (m)	2.03E+00
Garrick Freq Kg	1.820000E+00
Strouhal Number Sr	0.202763397

Table 6.8 CFD simulation setup of NACA0012 wing at Reynolds number 30,000

6.3.3 Boundary conditions

The NACA0012 wing is assumed to be fully rigid. It means that the root and tip of the wing have same trajectory in the oscillation direction. Hence, the symmetry boundary conditions are applied on the both ends of the wing. The outer boundary is kept as a farfield boundary by neglecting the top and bottom wall of the water tunnel.

6.3.3 Results

Figure 6.18 presents the instantaneous coefficient of thrust plots for the simulated NACA0012 wing with the experimental data. It is worth notice that the experimental data termed as ‘inflexible’ is closest to our simulated case. The main difference is that although termed as the ‘inflexible’, this experimental wing still has some small degree of flexibility. This flexibility is obvious in figure 6.17 as a small different between the motion profile of the root and tip.

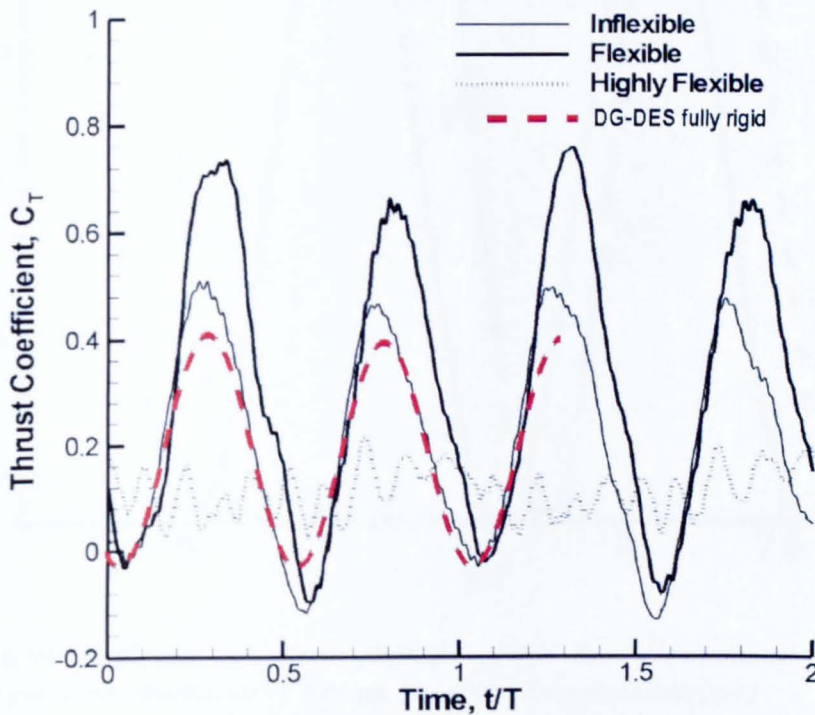


Figure 6.18 Instantaneous thrust coefficient as a function of time at $Re=30,000$, $k_G=1.82$.

The result of the instantaneous thrust coefficient C_T is quite encouraging. In fact, as presented in figure 6.17, the trajectory of Inflexible wing has tip displacement which may contribute to the gene

ration of thrust for experimental inflexible wing. A much finer grid with lesser dissipation and better capability of the resolving and preserving the separated flow structures may give better flowfield results. However, still the results are quite encouraging.

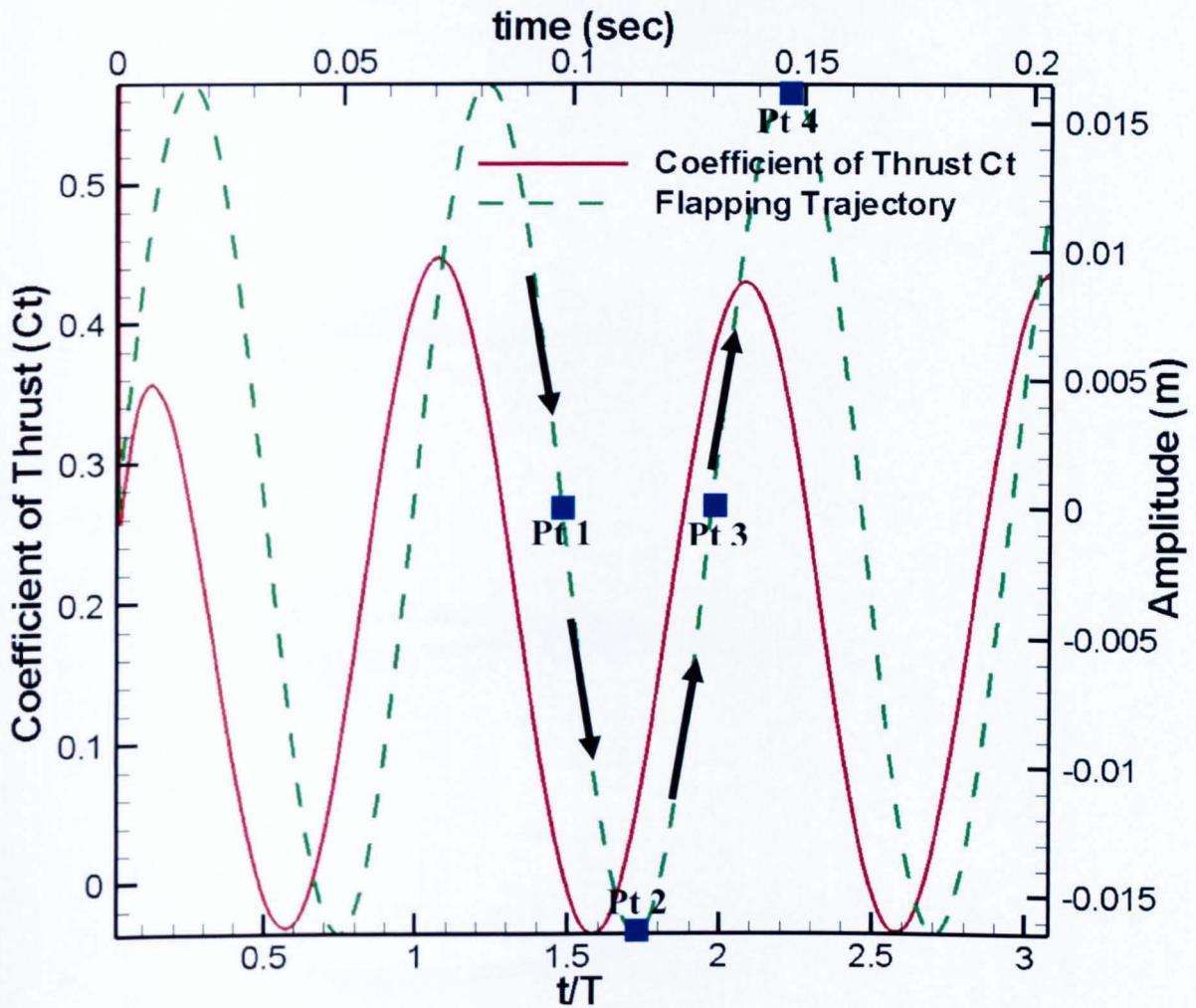


Figure 6.19 Coefficient of thrust plotted against non dimensional t/T ; Trajectory during flapping motion: Amplitude of motion (m) plotted against time(sec)
Flowfield data at Pt1, Pt2, Pt3 and Pt4, represented by blue rectangles, is discussed below

The trajectory of the flapping motion and the coefficient of thrust are plotted in Figure 6.19. It is to be noticed that both have different time scales along x-axis. The arrows describe the direction of motion and the flowfield results and mesh at marked points (Pt1-Pt4) are presented below. The dynamic effects are clearly observable from the lag of both trajectory and the coefficient of thrust.

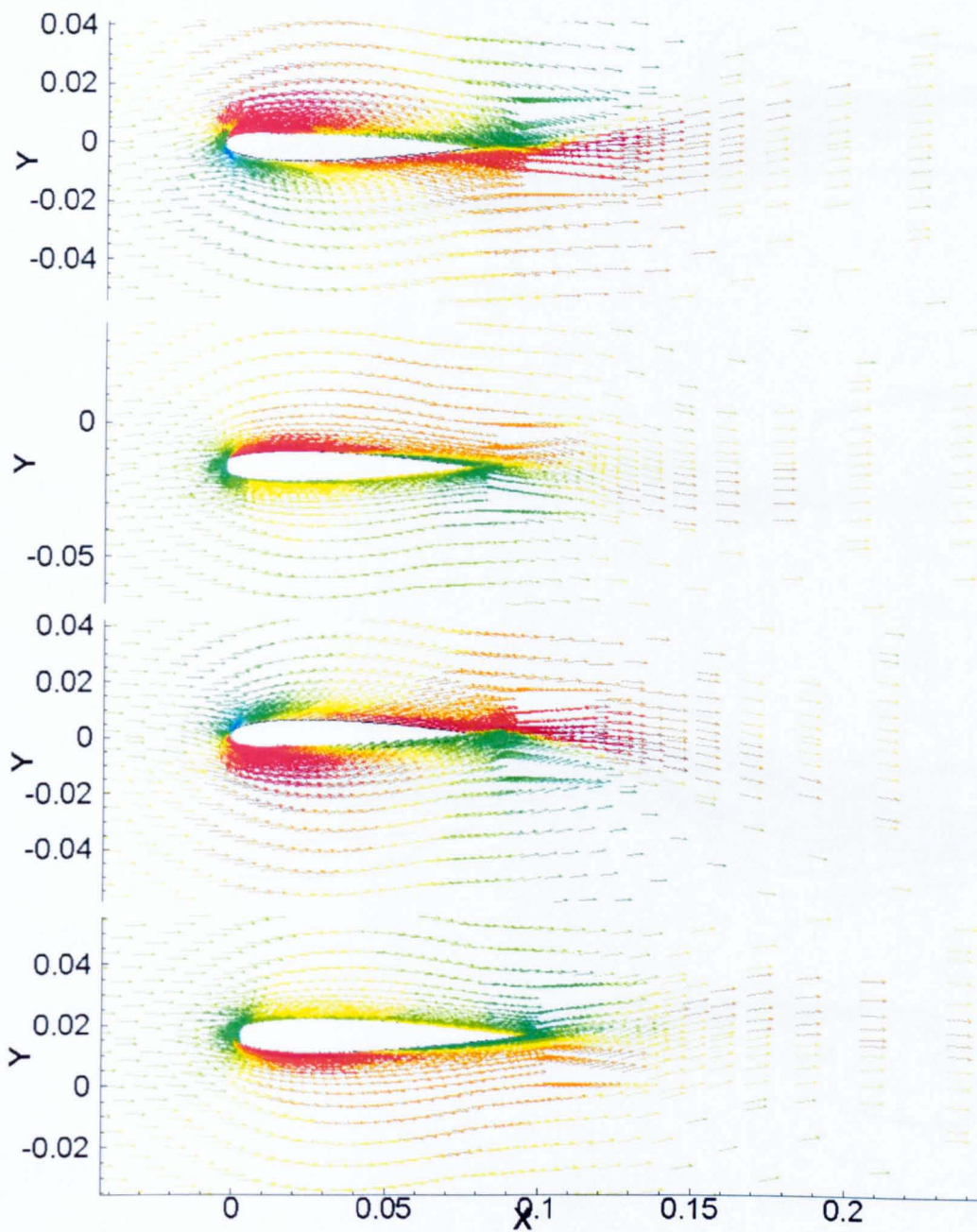


Figure 6.20 Vector plots of velocity colored with velocity magnitude (every 3rd vector is plotted for clarity). Flowfield description at Pt1, Pt2, Pt3 and Pt4 (from top to bottom)

The vector plot in figure 6.20 colored with velocity magnitude show the dynamics of the flow at different locations from Pt1 to Pt4 as defined in Figure 6.19. The sharp variations at the leading

and trailing edge of the wing make it essential to have a proper mesh resolution in these regions for better capturing of the flow physics.

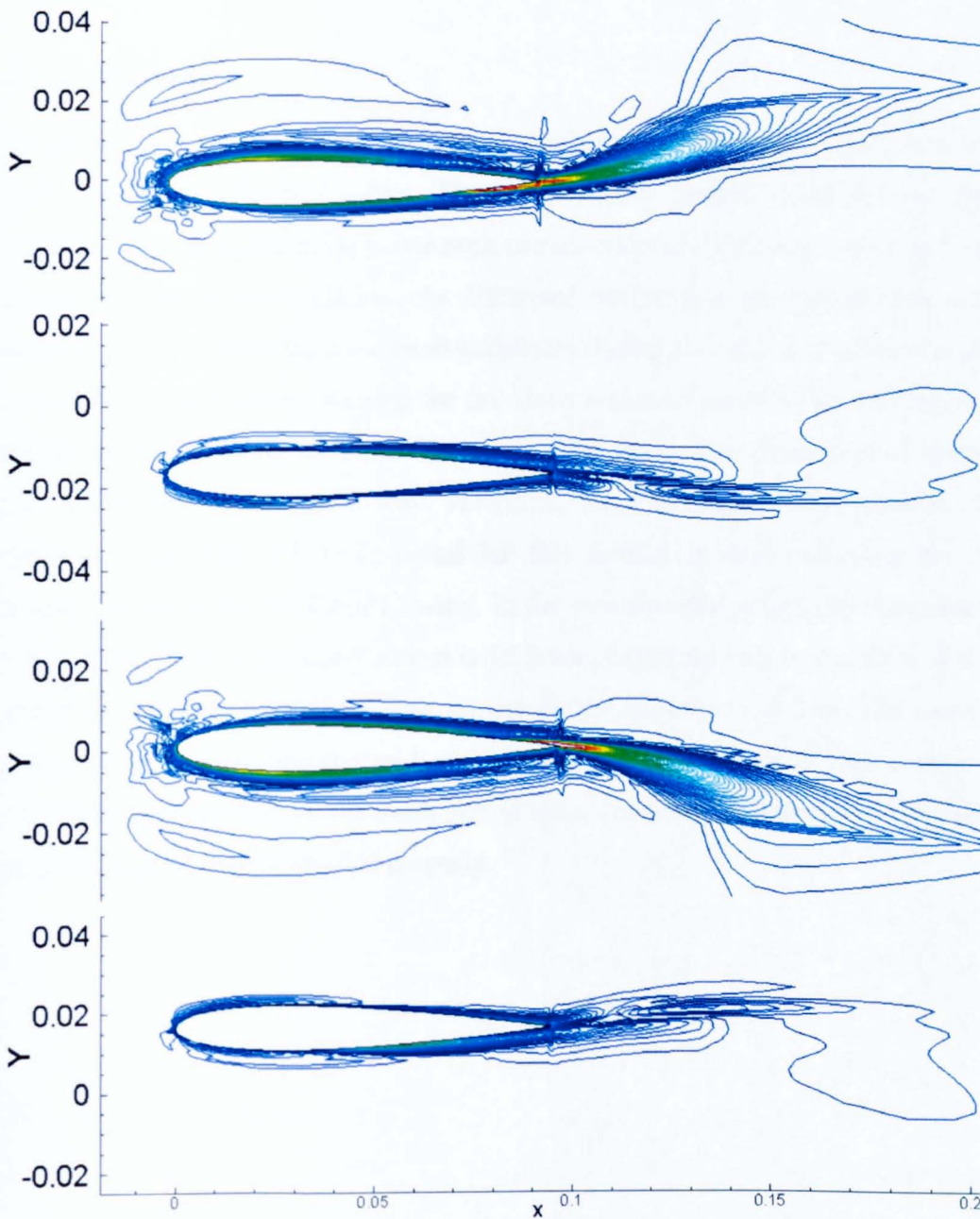


Figure 6.21 Line contour plots of vorticity magnitude. Flowfield description at Pt1, Pt2, Pt3 and Pt4 (from top to bottom)

Pt1 to Pt4 presented in Figure 6.21, show the vorticity line contours at different locations along the trajectory. The effect of mesh motion is clearly visible with the direction of downstream vorticity.

6.3.2 Conclusions

The Delaunay graph based mesh deformation scheme is successfully implemented in the serial and MPI version of DG-DES solver. The initial results presented are for the spanwise rigid NACA0012 wing. No appreciable bottle neck or reduction in efficiency is observed in the solution due the deforming mesh simulation. As discussed before that the master node does the mesh deformation and calculates the new mesh parameters during the time slot when it is otherwise idle (for non-moving meshes) and waiting for the slave nodes to pass on the convergence data. The speed and the quality of the deformed mesh are quite good. The simulation of spanwise flexible wing is to be done in the same way. However, for this study, only spanwise rigid wing is simulated as a test case. It is to be noted that this simulation does not cover the effect of wall region near the tip of the NACA0012 wing. In the experimental setup, the clearance between the wing tip and the floor of the water tunnel is $5c/3$ which corresponds to the 56% of the semi span. The effect of wall may have significant impact on the experimental data. The mesh used in this simulation is very coarse and the grid resolution in the LES region is very coarse. For a better hybrid RANS-LES simulation, the mesh size is to be considerably increased to be able to capture the unsteady separated flow physics properly.

7 Concluding Remarks, Recommendations and Future Work Perspectives

7.1 Conclusions

DES and DDES, in the frame work of hybrid RANLS-LES simulation techniques, provide significantly improved results for highly separated flows as compared with the RANS/ URANS simulations. The affordable computational cost and time, with the reasonable accuracy to simulate the highly separated flows, makes it a favourite choice for an increasing number of researchers in academia and industry.

The DDES scheme is suggested as an improved version of the original DES. However, for the cases with mild separation, the DDES becomes overly dissipative. For the A-airfoil case, the DES and DDES schemes behave very differently. The DES scheme captures the trailing edge separation but the DDES recovers to the URANS, failing to predict the separation. For the similar cases, DDES may prove overly dissipative to damp the natural unsteadiness in the flow. It may be argued that DDES performance may be improved for such cases by either reducing the delay in switching or by adding some forcing function or synthetic turbulence to augment the unsteadiness in the flow.

The switching mechanism in the DDES includes the turbulent viscosity in addition to the mesh parameters. This results in the RANS to LES switching region not as regular as that of DES which only relies on the mesh parameters. For the flows with weak instability, this may damp out the unsteadiness for the DDES simulations due to the presence of intermittent RANS regions.

Both the DES and DDES simulations predict similar time averaged flowfield parameters for the massively separated flows. Although the instantaneous outputs from both the schemes vary, the band of fluctuation of the instantaneous values for different flow variables is similar resulting in similar results for both the schemes.

The power spectral density comparison of the DES and DDES is carried out at a probe point by recording the instantaneous flow field data. This probe point is located along the centre line with two diameters downstream of the cylinder surface. The energy cascade associated with the size of the eddies is observed in line with the Kolmogorov's energy spectrum. It can be concluded that both the DES and DDES function properly in the highly separated regions, in accordance with the LES results.

For the cases with thick boundary layers and mild separation, even the best results from the DDES can not be expected to be very different from URANS. However, the original DES

schemes gives much better flowfield results, despite its possible premature switching to the LES mode within the boundary layer.

For the 'natural DES cases' such as the flow over a circular cylinder at high Reynolds numbers, the time step has an important role in delineating the flow structure details for both the DES and DDES. However, using a sufficiently small time scale that predicts the Strouhal number correctly, the impact of the time scale eddies is not very significant. It indicates an interesting corollary that after this threshold, further decrease in time step may produce those extra eddies which are skipped by the threshold time but the effect of these small time scale eddies is not critical to the overall flowfield parameters such as the shedding frequency.

The results of the turbulent statistics for the flow simulation over circular cylinder at the Reynolds number of 1.4×10^5 produces very encouraging results in comparison with the experimental data. The time averaged normalized velocity field and the turbulence statistics at this Reynolds number give much better agreement with the experimental data as compared with the previous published results.

The comparison between the modelled and resolved stresses computed by using the DES scheme for A-airfoil at maximum lift conditions and the flow over a circular cylinder at Reynolds number of 1.4×10^5 results in following observations:

- a. For the mild separation cases, or the flows with the attached boundary layers, the resolved stresses are not very significant. It is generally the modelled stresses that contribute to the turbulent Reynolds stresses.
- b. For highly separated flows, the resolved stresses are the major contributors in the turbulent Reynolds stresses. However, the modelled stresses still contribute to the turbulent Reynolds stresses, although to a much lower level. Thus for such flows, it may be recommended to combine both modelled and resolved stresses in order to compare with the experimental data.

The DES results from the oscillating NACA0012 wing agree quite well with the experimental data. Although the strength of the hybrid RANS-LES methods will be better predicted with the simulations including the flexibility in the spanwise direction (to analyze its 3D effects), the good prediction of thrust coefficient is very encouraging. This gives more confidence to use the hybrid RANS-LES simulation tool to study the turbulent flow around moving/ deforming shapes. For these cases, the results obtained using the URANS with S-A turbulence model gave very similar results as that of the DES simulation. This is because the mesh used is very coarse and the case is essentially two dimensional.

Using a global Delaunay Graph for the complete mesh deformation cycle provides a significant reduction in the computational cost and efficiency of the scheme. With a global Delaunay Graph, the connectivity and location of the mesh nodes in the respective parent Delaunay triangle is only done once and it results in huge speed up of the mesh motion process. However, it is less flexible as compared with the original Delaunay Graph methodology changing the Delaunay Graph at each deformation cycle. The quality of the Delaunay Graph may deteriorate if there is a concave region present in the domain. It is an inherent flaw with the 'qhull' software used to generate the Delaunay triangulation. Similarly, if the input points to generate Delaunay Graph are not carefully selected, the resulting Delaunay Graph may include highly skewed elements. This may deteriorate the mesh quality subsequently. Due to a range of issues with the spring analogy methods in terms of its strength, computational time and cost, the Delaunay Graph based mesh deformation offers a very efficient alternative. It can revitalize the otherwise relatively less proactive field of huge mesh sized flowfield simulations with the mesh motion/ deformation. It has a particular scope in the aeroelastic and fluid-structure interaction fields.

In order to make large scale computations feasible, the role of parallel computing is vital. High parallel efficiency is achieved using METIS and MPI in the Linux environment. CrayPAT, a performance analysis tool developed by the Cray Systems, was used to evaluate/ improve the performance of DG-DES. It uses several performance experiments that measure how an executable program consumes resources while it is being executed. Some very simple modifications in the DG-DES solver led to significant performance enhancement in it. It is very important to check the load balance of any MPI program to improve its performance and efficiency.

7.2 Future Work Perspective - Short recap and new trends

Hybrid RANS-LES methodologies such as DES (zonal and non-zonal) and its variants such as DDES etc. with different modifications have bridged the gap between the RANS and LES for a variety of flow problems. The feasible computational time and cost for the unsteady flow problems, compounded with the reasonable accuracy have attracted a sizeable scientific community in both academia and industry. However, the inherent reliance of all these methodologies on RANS solution brings the RANS turbulence modelling back in the spot light. The non-existence of a generalized or universally accepted RANS turbulence model catering for all type of flows is the biggest bottleneck being faced today. Hence, in near future, the RANS

turbulence modelling that seems to have become stagnant or saturated, needs to supplement some requirements of these new hybrid RANS-LES methodologies.

7.2.1 Generation of LES content

One of the very important requirements is the absence of the LES content (unsteadiness in terms of high frequency small size vortical structures) in the RANS boundary layers. As discussed in Chapter 5, if the flow is highly separated due to a blunt body such a circular cylinder, the downstream unsteadiness generated in the flow is quite strong and the resulting turbulence generated in the flow is primarily independent of the upstream turbulence. In such cases, described as ‘natural DES’ flow scenario, the dependence on the RANS for the LES contents in the flowfield is not very critical. However, for the flows with mild separation such as the A-airfoil case discussed in Chapter 4, the contribution of RANS is of vital significance. The RANS to LES switching requires the RANS to provide some level of LES content to capture the unsteadiness in the flow. For a normal RANS turbulence model in the boundary layer, the dissipation levels are very high and very high energy ^[135]. As described in section 1.4.4 that for other hybrid schemes such as Limited Numerical Scale (LNS), this LES is generated by introducing the grid spacing as a key parameter in the turbulence mode. However, without sufficient amount of the instability in the flow, it is still not possible to generate sufficient LES content. For these hybrid schemes, there are three common methodologies which are used to facilitate the generation of LES content:

- a) Synthetic turbulence^[74]
- b) Disturbances from similar calculations/ DNS data base^[69]
- c) Controlled forcing ^[95]

Options a) and c) are used together in Ref[95]. These methods have produced quite promising results as can be viewed in these references. In short, the hybrid RANS-LES methodologies have shown a great potential to solve industrial level separated flow and owing to their success, their application to different areas of interest is ever increasing. The controlled forcing has a very interesting role in the generation of the LES content. The RANS boundary layer contains few highly elongated turbulence structures (termed as super streaks). In order to break it down to numerous small LES content structures, it is required to add more energy to them through controlled forcing. This in effect breaks up the super streaks in to numerous small structures containing lesser turbulent kinetic energy. In view of the requirements outlined above, it may be appropriate to implement this in the DG-DES solver.

7.2.2 NASA Common Research Model (CRM)^[133]

All the turbulence models being used have lots of empirical parameters which are evaluated for very simple cases and geometries. One of the points highlighted in the colloquium 'LES Flows for External Flows'^[138], attended by the author, was the difference in operational scenario when the same is applied to a complex domain with different flowfield scenario. The evaluation of Cdes parameter in the DES scheme is done through Decaying Homogenous Isotropic Turbulence (DHIT) with the assumption of the production of turbulent kinetic energy in the domain equal to the destruction. It will be interesting to analyse the effect of such simplified evaluations of the variables on results when applied to more complex real life geometries. For the DES scheme, the implementation has already been done on full scale fighter aircraft with very encouraging results^[21,22]. However, the experimental data has proprietary rights and can not be shared. The unavailability of a detailed set of experimental data for a real life flow problem is one common problem faced by majority of the researchers during the course of validation of CFD codes. Drag Prediction Workshop (DPW) series have been a key source to provide such data. 4th Drag Prediction Workshop^[134] is going to be held in June 2009. A very interesting aspect of this workshop is the inclusion of a Common Research Model (CRM) as a test case. The geometry of this test case consists of wing/body/nacelle/pylon/horizontal-tail configuration. Further details can be found in Ref. [133]. This CRM will serve as a common research hub for CFD and fluid structure interaction validation with the detailed experimental data to be made available from wind tunnels at National Transonic Facility and the Ames in USA. Unfortunately, most of the geometrical data or ready to use meshes available online is not compatible with the Gambit software being used to generate the input mesh for DGDES. Problems were faced in importing the CRM geometry in IGES mode in Gambit. The FVUNS format was implemented and integrated in the code to bridge this gap during the last stages of this study. As a test case, a DLR-F6 aircraft with wing-body-nacelle-pylon was selected to validate this implementation. A mesh of size around 6.15 million cells was generated and imported in the DGDES. Some of the initial flowfield results for laminar flow at transonic speed of Mach 0.75 are presented in Appendix B. The main idea is to check the implantation of the FVUNS format in reading the mesh, its formatting to assign adjacent cells to a face, mesh partitioning, boundary conditions assignment and mesh parameter calculation.

7.2.3 Pre-processing tool (Gambit or Gridgen)

Gambit software^[128] has been used extensively during this study. However, despite its usefulness, its non-parametric character and limited support for various geometric options keeps it as a second option to Gridgen^[132]. The grid size limitation due to memory constraint for Gambit is observed to be more stringent than Gridgen. However, it is understandable that the Gridgen is a specialized mesh generation tool (with its new version coming as Pointwise) and is expected to be far more powerful than Gambit. Some of the new additions in Gridgen such as the ‘Anisotropic Tetrahedral Meshing’, makes it really easy to generate meshes over quite complicated geometries such as DLR-F6 aircraft with nacelles. Keeping in view the above factors and the discussion in the above section, the FVUNS format was implemented in the DGDES and integrated with option to directly use either FVUNS file from Gridgen or Neutral format file from Gambit. The initial results are presented in Appendix B for mesh input of DLR-F6 aircraft with nacelle generated by the author in Gridgen.

7.3 Hybrid RANS-LES methodology for wall layer models for LES (WMLES)

From the author’s point of view, a vast majority of the scientific community believe that the LES will be the ultimate scientific research tool in remote future, when the limitations of computational cost and time are addressed with the advent of increasingly innovative hardware and better numerical methodologies. With this theme in mind, there are efforts being carried on to improve the WMLES. Three main approaches are categorised in Ref.[74,135]. First approach is to use the equilibrium laws based on the logarithmic law (or on some similar assumed velocity profile). Second approach is to use zonal methods, in which the turbulent boundary layer equations are solved, weakly coupled to the outer layer LES. Third approach is to use hybrid methods in which the model changes from a RANS-based turbulent model near wall to the LES mode in the outer layer.

The results for using hybrid method as a WMLES have been a partial success. First such attempt by Nikitin et. al^[71] presented some encouraging results but suffered with Log-Layer mismatch. In this study, the DES was used as a SGS model for LES without adjustment. It is commented on page 11 of Ref. [74] “Hybrid methods are most accurate when the mean flow has some destabilizing perturbation that accelerates the generation of Reynolds-stress supporting eddies”. This field is open for experimentation by introducing new ideas.

7.4 Hybrid RANS-LES methods with moving grids

There are some initial results presented in chapter 6 for implementation of hybrid RANS-LES with moving grids using the Delaunay Graph based mesh deformation. This is a novel idea and research work. The simulations become more challenging due to the motion of the object. In this particular case, unlike the static cases, the boundary layer is subjected to a continuously varying velocity field due to the motion of the body. The initial results are presented with a quite a coarse grid and may be implemented in future to a much finer grid for appreciation of the better flow physics. Nevertheless, the results of coefficient of thrust for the rigid oscillating NACA0012 wing are very promising. This particular aspect may be given more attention due to its huge prospect. With the implementation of the Delaunay graph mapping based mesh deformation for DG-DES, the prospect of simulating full body motion cases gives DG-DES an edge over those solvers which rely on manipulating the boundary condition (such as the synthetic jets with the fluctuating boundary condition specified at the throat of the nozzle etc.).

References

1. H. Xia. "Dynamic Grid Detached-Eddy Simulation for Synthetic Jet Flows", PhD Thesis, University of Sheffield, November, 2005
2. S. B. Pope. "Turbulent Flows", Cambridge University Press, 2000.
3. <http://www.math.univ-montp2.fr/~mohamadi/dasilvaweb/Turbulence.pdf>
4. http://en.wikipedia.org/wiki/Amdahl's_law
5. M. Van Dyke. "Album of Fluid Motion". Parabolic Press, 1982.
6. K.R. Sreenivasan. "On the universality of the Kolmogorov constant", Phys. Fluids A, 7:2778-2784,1995
7. J. O. Hinze. "Turbulence ", McGraw-Hill, New York, 1975.
8. Kim, J., Moin, P. & Moser, R. D., "Turbulence statistics in fully developed channel flow at low Reynolds number", J. Fluid Mech. 177, 133-166, 1987
9. John C. Tannehill, Dale A. Anderson, Richard H. Pletcher, "COMPUTATIONAL FLUID MECHANICS AND HEAT TRANSFER", Taylor & Francis page 272, 2nd Edition 1997
10. www.stanford.edu/~temple/downloads/intro.ppt
11. P. Bradshaw, "An Introduction to Turbulence and its Measurement", Pergamon press. The commonwealth and international library of science technology engineering and liberal studies, 1971.
12. Scott A. Morton, Matthew B. Steenman, Russell M. Cummings, and James R. Forsythe, "DES GRID RESOLUTION ISSUES FOR VORTICAL FLOWS ON A DELTA WING AND F-18 C", AIAA 2003-1103, 2003.
13. T.J. Barber, L.M. Chiappetta, J.R. DeBonis, N.J.Georgiadis, and D.A. Yoder. "An Assessment of Parameters Influencing the Prediction of Shear Layer Mixing". AIAA Journal of Propulsion and Power, 15(1):45-53, 1999
14. M. Strelets, "Detached Eddy Simulation of Massively Separated Flows", 39th AIAA Aerospace Sciences Meeting and Exhibit, Reno, NV. January 8-11, 2001.
15. Roland von Kaenel, "LARGE-EDDY SIMULATION OF COMPRESSIBLE FLOWS USING THE FINITE-VOLUME METHOD". A dissertation submitted to the SWISS FEDERAL INSTITUTE OF TECHNOLOGY, ZURICH for the degree of Doctor of Technical Sciences, 2003.
16. Spalart, P. R., Jou W-H., Strelets M., Allmaras, S. R., "Comments on the Feasibility of LES for Wings and on a Hybrid RANS/LES Approach" Advances in DNS/LES, 1st AFOSR Int. Conf. on DNS/LES, Greyden Press, Columbus Oh, 4-8 August, 1997.
17. M. Shur, P.R. Spalart, M. Strelets and A. Travin, "Detached-eddy simulation of an airfoil at high angle of attach", 1999

18. A. Travin, M. Shur, M. Strelets and P. Spalart, "Detached-Eddy Simulation past a Circular Cylinder", *Journal of Flow, Turbulence and Combustion*, 63, 269-291, 1999.
19. G.S. Constantinescu, K.D. Squires, "LES and DES Investigations of Turbulent Flow over a Sphere", AIAA paper 2000-0540, 2000.
20. J.R. Forsythe, "Numerical Computation of Turbulent Separated Supersonic Flowfields", Doctoral Dissertation, Wichita State University, 2000.
21. J.R. Forsythe, K. D. Squires, K.E. Wurtzler, P.R. Spalart, "Detached-Eddy Simulation of Fighter Aircraft at High Alpha", AIAA paper, 2002-0591, January 2002.
22. K. D. Squires, J. R. Forsythe, S. A. Morton, D. C. Blake, M. Serrano, K.E. Wurtzler, W. Z. Strang, R.F. Tomaro, P.R. Spalart, "Analysis of Full Aircraft with Massive Separation using Detached-Eddy Simulation" *Computational Fluid Dynamics Journal ISCFD Japan*, Vol. 13, No. 3, January, 2005.
23. S.A. Morton, J.R. Forsythe, K.D. A. Mitchell, D. Hajek, "DES and RANS" Simulation of Delta Wing Vortical Flow", AIAA paper, 2002-0587, 2002.
24. K. D. Squires, J. R. Forsythe, S. A. Morton, W. Z. Strang, K.E. Wurtzler, R.F. Tomaro, M.J. Grismer, P.R. Spalart, "Progress on Detached-Eddy Simulation of Massively Separated Flows", AIAA paper, 2002-1021, January 2002.
25. S. A. Morton, J. R. Forsythe, K. D. Squires, K.E. Wurtzler, "Assessment of Unstructured Grids for Detached-Eddy Simulation of High Reynolds Number Separated Flows.", 8 ISGG Conference, Honolulu, June, 2002.
26. J.M. Weiss and W. A. Smith. "Preconditioning Applied to Variable and Constant Density Flows", *AIAA Journal*, 33(11):2050-2057, 1995.
27. Patankar, S. V., "Numerical Heat Transfer and Fluid Flow", McGraw-Hill, New York, 1980.
28. Beam, R. M., and Warming, R. F., "An Implicit Finite Difference Algorithm for Hyperbolic Systems in Conservation Law Form", *Journal of Computational Physics*, Vol. 22, pp. 87-110, 1976
29. Rhie, C. M., and Chow, W. L., "Numerical Study of the Turbulent Flow Past an Airfoil with Trailing Edge Separation." *AIAA Journal*, Vol. 21, pp. 1527-1532, 1984
30. Chorin, A. J., "A Numerical Method for Solving Incompressible Viscous Flow Problems," *Journal of Computational Physics*, Vol 2, No. 1, pp. 12-26, 1967.
31. Kwak, D., Chang, J. L., Shanks, S. P., and Chakravarthy, S. R., "A three dimensional incompressible Navier-Stokes Flow Solver using Primitive Variables," *AIAA Journal*, Vol 23, pp. 390-396, 1985.
32. Choi, Y. H., and Merkle, C. L., "The application of Preconditioning in Viscous Flows", *Journal of Computational Physics*, Vol. 105, pp. 207-233, 1993.

33. Turkel, E., "Preconditioned Methods for Solving the Incompressible and Low Speed Compressible Equations," *Journal of computational Physics*, Vol. 72, pp. 277-298, 1987.
34. Venkateswaran, S., Weiss, J. M. and Merkle, C. L., "Propulsion Related Flowfields Using the Preconditioned Navier-Stokes Equations," AIAA paper 92-3437, July 1992.
35. P. L. Roe, "Approximate Riemann Solvers, Parameters Vectors and Difference Schemes", *Journal of Computational Physics*, 43:357-372, 1981.
36. J. T. Batina, "A Fast Implicit Upwind Solution Algorithm for Three-Dimensional Unstructured Dynamic Meshes", AIAA Paper 92-0447, 1992.
37. N. T. Frink, "A Fast Upwind Solver for the Euler Equations on Three-Dimensional Unstructured Meshes", AIAA Paper 91-0102, January 1991.
38. V. Venkatakrishnan and D. J. Mavriplis, "Implicit Method for the Computation of Unsteady Flows on Unstructured Grids", Technical Report NASA CR-198206, Institute for Computer Applications in Science and Engineering, NASA Langley Research Center Hampton, VA 23681-0001, 1995.
39. P. R. Spalart and S. R. Allmaras, "A One-Equation Turbulence Model for Aerodynamic Flows", AIAA Paper 92-0439, January 1992.
40. O. Reynolds. "On the Extent and Action of the Heating Surface for Steam Boiler", *Proc. Manchester Lit. Phil. Soc.*, 14:7-12, 1874.
41. D. C. Wilcox. "Turbulence Modeling for CFD (2nd Edition)", DCW Insustries, Inc., California, 1998.
42. A. Travin, M. Shur, M. Strelets, and P. R. Spalart, "Physical and Numerical Upgrades in the Detached-Eddy Simulation of Complex Turbulent Flows", In 412 EUROMECH colloquium on LES of complex transitional and turbulent flows. Munich, 2000.
43. M. Strelets, "Detached Eddy Simulation of Massively Separated Flows" AIAA Paper 2001-0879, January 2001.
44. K. D. Squires, J. R. Forsythe, S. A. Morton, M. J. Grismer, and P. R. Spalart, "Progress on Detached-Eddy Simulation of Massively Separated Flows", AIAA Paper 2002-1021, 2002.
45. J. Dacles-Mariani, G. G. Zilliac, J. S. Chow, and P. Bradshaw. "Numerical / Experimental Study of a Wingtip Vortex in the Near Field", *AIAA Journal*, 33(9):1561-1568, 1995.
46. P. R. Spalart, "Young-Person's Guide to Detached-Eddy Simulation Grids", NASA/CR-2001-211031, pp. 23, July 2001.
47. P. D. Thomas and C. K. Lombard, "Geometric Conservation Law and its Applications to Flow Computations on Moving Grids", *AIAA Journal*, 17:1030-1037, 1979.

48. J. T. Batina. "Unsteady Euler Airfoil Solutions Using Unstructured Dynamic Meshes", *AIAA Journal*, 28(8):1381–1388, 1990.
49. J. T. Batina, "Unsteady Euler Algorithm with Unstructured Dynamic Mesh for Complex-Aircraft Aerodynamics Analysis", *AIAA Journal*, 29(3):327–333, 1991.
50. M. Murayama, K. Nakahashi, and K. Matsushima, "Unstructured Dynamic Mesh for Large Movement and Deformation", *AIAA Paper 2002-0122*, 2002.
51. C. Farhat, C. Degand, B. Koobus, and M. Lesoinne, "Torsional springs for two dimensional dynamic unstructured fluid meshes", *Computer Methods Appl. Mech. Engrg.*, 163:231–245, 1998.
52. X. Liu, N. Qin, and H. Xia, "Fast Dynamic Grid Deformation Based on Delaunay Graph Mapping", *Journal of Computational Physics*, 211(2):405–423, 2005.
53. J. W. Slater. ONERA M6 Wing: Study 1. NPARC Alliance Validation Archive, <http://www.grc.nasa.gov/WWW/wind/valid/m6wing/m6wing01/m6wing01.html>, 2002.
55. V. Schmitt and F. Charpin, "Pressure Distribution on the ONERA-M6-Wing at Transonic Mach Numbers", In *Experimental Data Base for Computer Program Assessment. Report of the Fluid Dynamics Panel Working Group 04*, AGARD AR 138, May 1979.
56. A. Le Moigne, "A Discrete Navier-Stokes Adjoint Method for Aerodynamic Optimization of Blended Wing-Body Configurations", PhD thesis, Cranfield University, United Kingdom, 2002.
57. B. J. Lee, C. S. Kim, C. Kim, O. H. Rho, and K. D. Lee, "Parallelized Design Optimization for Transonic Wings using Aerodynamic Sensitivity Analysis", *AIAA Paper 2002-0264*, 2002.
58. E. J. Neilsen and W. K. Anderson, "Recent Improvements in Aerodynamic Design Optimization on Unstructured Meshes", *AIAA Paper 2001-0596*, 2001.
59. E. Achenbach, "Distribution of Local Pressure and Skin Friction around a Circular Cylinder in Cross-Flow up to $Re = 5 \times 10^6$ ", *Journal of Fluid Mechanics*, 34(4):625–639, 1968.
60. G. Karypis and V. Kumar, "User Manual of METIS: A Software Package for Partitioning Unstructured Graphs, Partitioning Meshes and Computing Fill-Reduced Orderings of Sparse Matrices, Version 4.0", University of Minnesota, 1998.
61. Spalart, P., Deck, S., Shur, M., Squires, K., Strelets, M. K., and Travin, A., "A New Version of Detached-Eddy Simulation, Resistant to Ambiguous Grid Densities," *Theoretical and Computational Fluid Dynamics*. 0935-4964, pp.181-195, July 2006.
62. Bui, T., "A Parallel, Finite-Volume Algorithm for Large Eddy Simulation of Turbulent Flows," *NASA/TM-1999-206570*, 1999.
63. Bui, Trong Tri, "A parallel finite volume algorithm for large-eddy simulation of turbulent flows", Ph. D thesis, Stanford University, March 1998.

64. Shur, M., Spalart, P., et al., "Towards the prediction of noise from jet engines," *Int. J. Heat and Fluid Flow* 24, 551-561, 2003.
65. Lin, S. Y., Chen, Y. F., and Shih, S.C., "Numerical Study of MUSCL Schemes for Computational Aeroacoustics," AIAA paper 97-0023, Jan. 1997
66. Mohammed Gad-el-Hak, "Flow Control – Passive, Active and Reactive Flow Management, Cambridge University Press 2000.
67. John D. Anderson, JR., "Computational Fluid Dynamics – The basics with applications", McGraw-Hill Inc., 1995.
68. <http://cfd.mace.manchester.ac.uk/desider/>
69. Shia-Hui Peng, Werner Haase, "Advances in Hybrid RANS-LES Modelling", Papers Contributed to the 2007 Symposium of Hybrid RANS-LES Methods, Corfu, Greece, June 2007. Springer 2008.
70. <http://www.hrlm-3rd.gda.pl/>
71. Nikitin N. V., Nicoud F., Wasistho B., Squires K. D., Spalart, P.R., "An approach to wall modeling in Large-Eddy Simulations", *Phys. Fluids* 12, pp. 7-10, 2000
72. Menter, F.R., Kuntz, M., Bender, R., "A scale-adaptive simulation model for turbulent flow predictions", AIAA 2003-767, 2003.
73. Deck, S., "Zonal-Detached Eddy Simulation of the Flow around a High-Lift Configuration." *AIAA Journal* 43(11), 2372-2384, 2005.
74. Piomelli U., "Wall-layer models for large-eddy simulations", *Prog. Aerosp. Sci.* 44 6 437-446, 2008
75. Durrani, N, Qin, N., "Numerical Simulation of Flexible Flapping Airfoil Propulsion using Dynamic Mesh at Low Reynolds Numbers." AIAA-2008-654, 46th AIAA Aerospace Sciences Meeting and Exhibit, Reno, Nevada, Jan. 7-10, 2008.
76. A. Jameson, W. Schmidt, and E. Turkel, "Numerical Solutions of the Euler Equations by Finite Volume Methods Using Runge-Kutta Time-Stepping Schemes", AIAA Paper 1981-1259, 1981.
77. <http://www.grc.nasa.gov/WWW/wind/valid/raetaf/raetaf01/raetaf01.html>
78. Luo H., Baum, Joseph D., and Lohner R., "Extension of Harten-Lax-van Leer Scheme for Flows at All Speeds.", *AIAA Journal* 001-1452 vol. 43 no. 6 (1160-1166), 2005.
79. Liou, M.-S. and Steffen, C., "A New Flux Splitting Scheme," *J. Comput. Phys.*, Vol. 107, 23-39, 1993.
80. Liou, M.-S., "A Sequel to AUSM, Part II: AUSM+-up" *J. Comput. Phys.*, Vol. 214, 137- 170, 2006.
81. Edwards, J. R., Franklin, R., and Liou, M.-S., "Low-Diffusion Flux-Splitting Methods for Real Fluid Flows with Phase Transitions," *AIAA J.*, Vol. 38, 1624-1633, 2000.

82. Edwards, J. R. and Liou, M.-S., "Low-Diffusion Flux-Splitting Methods for Flows at All Speeds," AIAA J., Vol. 36, 1610-1617, 1998.
83. Kim, K. H., Kim, C., and Rho, O., "Methods for the Accurate Computations of Hypersonic Flows I. AUSMPW+ Scheme," J. Comput. Phys., Vol. 174, 38-80, 2001.
84. Harten, A., Lax, P.D., and van Leer, B., "On Upstream Differencing and Godunov-Type Scheme for Hyperbolic Conservation Laws," SIAM Review, Vol. 25, No. 1, p.35, 1983.
85. Toro, E. F., Spruce, M., and Speares, W., "Restoration of the Contact Surface in the HLL Riemann Solver," Shock Waves, Vol. 4, No. 25, 1994.
86. Davidson, L., "LESFOIL: A European project on large eddy simulations around a high-lift airfoil at high Reynolds number," Proceedings of ECCOMAS 2000, Barcelona, 11-14 September 2000.
87. S. Dahlstrom and L. Davidson, "LARGE EDDY SIMULATION OF THE FLOW AROUND AND AIRFOIL", AIAA 2001-0425, 39th AIAA Aerospace Sciences Meeting and Exhibit, Reno NV, 8-11 January 2001.
88. Huddeville, R., Piccin, O., and Cassouesalle, D., "Operation décrochage – mesurement de forttement sur profiles AS 239 et A 240 a la soufflerie F1 du CFM," Tech. Rep. RT-OA19/5025 (RT-DERAT 19/5025 DN), ONERA, 1987
89. Gleyzes, C., "Operation décrochage – resultats de la 2eme campagne d'essais a F2- mesures de pression et velocimetrie laser," Tech. Rep. RT-DERAT 55/5004, ONERA 1989.
90. Christopher P. Mellen, "Lessons from the European LESFOIL project on LES of flow around an airfoil", AIAA 2002-0111. 40th AIAA Aerospace Sciences Meeting and Exhibit, Reno , NV, January 14-17, 2002.
91. Cokljat, D. and Liu, F., "DES of turbulent flow over an airfoil at high incidence ," AIAA paper 2002-0590, at 40th Aerospace Sciences Meeting and Exhibit, 14-17 January 2002, Reno Nevada., 2002.
92. Schmidt, S. and Thiele F., "Detached Eddy Simulation of Flow around A-airfoil," Flow, Turbulence and Combustion, 71: 261-278, 2003.
93. P. Bradshaw, D. H. Ferriss and N. P. Atwell, "Calculation of boundary-layer development using the turbulent energy equation", Journal of Fluid Mechanics, 28:3:593-616, Cambridge University Press. Aerodynamics Division, National Physical Laboratory, Teddington, 1967.
94. Townsend, A. A., The Structure of Turbulent Shear Flow. Cambridge University Press.1956.
95. A. Keating, G. De Prisco, U. Piomelli, Interface conditions for hybrid RANS/LES calculations, Int. J. Heat and Fluid Flow, 27 (2006) 777-788, 2006.
96. Mueller, T. J., "Fixed and Flapping Wing Aerodynamics for Micro Air Vehicle Applications", Progress in Astronautics and Aeronautics Series, P. Zarchan, AIAA.

97. Knoller, R., "Die Gesetze des Luftwiderstandes," *Flug und Motortechnik* (Wien), Vol. 3, No. 21, pp. 1–7, 1909.
98. Betz, A., "Ein Beitrag zur Erklarung des Segefluges," *Zeitschrift fuer Flugtechnik und Motorluftschiffahrt*, Vol. 3, pp. 269–272, Jan. 1912.
99. Katzmayr, R., "Effect of Periodic Changes of Angle of Attack on Behavior of Airfoils," NACA Rept. 147, Oct. 1922 (translated from *Zeitschrift fuer Flugtechnik und Motorluftschiffahrt*, March 31, 1922, pp. 80–82, and April 13, pp. 95–101), 1922.
100. Birnbaum, W., "Das ebene Problem des schlagenden Flugels," *Zeitschrift f'ur Angewandte Mathematik und Mechanik*, Vol. 4, No. 4, pp. 277–292, 1924.
101. Birnbaum, W., "Der Schlag ugelpropeller und die kleinen Schwingungen elastisch befestigter Tragugel," *Zeitschrift fur Flugtechnik und Motorluftschiffahrt*, Vol. 15, , pp. 128–134 Nov.–Dec. 1924.
102. Theodorsen, T., "General Theory of Aerodynamic Instability and the Mechanism of Flutter", NACA, TR-496, 1935.
103. Garrick, I. E., "Propulsion of a Flapping and Oscillating Airfoil," NACA Rept. 567, 1936.
104. von Karman, T., and Burgers, J. M., "General Aerodynamic Theory-Perfect Fluids," *Aerodynamic Theory*, edited by W. F. Durand, Division E, Vol. 2, Julius–Springer, Berlin, 1943.
105. Silverstein, A., and Joyner, U. T., "Experimental Verification of the Theory of Oscillating Airfoils," NACA Report 673, 1939.
106. Bratt, J. B., "Flow Patterns in the Wake of an Oscillating Airfoil," *Aeronautical Research Council, R&M 2773*, March 1950.
107. Freymuth, P., "Propulsive Vortical Signature of Plunging and Pitching Airfoils," *AIAA Journal*, Vol. 26, No. 7, pp. 881–883, 1988.
108. Koochesfahani, M.M., "Vortical Patterns in the Wake of an Oscillating Airfoil," *AIAA Journal*, Vol. 27, No. 9, pp. 1200–1205, 1989.
109. Dohring, C.M., Platzer, M.F., Jones, K.D. and Tuncer, I.H., "Computational and Experimental Investigation of the Wakes Shed From Flapping Airfoils and Their Wake Interference/Impingement Characteristics, "Characterisation and Modification of Wakes from Lifting Vehicles in Fluids, Vol. 33, pp. 1–9, 1996.
110. Lai, J.C.S. and Platzer, M.F., "Jet Characteristics of a Plunging Airfoil," *AIAA Journal*, Vol. 37, No. 12, pp. 1529–1537, 1999.
111. Katz, J., and Weihs, D., "Hydrodynamic Propulsion by Large Amplitude Oscillation of an Airfoil with Chordwise Flexibility," *Journal of Fluid Mechanics*, Vol. 88, No. 3, pp. 485–497, 1978.

112. Murray, M. M., and Howle, L. E., "Spring Stiffness Influence on an Oscillating Propulsor," *Journal of Fluids and Structures*, Vol. 17, No. 7, pp. 915–926, 2003.
113. Isaac, K.M., Colozza, A. and Rolwes, J., "Force Measurements on a Flapping and Pitching Wing at Low Reynolds Numbers," AIAA paper 2006-450, 44th AIAA Aerospace Sciences Meeting and Exhibit, Reno, Nevada, 9-12 January 2006.
114. Heathcote, S. and Gursul, I., "Flexible Flapping Airfoil Propulsion at Low Reynolds Numbers," *AIAA Journal*, vol. 45, No. 5, pp. 1066-1079, 2007.
115. Blom, F. J., "Considerations on the Spring Analogy". *Int. J. Numer. Meth. Fluids*, 32:647–668, 2000.
116. Johnson, A. A. and Tezduyar T. E., "Simulation of Multiple Spheres Falling in a Liquid-filled Tube". *Comp. Meth. Appl. Mech. Eng.*, 134(4):351–373, 1996.
117. "Planetary Exploration using Biomimetics: An Entomopter for Flight on Mars", NASA Institute for Advanced Concepts (NIAC) Project Final Report, Ohio Aerospace Institute, October 2002
118. Solid State Aircraft, NASA Institute for Advanced Concepts (NIAC) Project Final Report, Ohio Aerospace Institute, May 2005
119. A. Jameson. "Time Dependent Calculations Using Multigrid with Application to Unsteady Flows past Airfoils and Wings," AIAA Paper 91-1596, June 1991.
120. Xueqiang Liu, Ning Qin, Hao Xia, "Fast dynamic deformation based on Delaunay graph mapping," *Journal of Computational Physics*, 211 (2006), pp 405-423
121. C. W. Hirt, A. A. Amsden, and J. L. Cook. An Arbitrary Lagrangian-Eulerian Computing Method for All Flow speeds. *Journal of Computational Physics*, 14(3):227–253, 1974 (reprinted in 1997).
122. Lewin, G. C., and Haj-Hariri, H., "Modelling Thrust Generation of a Two-Dimensional Heaving Airfoil in a Viscous Flow," *Journal of Fluid Mechanics*, Vol. 492, pp. 339-362, 2003.
123. Photograph by Sadatoshi Taneda, from Van Dyke, Milton, "An Album of Fluid Motion", The Parabolic Press, Stanford, Calif., 1982
124. C.W. Hirt, A. A. Amsden, and J.L. Cook. "An Arbitrary Lagrangian-Eulerian Computing Method for All Flow Speeds". *Journal of Computational Physics*, 14(3):227-253, 1974 (reprinted in 1997)
125. W.F. Noh. "CEL: A Time-Dependant Two-Space Dimensional Coupled Eulerian-Lagrangian Code." In B. Alder, S. Fernbach, and M. Rotenberg, editors, *Methods in Computational Physics*, pages 117-179. Academic Press, New York, 1964.
126. Menter, F.R., Kuntz, M, "Adaptation of Eddy Viscosity Turbulence Models to Unsteady Separated Flow Behind Vehicles." In: McCallen, R., Browand, F., Ross, J., (eds.) Symposium on "the aerodynamics of heavy vehicles: trucks, busses, and trains" Monterey, USA, 2-6 Dec 2002, Springer, Berlin Heidelberg New York, 2004.

127. Cantwell, B. and Coles, D., "An experimental study of entrainment and transport in the turbulent near wake of a circular cylinder." *Journal of Fluid Mechanics*, Vol. 136, pp. 321- 374, Nov. 1983.
128. <http://www.fluent.com/software/gambit>
129. Krishnan, V. and Squires, K. D., Forsythe, J. R., "Prediction of Flow Around a Circular Cylinder at High Reynolds Number", AIAA 2006-901, 44th AIAA Aerospace Sciences Meeting and Exhibit, Reno, Nevada, 9-12 January 2006.
130. Roshko, A., "Experiments on the Flow past a Circular Cylinder at Very High Reynolds Number", *Journal of Fluid Mechanics*, Vol. 10, No. 3, pp. 345-356, 1961.
131. Nunen, J. V., "Pressure and Forces on a Circular Cylinder in a Cross flow at High Reynolds Numbers", *Flow Induced Structural Vibrations*, Springer-Verlag, Berlin, pp. 748-754, 1974.
132. <http://www.pointwise.com>
- 133 Vassberg J. C., DeHaan M A., Rivers S. M., Wahls R. A., "Development of a Common Research Model for Applied CFD Validation Studies", AIAA-2008-6919, 2008.
134. <http://aac.larc.nasa.gov/tsab/cfdlarc/aiaa-dpw/>
135. Piomelli, U., "Wall layer models for LES", AIAA-2008-1319, 46th AIAA Aerospace Sciences Meeting and Exhibit. Reno, Nevada, 7-10 January 2008.
136. Batten, P., Goldberg, U., Chakravarthy, S., "LNS- an approach towards embeded LES". AIAA-2002-0427, 2002.
137. Tang, J., Viieru, J and Shyy W., "A Study of Aerodynamics of Low Reynolds Number Flexible Airfoils", *AIAA Paper*, AIAA 2007-4012, 37th AIAA Fluid Dynamics Conference and Exhibit, , Miami, FL. June 2007
138. Colloquium: "LES for external aerodynamic flows: status and prospects", Royal Aeronautical Society, Hamilton Place, London , 15th-16th March 2007
139. Heathcote, S., Wang, Z., and Gursul, I., "Effect of Spanwise Flexibility on Flapping Wing Propulsion", AIAA-2006-2870, 36th AIAA Fluid Dynamics Conference and Exhibit, San Francisco, California, June 5-8, 2006.
140. Ugo Piomelli, "Large-eddy and direct simulation of turbulent flows. CFD2001- a CFD Odyssey in annual conference of Canadian Society of CFD", 2001.
141. Spalart P. R., "Detached-Eddy Simulation", *Annual Review Fluid Mech.* 41:181-202, 2009.
142. Davidson, P.A., "Turbulence- An introduction for scientists and engineers", Oxford University Press, 2004.

List of Publications

Durrani N. and Qin N., "Numerical Simulation of Flexible Flapping Airfoil Propulsion using Dynamic Mesh at Low Reynolds Numbers", AIAA 2008-64, 46th AIAA Aerospace Sciences Meeting and Exhibit. Reno, Nevada, 7-10 January 2008.

Hamada, K, Smith T, Durrani N, Qin N, Howell RJ, "Unsteady Flow Simulation and Dynamic Stall around Vertical Axis Wind Turbine Blades", ASME Wind Energy Symposium, Reno, AIAA-2008-1319, 46th AIAA Aerospace Sciences Meeting and Exhibit. Reno, Nevada, 7-10 January 2008.

Edwards, J, Durrani, N, Howell RJ and Qin, N., "Wind Tunnel and Numerical Study of a Small Vertical Axis Wind Turbine", 27th ASME Wind Energy Symposium, AIAA-2008-1316, 46th AIAA Aerospace Sciences Meeting and Exhibit. Reno, Nevada, 7-10 January 2008.

Appendix A

3D preconditioning matrix

$$\underbrace{\Gamma \frac{\partial}{\partial \tau} \iiint_V Q dV}_{\text{Pseudotime term}} = -\mathbf{K}^{-1} \mathbf{K}^* \underbrace{\iint_A [\mathbf{F} - \mathbf{G}] dA}_{\text{Physical time term}} - \frac{\partial}{\partial t} \underbrace{\iiint_V W dV}_{\text{Physical time term}} \quad (\text{A.1})$$

$$\Gamma^{m-1} V^n \frac{\Delta Q^m}{\Delta \tau} = - \left[\mathfrak{R}^{m-1} + \frac{1}{\Delta t} \left(\mathbf{W}^{m-1} + \frac{\partial \mathbf{W}}{\partial \mathbf{Q}} \Delta \mathbf{Q}^m \right) V^n - \frac{\mathbf{W}^{n-1} V^{n-1}}{\Delta t} \right] \quad (\text{A.2})$$

$$\begin{aligned} V^n \frac{\Delta Q^m}{\Delta \tau} &= - \left(\Gamma^{m-1} + \frac{\Delta \tau}{\Delta t} \frac{\partial \mathbf{W}}{\partial \mathbf{Q}} \right)^{-1} \left[\mathfrak{R}^{m-1} + \frac{\mathbf{W}^{m-1} V^n - \mathbf{W}^{n-1} V^{n-1}}{\Delta t} \right] \\ V^n \frac{Q^m - Q^{m-1}}{\Delta \tau} &= - \left(\Gamma^{m-1} + \frac{\Delta \tau}{\Delta t} \frac{\partial \mathbf{W}}{\partial \mathbf{Q}} \right)^{-1} \left[\mathfrak{R}^{m-1} + \frac{\mathbf{W}^{m-1} V^n - \mathbf{W}^{n-1} V^{n-1}}{\Delta t} \right] \\ \frac{Q^m - Q^{m-1}}{\Delta \tau} &= - \frac{1}{V^n} \left(\Gamma^{m-1} + \frac{\Delta \tau}{\Delta t} \frac{\partial \mathbf{W}}{\partial \mathbf{Q}} \right)^{-1} \left[\mathfrak{R}^{m-1} + \frac{\mathbf{W}^{m-1} V^n - \mathbf{W}^{n-1} V^{n-1}}{\Delta t} \right] \\ \frac{Q^m - Q^{m-1}}{\Delta \tau} &= - \frac{1}{V^n} \left[\Gamma^* \right]^{-1} \left[\mathfrak{R}^{m-1} + \frac{\mathbf{W}^{m-1} V^n - \mathbf{W}^{n-1} V^{n-1}}{\Delta t} \right] \end{aligned} \quad (\text{A.3})$$

where, $\Gamma^* = \Gamma^{m-1} + \frac{\Delta \tau}{\Delta t} \frac{\partial \mathbf{W}}{\partial \mathbf{Q}}$, $\Theta = \frac{1}{U_r^2} - \frac{\rho_T}{\rho C_p}$

ε_0 is to facilitate higher order in time.

$$k_t = \varepsilon_0 \frac{\Delta \tau}{\Delta t}; \Gamma = \begin{bmatrix} \Theta & 0 & 0 & 0 & \rho_T \\ \Theta u & \rho & 0 & 0 & \rho_T u \\ \Theta v & 0 & \rho & 0 & \rho_T v \\ \Theta w & 0 & 0 & \rho & \rho_T w \\ \Theta H - 1 & \rho u & \rho v & \rho w & \rho_T H + \rho C_p \end{bmatrix};$$

$$\frac{\partial \mathbf{W}}{\partial \mathbf{Q}} = \begin{bmatrix} \rho_p & 0 & 0 & 0 & \rho_T \\ \rho_p u & \rho & 0 & 0 & \rho_T u \\ \rho_p v & 0 & \rho & 0 & \rho_T v \\ \rho_p w & 0 & 0 & \rho & \rho_T w \\ \rho_p H - 1 & \rho u & \rho v & \rho w & \rho_T H + \rho C_p \end{bmatrix}$$

$$K = \begin{bmatrix} 1 & 0 & 0 & 0 & 0 \\ -u & 1 & 0 & 0 & 0 \\ -v & 0 & 1 & 0 & 0 \\ -w & 0 & 0 & 1 & 0 \\ -(\mathbf{H} - |\mathbf{V}|^2) & -u & -v & -w & 1 \end{bmatrix}$$

$$|K| = 1$$

$$K^{-1} = \begin{bmatrix} 1 & 0 & 0 & 0 & 0 \\ u & 1 & 0 & 0 & 0 \\ v & 0 & 1 & 0 & 0 \\ w & 0 & 0 & 1 & 0 \\ \mathbf{H} & u & v & w & 1 \end{bmatrix}$$

$$K \frac{\partial W}{\partial Q} = \begin{bmatrix} \rho_p & 0 & 0 & 0 & \rho_T \\ 0 & \rho & 0 & 0 & 0 \\ 0 & 0 & \rho & 0 & 0 \\ 0 & 0 & 0 & \rho & 0 \\ -1 & 0 & 0 & 0 & \rho C_p \end{bmatrix}$$

$$\Gamma_{nc} = \begin{bmatrix} \Theta & 0 & 0 & 0 & \rho_T \\ 0 & \rho & 0 & 0 & 0 \\ 0 & 0 & \rho & 0 & 0 \\ 0 & 0 & 0 & \rho & 0 \\ -1 & 0 & 0 & 0 & \rho C_p \end{bmatrix}$$

$$\Gamma^* = \Gamma^{m-1} + \frac{\Delta \tau}{\Delta t} \frac{\partial W}{\partial Q}$$

$$\Gamma^* = \Gamma + k_t \frac{\partial W}{\partial Q}$$

$$\Gamma^* = K^{-1} \Gamma_{nc} + K K^{-1} k_t \frac{\partial W}{\partial Q}$$

$$\Gamma^* = K^{-1} \left(\Gamma_{nc} + k_t K \frac{\partial W}{\partial Q} \right)$$

(A.4)

$$\Gamma^* = K^{-1} \mathbf{B}$$

$$\Gamma^* = \begin{bmatrix} 1 & 0 & 0 & 0 & 0 \\ u & 1 & 0 & 0 & 0 \\ v & 0 & 1 & 0 & 0 \\ w & 0 & 0 & 1 & 0 \\ \mathbf{H} & u & v & w & 1 \end{bmatrix} \begin{bmatrix} \Theta + k_t \rho_p & 0 & 0 & 0 & \rho_T + k_t \rho_T \\ 0 & \rho + k_t \rho & 0 & 0 & 0 \\ 0 & 0 & \rho + k_t \rho & 0 & 0 \\ 0 & 0 & 0 & \rho + k_t \rho & 0 \\ -1 - k_t & 0 & 0 & 0 & \rho C_p + k_t \rho C_p \end{bmatrix}$$

$$\Gamma^* = \begin{bmatrix} 1 & 0 & 0 & 0 & 0 \\ u & 1 & 0 & 0 & 0 \\ v & 0 & 1 & 0 & 0 \\ w & 0 & 0 & 1 & 0 \\ \mathbf{H} & u & v & w & 1 \end{bmatrix} \begin{bmatrix} \Theta + k_t \rho_p & 0 & 0 & 0 & \rho_T + k_t \rho_T \\ 0 & \rho + k_t \rho & 0 & 0 & 0 \\ 0 & 0 & \rho + k_t \rho & 0 & 0 \\ 0 & 0 & 0 & \rho + k_t \rho & 0 \\ -1 - k_t & 0 & 0 & 0 & \rho C_p + k_t \rho C_p \end{bmatrix}$$

$$\Gamma^* = \begin{bmatrix} \Theta + k_i \rho_p & 0 & 0 & 0 & \rho_T k_{i1} \\ u(\Theta + k_i \rho_p) & k_{i1} & 0 & 0 & u \rho_T k_{i1} \\ v(\Theta + k_i \rho_p) & 0 & k_{i1} & 0 & v \rho_T k_{i1} \\ w(\Theta + k_i \rho_p) & 0 & 0 & k_{i1} & w \rho_T k_{i1} \\ \mathbf{H}(\Theta + k_i \rho_p) - k_{i1} & u k_{i1} & v k_{i1} & w k_{i1} & \mathbf{H} \rho_T k_{i1} + \rho C_p k_{i1} \end{bmatrix}$$

$$\mathbf{B} = \begin{bmatrix} \Theta + k_i \rho_p & 0 & 0 & 0 & \rho_T + k_i \rho_T \\ 0 & \rho + k_i \rho & 0 & 0 & 0 \\ 0 & 0 & \rho + k_i \rho & 0 & 0 \\ 0 & 0 & 0 & \rho + k_i \rho & 0 \\ -1 - k_i & 0 & 0 & 0 & \rho C_p + k_i \rho C_p \end{bmatrix}$$

Put $k_{i1} = 1 + k_i$

$$\mathbf{B} = \begin{bmatrix} \Theta + k_i \rho_p & 0 & 0 & 0 & \rho_T k_{i1} \\ 0 & \rho k_{i1} & 0 & 0 & 0 \\ 0 & 0 & \rho k_{i1} & 0 & 0 \\ 0 & 0 & 0 & \rho k_{i1} & 0 \\ -k_{i1} & 0 & 0 & 0 & \rho C_p k_{i1} \end{bmatrix}$$

$$|\mathbf{B}| = (\Theta + k_i \rho_p) (\rho k_{i1})^4 C_p + \rho_T k_{i1} \rho^3 (k_{i1})^4$$

$$|\mathbf{B}| = \rho^3 (k_{i1})^4 [\rho (\Theta + k_i \rho_p) C_p + \rho_T k_{i1}]$$

$$|\mathbf{B}| = \rho^3 (k_{i1})^4 \Psi$$

$$\text{where } \Psi = [\rho (\Theta + k_i \rho_p) C_p + \rho_T k_{i1}]$$

$$[\mathbf{B}]^{-1} = \frac{[(-1)^{i+j} a_{i,j}]^T}{|\mathbf{B}|}$$

$$a_{1,1} = (\rho k_{i1})^4 C_p$$

$$a_{1,2} = 0, a_{1,3} = 0, a_{1,4} = 0$$

$$a_{1,5} = \rho^3 (k_{i1})^4$$

$$a_{2,1} = 0, a_{3,1} = 0, a_{4,1} = 0$$

$$a_{5,1} = -\rho_T \rho^3 (k_{i1})^4$$

$$a_{2,2} = (\Theta + k_i \rho_p) (\rho k_{i1})^3 C_p + k_{i1} \rho_T k_{i1} (\rho k_{i1})^2$$

$$a_{2,2} = \rho^2 (k_{i1})^3 [(\Theta + k_i \rho_p) \rho C_p + \rho_T k_{i1}]$$

$$a_{2,2} = \rho^2 (k_{i1})^3 \Psi$$

$$a_{3,3} = \rho^2 (k_{i1})^3 \Psi$$

$$a_{4,4} = \rho^2 (k_{i1})^3 \Psi$$

$$a_{5,5} = (\Theta + k_i \rho_p) (\rho k_{i1})^3$$

$$\mathbf{B} = \begin{bmatrix} \Theta + k_i \rho_p & 0 & 0 & 0 & \rho_T k_{i1} \\ 0 & \rho k_{i1} & 0 & 0 & 0 \\ 0 & 0 & \rho k_{i1} & 0 & 0 \\ 0 & 0 & 0 & \rho k_{i1} & 0 \\ -k_{i1} & 0 & 0 & 0 & \rho C_p k_{i1} \end{bmatrix}$$

$$\mathbf{B}^{-1} = \begin{bmatrix} \frac{\rho C_p}{\Psi} & 0 & 0 & 0 & \frac{-\rho_T}{\Psi} \\ 0 & \frac{1}{\rho k_{i1}} & 0 & 0 & 0 \\ 0 & 0 & \frac{1}{\rho k_{i1}} & 0 & 0 \\ 0 & 0 & 0 & \frac{1}{\rho k_{i1}} & 0 \\ \frac{1}{\Psi} & 0 & 0 & 0 & \frac{(\Theta + k_i \rho_p)}{k_{i1} \Psi} \end{bmatrix}$$

$$[\Gamma^*]^{-1} = [K^{-1} \mathbf{B}]^{-1}$$

$$[\Gamma^*]^{-1} = \mathbf{B}^{-1} K$$

$$[\Gamma^*]^{-1} = \begin{bmatrix} \frac{\rho C_p}{\Psi} & 0 & 0 & 0 & \frac{-\rho_T}{\Psi} \\ 0 & \frac{1}{\rho k_{i1}} & 0 & 0 & 0 \\ 0 & 0 & \frac{1}{\rho k_{i1}} & 0 & 0 \\ 0 & 0 & 0 & \frac{1}{\rho k_{i1}} & 0 \\ \frac{1}{\Psi} & 0 & 0 & 0 & \frac{(\Theta + k_i \rho_p)}{k_{i1} \Psi} \end{bmatrix} \begin{bmatrix} 1 & 0 & 0 & 0 & 0 \\ -u & 1 & 0 & 0 & 0 \\ -v & 0 & 1 & 0 & 0 \\ -w & 0 & 0 & 1 & 0 \\ -(\mathbf{H} - |V|^2) & -u & -v & -w & 1 \end{bmatrix}$$

$$[\Gamma^*]^{-1} = \begin{bmatrix} \frac{\rho C_p + \rho_T (\mathbf{H} - |V|^2)}{\Psi} & \frac{u \rho_T}{\Psi} & \frac{v \rho_T}{\Psi} & \frac{w \rho_T}{\Psi} & \frac{-\rho_T}{\Psi} \\ \frac{u}{\rho k_{i1}} & \frac{1}{\rho k_{i1}} & 0 & 0 & 0 \\ \frac{v}{\rho k_{i1}} & 0 & \frac{1}{\rho k_{i1}} & 0 & 0 \\ \frac{w}{\rho k_{i1}} & 0 & 0 & \frac{1}{\rho k_{i1}} & 0 \\ \frac{k_{i1} - (\mathbf{H} - |V|^2)(\Theta + k_i \rho_p)}{k_{i1} \Psi} & \frac{-u(\Theta + k_i \rho_p)}{k_{i1} \Psi} & \frac{-v(\Theta + k_i \rho_p)}{k_{i1} \Psi} & \frac{-w(\Theta + k_i \rho_p)}{k_{i1} \Psi} & \frac{(\Theta + k_i \rho_p)}{k_{i1} \Psi} \end{bmatrix}$$

$$\Psi = [\rho(\Theta + k_i \rho_p) C_p + \rho_T k_{i1}]$$

$[\Gamma^*]^{-1}$ is the required preconditioning inverse matrix.

Appendix B

Implementation of reading the Gridgen FVUNS format input in DGDES – A test case of DLR-F6 Aircraft (wing-body-nacelle)

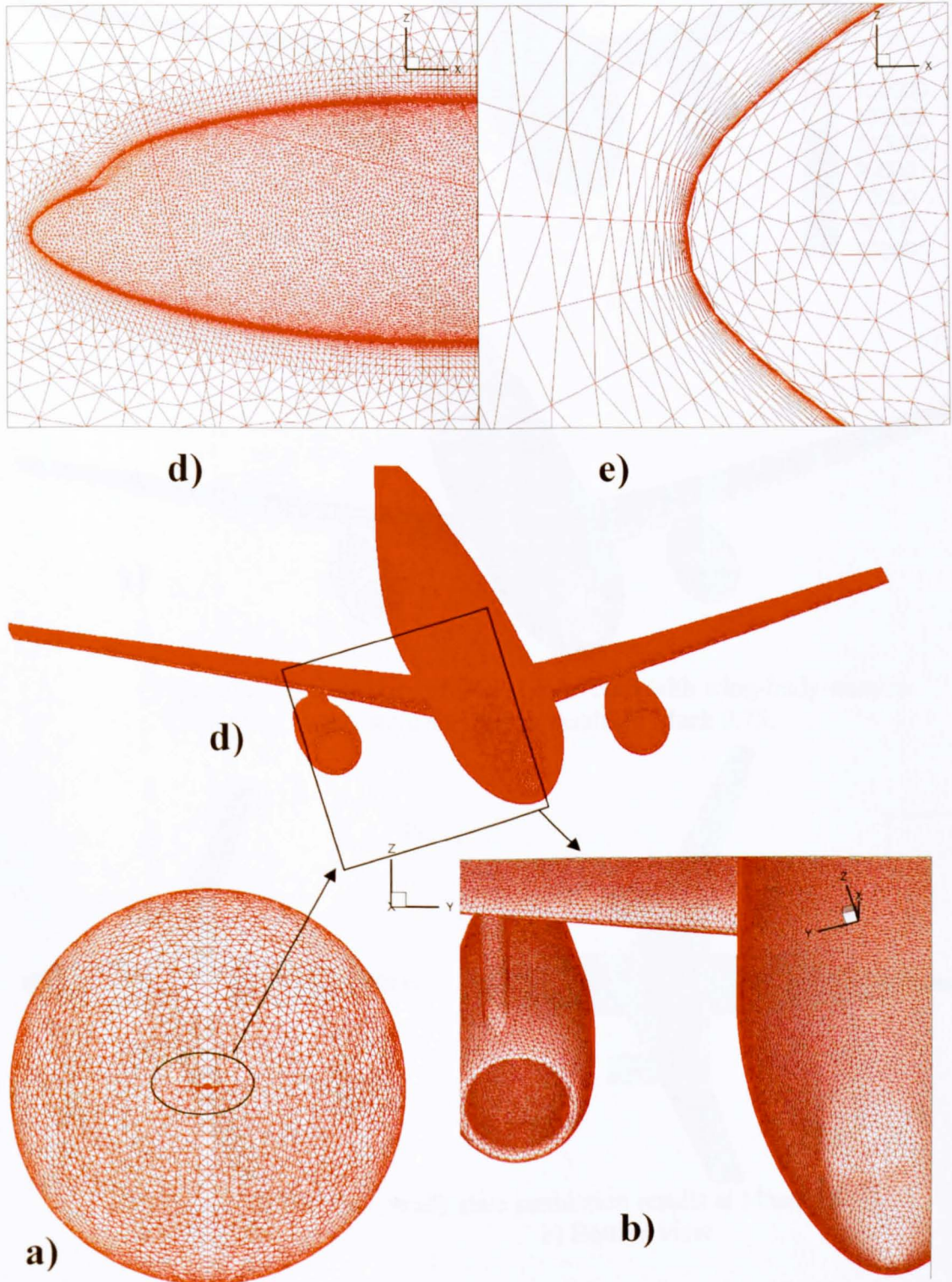


Figure A.1 a) Domain mesh with DLR-F6 wing-body-nacelle inside b) Zoom view of wing-body-nacelle section c) Surface mesh over DLR-F6 d) Symmetry plane view of the mesh over DLR-F6 e) Closeup view of nose section of the fuselage.

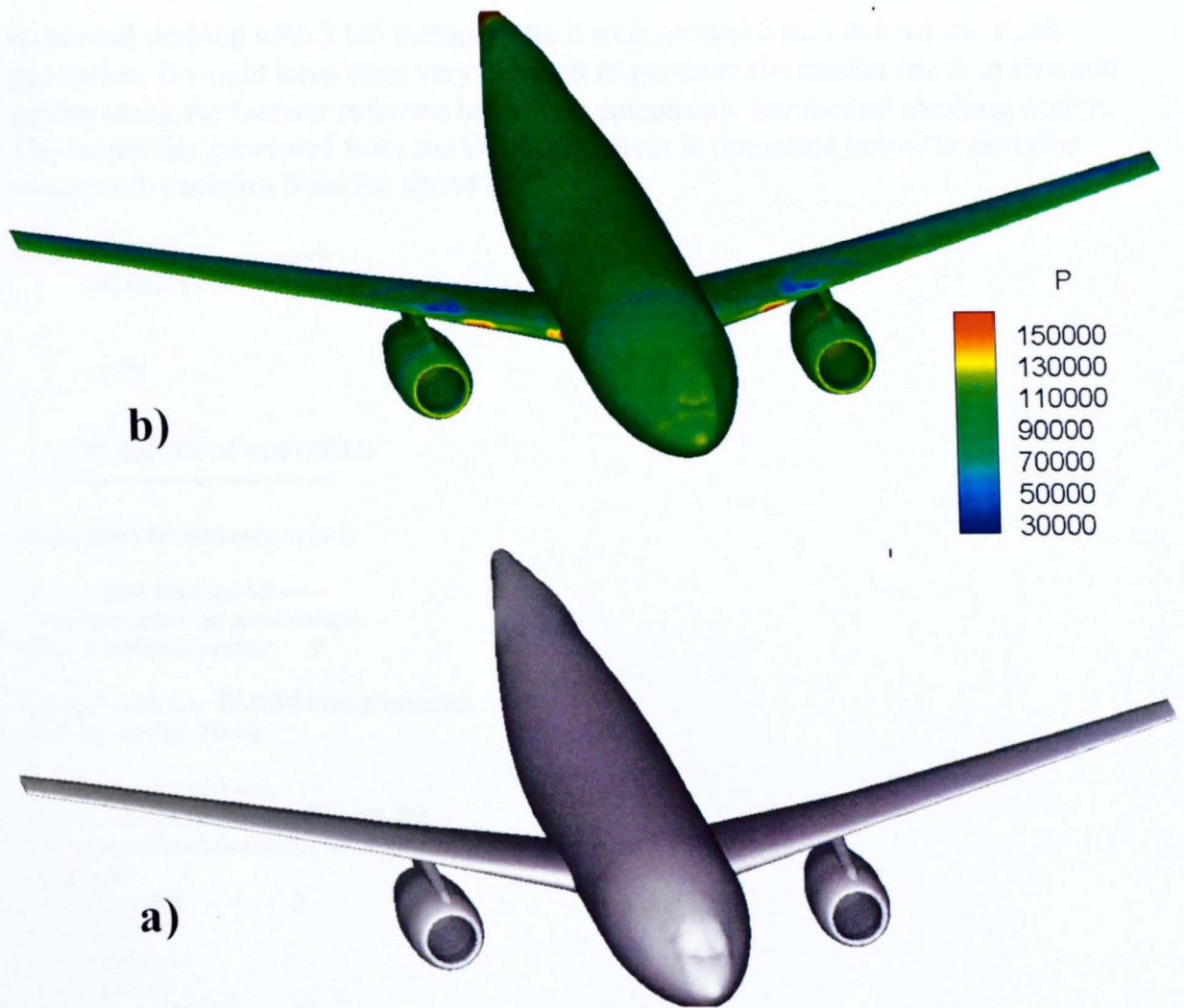


Figure A.2 a) Geometry of DLR-F6 Aircraft with wing-body-nacelle
 b) Laminar steady state simulation results at Mach 0.75.

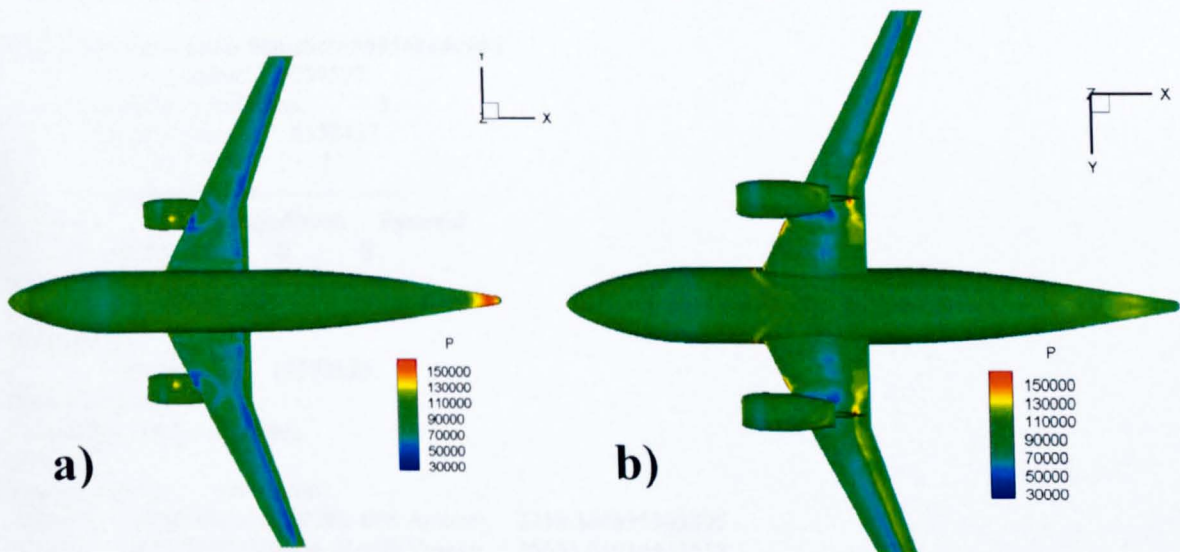


Figure A.3 Laminar steady state simulation results at Mach 0.75
 a) Top view
 b) Bottom view

Figure A.1 presents the different views with varying details of the mesh generated by the author using Gridgen software and imported in the DGDES solver. This mesh consists of 6.15 million cells with 12.37 million faces. It is generated using Gridgen

on normal desktop with 3 Gb memory and it took around 5 minutes for the mesh generation. It would have been very difficult to generate the similar mesh in size and quality using the Gambit software having no anisotropic tetrahedral meshing option. The output file generated from the DG-DES solver is presented below to describe some mesh statistics from the above file.

```
+-----+
      DG-DES v-1.0
```

By

UNIVERSITY OF SHEFFIELD

```
+-----+
```

Please select the start options (0-1)

```
0-->----Start from scratch-----
1-->Restart from last saved dataset
Selected option is option= 0
```

```
Selected mesh file: DLR-F6 final-generic.inp
Selected .ini file: F6.ini
```

```
----- Invoke fortex3d -----
Calling Grid Reader to read the mesh file
The selected mesh format is FieldView Unstructured Format...FVUNS
Zonenum= 1
BoundaryTable 3
  -1 Solid
  -6 Symmetry
  -2 Farfield
Nodes= 1059597
Faces(boundary)= 130502
Sum of boundary faces= 130502
Number of boundary conditions= 3
```

```
##### Mesh Statistics#####
```

```
  No of nodes: 1059597
  No of boundary conditions: 3
  No of elements: 6152437
  No of Zones: 1
```

```
-----Element Type-----
  Brick  Tetra Wedge/Prism  Pyramid
    0  6152437    0    0
```

```
File read successfully
Mesh Reading Completed.....
Formatting...
  No of faces: 12370125
```

```
Done Formatting.....
Calculating mesh parameters
Done.....
```

```
Parsing init file..... ..Mesh Info..
Amin= 5.3586309290383918E-005 Amax= 2259.304625303595
Vmin= 3.1229750752069467E-006 Vmax= 35631.61014411512
done.
```